SEMICONDUCTING AND DIELECTRIC PROPERTIES OF BARIUM TITANATES, TANTALATES AND NIOBATES WITH PEROVSKITE STRUCTURE

BY
TARAS KOLODIAZHNYI, M.S.

A Thesis
Submitted to the School of Graduate Studies
In Partial Fulfillment of the Requirements
For the Degree
Doctor of Philosophy

McMaster University

SEMICONDUCTING AND DIELECTRIC PROPERTIES OF BARIUM TITANATES, TANTALATES AND NIOBATES WITH PEROVSKITE STRUCTURE

DOCTOR OF PHILOSOPHY (2002) McMaster University
(Materials Science and Engineering) Hamilton, Ontario

TITLE:	Semiconducting and dielectric properties of barium titanates, tantalates and niobates with perovskite structure
AUTHOR:	Taras Kolodiazhnyi
SUPERVISOR:	Professor Anthony Petric
NUMBER OF PAGES:	xviii, 197

Abstract

The dielectric and semiconducting properties of two types of ceramics (n-type $BaTiO_3$ and dielectric $Ba(B'_{1/3}B''_{2/3})O_3$ where B' = Mg, Zn, Ni, and B'' = Nb, Ta) were characterized.

Complex impedance analysis and dc conductivity measurements of samples prepared at various P_{O_2} have ruled out oxygen chemisorption in favor of interfacial segregation of cation vacancies as the cause of the positive temperature coefficient of resistivity (PTCR) effect in n-type $BaTiO_3$.

The effect of preparation conditions, sintering atmosphere, stoichiometry, and post-sinter anneal on the defect chemistry of $BaTiO_3$ was studied using the electron paramagnetic resonance (EPR) technique. Several paramagnetic defects such as, Ti^{3+}, V_{Ba}, and V_{Ti} were detected and identified by EPR.

Current-voltage characteristics ($I - V$) of PTCR $BaTiO_3$ were analyzed in light of space-charge-limited-current, trap-filled-limited-current , Frenkel-Poole, small polaron, and double-Schottky barrier models. It was shown that for the double-Schottky barrier model, a partial stabilisation of the potential barrier is expected when the Fermi level is pinned at grain boundaries by a high density of the interface states. The deviation of $I - V$ characteristics of $BaTiO_3$ in the region of the PTCR effect can be explained by dependence of the population of the interface electron states on applied voltage.

Based on the Seebeck and Hall effect measurements, it was found that in the range of 100 - 300 K, the drift mobility of electrons in $BaTiO_3$ is not thermally activated, which supports the concept of conduction band electron transport rather than small radii polaron hopping. However, further study over a wider temperature range and on better quality crystals is required to unequivocally clarify the electron transport mechanism in $BaTiO_3$.

Phase composition, degree of cation ordering, and dielectric properties of complex perovskites with general formula $Ba(B'_{1/3}B''_{2/3})O_3$ where B' = Mg, Zn, Ni, and B'' = Nb, Ta were analyzed. It was shown that in $Ba(Mg_{1/3}Ta_{2/3})O_3$ both intrinsic and extrinsic dielectric loss affect the Q-factor, whereas in $Ba(Mg_{1/3}Nb_{2/3})O_3$ and $Ba(Ni_{1/3}Nb_{2/3})O_3$ extrinsic factors such as the second phase and point defects dominate the dielectric loss at microwave frequencies.

Acknowledgements

There is a number of people who helped me to accomplish this task and I want to express my gratitude to everyone.

First of all, I owe my special thanks to Prof. A. Petric, my supervisor, for his guidance, assistance and generous support of this work. He provided a knowledgeable direction, advice and opportunity to interact with international scientific community. I also wish to thank Prof. G. Johari for his important role in this project, particularly for his sincere interest, support and numerous technical resources.

Thanks are due to Prof. A. Belous and his group (Dr. O. Yanchevski, Dr. O. Vyunov, and Dr. O. Ovchar) from the Institute of General and Inorganic Chemistry (Kyiv, Ukraine) for their encouragement and fruitful co-operation in X-ray diffraction analysis and synthesis of several dielectric compounds.

I am grateful to a number of professors and graduate students from other departments and universities whose help and encouragement were very important. Particularly, Prof. J. Preston from Dept. of Engineering Physics for expert advice during the research, Prof. J. Barbier and Prof J. Greedan from Dept. of Chemistry for assistance in TEM and X-ray analysis, Prof. T. Timusk from Dept. of Physics and Astronomy for his valuable comments about measurements at cryogenic temperatures, Prof. J. Rink from Dept. of Geology and Dr. J Bartoll (a visiting post-doc) for their advice and interest in EPR measurements. I'm thankful to C. Bridges and A. Safa-Sefat for measurements of thermoelectric power and Prof. H. Kleinke from Dept. of Chemistry, University of Waterloo, for his comments on Seebeck effect.

I want to thank Prof. M. Niewczas for introducing me to the field of transmission electron microscopy and also for his help with Hall effect measurements which was always in time.

I wish to acknowledge several people from ComDev Corp. including A. Zybura and W. Fitzpatric for their technical consulting on microwave measurements and providing me with several dielectric resonator standards.

Technical resources provided by Prof. P. Smith and Prof. M Jamal Deen from the Communication Research Laboratory, McMaster, are greatly appreciated. I also want to thank Dr. O. Marinov for his advice on microwave measurements and for other useful discussions.

I want to acknowledge the timely help of technical personal, namely F. Pearson, A. Duft, F. Gibbs, E. McCaffery, C. Barry, G. Timmins, H. Dabkowska, A. Dabkowski, J. Garret and G. Wilson (University of Guelph)

I want to thank my colleagues, who contributed to my research and who made my stay at McMaster so pleasant. It is difficult to include all the names but I want to acknowledge Dr. S. Hui, Dr. I.

Zhitomirsky, Dr. D. Malakhov, J. Wu, X. Deng, G. Tsintzilonis, L. Yamarte, R. Dermishi, J. Wang, A. Obuchovska, H. Zurab and J. Duquette.

I wish to acknowledge the financial assistance of the Natural Sciences and Engineering Research Council of Canada for a graduate scholarship.

Finally I want to add a word of thanks to my friends, Doahna Diongson, Vlad and Lena Zamlynny, Svitlana Golego whom I met on Canadian soil; and to my late friend and best critic Nick Golego for their human support which I needed so much.

Contents

1 Introduction **1**

2 Physical and chemical properties of $BaTiO_3$ **4**

2.1 Crystallographic structure and dielectric properties 4

2.1.1 The prototype structure of $BaTiO_3$ 4

2.1.2 Structural phase transitions 5

2.1.3 Ferroelectricity 6

2.2 Defect chemistry 9

2.2.1 BaO-TiO_2 phase composition 10

2.2.2 Defect chemistry of undoped and acceptor doped $BaTiO_3$ 11

2.2.3 Defect chemistry of donor doped $BaTiO_3$ 15

2.2.4 Interfacial segregation of defects 18

2.3 Band structure and conductivity of $BaTiO_3$ 19

2.3.1 Bulk electronic structure of $BaTiO_3$ 19

2.3.2 Surface electronic structure of $BaTiO_3$ 21

2.3.3 Electron transport in $BaTiO_3$ 24

2.3.4 Resistivity anomaly in $BaTiO_3$ ceramics 27

3 $Ba(B'_{1/3}B''_{2/3})O_3$ perovskites **33**

3.1 Dielectrics for microwave band applications 34

3.1.1 Concept of a dielectric resonator 34

3.1.2 Main requirements for a dielectric resonator 35

3.1.3 Current microwave dielectrics and future needs 36

3.2 Origin of dielectric loss at microwave frequencies 38

3.2.1 Extrinsic losses 38

3.2.2 Intrinsic losses 39

3.3 Structure and properties of Ba(B$'_{1/3}$B$''_{2/3}$)O$_3$ perovskites 42

3.3.1 Types of ordering in Ba(B$'_{1/3}$B$''_{2/3}$)O$_3$ perovskite 42

3.3.2 Dielectric properties of Ba(B$'_{1/3}$B$''_{2/3}$)O$_3$ perovskites 45

3.3.3 Aspects of synthesis of Ba(B$'_{1/3}$B$''_{2/3}$)O$_3$ perovskites 46

4 Experimental **48**

4.1 Sample preparation 48

4.1.1 Nominal composition 49

4.1.2 Preparation process 50

4.2 Thermal, crystallographic and microstructure analysis 52

4.2.1 Thermal analysis 52

4.2.2 Crystallographic analysis 52

4.2.3 Microstructure analysis 52

4.3 Measurements of electronic and dielectric properties 53

4.3.1 Electrodes 53

4.3.2 Low-field DC conductivity measurements 54

4.3.3 Measurements of current-voltage characteristics 54

4.3.4 Complex impedance measurements 54

4.3.5 Electron paramagnetic resonance measurements 55

4.3.6 Seebeck coefficient measurements 55

4.3.7 Dielectric measurements in X-band 56

5 BaTiO$_3$: Synthesis and low field resistivity **58**

5.1 Synthesis 58

5.1.1 Thermal Analysis 59

5.1.2 Phase composition 60

5.1.3 Density and microstructure 61

5.2 Electrodes 63

5.2.1 Introduction 63

5.2.2 Results and discussion 65

5.3 Room temperature DC resistivity 68
5.3.1 Introduction 68
5.3.2 Results and discussion 70
5.4 Effect of P_{O_2} on resistivity 72
5.4.1 Introduction 72
5.4.2 Results and discussion 73

6 Thermoelectric power, Hall effect and mobility 85
6.1 Inroduction 85
6.2 Experimental 86
6.3 Results and discussion 87
6.3.1 Single crystal 87
6.3.2 $BaTiO_3$ sintered at $P_{O_2}=10^{-17}$ atm 91
6.3.3 $BaTiO_3$ sintered at $P_{O_2}=10^{-15}$ atm 94
6.3.4 Activation energy of grain bulk and grain boundary resistance 97

7 Electron paramagnetic resonance of $BaTiO_3$ 104
7.1 Introduction 104
7.2 Experimental 105
7.3 Results and discussion 106
7.3.1 EPR signal associated with n-type conductivity in $BaTiO_3$ 106
7.3.2 EPR signals with g = 1.974 and g = 2.004 108
7.3.3 Temperature dependence of EPR features 111
7.4 Conclusions 119

8 Current-voltage dependence of n-doped $BaTiO_3$ 120
8.1 Introduction 120
8.2 Experiment 121
8.3 Results and discussion 122
8.3.1 Space charge limited current model 124
8.3.2 Frenkel-Poole effect 125
8.3.3 Small radii polaron transport in $BaTiO_3$ 127
8.3.4 Double-Schottky barrier model 128
8.4 Conclusions 134

9 Synthesis and dielectric properties of $Ba(Mg_{1/3}Ta_{2/3})O_3$ 135

9.1 Introduction 135

9.2 Experimental procedure 136

9.3 Synthesis 137

9.3.1 Thermal analysis 137

9.3.2 Phase composition 138

9.3.3 1:2 cation ordering 141

9.3.4 Microstructure and density 143

9.4 Dielectric properties 145

9.5 Discussion 148

9.6 Conclusions 150

10 Synthesis and properties of BMN, BZN, BNN and BNT 151

10.1 Introduction 151

10.2 Synthesis of BMN, BZN, BNN, and BNT 152

10.2.1 Thermal analysis 153

10.2.2 Phase composition 153

10.2.3 1:2 cation ordering 156

10.3 Density and microstructure 163

10.4 Dielectric properties 167

10.4.1 dielectric constant 167

10.4.2 Q-factor 167

10.4.3 Temperature coefficient of the resonance frequency 170

10.5 Conclusions 171

11 Summary 172

List of Figures

2.1 Ideal perovskite structure 5

2.2 Temperature dependence of unit cell parameters of $BaTiO_3$. From Ref. [22] 5

2.3 Structure of tetragonal $BaTiO_3$ showing development of electric dipole moment of the unit cell. The arrows indicate the directions of displacement of Ti and O ions along [100]. 6

2.4 Temperature dependence of dielectric permittivity of single crystal $BaTiO_3$ along a -axis and c-axis (according to Merz [31]). 7

2.5 Disordered structure of $BaTiO_3$ in cubic phase. From ref. [59] 10

2.6 The phase diagram of the BaO–TiO_2 system. From ref. [85] 11

2.7 Equilibrium electrical conductivity of undoped $BaTiO_3$ (Ba/Ti=1.000) from Ref.[89] 12

2.8 Equilibrium electrical conductivity of undoped and Al-doped $BaTiO_3$ at 1000 °C. Concentrations of Al in molar ppm (gram atoms Al per 10^6 formula units $BaTiO_3$) from Ref. [90] 14

2.9 Equilibrium electrical conductivity of $BaTiO_3$ at 1000 °C with increasing additions of Nb and with Ba/Ti+Nb=1.00. From ref. [99] 16

2.10 Equilibrium electrical conductivity at 1300 °C of $BaTiO_3$, undoped and doped with different amounts of Ce. From ref. [89] 17

2.11 Symmetry-adapted linear combinations of oxygen $2p$ orbitals arising in TiO_6 octahedron, shown with a bonding combination of an appropriate Ti orbital. The type of bonding (σ or π) is indicated. Only one of the triply degenerate Ti 3d t orbitals in the cubic $BaTiO_3$ is shown. 20

2.12 Schematic energy-level diagram for $BaTiO_3$ 21

2.13 Splitting of d orbitals resulting from the tetragonal distortion of an oxygen octahedron 22

2.14 Band structures for $BaTiO_3$ in the cubic phase from ref. [107]. a) Surface-projected bulk band structure. b) BaO-terminated surface. c) TiO_2-terminated surface. The zero of energy corresponds to the bulk valence-band maximum. Only Ti 3d conduction bands are shown. 23

2.15 Progress in optimization of the PTCR behaviour of $BaTiO_3$ ceramics. 27

2.16 Schematic of a) the band energy diagram of the double Schottky barrier and b) the charge density distribution at the grain boundary of $BaTiO_3$. The negative GB charge, Q_{GB}, and positive charge of the depletion layer Q_b of thickness b are indicated. The potential barrier and the valence and conduction band edges are depicted as φ_0, E_v, and E_c respectively. The energy of the interface electron states E_t and the Fermi level E_F are also indicated. 29

2.17 Ferroelectric domain configuration at the GB of semiconducting $BaTiO_3$. The head of the vector of spontaneous polarization P_s has a positive charge, whereas the tail has a negative charge. The GB charge associated with the spontaneous polarization is equal to the difference between the normal components of the P_s of grain I and II. From Ref. [155] 31

3.1 Electric and magnetic field distribution in $TE_{01\delta}$ and $TM_{01\delta}$ mode DR. Only equatorial and meridian planes are shown. From ref [173]. 34

3.2 Two types of $Ba(B'_{1/3}B''_{2/3})O_3$ crystal structures: disordered a), and ordered b). . . 43

4.1 Schematic of the sample holder unit for thermopower measurements 56

5.1 DTA and TG curves of $BaCO_3$ 59

5.2 DTA and TG curves of $BaCO_3$ +TiO_2 60

5.3 XRD patterns of 0.4 at.% Y-doped $BaTiO_3$ samples with different (Ba+Y)/Ti ratio sintered in air at 1300 °C. The Ba_2TiO_4 phase is indicated by * 62

5.4 Scanning electron micrographs of the polished and thermally etched sections of $Ba_{1-x}Y_xTiO_3$ samples with a) x = 0, b) x = 0.001, c) x = 0.003, d) x = 0.004, e) x = 0.006, and f) x = 0.008 sintered in air at 1380 °C. The white bar represents 20 μm. 63

5.5 Scanning electron micrographs of the polished and thermally etched sections of $Ba_{1-x}Y_xTiO_3$ samples with a) x = 0, b) x = 0.002, c) x = 0.004, and d) x = 0.008, sintered in forming gas at 1380 °C. The white bar represents 50 μm. 64

5.6 Time dependence of the low field electrical resisitivity of $Ba_{0.998}Y_{0.002}TiO_3$ ceramics with In-Ga, Ni, and Al electrodes 66

5.7 Complex impedance of $Ba_{0.998}Y_{0.002}TiO_3$ ceramics with In-Ga electrodes. 67

5.8 Time dependence of the low field electrical resisitivity of $Ba_{0.998}Y_{0.002}TiO_3$ ceramics with Ag, Au, and Pt electrodes 68

5.9 Schematic of the band diagram for a Schottky barrier 69

5.10 Room temperature resistivity of $Ba_{1-x}Y_xTi_{1.0}O_3$ (x=0, 0.0002, 0.0005, 0.001, 0.002, 0.003, 0.004) sintered at 1380 °C in air and forming gas 70

5.11 Room temperature resistivity of $Ba_{1-x}Y_xTi_{1.02}O_3$ (x=0, 0.001, 0.002, 0.003, 0.004, 0.005, 0.006, 0.008) sintered at 1380 °C in air and forming gas. 71

5.12 Room temperature resistivity of $Ba_{1+x}Y_{0.002}Ti_{1.0}O_3$ (x=0, 0.006, 0.016, 0.046) sintered at 1380 °C in air and forming gas. 72

5.13 Complex impedance of $Ba_{0.998}Y_{0.002}Ti_{1.0}O_3$ sintered at a) $P_{O_2} = 10^{-17}$ atm, b) $P_{O_2}= 10^{-15}$ atm, c) $P_{O_2}= 10^{-12}$ atm, d) $P_{O_2}= 0.2$ atm at 1380 °C. All spectra were measured at 77 K. The letters B and GB indicate grain bulk and grain boundary. . . 75

5.14 Complex impedance of $Ba_{0.998}Y_{0.002}Ti_{1.0}O_3$ sintered at $P_{O_2}= 0.2$ atm and measured at 77 K. The letters B and GB indicate grain bulk and grain boundary resistivity. . 76

5.15 Frequency dependence of the real part of dielectric constant of $Ba_{0.998}Y_{0.002}Ti_{1.0}O_3$ sintered at various P_{O_2}. The solid line represents the ε' of undoped $BaTiO_3$ sintered in air at 1380 °C. All spectra were measured at 77 K. 77

5.16 Grain bulk conductivity of $Ba_{0.998}Y_{0.002}Ti_{1.0}O_3$ sintered at vaious P_{O_2} and measured at 77 K. 78

5.17 Time dependence of the ratio of the concentration of chemisorbed oxygen at the center of the plane sheet of thickness 1.2 mm to the concentration at the surface, calculated according to Eq. 5.6 for different temperatures. 79

5.18 Complex impedance of the $Ba_{0.996}Y_{0.004}TiO_3$ samples sintered at $P_{O_2}=10^{-17}$ atm and annealed at 800 °C in air for 2 hours. The spectra were measured at 77 K. . . . 80

5.19 Frequency dependence of dielectric constant of the $Ba_{0.996}Y_{0.004}TiO_3$ samples sintered at $P_{O_2}=10^{-17}$ atm and annealed at 800 °C in air for 2 hours. The measurements were performed at 77 K. 81

5.20 Temperature dependence of resistivity of the $Ba_{0.996}Y_{0.004}TiO_3$ samples of 1 mm thickness sintered at $P_{O_2}=10^{-12}$ atm and annealed at different temperatures in air for 2 hours: a) as sintered, b) 800 °C, c) 1000 °C, d) 1250 °C. 82

5.21 Temperature dependence of resistivity of the $Ba_{0.996}Y_{0.004}TiO_3$ samples reported in Fig.5.20 after 1 hour annealing in forming gas at 400 °C. 83

6.1 Temperature dependence of resistivity of $BaTiO_3$ single crystal 87

6.2 Temperature dependence of thermoelectric power of a $BaTiO_3$ single crystal 89

6.3 Temperature dependence of n and σ in rhombohedral and orthorhombic phases . . . 90

6.4 Temperature dependence of drift mobility in rhombohedral and orthorhombic phases of single crystal $BaTiO_3$. 91

6.5 Temperature dependence of Hall constant and resistivity of single crystal $BaTiO_3$. . . 92

6.6 Temperature dependence of Hall mobility of single crystal $BaTiO_3$. 93

6.7 Temperature dependence of resistivity of the $Ba_{0.996}Y_{0.004}TiO_3$ sample sintered at $P_{O_2} = 10^{-17}$ atm. The resistivity was measured in both cooling and heating directions. These directions are indicated by arrows. 94

6.8 Temperature dependence of thermoelectric power of the $Ba_{0.996}Y_{0.004}TiO_3$ sample sintered at $P_{O_2} = 10^{-17}$ atm. 95

6.9 Temperature dependence of resistivity of the $Ba_{0.996}Y_{0.004}TiO_3$ sample sintered at $P_{O_2} = 10^{-15}$ atm. 96

6.10 Temperature dependence of thermoelectric power of the $Ba_{0.996}Y_{0.004}TiO_3$ sample sintered at $P_{O_2} = 10^{-15}$ atm. 97

6.11 Temperature dependence of the drift mobility of the $Ba_{0.996}Y_{0.004}TiO_3$ sample sintered at $P_{O_2} = 10^{-15}$ atm. 98

6.12 Temperature dependence of the Hall constant and resistivity of the $Ba_{.996}$ $Y_{.004}TiO_3$ sample sintered at $P_{O_2} = 10^{-15}$ atm. 99

6.13 Temperature dependence of Hall mobility of the $Ba_{0.996}Y_{0.004}TiO_3$ sample sintered at $P_{O_2} = 10^{-15}$ atm. 100

6.14 Complex impedance measured at different temperatures of $Ba_{0.996}Y_{0.004}TiO_3$ sintered at $P_{O_2} = 10^{-15}$ atm. 101

6.15 Arrhenius plot of grain and grain boundary resistivity of $Ba_{0.996}Y_{0.004}TiO_3$ sintered at $P_{O_2} = 10^{-15}$ atm. 101

6.16 Arrhenius plot of grain and grain boundary resistivity of $Ba_{0.996}Y_{0.004}TiO_3$ sintered at $P_{O_2} = 10^{-15}$ atm and oxidized in air at 800 °C for 5 hours. 102

6.17 Arrhenius plot of grain and grain boundary resistivity of $Ba_{0.996}Y_{0.004}TiO_3$ sintered at $P_{O_2} = 10^{-15}$ atm and oxidized in air at 1100 °C for 5 hours. 102

6.18 Arrhenius plot of grain and grain boundary resistivity of $Ba_{0.996}Y_{0.004}TiO_3$ sintered at $P_{O_2} = 10^{-15}$ atm and oxidized in air at 1200 °C for 5 hours. 103

7.1 EPR spectra of $Ba_{0.996}Y_{0.004}TiO_3$ sintered in reducing atmosphere of forming gas and acquired at 77 K and at 295 K. 107

7.2 An example of EPR spectra of a) unreduced and b) reduced $BaTiO_3$ single crystals measured at 77 K. The spectra shown are only for one orientation of the crystal. . . 108

7.3 Dependence of the g-values of several paramagnetic defects of reduced $BaTiO_3$ single crystal measured at 77 K. 109

7.4 Room temperature EPR spectra of a) $Ba_{0.996}Y_{0.004}TiO_3$ sintered in a reducing atmosphere of forming gas and annealed in air at b) 1000 °C, c) 1200 °C, d) 1300 °C, and e) 1400 °C for 5 hours. 110

7.5 EPR spectra of a) $Ba_{0.996}Y_{0.006}TiO_3$ ceramics sintered in reducing atmosphere of forming gas and annealed in air at b) 1000 °C, c) 1200 °C, d) 1300 °C, and e) 1400 °C for 5 hours. All spectra were taken at 77 K. 111

7.6 EPR spectra of $Ba_{1-x}Y_xTi_{1.01}O_3$ ceramics with x = 0.0005, 0.002, 0.004, 0.006, 0.008 sintered in air. All spectra were obtained at 77 K. 112

7.7 Room temperature EPR spectra of $BaY_{0.004}TiO_3$ ceramics for a) Ba+Y/Ti = 1.03, b) Ba+Y/Ti = 1.02, and c) Ba+Y/Ti = 1.00. The samples were sintered in air. . . 113

7.8 Room temperature EPR spectra of $BaY_{0.004}TiO_3$ ceramics containing Fe^{3+} impurity. 113

7.9 Temperature dependence of EPR spectra of $BaY_{0.004}TiO_3$ ceramics in tetragonal and cubic phases. 114

7.10 Temperature dependence of EPR spectra of undoped polycrystalline $BaTiO_3$ sintered in air at 1380 °C. 115

7.11 EPR spectra of tetragonal and cubic $BaY_{0.004}TiO_3$ polycrystal sintered in reducing atmosphere. 116

7.12 EPR spectra of undoped single crystal $BaTiO_3$. 117

7.13 Temperature dependence of the double integrated intensity of the g=2.004 signal and resistivity of $BaY_{0.004}Ti_{1.01}O_3$ sample 118

7.14 Temperature dependence of the double integrated intensity of the Mn^{2+} complex center and resistivity of polycrystalline $BaY_{0.004}Ti_{1.01}O_3$ 118

8.1 SEM images of samples A and B. The white bar indicates 10 μ m. 121

8.2 Temperature dependence of resistivity of samples A and B. Arrows indicate the temperatures where $j(V)$ characteristics were measured. 122

8.3 The $j(V)$ characteristics of samples A and B measured at various temperatures. . . . 123

8.4 Voltage dependence of normalized conductivity σ/σ_0 for samples A and B measured at various temperatures. 126

8.5 Polaronic fit of $j(V)$ dependence of sample B at 300 °C, α= 3.9. 128

8.6 An illustration of the double-Schottky barrier at nonzero voltage. 130

8.7 Calculated temperature dependence of φ_0 and N_t for samples A and B. 131

8.8 Dependence of φ and γ on applied voltage for samples A and B at various temperatures. 132

8.9 Normalized $j(V)$ characteristics for sample A at various temperatures. Solid line, measured$j(V)$; dashed line, calculated $j(V)$. 133

8.10 Normalized $j(V)$ characteristics for sample B at various temperatures. Solid line, measured$j(V)$; dashed line, calculated $j(V)$. 134

9.1 DTA and TG of $Ba(Mg_{1/3}Ta_{2/3})O_3$ 137

9.2 XRD patterns of method I BMT calcined at different temperatures. Superstructure reflectios from 1:2 ordered domains are indicated by $*$. The arrows show the traces of the second phase. 138

9.3 XRD patterns of method II BMT calcined at different temperatures. Superstructure reflections from 1:2 ordered domains are indicated by $*$. 139

9.4 XRD patterns of method I (1) and method II (2) BMT sintered at 1650 °C for 20 h. Vertical bars represent the relative intensity of reflections from $Ba_3Ta_5O_{15}$ phase. The arrows indicate traces of $Ba_3Ta_5O_{15}$ phase in method II BMT. 141

9.5 Dependence of the ordering parameter on the sintering temperature of the method II BMT. 142

9.6 Bright field TEM image of BMT sample sintered at 1580 °C for 20 h. The inset shows the SAD pattern from 1:2 ordered domains. 143

9.7 SEM images of a) method I and b) method II BMT sintered at 1650 °C for 20 h. . . 144

9.8 Dependence of the density of the BMT samples on sintering temperature. The samples were sintered for 20 h. 145

9.9 Dependence of the dielectric constant at 10 GHz on sintering temperature of the BMT ceramics. 146

9.10 Dependence of the dielectric constant on the density of BMT samples. The solid line was calculated from Eq. 9.10. 147

9.11 Dependence of $Q \times f$ on the sintering temperature of BMT samples. The samples were sintered for 20 h. 148

9.12 Temperature dependence of the shift of the resonance frequency of method I BMT dielectric resonators sintered at different temperatures. 149

10.1 DTA and TG of $MgNb_2O_6$ + $BaCO_3$ 153

10.2 DTA and TG of $ZnNb_2O_6$ + $BaCO_3$ 154

10.3 DTA and TG of $NiNb_2O_6$ + $BaCO_3$ 154

10.4 DTA and TG of $NiTa_2O_6$ + $BaCO_3$ 155

10.5 XRD patterns of $Ba(Mg_{1/3}Nb_{2/3})O_3$ samples calcined at 1) 800°C, 2) 900°C, 3) 1000°C, 4) 1100°C, 5) 1200°C, 6) 1360°C, 7) 1400°C, 8) 1445°C, 9) 1500°C, 10) 1620°C. Superstructure reflections from 1:2 ordered phase are indicated by $*$ 156

10.6 XRD patterns obtained with a) Co K_α source and b) Cu K_α source of $Ba(Zn_{1/3}Nb_{2/3})O_3$ samples calcined at 1) 800°C, 2) 850°C, 3) 900°C, 4) 1000°C, 5) 1100°C, 6) 1200°C, 7) 1380°C, 8) 1460°C. Superstructure reflections from 1:2 ordered phase are indicated by $*$. High temperature second phase is indicated by arrows. 157

10.7 XRD patterns of $Ba(Ni_{1/3}Nb_{2/3})O_3$ samples calcined at 1) 800°C, 2) 900°C, 3) 1000°C, 4) 1100°C, 5) 1200°C, 6) 1320°C, 7) 1360°C, 8) 1400°C, 9) 1450°C, 10) 1500°C. Superstructure reflections from 1:2 ordered phase are indicated by $*$. 158

10.8 XRD patterns of $Ba(Ni_{1/3}Ta_{2/3})O_3$ samples calcined at 1) 800°C, 2) 900°C, 3) 1000°C, 4) 1100°C, 5) 1200°C, 6) 1570°C, 7) 1610°C. Superstructure reflections from 1:2 ordered phase are indicated by $*$. 159

10.9 Ordering parameter for BMN, BZN, BNN, and BNT samples sintered at different temperatures 162

10.10 Density of BMN, BZN, BNN, and BNT samples sintered at different temperatures for 20 h. 163

10.11 SEM image of thermally etched surface of BZN sample sintered at 1380 °C. 164

10.12 SEM image of fractured surface of BZN samples sintered at a) 1380 °C, b) 1420°C, and c) 1460 °C 164

10.13 EDS spectrum of fractured surface of BZN sample sintered at 1380 °C 165

10.14 EDS spectrum of the second phase formed during thermal etching of BZN sample sintered at 1380 °C 165

10.15 SEM image of polished surface of BMN samples sintered at a) 1400 °C, b) 1460°C, and c) 1620 °C 166

10.16 SEM image of polished surface of BNN samples sintered at a) 1400 °C, b) 1420°C, and c) 1500 °C 166

10.17 SEM image of polished surface of BNT samples sintered at a) 1570 °C, b) 1600°C, and c) 1610 °C 166

10.18 Effect of sintering temperature on dielectric constant of BMN, BZN, BNN, and BNT ceramics. 167

10.19 Effect of sintering temperature on $Q \times f$ of BMN, BZN, BNN, and BNT ceramics. . 168

10.20 Room temperature EPR spectra of BMN, BZN, BNN, and BNT ceramics. 169

10.21 Effect of sintering temperature on τ_f of BMN, BZN, BNN, and BNT ceramics. . . . 170

List of Tables

2.1 Electron tranport parameters of $BaTiO_3$ 26

3.1 Dielectric properties of materials for DR applications 37

3.2 Data on order-disorder transitions in several $Ba(B'_{1/3}B''_{2/3})O_3$ 45

3.3 Tolerance factor and dielectric properties of several $Ba(B'_{1/3}B''_{2/3})O_3$ compounds. . 46

4.1 Raw chemicals, purity, and manufacturers 48

4.2 Nominal compositions of Y doped $BaTiO_3$ 49

4.3 Nominal compositions of complex barium tantalates and barium niobates 50

5.1 Phase composition of mixtures of $BaCO_3$ and TiO_2 after 2 h anneal. 61

5.2 The density of $Ba_{1-x}Y_xTiO_3$ ceramics sintered in air and forming gas 61

6.1 Grain bulk and grain boundary activation energy of resistance of the $BaTiO_3$ rhombohedral phase 103

7.1 g-Values of several paramagnetic centers in $BaTiO_3$ 105

9.1 Phases comprising method I and II BMT samples prepared at different temperatures and soaking. 140

9.2 Grain size, d, temperature coefficient of resonance frequency, τ_f and dielectric constant, ε' of BMT ceramics prepared by 2 different methods and sintered for 20 hours. 144

10.1 Delectric properties of several $Ba(B'_{1/3}B''_{2/3})O_3$ compounds. 152

10.2 Phase composition of calcined powders of $BaCO_3$ + $MgNb_2O_6$ 155

10.3 Phase composition of calcined powders of $BaCO_3$ + $ZnNb_2O_6$ 160

10.4 Phase composition of calcined powders of $BaCO_3$ + $NiNb_2O_6$ 160

10.5 Phase composition of calcined powders of $BaCO_3$ + $NiTa_2O_6$ 161

10.6 Theoretical values of structure factors and $I_{100}/I_{110,012,102}$ for several $Ba(B'_{1/3}\,B''_{2/3})O_3$ compounds with ordered 1:2 structure 161

Chapter 1

Introduction

Owing to their outstanding electronic, dielectric and magnetic properties, metal oxide ceramics with perovskite structure continue to attract considerable scientific and commercial interest resulting in a variety of industrial applications. Among them are $Pb(Mg,Nb)O_3$-based piezoelectrics, $BaTiO_3$-based capacitors and positive temperature coefficient (PTC)-thermistors, $Ba(Mg,Ta)O_3$ and $Ba(Zn,Ta)O_3$ dielectric resonators for wireless communication, $Ba(La,Mn)O_3$ colossal magnetoresistors, etc. This thesis focuses on two types of materials with perovskite structure, namely

1. doped n-type $BaTiO_3$ and
2. $Ba(B'_{1/3}B''_{2/3})O_3$ where B′ = Mg, Zn, Ni, and B″ = Nb, Ta.

N-type $BaTiO_3$ is well known for its positive temperature coefficient of resistivity (PTCR). The electrical resistance of n-type $BaTiO_3$ polycrystals sintered in air changes by up to 6 orders of magnitude at the temperature of the ferroelectric-to-paraelectric transition. In the temperature range of ca. 120 - 250 °C, the temperature coefficient of resistivity of $BaTiO_3$ has a positive sign in contrast to the vast majority of known semiconductors. Despite the fact that PTCR $BaTiO_3$ has been utilized in industry for more than 40 years, the physical nature of the PTCR effect is not completely clear. The most widely accepted (and yet most criticized) model explains the PTCR effect in terms of temperature dependent double-Schottky barriers (DSB) formed at the grain boundaries [1]. To form such a grain boundary potential barrier, the modern theories of the PTCR effect [1, 2, 3, 4] require the presence of the in-gap acceptor states (or electron traps) to be localized in the grain boundary layer. However, the nature of these electronic states (i.e., whether they are chemisorbed oxygen ions or segregated cation vacancies) constitutes one of the topics of modern scientific debate and is investigated in this thesis.

The effect of preparation conditions on the resistivity of $BaTiO_3$ and post-sinter annealing at different oxygen partial pressures was also studied in this work. Complex impedance analysis at cryogenic temperatures was used to distinguish between the grain bulk and grain boundary properties at different oxidation conditions. The results of the complex impedance analysis together with evaluation of the grain boundary diffusion of oxygen are presented in Chapter 5.

A few papers about analysis of the paramagnetic point defects in polycrystalline $BaTiO_3$ provide contradictory results [5, 6, 7]. However, correct identification of these defects is very important in understanding the point defect chemistry of $BaTiO_3$ and its effect on the PTCR properties. Hence, one of the goals of this work was to perform a comprehensive study of the paramagnetic point defects in $BaTiO_3$ including the effect of oxygen partial pressure, post-sinter anneal, and stoichiometry. Analysis of the paramagnetic point defects in $BaTiO_3$ is presented in Chapter 7.

Another goal of this thesis was to understand the current-voltage ($I - V$) characteristics of n-doped polycrystalline $BaTiO_3$. In PTCR $BaTiO_3$, the current shows a non-linear dependence on voltage above the ohmic region. This is called a varistor effect. In his original model, Heywang [1] interpreted the $I - V$ dependence in terms of thermionic emission over the voltage-dependent potential barriers which yields $I \propto exp(V/2k_BT)$. Later studies, however, revealed that the current-voltage characteristics deviate from ideal exponential dependence. Several mechanisms including electron diffusion [8], Frenkel-Poole effect [9], space charge limited current [10], electron tunnelling [11], were proposed to explain the electron transport through the grain boundary in PTCR $BaTiO_3$. In the author's opinion, the major difficulty in early interpretation of the $I - V$ characteristics in $BaTiO_3$ was due to insufficient understanding of the effect of external voltage on the population of the grain boundary electron traps. It was not until the pioneering work of Pike [12] on polycrystalline silicon and the comprehensive study of Blatter and Greuter [13] on ZnO-varistors, that the effect of external voltage on the interfacial charge in polycrystalline ceramics was well understood. The problem of the current-voltage dependence in $BaTiO_3$ including the effect of the voltage-dependent population of interface states is revisited in Chapter 8.

In addition to the grain boundary electronic properties, electron transport of bulk $BaTiO_3$ was also investigated, in particular, whether to ascribe the charge carriers in $BaTiO_3$ to conduction band electrons or small radii polarons [14, 15, 16]. To answer this question it is important to know simultaneously the temperature dependence of the drift mobility and concentration of the charge carriers. In this work, these two parameters were independently measured for polycrystalline and single crystal $BaTiO_3$ in the temperature range of 150 - 300 K. The results are reported in Chapter 6.

Another topic of this investigation is the dependence of the dielectric properties of $Ba(B'_{1/3}B''_{2/3})O_3$ (where B$'$ = Mg, Zn, Ni, and B$''$ = Nb, Ta) ceramics on cation ordering within the complex perovskite structure. The interest in these materials is governed by their application in the rapidly growing wireless communication industry [17]. A general review of dielectric materials for microwave resonators with emphasis on the origin of dielectric loss is given in Chapter 3. $Ba(B'_{1/3}B''_{2/3})O_3$ compounds have dielectric constants of 20 - 40 and very low dielectric loss, which makes them suitable candidates for dielectric resonators at microwave frequencies (5 - 40 GHz). However, factors affecting their dielectric loss are insufficiently studied. Until recently [18], it was considered that intrinsic dielectric loss due to incomplete ordering of B-site cations in $Ba(B'_{1/3}B''_{2/3})O_3$ is the major contribution to tan δ. However, several reports [19, 20] indicate that extrinsic dielectric loss due to the presence of the second phase and point defects could be dominant at microwave frequencies in these compounds. Hence, the final goal of this study was to investigate the effect of preparation conditions on B-site cation ordering and dielectric properties of $Ba(Mg_{1/3}Ta_{2/3})O_3$, $Ba(Mg_{1/3}Nb_{2/3})O_3$, $Ba(Zn_{1/3}Nb_{2/3})O_3$, $Ba(Ni_{1/3}Ta_{2/3})O_3$ and $Ba(Ni_{1/3}Nb_{2/3})O_3$. The results are presented in Chapters 9 and 10.

Chapter 2

Physical and chemical properties of $BaTiO_3$

2.1 Crystallographic structure and dielectric properties

2.1.1 The prototype structure of $BaTiO_3$

Barium titanate belongs to the $A^{2+}B^{4+}O_3$ perovskite family of crystals with its prototype, $CaTiO_3$. The name *perovskite* has been dated back to 1839 when, a Russian mineralogist, discovered a new mineral $CaTiO_3$, which he named *perovskite* after the then Russian Minister of Lands, count L.A. Perovsky. This name has since been used to designate the large ABO_3 family.

In its cubic allotrope (above 120 °C), $BaTiO_3$ can be viewed as a cube with Ba ions located at the cube corners, Ti ion at the body center, and oxygens at the face centers, forming octahedra around each Ti ion as shown in Fig. 2.1(a). Alternatively, Fig. 2.1(b) shows the structure as a three-dimensional network of TiO_6 corner-sharing octahedra arranged in a simple cubic pattern. In each octahedron, the Ti ion is located at the center while the oxygens at the apices are shared with neighboring octahedra. The Ba ion occupies the space formed between eight neighboring octahedra, giving the Ba ion twelve-fold coordination with an ionic radius of $R_{Ba^{2+}} = 0.161$ nm. The Ti ion has six-fold coordination with an ionic radius of $R_{Ti^{4+}} = 0.0605$ nm. The oxygen ion also has six-fold coordination in $BaTiO_3$ with $R_{O^{2-}} = 0.140$ nm. It has been shown by Goldschmidt [21] that the perovskite structure is stable for a range of tolerance factors between 0.8 and 1.0, where the tolerance factor, t, is defined as

$$t = \frac{R_A + R_O}{\sqrt{2}(R_B + R_O)}, \tag{2.1}$$

and t for $BaTiO_3$ equals 1.06. $BaTiO_3$ can accept substitution of foreign cations on two distinct sites, the A-site (Ba) and the B-site (Ti). The incorporation of a foreign cation into the $BaTiO_3$

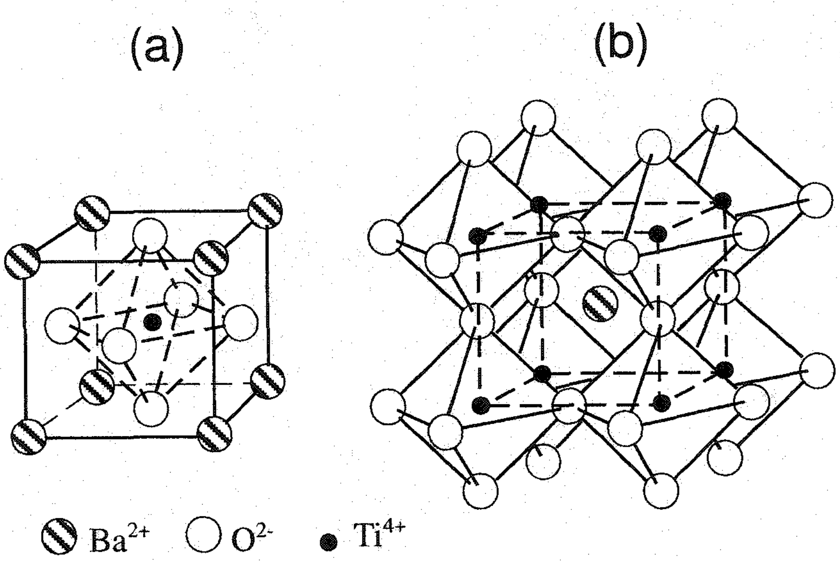

Figure 2.1: Ideal perovskite structure

lattice depends on the ionic size and electronic structure of both the foreign ion and the host site. $BaTiO_3$ forms solid solutions with a number of other ABO_3 compounds (e.g. $SrTiO_3$, $CaTiO_3$, $PbTiO_3$, $CdTiO_3$, $BaSnO_3$, $BaZrO_3$). The effect of these substitutions on the crystal structure and ferroelectric properties is discussed in the next section.

2.1.2 Structural phase transitions

$BaTiO_3$ undergoes a series of structural phase transitions upon cooling from high temperature. In

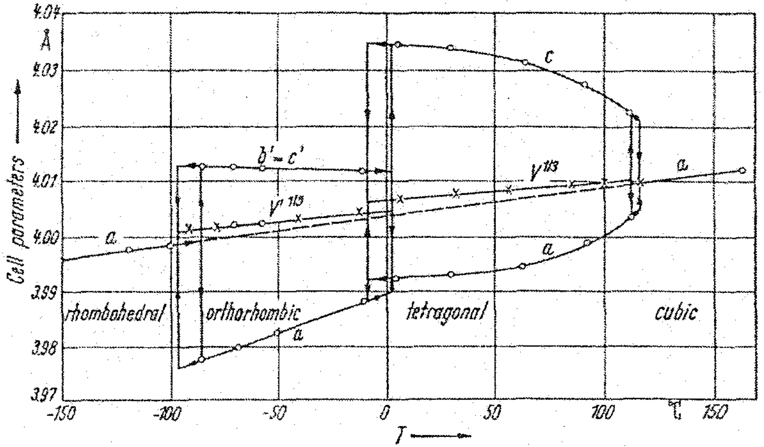

Figure 2.2: Temperature dependence of unit cell parameters of $BaTiO_3$. From Ref. [22]

the temperature range of 1430 °C to 1620 °C barium titanate assumes a hexagonal structure which can be preserved at room temperature by quenching [23]. In the 120 - 1433 °C range, $BaTiO_3$ is cubic and non-polar (space group *Pm3m*), thus centrosymmetrical and non-piezoelectric. At 120 °C the cubic lattice parameter is $\mathbf{a}$ = 4.01 Å. Below 120 °C, $BaTiO_3$ undergous spontaneous distortion along the [100] direction into a tetragonal phase (*P4mm*). Below +5 °C, a distortion along [110] direction leads to the orthorhombic phase (*C2mm*) and, finally, below -90 °C, distortion along [111] results in the rhombohedral structure (*R3m*). The temperature dependence of lattice parameters is shown in Fig. 2.2.

2.1.3 Ferroelectricity

Corresponding to the three structural phase transitions discussed above, three ferroelectric phase transitions occur in $BaTiO_3$. The first transition from paraelectric to ferroelectric phase occurs at T_C = 120 °C and can be described by a displacement of the Ti^{4+} ion along [100] direction from its centrosymmetric position within the oxygen octahedron. In turn, oxygen ions all shift in the opposite direction, [$\bar{1}$00], as illustrated in Fig. 2.3. As revealed by X-ray [24, 25] and neutron [26] diffraction however, the magnitude of atomic displacements differs for two types of oxygen ions (e.g., O_I and O_{II} in Fig. 2.3). Not only does this result in distortion of oxygen octahedron, but the opposite displacement of negative and positive charges within the unit cell leads to formation of an electric dipole moment, and hence to the appearence of spontaneous polarization and ferroelectric properties. In the tetragonal phase, the direction of the vector of spontaneous polarization $\mathbf{P}_S$ (i.e., polar direction) lies parallel to the direction of one of the original cubic $< 100 >$ directions. Since there are 6 equivalent $< 100 >$ axes in the cubic phase, the polar axis can be parallel to any of these six equivalent directions. This gives rise to complicated ferroelectric domain patterns of $BaTiO_3$. In the orthorhombic ferroelectric phase, the direction of spontaneous polarization is parallel to one of the original cubic $< 110 >$ directions. Finally, in the rhombohedral ferroelectric phase, $\mathbf{P}_S$ lies along one of the original cubic $< 111 >$ axes. The vector of spontaneous polarization changes not only its

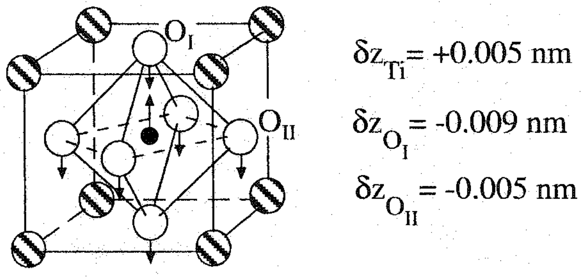

Figure 2.3: Structure of tetragonal $BaTiO_3$ showing development of electric dipole moment of the unit cell. The arrows indicate the directions of displacement of Ti and O ions along [100].

orientation but also its magnitude depending on the crystal symmetry. The investigations of Känzig and Meier [27] and those of Merz [28], have shown that the onset of spontaneous polarization at T_C is discontinuous, indicating a first-order phase transition. For very good crystals, the value of spontaneous polarization is 26×10^{-6} C/cm^2 at room temperature [28].

The ferroelectricity occurs as a result of coupling of electric dipole moments along an identical direction. In order to minimize the arising depolarization energy and strain energy resulting from the formation of the electric moments, ferroelectric dipoles with 180° walls and 90° walls are formed. These can be observed with polarized light using optical microscopy [29] as well as by TEM [30]. The dielectric polarization of ferroelectric $BaTiO_3$ in a high electric field is achieved by the motion of the domain walls and by nucleation and growth of new domains in the "old" domain marix. The dielectric constant, ε, of $BaTiO_3$ is a second rank tensor which exhibits nonlinear dependence on temperature [31], frequency [32, 33, 34, 35], pressure [36], and electric field strength [37]. Fig. 2.4 shows the typical dependence of the dielectric constant on temperature for single crystal $BaTiO_3$. It can be seen that anomalies in the dielectric constant are related to the structural phase transitions shown in Fig. 2.2. Besides the dielectric anomaly around the paraelectric-ferroelectric phase transition temperature, other anomalies were found at +5 °C and -80 °C. Anomalies in the piezoelectricity and specific heat have also been reported [38]. In the paraelectric phase, the temperature dependence of the real part of ε obeys the Curie-Weiss law,

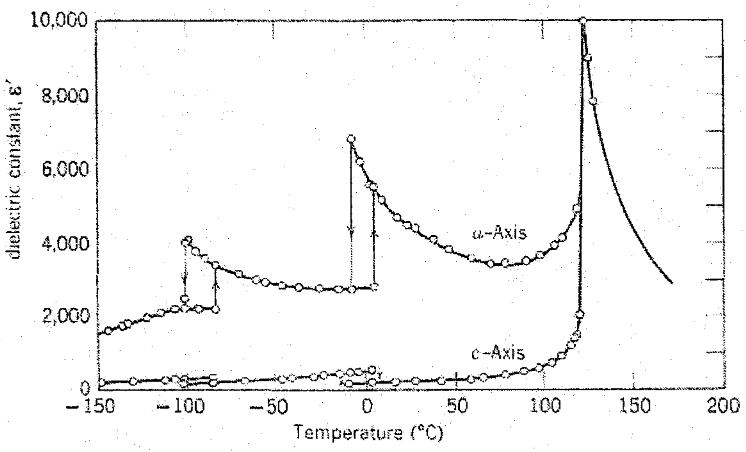

Figure 2.4: Temperature dependence of dielectric permittivity of single crystal $BaTiO_3$ along a-axis and c-axis (according to Merz [31]).

$$\varepsilon' = \frac{C}{T - T_0} \tag{2.2}$$

where $C = 1.5\times10^5$ K, is the Curie constant for barium titanate and $T_0 = 383$ K is the Curie-Weiss temperature.

The dielectric permittivity of $BaTiO_3$ ceramics is strongly influenced by the grain size. This effect was studied by Kinoshita and Yamaji [39] and Hennings [40]. It was found that ε is greatly decreased when the grain size is smaller than 2 μm. It has also been found that thin films of $BaTiO_3$ grown by MBE, spray pyrolysis [41], laser ablation [42] etc., have a cubic symmetry at room temperature and show low values of dielectric permittivity (e.g., ε = 60 - 200). Attempts have been made to explain this so-called grain size effect in terms of internal stress due to the rare presence of 90° domain walls [43] and of small domain size [44]. Up to now, however, the size effect has not been completely understood, although various interpretations have been proposed [45, 46].

As is evident from Fig. 2.4, the dielectric permittivity of pure $BaTiO_3$ has a maximum at T_C = 120 °C, the temperature of the ferroelectric to paraelectric phase transition. However, some practical applications (e.g., ceramic capacitors) require high, and often temperature independent ε at room temperature. For other applications, such as PTC-thermistors, the temperature of the ferroelectric to paraelectric phase transition has to be tunable in the -50 to +400 °C range. Both the temperature dependence of the dielectric permittivity and T_C can be altered by substitution of various ions on the Ba or Ti sublattices. As reported by Yasuda [47], Hennings [48], and Zhuang [49], substitution of Sn, Zr, or Ca for Ti shifts T_C to lower values and leads to broadening of the permittivity peak.* Lowering the temperature of the ferroelectric to paraelectric phase transition can be also achieved by substitution of Sr into the Ba-sublattice without significant broadening of the permittivity peak [51]. $BaTiO_3$ and $SrTiO_3$ form a complete range of solid solution due to their identical structures and similar ionic radii.

Upon cooling, the crystal structure of $SrTiO_3$ changes from cubic to tetragonal at 108 K, then to orthorhombic at 65 K, and finally to rhombohedral at 35 K [52]. It is worth mentioning, that although $SrTiO_3$ has a polar soft mode, it does not exhibit a ferroelectric phase transition. This phenomenon has been explained by stabilization of its paraelectric phase by quantum fluctuations [53]. While shifting of the T_C of $BaTiO_3$ towards lower temperatures can be easily accomplished by isovalent substitutions of a number of ions in Ti- or Ba sublattices, tuning of T_C above 120 °C appears to be more challenging. So far this can only be achieved by substitution of Pb for Ba. By analogy with $SrTiO_3$, $PbTiO_3$ (another perovskite compound with a ferroelectric to paraelectric phase transition at 495 °C), forms a complete range of solid solutions with $BaTiO_3$. However, the major technical and environmental problem of lead containing perovskites is a high partial pressure of Pb vapour at sintering temperatures.

Although ferroelectricity of $BaTiO_3$ has been known for more than half a century, there are still questions regarding the nature of the ferroelectric to paraelectric phase transition. According to the classical definition, a ferroelectric phase transition falls into either a displacive or an order-disorder transition. With recent experimental findings, numerous ferroelectrics, such as $BaTiO_3$ and $KNbO_3$, which were originally thought to be traditional displacive ferroelectrics, unambiguously displayed a

---

*The broadening of ε peak and appearance of the low frequency dispersion of ε in complex perovskites was first reported by Smolensky [50] and was named "ferroelectric relaxor behaviour".

substantial order-disorder behaviour [54, 55]. A displacive and an order-disorder phase transition were proved to be not distinctly separated in $BaTiO_3$.

According to the lattice dynamics of the cubic $BaTiO_3$, there are 15 vibrational modes. Six of them are due to the vibration of Ti^{4+} ions in the oxygen octahedra. With decreasing temperature, the transverse optical (TO) mode of the Ti^{4+} ion at the Brillioun zone center becomes heavily overdamped due to the anharmonic component of the lattice vibration. When the temperature approaches T_C, the frequency of the TO mode approaches zero (i.e., the TO mode "softens") and the cubic stucture undergoes a tetragonal distortion along its <100> direction. The occurrence of ferroelectricity in $BaTiO_3$ is closely associated with the coupling of the arising dipole moments which in turn result from the displacive ferroelectric transition. The displacement of the titanium ion from its central position due to the softening of the TO mode was found to be about 0.14Å [24].

On the other hand, Müller et al. [55, 56] have shown by EPR measurements of Fe^{3+} and Mn^{4+} tracer ions that $BaTiO_3$ possesses a substantial order-disorder behaviour. Experiments with Mn^{4+} [56] doping on the Ti-site have demonstrated that the Ti^{4+} is located off-center along equivalent <111> directions and reorients in high-temperature phases with a frequency of $\nu \geq 10^{10}$ sec^{-1}. The results of far infrared reflectivity measurements [57] of the soft mode of $BaTiO_3$ as well as soft-mode spectroscopy in cubic $BaTiO_3$ by hyper-Raman scattering [58] have provided substantial evidence of an order-disorder phase transition in $BaTiO_3$. In particular, the deviation of the frequency of the soft mode, Ω_s, from the Curie-Weiss law [57],

$$\Omega_s^2 = A(T - T_C) \tag{2.3}$$

occurs over a hundred degrees above the tetragonal-cubic phase transition [54]. Recent Raman scattering measurements conducted on a single crystal suggest that $BaTiO_3$ above the Curie temperature exhibits some disorder behaviour [58]. Itoh et al. [59] found by an X-ray structural study that above 180 °C, $BaTiO_3$ possesses the ideal cubic structure. However, at temperatures T_C < T < 180 °C, the Ti^{4+} ion is displaced by 0.1Å from its central position along the <111> direction and has eight local disorder positions. In addition to this disorder, Itoh et al. [59] have found that the Ba^{2+} ion is displaced from the cell corner along the <110> direction leading to twelve local disorder positions and the O^{2-} ions are uniformly distributed on rings in their face centered planes (Fig. 2.5). It was found that upon approaching T_C from higher temperatures, short-range order of the Ti dipoles exists owing to the correlated order parameter fluctuations, which yielded a saturating soft mode [55]. Accordingly, a crossover from the soft mode to an order-disorder behaviour was proposed [60].

2.2 Defect chemistry

Stoichiometric $BaTiO_3$ is considered to be an insulator or a wide band-gap semiconductor. Its room temperature resistivity can reach 10^{12} Ω·cm. Depending on processing conditions, the band gap

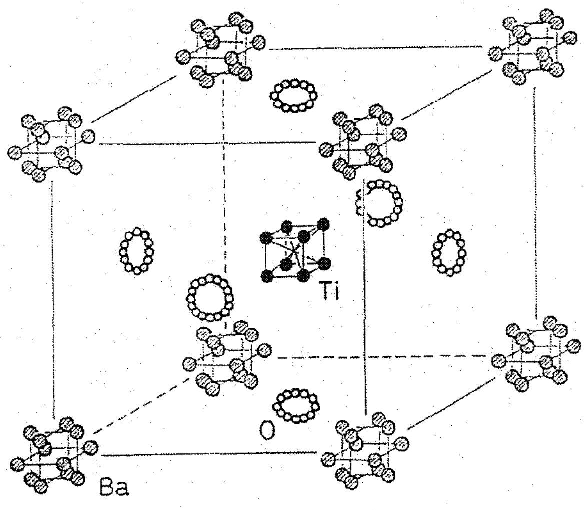

Figure 2.5: Disordered structure of $BaTiO_3$ in cubic phase. From ref. [59]

width of $BaTiO_3$ varies from 2.9 to 3.3 eV as revealed by measurements of temperature activated conductivity [61] and optical absorption band edge [62]. Electrical, optical and dielectric properties are very sensitive to the type of defects present in $BaTiO_3$. However, it should be mentioned beforehand that a complete picture of the defect chemistry in this compound is not resolved so far. The bulk and surface defect chemistry of barium titanate have been studied by measurements of electrical conductivity [61, 63, 64, 65, 66], thermogravimetry [67, 68], mass spectrometry [69], LEED [70], Auger [71], UPS [72, 73], XPS [72, 74], STM [75], microanalysis [76], EPR [5, 77, 6], and optical absorption [78]. Theoretical calculations of the formation energy of bulk and surface point defects have been conducted by Lewis and Catlow [79]. In this section the defect chemistry of undoped, acceptor and donor doped $BaTiO_3$ will be discussed. The effect of intrinsic defects as well as the effect of oxygen partial pressure on the bulk defect chemistry and interfacial segregation will be addressed.

2.2.1 BaO-TiO_2 phase composition

The phase equilibria in the BaO-TiO_2 system have been studied by Stratton [80] and by Rase and Roy [81]. Phase relations in the TiO_2-rich portion of system were studied by Negas et al. [82], O'Bryan and Thomson [83], and Kirby and Wechsler [23]. Hu et al.[84] investigated the solubility limit of BaO in $BaTiO_3$. The phase diagram of the BaO–TiO_2 system is shown in Fig. 2.6. Kirby and Wechsler [23] found that the solid solubility of TiO_2 in $BaTiO_3$ extends to at least 51 mol% in the hexagonal phase and to 52.5 mol% in cubic $BaTiO_3$. On the other hand, direct microscopic examinations by Hu et al. [84] revealed a Ba_2TiO_4 second phase in samples containing $\geq$0.1 mol% excess BaO. Thus, it was found that the solubility of BaO in $BaTiO_3$ is limited to 1000 ppm (0.1

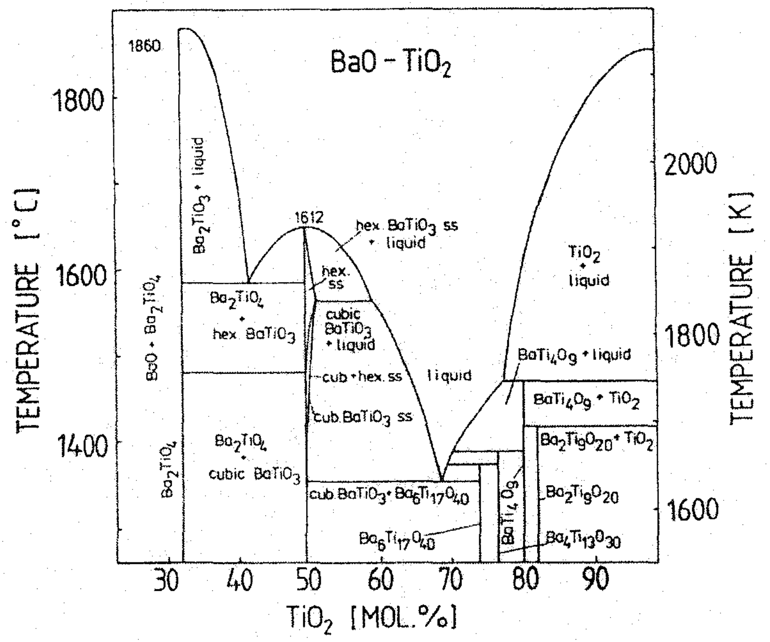

Figure 2.6: The phase diagram of the BaO–TiO_2 system. From ref. [85]

mol%). This is in contrast to $SrTiO_3$ were excess SrO dissolves in the $SrTiO_3$ matrix, leading to formation of the Ruddlesden-Popper (i.e., $SrO \cdot nSrTiO_3$) type of superlattice [86].

2.2.2 Defect chemistry of undoped and acceptor doped $BaTiO_3$

Slight deviations from the ideal Ba/Ti ratio as well as incorporation of accidental or intentional donors or acceptors can be compensated in $BaTiO_3$ by point defects. While trying to draw up a defect model of $BaTiO_3$, one needs to find the smallest possible set of defects. On account of high packing density of the perovskite lattice of $BaTiO_3$, all interstitial defects are usually excluded [64]. This approach has been supported by the defect energy calculations of Lewis and Catlow [79] who found that formation of interstitial defects (Frenkel disorder) requires an energy of 4.49 to 7.57 eV/defect, while Schottky disorder requires only 2.29 to 2.91 eV/defect. Hence, Schottky defects are assumed to be the dominant intrinsic defects in $BaTiO_3$. However, several factors, such as cation or anion nonstoichiometry, and accidental or intentional acceptor or donor doping can easily render the system extrinsic.

Using conventional Kröger-Vink [87] notation of the lattice defects, the generalised electroneutrality condition for $BaTiO_3$ is given by

$$\begin{aligned} n + [A'] + [V'_{Ba}] + 2[V''_{Ba}] + [V'_{Ti}] + 2[V''_{Ti}] + 3[V'''_{Ti}] + 4[V''''_{Ti}] = \\ = p + [V^{\cdot}_{O}] + 2[V^{\cdot\cdot}_{O}] + [D^{\cdot}] \end{aligned} \tag{2.4}$$

where $[V_i']$, $[V_i'']$, $[V_i''']$, $[V_i'''']$ are the concentrations of single, double, triple, and quadruple negatively ionised cation vacancies, $[V_O^{\cdot}]$ and $[V_O^{\cdot\cdot}]$ are the concentrations of single and double positively ionised oxygen vacancies, $[D^{\cdot}]$ is the concentration of A-site trivalent and/or B-site pentavalent donor ions, $[A']$ is the concentration of single ionised acceptor ions, and n and p are the concentrations of electrons and holes respectively.

At high temperatures, information about the dominant defects in metal oxides can be obtained from measurement of the equilibrium conductivity as a function of oxygen partial pressure [88]. As evident from Fig. 2.7, the equilibrium conductivity of undoped $BaTiO_3$ has three distinct regions. In the oxygen deficient region, the conductivity increases with decreasing P_{O_2}. In the region of the oxygen excess, the conductivity increases with increasing P_{O_2}. These two regions are separated by a conductivity minimum where the only source of charge carriers comes from direct activation of electron-hole pairs across the bandgap. As can be seen from Fig. 2.7, the conductivity minimum shifts to higher oxygen pressure with increasing temperature. The conductivity of acceptor doped $BaTiO_3$ shows a similar trend, although the conductivity minimum shifts to lower oxygen partial pressure with increase of acceptor doping [90].

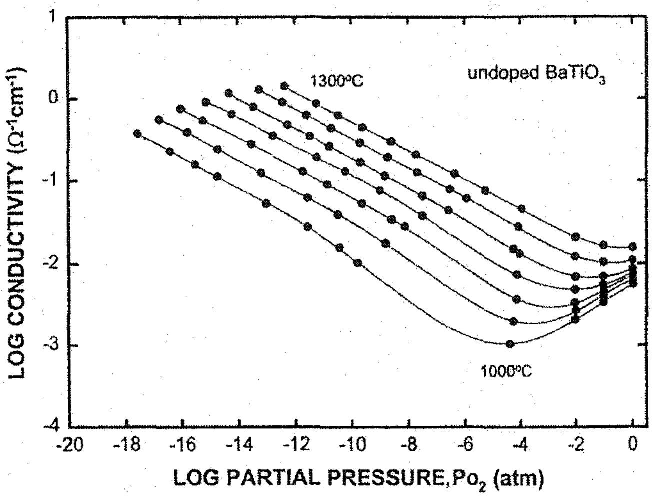

Figure 2.7: Equilibrium electrical conductivity of undoped $BaTiO_3$ (Ba/Ti=1.000) from Ref.[89]

As was shown by Seebeck coefficient measurements [91] in the 700 - 1100 °C range, at low oxygen partial pressure ($P_{O_2} < 10^{-6}$ atm) the conductivity is n-type, whereas at high oxygen pressure (P_{O_2} $> 10^{-3}$ atm) the conductivity becomes p-type. The dependence of σ on P_{O_2} beyond the conductivity minimum can be approximated by

$$\sigma \propto P_{O_2}^{1/m} \tag{2.5}$$

where m is determined from the slope of the log σ versus log P_{O_2} dependence. In the region of high oxygen partial pressure several authors [64, 63, 66, 61] have found that $m \approx 4$. This has led to two different defect models in undoped $BaTiO_3$ at high P_{O_2}, namely *$V_{Ba}{}'$ compensation* and *acceptor impurity compensation.*

V'_{Ba} compensation

Daniels and Härdtl [64] assigned p-type conductivity at high P_{O_2} to the presence of singly ionised barium vacancies. Their model requires a small BaO deficiency, possibly in the form of $(V''_{Ba}V^{\cdot\cdot}_O)$ complexes. The BaO deficiency makes available systematic oxygen vacancies which might accomodate a stoichiometric excess of oxygen without a need of creating a crystallographic excess according to

$$(V''_{Ba}V^{\cdot\cdot}_O) + \frac{1}{2}O_2 \rightleftharpoons O_O + V'_{Ba} + h^{\cdot} \tag{2.6}$$

The mass action relation for eq. 2.6 is given by

$$\frac{[V'_{Ba}][p]}{[(V''_{Ba}V^{\cdot\cdot}_O)]} \propto P^{1/2}_{O_2} \tag{2.7}$$

In order to produce $\sigma \propto {P_{O_2}}^{1/4}$ dependence, the barium vacancy should be singly ionized with corresponding charge neutrality condition

$$[V'_{Ba}] = p \tag{2.8}$$

The combination of Eqs. 2.8 and 2.7, however, indicates that p and therefore conductivity should be proportional to $[(V''_{Ba}V^{\cdot\cdot}_O)]^{1/2}$. Chan et al. [92] and Hu et al. [84] have investigated undoped $BaTiO_3$ with different Ba/Ti ratio and did not confirm $\sigma \propto [(V''_{Ba}V^{\cdot\cdot}_O)]^{1/2}$ dependence. Therefore, the V'_{Ba} compensation model in undoped $BaTiO_3$ has been discarded. However, the EPR results presented in Chapter 7 show that barium vacancies do exist in undoped $BaTiO_3$ ceramics. Moreover, the concentration of this type of defect depends on the oxygen partial pressure and Ba/Ti ratio.

Acceptor impurity compensation

A number of authors [93, 63, 66, 61] favoured the idea of accidental acceptor impurities in order to explain the $p \propto {P_{O_2}}^{1/4}$ dependence at high P_{O_2}. Indeed, the potential acceptor elements in $BaTiO_3$ are naturally much more abundant than potential donor impurities. The most common acceptor impurities detected by EPR in nominally pure $BaTiO_3$ are Fe, Mn, Cr, Al, Mg, K, Na. The incorporation of the accidental acceptor impurities (e.g. A_2O_3, where A = Mn, Fe, Cr, Al) into the Ti sublattice can be described by

$$A_2O_3 + 2BaO \rightarrow 2Ba_{Ba} + 2A'_{Ti} + 5O_O + V^{\cdot\cdot}_O \tag{2.9}$$

Similarly, the incorporation of the acceptor impurities (e.g. A_2O, where A = Na, K) into the Ba sublattice can be described by

$$A_2O + TiO_2 \rightarrow 2A'_{Ba} + Ti_{Ti} + 3O_O + V^{\cdot\cdot}_O \tag{2.10}$$

At high oxygen pressure ($P_{O_2} > 10^{-3}$ atm) the extrinsic $V_O^{\cdot\cdot}$ are partially filled by oxygen atoms, producing holes, according to

$$V_O^{\cdot\cdot} + \frac{1}{2}O_2 \rightleftharpoons O_O + 2h^{\cdot} \tag{2.11}$$

with the mass action relation given by

$$\frac{[p]^2}{[V_O^{\cdot\cdot}]} \propto P_{O_2}^{1/2} \tag{2.12}$$

As long as an insignificant fraction of the impurity-related oxygen vacancies have been filled, the charge neutrality condition in the near stoichiometric region reduces to

$$2[V_O^{\cdot\cdot}] = [A'] \tag{2.13}$$

The combination of Eqs. 2.13 and 2.12 gives the desirable dependence of the conductivity on the oxygen partial pressure

$$\sigma \propto p \propto [A']P_{O_2}^{1/4} \tag{2.14}$$

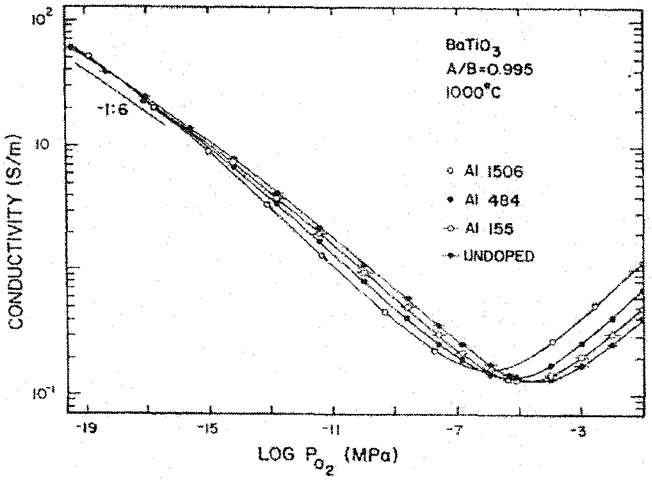

Figure 2.8: Equilibrium electrical conductivity of undoped and Al-doped $BaTiO_3$ at 1000 °C. Concentrations of Al in molar ppm (gram atoms Al per 10^6 formula units $BaTiO_3$) from Ref. [90]

When $BaTiO_3$ is deliberately doped with acceptors at Ti or Ba sites, Eqs. 2.9 and 2.10 still hold and the defect chemisry of acceptor doped $BaTiO_3$ is directly the extension of that of undoped $BaTiO_3$. As was shown by Chan et al. [90] with an increase in acceptor concentration, the minimum of conductivity shifts toward lower P_{O_2} and also broadens with increasing acceptor content (Fig. 2.8). Computer simulations by Lewis and Catlow [79] have shown that at sufficiently high acceptor doping the formation of the $V_O^{\cdot\cdot}$ - A′ complex may also occur. The binding energy of $V_O^{\cdot\cdot}$ - A′ complex depends on the size mismatch of the cations and their effective charge.

Concerning the low oxygen pressure region, it is assumed that the n-type conductivity results from the loss of lattice oxygen, according to

$$O_O \rightleftharpoons \frac{1}{2}O_2 + V_O^{\cdot\cdot} + 2e' \qquad (2.15)$$

with the mass-action expression

$$[V_O^{\cdot\cdot}]n^2 \propto P_{O_2}^{-1/2} \qquad (2.16)$$

The data in Fig. 2.8 indicate that at low P_{O_2}, the electrical neutrality condition should be

$$n \approx 2[V_O^{\cdot\cdot}] \qquad (2.17)$$

to give

$$\sigma \propto n \propto P_{O_2}^{-1/6} \qquad (2.18)$$

Although Daniels and Härdtl [64] suggested the presence of singly ionized oxygen vacancies at intermediate oxygen partial pressures, the results of other workers [61, 63, 66] indicated that double ionized oxygen vacancies are predominant at low P_{O_2}. These results, however, are based on high temperature conductivity measurements. As revealed by Lewis and Catlow [79], the electron is weakly bound to the double ionized oxygen vacancy with a trapping energy of 0.12 eV. Therefore, the existence of singly ionized oxygen vacancies at lower temperatures cannot be ruled out. The EPR analysis of defect centers in reduced $BaTiO_3$ single crystals [94] at 40 - 80 K suggests that ionized oxygen vacancies may form a complex paramagnetic defect, such as Ti^{4+}-$V_O^{\cdot}$ or Ti^{3+}-$V_O^{\cdot\cdot}$.

In conclusion, the data about undoped and acceptor doped $BaTiO_3$ can be summarized as follows:

- The defect chemistry of undoped $BaTiO_3$ is dominated by unavoidable acceptor impurities.
- At low P_{O_2} the deficient charge from acceptors is compensated by $V_O^{\cdot\cdot}$ and electrons, resulting in n-type conductivity with the total neutrality condition $2[V_O^{\cdot\cdot}]=n+[A']$.
- At high P_{O_2}, acceptors are mainly compensated by $V_O^{\cdot\cdot}$, resulting in very weak p-type conductivity at room temperature. The neutrality condition is $2[V_O^{\cdot\cdot}] \approx [A']$.
- The role of $(V_{Ba}''V_O^{\cdot\cdot})$ complex is not sufficiently understood.

2.2.3 Defect chemistry of donor doped $BaTiO_3$

Most of the interest in defect chemistry of donor doped $BaTiO_3$ is credited to the positive temperature coefficient of resistivity (PTCR) effect in n-doped $BaTiO_3$. Phase equilibria in BaO-TiO_2-M_2O_3 and BaO-TiO_2-M_2O_5 ternary oxides where M is a rare earth ion or Nb or Ta, have been studied by Jonker and Havinga [95], Shaikh and Vest [96] and by Makovec et al. [97]. The EPR analysis of paramagnetic point defects in n-doped $BaTiO_3$ ceramics has been performed by Kutty et al. [5], Hari et al. [98], and Er et al. [6]. The high-temperature conductivity versus P_{O_2} was studied by Daniels and Härdtl [64], Chan and Smyth [99], and Hwang and Han [89].

The positive charge of the donor center in $BaTiO_3$ can be compensated by cation vacancies of either kind or by electrons. As reported by Chan and Smyth [99], at low donor concentrations (up to 0.2 at%) the donors are solely compensated by electrons in the wide P_{O_2} range (see Fig. 2.9) The conductivity of n-doped $BaTiO_3$ is impurity insensitive at very low P_{O_2} and high temperatures where double ionized oxygen vacancies are the major source of defects, similar to undoped $BaTiO_3$. At higher n-dopant level, the compensation mechanism changes from electronic to cation vacancy type with $\sigma \propto {P_{O_2}}^{-1/4}$ in the high oxygen activity region (see Fig. 2.10). Several types of cation vacancies were proposed to account for the ${P_{O_2}}^{-1/4}$ dependence of conductivity. Subbarao and Shirane [100] and Hwang and Ho [89] suggested that both barium and titanium vacancies compensated the donors. Daniels and Härdtl [64] favored barium vacancy compensation, whereas Jonker and Havinga [95], Chan et al. [101], Millet et al. [102], and Makovec [97] proposed that at high doping levels (above 1 at%), donors were compensated by titanium vacancies. Possible cation vacancy incorporation reactions for addition of donors into the $BaTiO_3$ lattice are as follows:

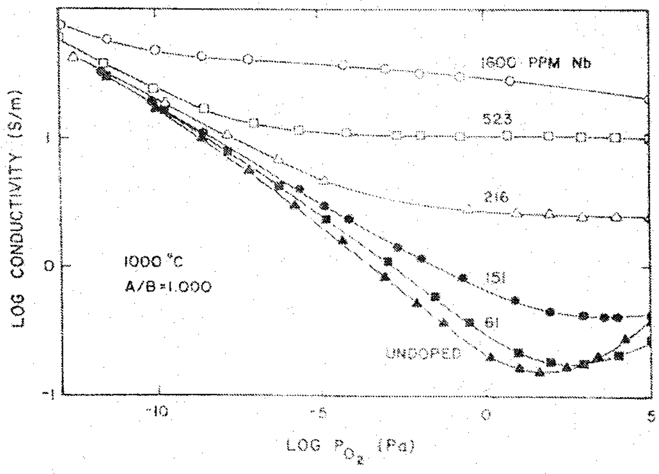

Figure 2.9: Equilibrium electrical conductivity of $BaTiO_3$ at 1000 °C with increasing additions of Nb and with Ba/Ti+Nb=1.00. From ref. [99]

- Ba vacancy compensation model: $[Nb^{\cdot}_{Ti}]=2[V''_{Ba}]$ or $[La^{\cdot}_{Ba}]=2[V''_{Ba}]$

$$BaO + Nb_2O_5 \rightarrow Ba_{Ba} + V''_{Ba} + 2Nb^{\cdot}_{Ti} + 6O_O \qquad (2.19)$$

$$TiO_2 + La_2O_3 \rightarrow Ti_{Ti} + V''_{Ba} + 2La^{\cdot}_{Ba} + 5O_O \qquad (2.20)$$

- Titanium vacancy compensation model: $[Nb^{\cdot}_{Ti}]=4[V''''_{Ti}]$ or $[La^{\cdot}_{Ba}]=4[V''''_{Ti}]$

$$5BaO + 2Nb_2O_5 \rightarrow 5Ba_{Ba} + V''''_{Ti} + 4Nb^{\cdot}_{Ti} + 15O_O \qquad (2.21)$$

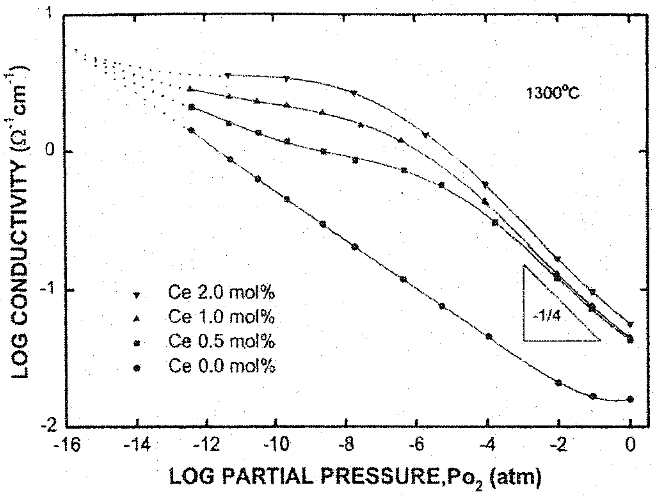

Figure 2.10: Equilibrium electrical conductivity at 1300 °C of $BaTiO_3$, undoped and doped with different amounts of Ce. From ref. [89]

$$3TiO_2 + 2La_2O_3 \rightarrow 3Ti_{Ti} + V_{Ti}^{''''} + 4La^{\cdot}_{Ba} + 12O_O \tag{2.22}$$

- Barium and titanium vacancy compensation model: $[Nb^{\cdot}_{Ti}] = 4[V_{Ti}^{''''}]+ 2[V_{Ba}^{''}]$ or $[La^{\cdot}_{Ba}] = 4[V_{Ti}^{''''}]+ 2[V_{Ba}^{''}]$

$$6BaO + 3Nb_2O_5 \rightarrow 6Ba_{Ba} + V_{Ba}^{''} + V_{Ti}^{''''} + 6Nb^{\cdot}_{Ti} + 21O_O \tag{2.23}$$

$$6TiO_2 + 3La_2O_3 \rightarrow 6Ti_{Ti} + V_{Ba}^{''} + V_{Ti}^{''''} + 6La^{\cdot}_{Ba} + 21O_O \tag{2.24}$$

Interestingly enough, all three compensation mechanisms will result in identical $\sigma \propto {P_{O_2}}^{-1/4}$ dependence. This is explained as follows. According to Lewis and Catlow [79], three types of intrinsic (Schottky) disorder that may influence the defect properties of $BaTiO_3$ are given below

$$null \rightarrow V_{Ba}^{''} + V_{Ti}^{''''} + 3V_O^{\cdot\cdot} \tag{2.25}$$

$$null \rightarrow V_{Ba}^{''} + V_O^{\cdot\cdot} \tag{2.26}$$

$$null \rightarrow V_{Ti}^{''''} + 2V_O^{\cdot\cdot} \tag{2.27}$$

The reduction equation for each compensation mechanism described by Eqs. 2.25, 2.26, and 2.27 can be written as

$$3O_O + V_{Ba}^{''} + V_{Ti}^{''''} \rightarrow \frac{3}{2}O_2 + 6e' \tag{2.28}$$

$$O_O + V_{Ba}^{''} \rightarrow \frac{1}{2}O_2 + 2e' \tag{2.29}$$

$$2O_O + V_{Ti}^{''''} \rightarrow O_2 + 4e' \tag{2.30}$$

The corresponding mass action expressions for $V_{Ti}'''' + V_{Ba}''$, V_{Ba}'', and V_{Ti}'''' compensation mechanisms are given as

$$n \propto [V_{Ba}''][V_{Ti}'''']P_{O_2}^{-1/4} \tag{2.31}$$

$$n \propto [V_{Ba}'']P_{O_2}^{-1/4} \tag{2.32}$$

$$n \propto [V_{Ti}'''']P_{O_2}^{-1/4} \tag{2.33}$$

Hence, it is obvious, that the equilibrium conductivity measurements alone cannot give an unequivocal answer as to what type of cation vacancies predominate at high oxygen partial pressure. The point defect analysis using EPR technique performed in this work revealed that both titanium and barium vacancies are present in n-doped ceramics sintered or annealed at high P_{O_2} (see Chapter 7).

In conclusion, at low doping levels and at low P_{O_2}, the compensation of donors in $BaTiO_3$ is accomplished by electrons so that n-type semiconduction results. At higher doping levels (above 0.5 at%) the fraction of vacancy-compensated donors increases. However, there is some controversy over which cation vacancy compensates the donors. At much higher donor concentrations (e.g., > 5 at%), the X-ray and microprobe data [101] suggest that these are titanium vacancies, as do the results of atomistic simulations [79]. On the other hand, the relaxation of electrical conductivity in donor-doped $BaTiO_3$ occurs with an activation energy of 2.8 eV [93, 103], which suggests barium vacancies since the calculated migration energy of the titanium vacancy is $\approx$ 15 eV [79].

2.2.4 Interfacial segregation of defects

The complexity of the defect chemistry of $BaTiO_3$ is extended further by considering the interfacial segregation of defects. While the equilibrium point defect chemistry of the bulk is governed by the mass action relationships, the interfacial concentration of defects is determined by their formation energy. The difference in the individual intrinsic (Schottky) formation energies leads to preferential enrichment of the interface in the ion of lower vacancy formation energy, and the formation of the adjacent space charge layer enriched in that vacancy. However, when extrinsic solutes raise lattice defect concentrations above thermally generated concentrations, they determine the sign of the grain boundary and the space charge.

According to the ionic space-charge theory of segregation [104] elaborated for $BaTiO_3$ by Chiang and Takagi [76] and Desu and Payne [71], the sign of the interface potential barrier thus formed, would change from negative in the case of acceptor doping to positive for donor doping. That is, the space-charge theory predicts that in case of reduction or acceptor doping, the defects of negative effective charge will accumulate in the space charge region, whereas defects of the positive effective charge will be repelled from the boundary. The grain boundary will be cation-rich to accommodate the positive charge. In case of donor-doping, the predicted interface potential is positive, and donors and other defects of positive effective charge should accumulate in the space charge region.

While Desu and Payne [71] found that this indeed took place in $BaTiO_3$, Chiang and Takagi [76] showed that the interface potential barrier remained negative, independent of solute doping. This disagreement still remains unresolved.

2.3 Band structure and conductivity of $BaTiO_3$

Interest in the surface and bulk electronic structure of $BaTiO_3$ and $SrTiO_3$ was initiated by the discovery of photoelectrolysis of water by TiO_2 [105]. It was found that $SrTiO_3$ has slightly higher efficiency than TiO_2. It is considered that d-electron surface states have the proper symmetry and energies for interaction with the antibonding orbitals of many diatomic molecules. This may result in dissociative chemisorption of molecular hydrogen or oxygen on the surface of the perovskite by electron transfer from an occupied surface state into empty molecular antibonding states. More recently, there has been increased interest in the surface electronic properties of $SrTiO_3$ and its solid solution with $BaTiO_3$ as a suitable substrate for growth of high-temperature superconductors [106, 107] In the following sections the existing data about the bulk and surface electronic structure of $BaTiO_3$ and their effect on electron transport are reviewed.

2.3.1 Bulk electronic structure of $BaTiO_3$

The bulk electronic band structure of $BaTiO_3$ and $SrTiO_3$ has been analyzed both theoretically [108, 109, 110, 111] and experimentally [112, 113, 73, 114]. The electronic structure of undoped stoichiometric $BaTiO_3$ within a few electron volts of the band gap consists of the five empty conduction bands (3 t_{2g} and 2 e_g) formed by Ti 3d orbitals and nine occupied valence bands derived from the three 2p orbitals of the three oxygen ions. Due to the different degrees of interaction with the t_{2g} and e_g orbitals, shown schematically in Fig. 2.11, the oxygen 2p orbitals split into $2p_\sigma$ and $2p_\pi$ orbitals centered on an oxygen with lobes respectively parallel and perpendicular to the Ti–O axis. The filled oxygen 2p valence band is separated from the empty 3d Ti band by the band gap of 3 eV. The highest filled (5p) and the lowest empty (6s) Ba orbitals are significantly farther away from the Fermi level, E_F, than are the O 2p and Ti 3d levels (see Fig. 2.12). That is why the $ATiO_3$ perovskites in which the A cation has a 2+ valence, are very similar in their valence electron structure to TiO_2. Since bandwidth in solids arises from the overlap of orbitals, an important property of d orbitals is that they are quite contracted in size compared with valence s and p orbitals, and so have relatively poor overlap with surrounding atoms. Hence, the Ti 3d conduction band is quite narrow, so that other interactions (e.g., electron-electron and electron-phonon) compete seriously with the band properties of electrons. In some oxides of the early transition elements, such as TiO_2, some direct overlap of the 3d orbitals on neighboring Ti ions is possible and can contribute to the width of the d band. But the 3d orbitals contract rapidly with increasing atomic number and with increasing ionic charge, and for later transition-metal elements such as Ni direct overlap is very small. In most

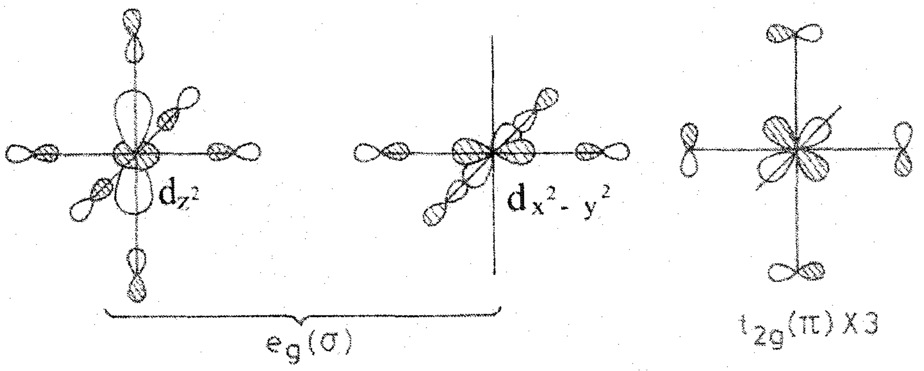

Figure 2.11: Symmetry-adapted linear combinations of oxygen $2p$ orbitals arising in TiO_6 octahedron, shown with a bonding combination of an appropriate Ti orbital. The type of bonding (σ or π) is indicated. Only one of the triply degenerate Ti 3d t orbitals in the cubic $BaTiO_3$ is shown.

transition-metal oxides, the d bandwidth is largely a consequence of indirect bonding interactions via metal–oxygen–metal linkages. It is thus very sensitive to structural and electronic factors. This can be illustrated in $ATiO_3$ perovskites where a small variation in the lattice constant results in quite different mechanisms of electron transport, namely band conduction in $SrTiO_3$ [115, 116], and small radii polaron hopping in $BaTiO_3$ [117] †. As the bands become narrower, a point is reached where the band model fails totally and electrons become localized; this is known generally as the Mott transition. NiO is an example of a magnetic insulator with $3d^8$ electron configuration of the conduction band. According to the traditional band model, the conduction band of NiO is partially filled, and the Hubbard potential, U, for electron transfer

$$Ni^{2+} + Ni^{2+} \rightarrow Ni^{+} + Ni^{3+} \tag{2.34}$$

is larger than the bandwidth so that electron remains localized [118]. Although stoichiometric $BaTiO_3$ does not fall into the category of "magnetic insulator", the Hubbard model is often invoked when transition-metal dopants are introduced into the Ti sublattice.

The 3d orbitals have a five-fold degeneracy in the free Ti^{4+} ion. As was mentioned before, when a Ti^{4+} ion is introduced into the octahedral environment of six oxygen ions, the five-fold degeneracy is removed due to crystal-field splitting. The result is a doubly degenerate e_g and a triply degenerate t_{2g} orbital. In $BaTiO_3$ this scenario is only applicable for the cubic phase. Below T_C, additional splitting of d orbitals occurs, resulting from the tetragonal distortion of the octahedra. Fig. 2.13 shows the splitting of d orbitals in the case of centrosymmetric tetragonal distortion, which for example, occurs in $SrTiO_3$ at 108 K. Both e_g and t_{2g} sets split in the lower symmetry, but the effect on e_g orbitals is much larger because of their stronger interactions with the ligands. It can also

---

† The small radii polaronic transport in $BaTiO_3$ is still a subject of discussion

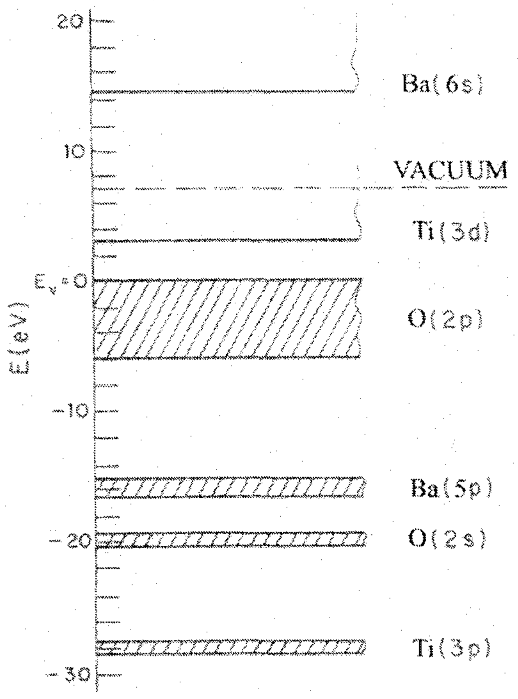

Figure 2.12: Schematic energy-level diagram for $BaTiO_3$

be seen that the lowering of d_{z^2} orbitals is energetically favorable for this configuration. Although similar trends might be expected for $BaTiO_3$, the magnitude of orbital splitting will be different since $BaTiO_3$ undergoes noncentrosymmetric tetragonal distortion (i.e., Ti^{4+} shifts from the center of the oxygen octahedron in the tetragonal phase). As revealed in Fig. 2.13, one would expect an increase in the width of the 3d conduction band at the cubic to tetragonal phase transition in $BaTiO_3$. However, no attempt has been made to calculate the band structure of $BaTiO_3$ in tetragonal or other lower symmetry phases.

2.3.2 Surface electronic structure of $BaTiO_3$

The study of the surface electronic structure of $BaTiO_3$ is important to catalytic properties and electron transport in polycrystalline $BaTiO_3$. For these purposes, it is of major interest to establish whether surface electronic states are present in the band gap of $BaTiO_3$. Computer simulations of the surface electronic structure of $BaTiO_3$ has been performed by Wolfram et al. [119], Ellialtioglu and Wolfram [120], Ellialtioglu et al. [121], and later by Cohen [110] and Padilla [107]. The surface electronic structure of $BaTiO_3$ has been analysed experimentally by means of XPS [72, 122], LEED [70], UPS [113, 73], STM [75, 123, 124].

Generally, two different types of surface states (SS) have been considered for the crystalline

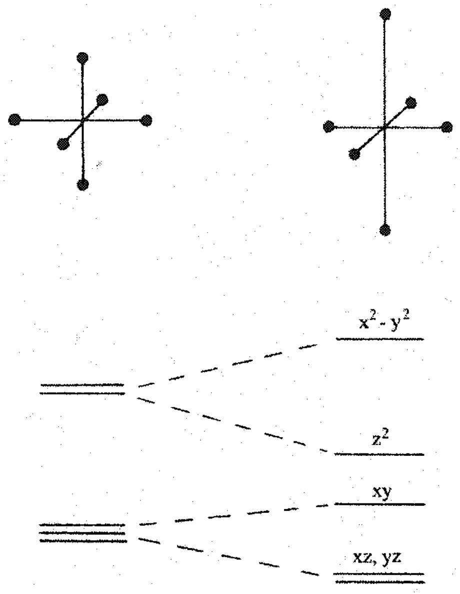

Figure 2.13: Splitting of d orbitals resulting from the tetragonal distortion of an oxygen octahedron

solid; i) intrinsic SS, which may exist at the ideally perfect surface and ii) extrinsic SS, created by surface defects and impurities. Intrinsic SS originate from interruption of the perfect periodicity of the crystal lattice at the surface. Depending on the overlap magnitude of their wavefunctions, these surface states can form a two-dimensional band with a continuous range of energies, which may extend into the bulk band gap. These wave functions are evanescent waves which decay exponentially with distance from the surface. They are therefore spatially localized on the surface in contrast to the Bloch waves which propagate through the crystal. Such surface states were first predicted by Tamm [125] and Shockley [126] and can only exist at the surface of a crystal. The wave functions which make up the surface states are drawn from those which would constitute the valence and conduction bands of an infinite crystal, so that the densities of states in the valence and conduction bands are diminished close to the surface. For intrinsic semiconductors, the neutrality conditions will be satisfied if half of the surface states are occupied, resulting in flat valence and conduction bands at the surface. Any n- or p-type doping will cause a shift of the Fermi level and, consequently, will induce a surface charge due to the change of the population of the surface states [127].

Little work is available on the theoretical analysis of intrinsic SS in $BaTiO_3$. Wolfram and coworkers [119], using the linear combination of atomic orbitals cluster method, predicted mid-gap surface states for $BaTiO_3$, in disagreement with experimenal investigations [72]. Cohen [110] studied non-polar (001) and polar (111) surfaces by means of linearized augmented plane wave (LAPW) calculations. Although no mid-gap SS were found, some shallow SS were predicted on the (111) plane. The author also reported that the surface band gap was significantly reduced,

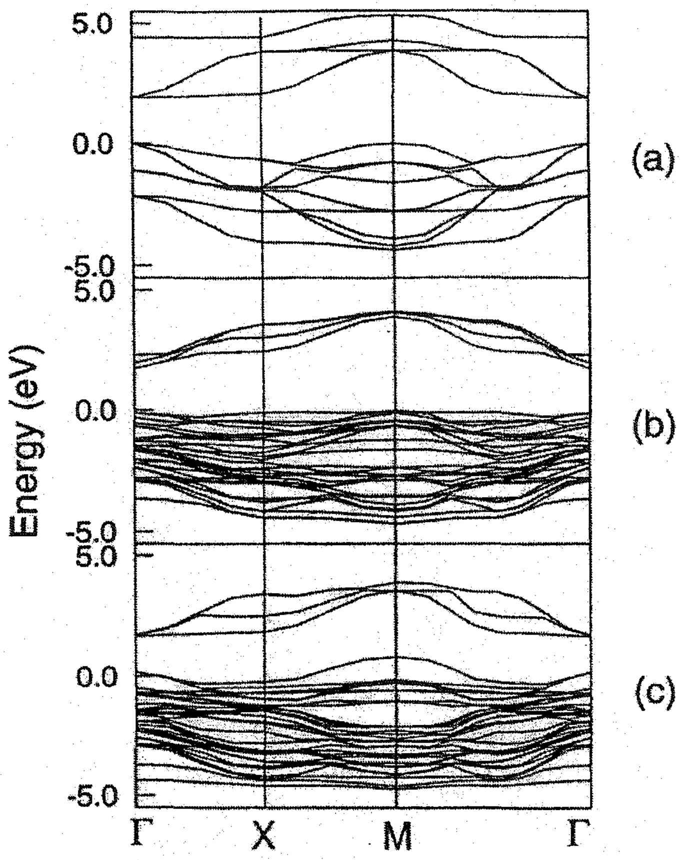

Figure 2.14: Band structures for $BaTiO_3$ in the cubic phase from ref. [107]. a) Surface-projected bulk band structure. b) BaO-terminated surface. c) TiO_2-terminated surface. The zero of energy corresponds to the bulk valence-band maximum. Only Ti 3d conduction bands are shown.

compared with that of the bulk. Using a plane-wave ultrasoft-pseudopotential approach, Padilla and Vanderbilt [107] did not find in-gap SS on non-polar BaO- and TiO_2-terminated (001) surfaces for both tetragonal and cubic $BaTiO_3$. However, a narrowing of the surface band gap, especially for a TiO_2-type of surface, was observed in accord with Cohen's data (see Fig. 2.14).

On the other hand, in-gap extrinsic SS have been experimentally observed by photoelectron spectroscopy (UPS) [113, 73] and scanning tunneling spectroscopy (STS) [75, 124]. Both techniques detected SS located about 0.9 eV below the Fermi level. The origin of this surface state has been assigned to a Ti^{3+} ion adjacent to the surface oxygen vacancy site. Such a deep localization of the Ti $3d^1$ electron is due to the attractive Madelung potential of the positively charged surface oxygen vacancy. It has been further detected by LEED [70] that heavily reduced samples exhibit ordering of the Ti^{3+} - $V_O^{\cdot\cdot}$ complex resulting in 2×2 or two mutually perpendicular 2×1 surface superlattices. Subsequent exposure to oxygen removes this surface state from the band gap indicating that oxygen adsorbs at defect sites. Although a Ti^{3+} - $V_O^{\cdot\cdot}$ complex would result in formation of an electric dipole at the surface of $BaTiO_3$, the total surface charge would remain unchanged. This is in contrast to non-transition metal oxides, such as ZnO. On both polar and nonpolar surfaces of ZnO, formation of the surface oxygen vacancies would result in surface band bending since the charge compensation is accomplished in this case by the depletion layer [128].

2.3.3 Electron transport in $BaTiO_3$

Despite the fact that the semiconducting properties of $BaTiO_3$ have been known for more than 40 years, it still remains uncertain whether the charge carrier is a small polaron or conduction band electron [91, 129, 130]. In the temperature range where the ionic contribution to conductivity is negligible, the electrical conductivity, σ of n-type semiconductors is given by:

$$\sigma = en\mu_D \tag{2.35}$$

where e is the electron charge, n is the concentration of mobile electrons, and μ_D is the drift mobility of electrons. In the case of the conduction band electron approximation, the major contribution to the $\sigma(T)$ dependence comes from the n term, whereas for a small polaron model, the thermally activated mobility plays the major role.

A conduction band electron is envisaged as a Bloch wave localized in k-space (or wave vector space) and delocalized in r-space (or real lattice space). Common examples of this behaviour include "classical" semiconductors (e.g., Si, Ge, GaAs, GaN, etc.) with small lattice polarization. The electron effective mass is low in such materials ($0.1m_0$ - $0.9m_0$) and the drift mobility is large (10^3 - 10^5 cm^2/V s). As the polarization becomes larger and the conduction band width narrower, the lattice contribution to polarization starts to act as a "drag" on the motion of the carrier, and an electron or hole accompanied by its lattice polarization is known as a *polaron*[‡]. In the *large polaron* limit, the effect is to increase the effective mass of the charge carrier, but if polarization energy is sufficiently large compared with the bandwidth, a *small polaron* may result. In this case the carrier is essentially localized in r-space by the strong lattice polarization it produces [132]. In the adiabatic approximation, the transport of small polarons between ions involves the excitation of both the occupied and empty sites to the same energy, so that the electron can tunnel backwards and forwards between them [133]. This excitation involves an activation energy $E_p/2$, where E_p is the polaron binding energy, and the excitation can occur through the action of temperature or by quantum-mechanical tunnelling at low temperatures. In the former case, the polaron moves by thermally activated hopping, with a diffusion coefficient, D_H, given by [132]

$$D_H = \omega a^2 exp\left(-\frac{E_p}{2k_BT}\right) \tag{2.36}$$

[‡] The concept of polarons was first introduced by Landau [131]

where a is the distance between ions. In the latter case, for $k_B T < \hbar\omega/2$, the motion is coherent, and the polaron behaves like a heavy particle with mass

$$m^* \propto exp\left(\frac{E_p}{\hbar\omega}\right) \tag{2.37}$$

and with a mean free path determined by phonon and impurity scattering. Here ω is a characteristic phonon frequency i.e., for $BaTiO_3$, $\omega = 7\times10^{13}$ s^{-1}, is a frequency of the longitudinal optical phonon mode [134]).

The 'world' of polarons is extremely rich. Polarons can be classified by the alternatives 'small–large', 'electron–hole', 'single polaron–bipolaron', 'free–bound', 'adiabatic–nonadiabatic'. Polarons exhibit interesting light absorption properties [135, 78]; polarons are coupled not only with phonons but also between themselves resulting in *polaronic plasmons* [132]. Large bipolarons are Cooper pairs in high temperature superconductors [132]. For recent overviews on polarons the reader may refer to Devreese [136] and on small polarons specifically to Shluger and Stoneham [137]

The first indication of polaronic-type transport in $BaTiO_3$ was provided by Cox and Tredgold [138] who detected very low drift mobility of holes in undoped $BaTiO_3$. By using a high electric field transient photoconduction technique, the authors [138] obtained μ_D values ranging from 2.0×10^{-4} cm^2/Vs to 4.3×10^{-4} cm^2/Vs at 90 °C. Cox and Tredgold [138] assigned these exceptionally low values of mobility to the hole trapping mechanism by accidental impurity centers in dielectric $BaTiO_3$. Using Seebeck coefficient measurements, Ridpath and Wright [139] estimated the electron drift mobilities in reduced $BaTiO_3$ single crystals to be 5×10^{-4} cm^2/Vs at 25 °C. These values, however, were explained in terms of a small polaron hopping model. Bursian et al. [78] investigated the effect of concentration of charge carriers on the light absorption peak at 2 μm (i.e., 0.62 eV) and concluded that this absorption is caused by optical excitation of small polarons according to the 'photon-assisted hopping' model [133]. Explaining the electrical properties in terms of conduction band electrons requires an assumption that the optical absorption maximum is caused by electron excitation from donor levels being about 0.6 eV below the conduction band edge. However, extensive defect chemistry investigations reported by several authors [79, 64] give no indication of defect or impurity levels in this range. On the other hand, when small polarons are assumed they should satisfy the general relation between the small polaron binding energy, E_p, thermal hop energy, E_H, and optical hop energy, $\hbar\omega$:

$$\hbar\omega = 2E_p = 4E_H. \tag{2.38}$$

The energy $\hbar\omega$ is required to transfer an electron optically from one ion to another, without moving the ions (i.e., according to the Franck-Condon principle). Several authors reported the infrared absorption peak centered at 2-2.3 μm in semiconducting $BaTiO_3$ [140, 141, 142, 78]. It was shown that the optical absorption maximum does not depend on the conductivity, contrary to the behaviour of free carriers. However, based on the small polaron model, the optical absorption maximum gives a thermal activation energy, E_H for a small polaron hop which is too high compared with the drift mobility data given by

$$\mu \propto T^{-3/2} exp\left(-\frac{E_H}{k_B T}\right). \tag{2.39}$$

Another challenge is that within the small polaron model, the values of the Hall and drift mobilities should differ by several orders of magnitude, as given by

$$\frac{\mu_H}{\mu_D} = \frac{k_B T}{J} exp\left(\frac{2E_H}{3k_B T}\right), \tag{2.40}$$

where J is the electron transfer integral between neighboring Ti ions. However, due to the widespread values of the drift mobilities which exist in the literature, Eq. 2.40 is not always satisfied [143]. In fact, measurement of drift and Hall mobilities in low-mobility $BaTiO_3$ is quite a difficult task. The values of drift and Hall mobilities as well as the energies of thermal activation of conductivity, E_σ, and mobility E_μ are listed in Table 2.1.

Table 2.1: Electron tranport parameters of $BaTiO_3$

$BaTiO_3$	μ_D, cm^2/Vs	μ_H, cm^2/Vs	E_μ, eV	E_σ, eV	Reference
reduced s.c.	5×10^{-4}		0.074		[139]
undoped s.c.	3.5×10^{-3}		0.15		[117]
undoped s.c.	2.0×10^{-4}				[138]
Nb-doped s.c.				0.092	[130]
n-doped s.c.	0.2		0.04		[144]
reduced s.c.		1.0, 0.13			[14]
reduced s.c.		0.5			[140]
ceramic at 1470 K	0.1				[64]
n-type ceramic				0.072	[129]
reduced s.c. at 700 °C				0.107	[145]
reduced s.c. at 1300 °C				0.064	[145]
reduced s.c.		0.1		0.085	[140]

In order to explain the anomaly of too low thermal activation energy and too high drift mobility in $BaTiO_3$, Ihrig and Hennings [146] invoked Emin's "correlated small polaron hopping" model [147]. In Emin's model, two successive polaron hops are correlated with one another because the electron is able to hop to a third site before the initially occupied lattice site relaxes. In the correlated hopping model, Hall and drift mobility need not be far from equal as is usually the case for uncorrelated small polaron hopping. The experimental values of thermal activation energy are therefore underestimated which results in lower values of the optical excitation energy.

In conclusion, a number of experimental results consistently support the idea that the electric current in barium titanate is carried by small polarons having an enhanced drift mobility due to the correlation of successive polaron hops. However, transport properties at low temperatures have not been studied sufficiently. There is no data about thermoelectric power behaviour in rhombohedral and orthorhombic phases of $BaTiO_3$. The Hall and drift mobilities of charge carriers below 273 K are unknown. The conductivity in low temperature phases is also poorly studied. This information, however, might be very useful in further development of the small polaron model in $BaTiO_3$.

2.3.4 Resistivity anomaly in $BaTiO_3$ ceramics

One of the most interesting features of barium titanate is a resistivity anomaly occurring at the ferroelectric-to-paraelectric phase transition. When a properly doped semiconducting $BaTiO_3$ polycrystal is heated above the Curie temperature, its electrical resistivity rises by up to 6 - 7 orders of magnitude, exhibiting a large positive temperature coefficient of resistivity (PTCR). Fig. 2.15 shows the progress in optimization of the temperature dependence of resistivity of $BaTiO_3$ ceramics over the last 40 years. It is surprising that single crystals of n-doped barium titanate do not demonstrate any change in their temperature coefficient of resistivity and remain semiconducting above the Curie temperature [148]. Direct measurements of the electrical resistivity of the ceramic's single grains and grain boundaries performed by Gerthsen and Hoffmann [149], Nemoto and Oda [10], Sumino et al. [150], and Kuwabara et al. [151] have confirmed that the PTCR effect in $BaTiO_3$ is exclusively a grain boundary phenomenon. PTCR devices based on semiconducting $BaTiO_3$ have found wide application in electronic and automotive industries [152]. Their worldwide production reached

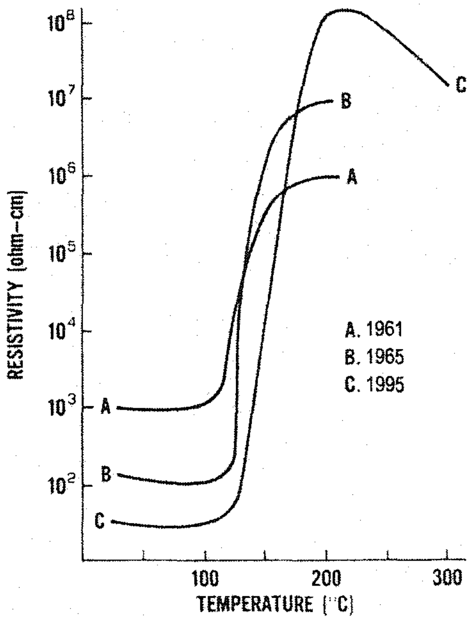

Figure 2.15: Progress in optimization of the PTCR behaviour of $BaTiO_3$ ceramics.

500×10^6 pieces per year in 1995. Although the PTCR effect in barium titanate was discovered four decades ago, the comprehensive theory of this phenomenon is still under construction due to the confluence of both semiconducting and ferroelectric properties, complicated further by the material's polycrystalline structure. Investigation of the nature of the resistivity anomaly in $BaTiO_3$ ceramics is one of the objectives of the present work. The following sections summarize the recent progress in understanding the PTCR anomaly.

Peria model

Peria et al. [153] proposed that the contacts between $BaTiO_3$ ceramic grains are pressure-sensitive and that the strain introduced by the changes in lattice parameters that accompanies the tetragonal to cubic transition at the Curie temperature is responsible for a change in contact resistance between the grains. This model, however could not account for the effects of processing conditions on the PTCR behaviour. Particularly, it cannot explain the effect of sintering atmosphere and acceptor doping on the resistivity anomaly.

Double Schottky barrier model

The most widely accepted model of the PTCR effect in $BaTiO_3$ was proposed by Heywang [154, 1] and was refined by Jonker [155]. According to Heywang, the resistivity behaviour of $BaTiO_3$ can be explained in terms of temperature dependent double Schottky potential barriers at the ceramic's grain boundaries (GB) (see Fig. 2.16(a).

These potential barriers originate from the negatively charged two-dimensional layer of surface acceptor states (electron traps). Originally the surface states were proposed to be monoenergetic, with energy E_t lying well below the Fermi level E_F at room temperature. According to Fermi-Dirac statistics, the density of the trapped electrons, N_t at the surface is given by:

$$N_t = \frac{N_T}{1 + exp\left\{\frac{\varphi_0 - E_F + E_t}{k_B T}\right\}}, \tag{2.41}$$

where N_T is the total surface density of electronic traps, and φ_0 is the potential barrier height. The electric field generated by the charged grain boundary gives rise to band bending in the adjacent grains and to the formation of a depletion layer with a thickness, b:

$$b = \frac{N_t}{2N_D}, \tag{2.42}$$

where N_D is the concentration of ionized donors. This depletion layer is positively charged to compensate for the negative charge of the interface. By solving the Poisson equation for the charge distribution shown in Fig 2.16(b), one can obtain the potential barrier height

$$\varphi_0 = \frac{eN_t^2}{8\varepsilon\varepsilon_0 N_D}, \tag{2.43}$$

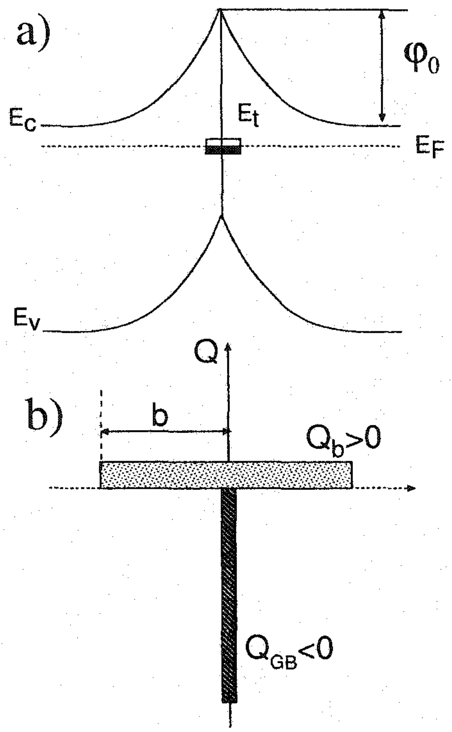

Figure 2.16: Schematic of a) the band energy diagram of the double Schottky barrier and b) the charge density distribution at the grain boundary of $BaTiO_3$. The negative GB charge, Q_{GB}, and positive charge of the depletion layer Q_b of thickness b are indicated. The potential barrier and the valence and conduction band edges are depicted as φ_0, E_v, and E_c respectively. The energy of the interface electron states E_t and the Fermi level E_F are also indicated.

where ε is the dielectric permittivity of the sample, ε_0 that of the vacuum, and e is the electronic charge.

For carrier transport through the grain boundary within the thermionic emission model (i.e., mean free electron path is larger than the barrier width) the low voltage resistivity, ρ_{GB} of a 1 cm^2 barrier area is given by [1]

$$\rho_{GB} = Aexp\left(\frac{\varphi_0}{k_B T}\right), \tag{2.44}$$

where A is proportional to T^2.

In the paraelectric phase, the dielectric constant follows the Curie-Weiss law (Eq. 2.2), and the potential barrier φ_0 should increase linearly with temperature. By substitution of Eq. 2.43 into Eq. 2.44 one obtains the temperature dependence of the GB resistivity as:

$$\rho_{GB} = Aexp\left[B\left\{1 - \frac{T_0}{T}\right\}\right], \tag{2.45}$$

where B is a constant. According to Eq 2.45, the GB resistivity will increase with temperature in the paraelectric phase. The potential barrier will continue to rise until the Fermi level at the GB approaches the energy of the surface states. At this point the resistivity will reach its maximum value. Further heating will cause a reduction of the surface charge due to a decrease in the density of trapped electrons. As a result, φ_0 will saturate and ρ_{GB} will start to fall since from this point, the only factor which will determine the resistivity behaviour is the thermal emission of electrons over the barrier. According to the Heywang theory, for typical PTCR material with a jump in resistivity of 4 to 5 orders of magnitude, the maximum value of φ_0 is around 0.65 eV. In order to reach such barrier potentials, a density of surface electron states, N_t, as high as 10^{14} cm^{-2} is needed.

Regarding the nature of these interface electron states, a general agreement has not been reached so far. Heywang and Brauer [156] assumed preferential segregation of acceptor impurities at the GB, whereas Jonker [155, 157] attributed the interface states to chemisorbed oxygen. Based on their defect chemistry and diffusion studies, Daniels et al. [64] proposed that the grain boundary potential barriers originate primarily from the Ba vacancy-rich grain boundary layer formed during cooling from high temperatures. Later, Desu and Payne [71] proposed segregated donors and titanium vacancies as electron traps near the GB region.

Concerning the low resistivity of PTCR ceramics below the Curie point, a very plausible argument was provided by Jonker [155] who pointed to a specific effect, related to the ferroelectric nature of $BaTiO_3$. He proposed that below T_C, the resistivity is small because the spontaneous polarization depresses the grain boundary barrier. In a polycrystalline ferroelectric sample, each crystal consists of ferroelectric domains which are spontaneously polarized. In the tetragonal phase, the polarization direction is along the tetragonal axis, which changes in direction from domain to domain. At the contact between two crystals of different orientation, the domain structure does not fit. As a result there would be a non-continuous normal component of polarization through the surface. As this is impossible, domain structures are formed with some degree of mismatch and the surface layers must be strained in order to get a complete fit.

In semiconducting crystals the non-fitting problem does not exist because there is a possibility of compensation by interface charge. This occurs because the domain pattern below the Curie point forms in such a way that the negative surface charge of trapped electrons compensates the difference in the normal component of polarization on both sides of the boundary, and no depletion layer is formed (Fig.2.17). This occurs in half of the GB area. In the other half, the barriers are reinforced by the ferroelectric domains, but since these are electrically in parallel, a low overall resistance is observed. Indeed, the reported value of spontaneous polarization, P_s, for $BaTiO_3$ is about 26 μC/cm^2, which is equivalent to a density of surface electronic states of 1.6×10^{14} electrons/cm^2. Hence, according to Jonker, in the ferroelectric phase, negative surface charge can be completely compensated by spontaneous polarization resulting in the low electrical resistivity values.

Despite an insufficient understanding of the nature of the surface electron traps, the Heywang model provided a good quantitative explanation of the temperature dependence of electrical resistiv-

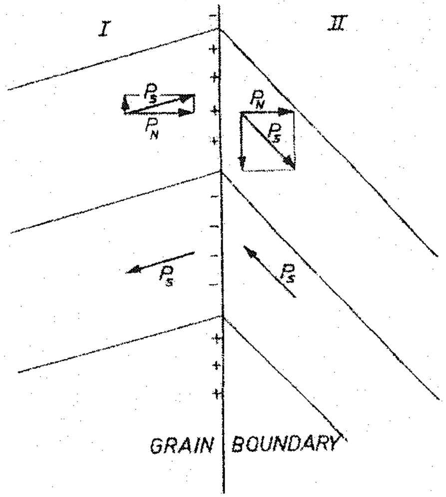

Figure 2.17: Ferroelectric domain configuration at the GB of semiconducting $BaTiO_3$. The head of the vector of spontaneous polarization P_s has a positive charge, whereas the tail has a negative charge. The GB charge associated with the spontaneous polarization is equal to the difference between the normal components of the P_s of grain I and II. From Ref. [155]

ity in PTCR $BaTiO_3$ ceramics. Nevertheless, there are several features that the original model could not explain, particularly the low capacitance of a single grain boundary [149, 151], non-exponential dependence of the current-voltage characteristics [149, 9, 10, 151, 158], and anomalous behaviour of the thermoelectric power at T_C [159, 160]. Gerthsen and Hoffmann [149], and Kuwabara et al. [151] reported that the measurements of differential capacitance of the PTCR $BaTiO_3$ single grain boundaries yielded values between 1×10^{-7} and 5×10^{-7} F·cm^{-2}, which are more than an order of magnitude lower than the theoretical capacitance of a double Schottky barrier in PTCR barium titanate. To improve the fit, Gerthsen and Hoffman proposed the existence of an intermediate titania-rich layer. This second phase layer of a thickness of 500 nm and with a dielectric constant of 200 should be present between the $BaTiO_3$ grains. However, TEM analysis performed by Haanstra and Ihrig [30] could not identify any second phase, leaving the question of the low capacitance unexplained.

Another weak point of the original Heywang model is disagreement of the calculated and measured current-voltage ($I-V$) characteristics. This was addressed by Gerthsen and Hoffmann [149], Kvaskov and Valeev [9], Nemoto and Oda [10], Kuwabara et al.[151], Belous et al. [158], and Al-Allak et al. [161]. A comprehensive analysis of the $I-V$ models in $BaTiO_3$ undertaken during this study is presented in Chapter 8.

Electron trap activation model

In contrast to the Heywang model which requires that the surface electron traps be completely occupied below T_C and that the concentration of free charge carriers doesn't change above T_C, Hari et al.[98] proposed that the PTCR effect is associated with a decrease in charge carrier density at T_C. Their theory is based on electron paramagnetic resonance (EPR) measurements in a temperature range of -195 °C to +277 °C. At 120 °C they observed a strong increase of the EPR signal corresponding, as they claim, to a singly ionized barium vacancy. In the tetragonal phase, the barium vacancy was found to be neutral so that the conversion is associated with charge trapping and thereby increases the electrical resistivity because of the diminished charge carrier density. The increase in the activation energy of the ionized barium vacancy was associated by the authors [98] with the disappearance of spontaneous polarization above T_C. The authors also observed a similar behaviour of electron trapping for PTCR $BaTiO_3$ samples which were intentionally doped with small amounts of acceptor dopant (Mn) to increase the PTCR effect. Hari et al. reported that the EPR signal from Mn^{2+} appears only above 120 °C and below -78 °C. It has been concluded that in tetragonal and orthorhombic phases, Mn exists as Mn^{3+}. Above T_C, Mn^{3+} traps an electron and becomes Mn^{2+}, causing a decrease in the charge carrier concentration. However, it is not clear why the manganese, whose concentration is more than an order of magnitude less than the donor concentration, can cause a significant increase (up to three orders of magnitude) in the resistivity jump. Nevertheless, this model seems quite interesting and deserves further examination. A comprehensive EPR investigation of both $BaTiO_3$ polycrystals and single crystals in reduced and oxidized forms was performed in this work and is presented in Chapter 7.

Chapter 3

$Ba(B'_{1/3}B''_{2/3})O_3$ perovskites

Low loss dielectric materials are used extensively in modern microwave electronics as dielectric resonators (DR) [162], and substrates for high-T_C superconductor (HTS) filters [163, 164, 165]. Since in the dielectric medium with permittivity ε, the electromagnetic wavelength decreases as $\varepsilon^{-1/2}$, solid dielectric materials provide the possibility of reducing component size according to the $\varepsilon^{-1/2}$ dependence. From the early 1980's this property was successfully utilized in communication satellites where DRs have replaced the traditional bulky vacuum-filled cavity filters [166]. A number of other applications of DRs include output multiplexers in communication base stations [167], feedback circuits for microwave oscillators [168, 169], down converters, frequency standards for the X (8-12 GHz), K_u (12-18 GHz), and K (18-27 GHz) electromagnetic bands. Demand in DR's is increasing along with development of millimeter-wavelength local area networks (LAN's), collision-avoidance radar, etc. Recent breakthroughs in the design of the HTS-shielded dielectric resonators have opened a new horizon in development of extremely low-loss microwave radar and communication systems [170, 171].

In this chapter the reader will first be introduced to the concept of the dielectric resonator and to the major requirements of dielectric materials for microwave applications. Then the properties of existing microwave dielectric materials will be reviewed together with the mechanism of dielectric loss in nonpolar ionic crystals. The rest of the chapter will focus on synthesis and properties of specific dielectric materials, namely $Ba(B'_{1/3}B''_{2/3})O_3$ perovskites, where B$'$ is Mg, Zn, or Ni; and B$''$ is Nb or Ta. The choice of these materials for the present project was governed by their exclusive dielectric properties.

3.1 Dielectrics for microwave band applications

3.1.1 Concept of a dielectric resonator

The physics behind the dielectric resonator's performance is based on Maxwell's theory of electromagnetism. When an electromagnetic wave enters the medium with dielectric permittivity ε and magnetic permeability μ, its wavelength decreases as

$$\lambda = \frac{\lambda_0}{\sqrt{\varepsilon\mu}} \tag{3.1}$$

where λ_0 is the wavelength in vacuum. This opens the possibility of reducing the size of the dielectric resonator by a factor of $\varepsilon^{1/2}$ and planar dimensions of microwave circuits by a factor of ε. The concept of DR was introduced by Richtmyer [172] who showed that suitably shaped objects made of a dielectric material can function as resonators for high frequency oscillators. Depending on its shape, the DR will have a different set of resonance modes with corresponding resonance frequencies. The field distribution of electric and magnetic components is shown in Fig. 3.1 for $TE_{01\delta}$ and $TM_{01\delta}$ resonance modes in cylindrical DRs. For dielectric constant $\varepsilon > 35$, more than 95 % of the stored

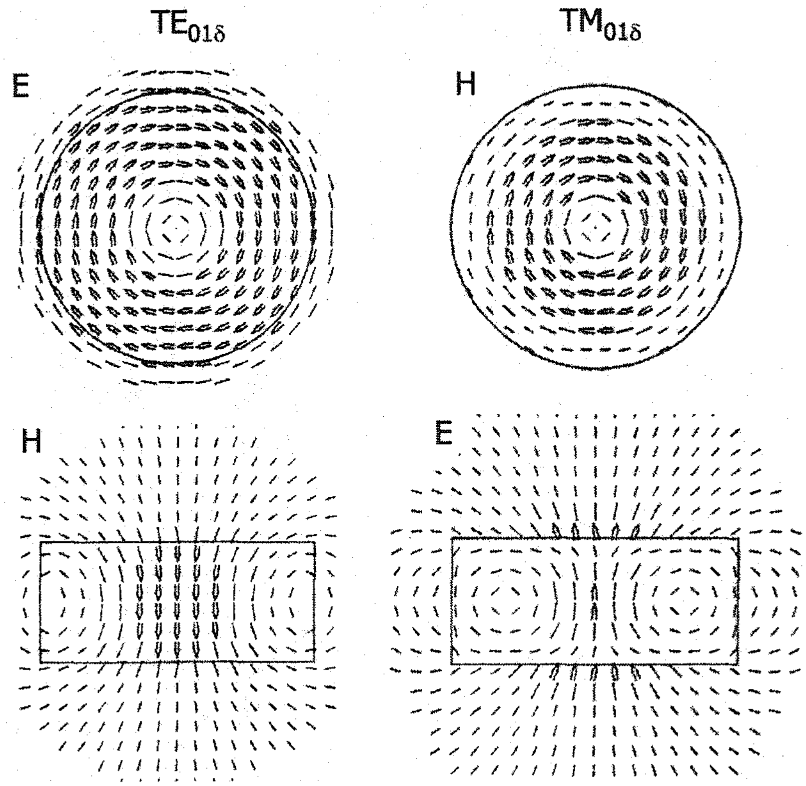

Figure 3.1: Electric and magnetic field distribution in $TE_{01\delta}$ and $TM_{01\delta}$ mode DR. Only equatorial and meridian planes are shown. From ref [173].

electric energy of the $TE_{01\delta}$ mode, as well as over 60 % of the magnetic energy are stored within the dielectric cylinder. For a distant observer the $TE_{01\delta}$ mode appears as a magnetic dipole. Hence it is sometimes termed the "magnetic dipole mode". Similarly, the $TM_{01\delta}$ mode appears as the electric dipole. The accurate calculation of the resonance frequencies of DR involves a solution of Bessel functions which satisfy the boundary conditions at the surface of the resonator. Nowadays suitable software packages are used for this type of calculation [162]. However, simple empirical solutions exist for the lowest frequency of TE and TM resonance modes of the cylindrical resonators.

3.1.2 Main requirements for a dielectric resonator

There are three major requirements for materials used as dielectric resonators. The primary demands for any candidate material are as follows:

1. High dielectric constant ε, ($\varepsilon > 20$) to minimize the microwave device size.
2. High unloaded quality factor Q, to minimize dielectric losses of electromagnetic energy.
3. Small and tunable temperature coefficient of resonance frequency τ_f, (-5 ppm/K $< \tau_f <$ $+5$ ppm/K) to avoid the temperature drift of the microwave parameters.

Despite the abundance of dielectric materials, there are few suitable candidates which satisfy all of these three requirements.

Dielectric permittivity

A number of different polarization mechanisms including electronic, ionic, and dipolar contribute to the total dielectric permittivity. A high polarizability without strong energy absorption in the 10^9-10^{11} Hz range can only be realized through optical and infrared polarization. However, the dielectric contribution from optical polarization is usually small in most crystals. The infrared contribution to polarization comes from the induced displacement of cation and anion sublattices by an electric field. That is why ionic solids have higher values of ε than covalently bonded crystals (e.g., ε_{BaTiO_3}=2000, $\varepsilon_{Pb(Mg_{1/3}Nb_{2/3})O_3}$=15000, ε_{SrTiO_3}=300, ε_{TiO_2}=90, ε_{Si}=11, ε_{Ge}=14,). However, materials with very high dielectric constant (e.g., $BaTiO_3$, $SrTiO_3$, $LiNbO_3$, $KTaO_3$, etc.) usually reveal a strong dispersion of ε with frequency due to the dipolar orientation polarization or due to the paraelectric contribution from the soft mode. A dispersion of dielectric constant is always accompanied by the high dielectric loss. That is why, a search for suitable materials is usually limited to nonpolar dielectrics with high ionic polarization.

Q-factor

The quality factor, Q_d, of dielectric material is a reciprocal of the dielectric loss:

$$Q_d = \frac{1}{tan\delta}. \tag{3.2}$$

However, it is impossible to measure this quantity at microwave frequencies. Strictly speaking, the measured quality factor, Q, is always lower than the quality factor of the dielectric, since it includes the losses in the waveguide or the resonance cavity (depending on the method of measurement)

$$\frac{1}{Q} = \frac{1}{Q_d} + \frac{1}{Q_w} \tag{3.3}$$

where $1/Q_w$ is the loss in the waveguide walls. Fortunately, high quality metal waveguides have very low loss (Q_w = 35 000 – 40 000) so that $Q \approx Q_d$ for dielectrics with moderate loss. The effect of the conductive losses in the waveguide walls become significant, however, when ultra low loss dielectrics with $Q_d > 30\,000$ are analyzed. This becomes extremely important at cryogenic temperatures where the Q-factor of dielectrics may reach 1×10^6. In this case, to measure the actual loss in dielectrics, high temperature superconductor (HTS) clad waveguides must be used. Several authors reported extremely low dielectric loss for DRs measured with HTS clad resonant cavities [174, 175, 176].

Temperature coefficient of resonant frequency

Two factors determine the temperature coefficient of the resonance frequency, τ_f, namely, thermal expansion of material, α, and temperature coefficient of dielectric constant, τ_ε

$$\tau_f = -\alpha - \frac{1}{2}\tau_\varepsilon. \tag{3.4}$$

The linear thermal expansion coefficient appears as a result of the anharmonicity of the lattice vibrations. For ionic solids, α is in the range of 8 - 15 ppm/K. Eq. 3.4 implies that potential microwave dielectric materials should have a negative τ_ε in the range of -15 ppm/K $< \tau_\varepsilon <$ -5 ppm/K. However, there are not many single phase materials that satisfy this latter condition. Alternative ways of achieving temperature stable DRs include synthesis of multiphase compositions with τ_ε values of the opposite sign[177, 178, 179] or preparation of a single phase solid solution from two end members having opposite sign of τ_ε [180, 181, 182], or preparation of the gradient materials with different τ_ε values [183]. Various methods of temperature compensation utilized in microwave DRs have been reviewed recently by Belous [184].

3.1.3 Current microwave dielectrics and future needs

Current dielectric resonators for microwave applications can be classified according to their dielectric constant value. Following this approach, dielectric materials form three major families, i.e., the first one with large ε ($\varepsilon > 70$), the second one with medium ε ($32 < \varepsilon < 45$), and the third one with relatively small ε ($20 < \varepsilon < 32$). Examples of these materials together with their dielectric properties are given in Table 3.1.

Dielectric resonators with $\varepsilon > 70$ are utilized in the UHF (0.3-1 GHz), L (1 - 2 GHz), and S (2 - 4 GHz) bands, which are primarily allocated for ISM (0.93GHz), USCT (0.90 GHz), CT1 (0.959 GHz), GPS*(1.5 GHz), W-LAN†(2.4 GHz), DECT‡(1.89 GHz), PCN § (1.85 GHz) and PCS¶ (1.87 GHz) systems.

Table 3.1: Dielectric properties of materials for DR applications

Composition	ε	Q×f, THz	τ_f, ppm/K	Ref.
$BaO \cdot Sm_2O_3 \cdot TiO_2$	78...84	9.5...11	-15...+25	[179, 185]
$BaO \cdot Nd_2O_3 \cdot TiO_2$	90...95	5.1...6.2	-10...+10	[178]
$BaTi_4O_9$	34...36	55	-5...+6	[83, 186]
$Ba_2Ti_9O_{20}$	36...39	50	-5...+6	[187, 188]
$Zr_{0.8}Sn_{0.2}TiO_4$	38	51	-10...+10	[189, 190]
$(BaSr)(Ni_{1/3}Nb_{2/3})O_3$	34	100	0	[181]
$Ba(Zn_{1/3}Ta_{2/3})O_3$	30	120	-5...+5	[182]
$Ba(Mg_{1/3}Ta_{2/3})O_3$	23...24	200...300	-5...+5	[191]

Dielectric resonators with $32 < \varepsilon < 45$ were initially used in the output multiplexers of satellite and terrestrial communication systems operating in the C (4-8 GHz) and X (8-12 GHz) bands. Nowadays, they are being displaced from applications in the X-band by ultra low loss dielectrics. However, resonators with $32 < \varepsilon < 45$ are becoming the material of choice in high power low loss terrestrial base stations operating in the L- and S-bands. Finally, dielectric resonators with low ε ($20 < \varepsilon < 32$) have found a variety of applications in X (8-12 GHz) K_u (12-18 GHz) and K (18-26.5 GHz) bands for feedback circuitry of stabilized oscilators in radar, band-stop and band-pass filters for output multiplexers, down-convertors for satellite TV receivers, etc. Owing to their exceptionally high Q-factors (see Table 3.1), DRs based on the $Ba(Mg_{1/3}Ta_{2/3})O_3$ composition are potential candidates for future K_a- and V-band applications [171, 168].

There are two major trends which govern research into microwave dielectric materials. First, consumer demands for multifunctional pocket-sized devices are accelerating the pace in the devel-

---

*Global Positioning System

†Wireless Local Area Network

‡Digital European Cordless Telephone

§Personal Communication Network

¶Personal Communication System

opment of dielectric materials with increased dielectric permittivity. Second, increasing the output power of the communication satellites and terrestrial base stations will reduce the total number of these devices worldwide and increase of their operation range. To satisfy this latter demand, dielectric materials with ultra low loss (high Q-factors) are required.

3.2 Origin of dielectric loss at microwave frequencies

3.2.1 Extrinsic losses

Generally, dielectric losses can be characterized as *intrinsic* and *extrinsic*. Intrinsic dielectric losses originate in a perfect crystal as a result of interaction of the a.c. electric field with the phonon system of the crystal. Intrinsic losses are discussed in detail in paragraph 3.2.2. Extrinsic losses, on the other hand, are peculiar to different imperfections in the crystal such as impurity atoms, interstitials, vacancies, dislocations, pores, grain boundaries, and second phases. Such defects will affect both the absolute value of the loss and the temperature dependence of the loss. Extrinsic losses are discussed briefly below.

Impurities

Losses due to the different types of defects exhibit different frequency and temperature dependence. A common type of defect in ceramics containing titanium oxide is the Ti^{3+} ion which forms during sintering at high temperature. Recently Templeton et al. [192] examined the dielectric loss of polycrystalline TiO_2 due to the presence of oxygen vacancies and Ti^{3+}. They found that very pure TiO_2 displayed high tan δ at 300 K. Upon cooling, ceramics showed a dramatic reduction in tan δ at around 100 K. This was interpreted as a carrier freeze-out. When TiO_2 was doped with acceptor impurities, the tan δ decreased considerably, dropping smoothly as a function of temperature.

In general, point defects or crystal disorder may induce absorption of the microwave electromagnetic energy by a one-phonon absorption process. This is caused by relaxation of the energy and momentum conservation rule (see Eqs. 3.8 and 3.9) due to the breakdown of the translational symmetry of the crystal. One-phonon absorption is temperature independent as long as the concentration of defects is low and does not change with temperature. For frequencies much lower than the optical phonon eigenfrequency, the microscopic calculations yield [193] $\varepsilon'' \propto \omega$ for uncorrelated charged point defects and uncharged planar defects, $\varepsilon'' \propto \omega^2$ for uncharged linear defects and $\varepsilon'' \propto \omega^3$ for uncharged point defects [194].

Porosity

Porosity plays an important role in determining the dielectric loss. Poorly sintered ceramics always exhibit high tan δ [189, 195]. It is possible that the losses are related to the surface area of the pore as the structure of the free crystal surface may undergo different types of relaxation or reconstruction [196, 197, 127]. The phonon spectrum of the surface is different from that of the bulk. Relaxation of the surface changes the surface phonon spectrum and its interaction with an a.c. field [127].

Grain size

The data about the influence of the grain size on the dielectric loss are conflicting. In alumina, the tan δ increases with grain size [198], but in polycrystalline TiO_2, there seems to be no correlation with grain size [192]. In $Ba(Mg_{1/3}Ta_{2/3})O_3$, the effect of grain size was not systematically studied. However, different papers reported similar dielectric loss for ceramics with a grain size of 2 μm [199] and 20 μm [200].

Second phase

Addition of a second phase to the ceramic matrix is a common practice in the dielectric materials technology. Usually, the second phase is added to tune the temperature coefficient of the resonance frequency or to improve the sinterability. For example, addition of ZnO to $BaTi_4O_9$ improves the temperature stability of permittivity [201]. However, in most cases the second phase degrades the Q-factor of pure ceramics. For example, $BaZrO_3$ is a good mineralizer for $Ba(Zn_{1/3}Ta_{2/3})O_3$ since it decreases the sintering time by a factor of two or more. However, addition of 5 mol% $BaZrO_3$ decreases the Q-factor at 10 GHz from 16800 to 12000 [189, 182]. Despite these results, Davies et al. [202] proposed a theory for improvement of the Q-factor in the $Ba(Zn_{1/3}Ta_{2/3})O_3$–$BaZrO_3$ system due to "stabilization of the ordering-induced domain boundaries via the partial segregation of Zr cations". Later, Akbas and Davies [203] extended this model for the $Ba(Mg_{1/3}Nb_{2/3})O_3$–$BaZrO_3$ system. They reported 100 % improvement of the Q-factor of $Ba(Mg_{1/3}Nb_{2/3})O_3$ after addition of 5% of $BaZrO_3$. However, as shown in Chapter 10, the improved value of the Q-factor in $Ba(Mg_{1/3}Nb_{2/3})O_3$–$BaZrO_3$ obtained by Akbas and Davies [203] is still 50 % lower than that of pure $Ba(Mg_{1/3}Nb_{2/3})O_3$ obtained in the present work.

3.2.2 Intrinsic losses

Debye loss

Although the Debye losses do not conform exactly to the definition of intrinsic loss, i.e., they are not caused by the interaction of the a.c. electric field with the *phonon* system of the crystal, it seems justified to assign them to the intrinsic type of loss(or at least to describe them in the intrinsic loss section), since they can be observed in ideal crystals and possess a fundamental nature. The problem of calculation of the dielectric loss was formulated by Debye [204] who investigated the loss in polar liquids whose molecules have a permanent dipole moment. The a.c. field tends to orient the dipoles along the field direction. The Debye loss in a liquid arises from the viscous friction of rotating dipoles against neighbouring molecules of the liquid. Debye came to the conclusion that dipolar polarization and the loss due to relaxation of the dipolar polarization can be described via real and imaginary parts of the dielectric constant [205]:

$$\varepsilon'(\omega) = \varepsilon_\infty + \frac{\varepsilon_s - \varepsilon_\infty}{1 + \omega^2\tau^2} \tag{3.5}$$

$$\varepsilon''(\omega) = (\varepsilon_s - \varepsilon_\infty)\frac{\omega\tau}{1 + \omega^2\tau^2} \tag{3.6}$$

$$tan\delta = \frac{\varepsilon''(\omega)}{\varepsilon'(\omega)} = \frac{(\varepsilon_s - \varepsilon_\infty)\omega\tau}{\varepsilon_s + \varepsilon_\infty\omega^2\tau^2} \tag{3.7}$$

where ε_s and ε_∞ are the static and optical dielectric permittivities, respectively, ω is the angular frequency of the a.c. field and τ is the relaxation time of the dipole. An important conclusion of the Debye model is that tanδ tends to zero at high frequencies. This classical work by Debye was so important that the dielectric loss in various crystals (not only in liquids or solids containing polar dipoles) is called Debye loss. This, however, is not well justified. In fact, the Debye theory is not applicable to analysis of dielectric loss in crystals which do not contain permanent dipole moments [205].

The modern theory of intrinsic loss at microwave frequencies in all 32 symmetry groups was developed by Gurevich [206] and Gurevich and Tagantsev [193]. The theory predicts different temperature and frequency dependence of the dielectric loss for different crystal symmmetries. Moreover, for crystals with uniaxial anisotropic permittivity such as Al_2O_3 and TiO_2, the temperature and frequency dependence of tan δ are different in the directions parallel and perpendicular to the c-axis [207]. However, the major prediction of the theory is that dielectric loss *increases* with frequency for all symmetry groups [193].

Three-quantum loss

The interaction of the electromagnetic field with optical vibrations of a lattice has a resonant harmonic character when the frequency of the electromagnetic field is approximately equal to the eigenfrequencies of the optical phonons (e.g., 10^{13}–10^{14} Hz). In the microwave range, there are no such phonons whose frequency and wave-vector are equal to the microwave quanta. This energy difference makes it difficult to satisfy the energy and momentum conservation laws in processes involving the absorption of the field quanta. In such a complicated situation there are three most efficient sources of absorption, which correspond to the three main lattice loss mechanisms: (1) three-quantum loss, (2) four-quantum loss and (3) quasi-Debye loss.

In the three-quantum loss, an incident photon couples to a reststrahlen transverse optical phonon which in turn couples to two other phonons. One phonon is absorbed and another created with the energy difference being equal to the energy of the incident photon. Hence this process is also known as a two-phonon difference absorption. This absorption should satisfy both energy and quasi-momentum coservation laws of the form

$$\Omega_j(\mathbf{k}) \pm \Omega_{j1}(\mathbf{k_1}) = \omega \tag{3.8}$$

$$\mathbf{k} \pm \mathbf{k_1} = 0 \tag{3.9}$$

where Ω_j and Ω_{j1} are angular eigenfrequencies of j and $j1$ phonons, respectively, $\mathbf{k}$ is the phonon wavevector, and ω is the angular frequency of the field quanta. Modelling of this process has led to predictions for the loss tangent [208] which can be simplified for $f < 1$ THz to yield

$$tan\delta \propto \frac{\hbar\omega}{k_B T} n(\Omega) \left[tan^{-1}\left(\frac{\Omega_{TO}}{\gamma}\right) - tan^{-1}\left(\frac{\Delta\Omega}{\gamma}\right)\right] \tag{3.10}$$

where ω is the angular frequency of the electromagnetic field, Ω_{TO} is the frequency of the fundamental reststrahlen phonon, $n(\Omega)$ is the Bose occupation factor, γ is the phonon linewidth, and $\Delta\Omega$ is the frequency difference between the high density of the states regions of the Brillouin zone. The linear frequency dependence of tan δ predicted by Eq. 3.10 has been experimentally observed for a number of crystals and ceramics [194]. It is this two-phonon absorption process which leads to the constant value of the product $Q \times f$ in low loss dielectric resonators.

Gurevich and Tagantsev [193] have discussed separately the case in which the sample temperature is much lower than the Debye temperature of the crystal ($T \ll \Theta$) and the one in which the temperature is of the same order or higher than the Debye temperature ($T \sim \Theta$). In the former temperature range, one is allowed to consider the interaction of the electromagnetic field with the acoustic phonons only. In the latter, at least one of the optical phonon branches is excited into interaction with the electromagnetic field. Since the two-phonon difference mechanism requires an optical phonon to be absorbed, it is strongly temperature dependent (e.g. tan $\delta \propto T^n$, where $3 < n < 5$). The two-phonon absorption mechanism vanishes as the population of the optical phonon branch decreases [175]. In summary, the three-quantum loss corresponds to transitions between states of the different branches in a small region of wave-vector space where the branches either approach one another so that the energy gap satisfies the relation $\Omega_j - \Omega_{j1} \approx \omega$ or even overlap on account of their natural linewidth.

Four-quantum loss

The four-quantum mechanism of dielectric loss was predicted by Stolen and Dransfeld [209] who showed that at $T \geq \Theta$, the corresponding contribution to tan δ is proportional to T^2. This mechanism involves three phonons with the conservation laws given by [193]

$$\Omega_j(\mathbf{k}) \pm \Omega_{j1}(\mathbf{k_1}) \pm \Omega_{j2}(\mathbf{k_2}) = \omega \tag{3.11}$$

$$\mathbf{k} \pm \mathbf{k_1} \pm \mathbf{k_2} = \mathbf{b} \tag{3.12}$$

where **b** is a reciprocal lattice vector. The probability of the four-quantum process is proportional to a higher power (in comparison with the three-quantum process) of the small parameter describing lattice anharmonicity, and it would be expected that the contribution to tan δ from the three-phonon difference absorption would be small in comparison with the two-phonon difference absorption. In most cases, three-phonon losses are usually negligible with respect to the two-phonon losses, but can become dominant in certain frequency ranges due to a greater range of available **k** values which can participate in the absorption process [210]. The four-quantum loss corresponds to phonon transitions which take place between states of different phonon branches and are quite uniform over **k** space.

Quasi-Debye loss

The quasi-Debye loss occurs only in noncentrosymmetric crystals. This type of dielectric loss involves absorption of the electromagnetic quanta accompanied by the phonon transitions which take place between states of the same branch because of its finite linewidth. According to Gurevich [193] the quasi-Debye loss should result in non-monotonic frequency dependence of tan δ. An increase in the dielectric loss in d.c. - biased $SrTiO_3$ has been recently assigned to the quasi-Debye loss mechanism, which is forbidden by the central symmetry of $SrTiO_3$ under zero bias [211].

3.3 Structure and properties of $Ba(B'_{1/3}B''_{2/3})O_3$ perovskites

3.3.1 Types of ordering in $Ba(B'_{1/3}B''_{2/3})O_3$ perovskites

$Ba(B'_{1/3}B''_{2/3})O_3$-type compounds constitute a large subgroup of complex perovskites with general formula $A(B'B'')O_3$ [212]. Other examples of complex perovskites with two different ions occupying the B-site sublattice include $A^{2+}(B^{3+}{}_{2/3}\ B^{6+}{}_{1/3})O_3$, $A^{2+}(B^{3+}{}_{1/2}\ B^{5+}{}_{1/2})O_3$, $A^{2+}(B^{2+}{}_{1/2}\ B^{6+}{}_{1/2})O_3$, $A^{2+}(B^{1+}{}_{1/2}\ B^{7+}{}_{1/2})O_3$, $A^{3+}(B^{2+}{}_{1/2}\ B^{4+}{}_{1/2})O_3$, and $A^{2+}(B^{1+}{}_{1/4}\ B^{5+}{}_{3/4})O_3$. In some cases the B-site cations can form a chemically ordered structure [212]. The typical A-site cations in these compounds are Ba, Sr, Pb, Ca, and La. They are always larger than the B-site cations in order to satisfy the general requirement for the tolerance factor of the perovskite structure.

It was postulated by Galasso et al. [213] that an ordered distribution of B ions is most probable when there is a large difference in either their charges or ionic radii. Later Setter and Cross [214] proposed five conditions to determine whether ordering could occur in an $A(B'B'')O_3$ system. These conditions include a simple crystal structure (e.g., perovskite), cation ratio $B'/B'' = 1/1$ or close to unity, a large difference in the valence of B' and B'' cations, a large difference in the size of B' and B'' ions, and a small size of the A cation to increase elastic drive towards ordering. These five conditions have consistently explained ordering in a large number of complex perovskites [215].

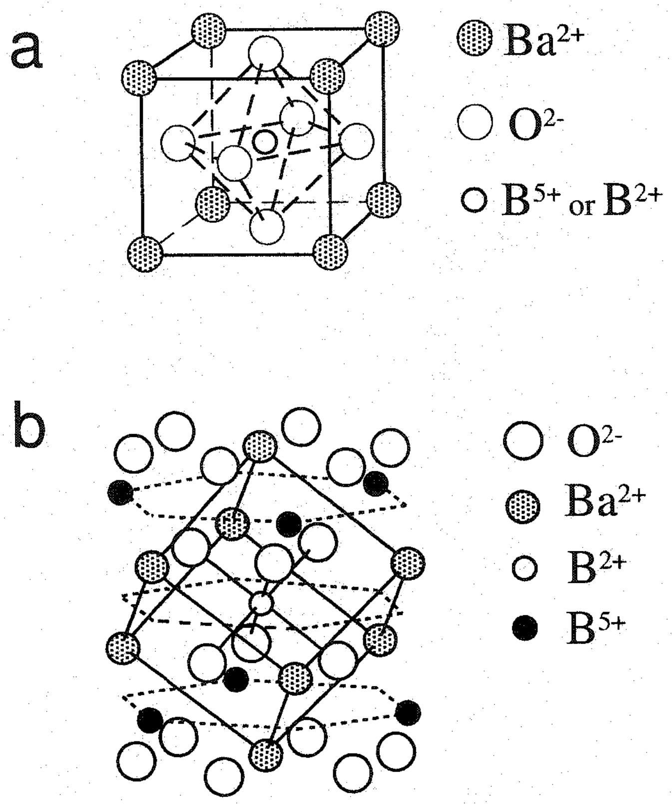

Figure 3.2: Two types of $\mathrm{Ba(B'_{1/3}B''_{2/3})O_3}$ crystal structures: disordered a), and ordered b).

Depending on the preparation conditions, $\mathrm{Ba(B'_{1/3}B''_{2/3})O_3}$ (where $\mathrm{B'}$ = Mg, Zn, Ni and $\mathrm{B''}$ = Nb and Ta) can form disordered ($Pm3m$) or 1:2 ordered ($P\bar{3}m1$) crystal structures (see Fig. 3.2). In addition to these two structure types, $\mathrm{Ba(B'_{1/3}B''_{2/3})O_3}$ can also adopt the 1:1 ordered ($Fm\bar{3}m$) structure when properly doped with aliovalent cations [216, 217, 218, 219, 220, 221, 222].

When completely disordered, $\mathrm{B'}$ and $\mathrm{B''}$ ions are arranged randomly on the B-site, and $\mathrm{Ba(B'_{1/3}B''_{2/3})O_3}$ has a simple cubic structure (Fig. 3.2(a)). In the case of 1:2 ordering, the $\mathrm{B'}$ and $\mathrm{B''}$ cations are distributed on individual (111) planes of the perovskite subcell with alternating $\mathrm{B'}$, $\mathrm{B''}$, $\mathrm{B'}$ layers. The ordered phase has a hexagonal crystal structure as shown in Fig. 3.2(b). Upon ordering, the cubic unit cell is transformed into a hexagonal unit cell, so that $a_h = \sqrt{a}$ and $c/a_h = \sqrt{3/2}$=1.2247 (where a_h is a size of the hexagonal unit cell along <110> direction of the original cubic cell a, and c is the size of the hexagonal cell along <111> direction of the original cubic cell). The ordering of $\mathrm{B'}$ and $\mathrm{B''}$ cations causes lattice distortion and expands the original perovskite cubic cell along <111> direction so that in the ordered state, the c/a ratio has a value greater than $\sqrt{3/2}$. This is accompanied by a different degree of distortion of the oxygen octahedra around $\mathrm{B'}$ and $\mathrm{B''}$ sites. Lattice distortion caused by $\mathrm{B'}$ and $\mathrm{B''}$ ordering can be evaluated by the split of the (422) and (226) reflections in the X-ray diffraction pattern [200, 223]. A number of techniques were utilized for evaluation of the degree of ordering in $A(B'B'')O_3$ compounds including far infrared spectroscopy [224, 225, 226, 227, 228, 229, 230], Raman spectroscopy [226, 231, 232], electron diffraction [233, 202], and X-ray or neutron diffraction [234, 223, 235]. However, only the last two methods provide accurate quantitative data about the degree of 1:2 ordering. Superlattice reflections, characteristic of the 1:2 ordered structure are generated by crystallographic planes whose indices are $(2h+k+l)/3 \neq$ integer. Since the 100 reflection is the strongest among superlattice reflections, the degree of 1:2 ordering is usually determined as [236]

$$s = \sqrt{\frac{(I_{100}/I_{110,012,102})_{obs}}{(I_{100}/I_{110,012,102})_{calc}}} \tag{3.13}$$

where I_{100} is an integrated intensity of the 100 superlattice reflection and $I_{110,012,102}$ is the integrated intensity of the main 110, 012 and 102 reflections.

The ordering of the B-site cations has a large influence on the dielectric loss at microwave frequencies [223, 237]. One of the reasons for ordering is a large difference in electronic polarization of the B′ and B″ cations. For example, the contribution of electronic polarization as well as long-range electrostatic and short-range Born-Mayer type interactions into the long-range order of Zn and Ta ions in $Ba(Zn_{1/3}Ta_{2/3})O_3$ (later abbreviated as BZT) were examined by Sagala and Nambu [238]. They have shown that the lattice energy of the ordered BZT structure is 2.5 eV lower than that of disordered BZT. Due to the difference in the mass of B′ and B″ cations, tantalates are more prone to ordering than niobates. Until recently, $Ba(Ni_{1/3}Nb_{2/3})O_3$ (BNN) and $Ba(Zn_{1/3}Nb_{2/3})O_3$ were considered to exist only as a disordered phase in contrast to $Ba(Ni_{1/3}Ta_{2/3})O_3$ (BNT) and $Ba(Zn_{1/3}Ta_{2/3})O_3$ (BZT) [239, 181]. However, Hong et al. [240] have shown that BNN and BZN can be obtained in ordered form when sintered at temperatures below the order-disorder phase transition of *ca.* 1400 °C.

The low symmetry 1:2 ordered phase remains thermodynamically stable below a critical temperature, T_C, and becomes disordered above this temperature. The temperature of the order-disorder phase transition in $A(B'B'')O_3$ complex perovskites is the subject of intensive theoretical and experimental investigations [241, 242, 243, 244, 245, 18, 246, 247]. Knowledge of the temperature of the order-disorder phase transition has great technological importance since T_C determines the highest temperature at which a sample can be annealed to induce cation ordering. Despite significant theoretical efforts towards understanding the order-disorder transition in $A(B'B'')O_3$, the difference in the calculated and measured temperatures exceeds 700 – 1000 °C for a large number of complex perovskites [245]. Not only theoretical but also experimental results are controversial. This is illustrated in Table 3.2 where the data on the order-disorder phase transitions of several $Ba(B'_{1/3}B''_{2/3})O_3$ are presented. The process of disordering involves interdiffusion of B′ and B″ cations. In order to occupy the B″ site by the B′ cation, the B″ site must be vacant. B-site vacancies can be formed by either Frenkel or Schottky mechanisms, which strongly depend on the ion packing density of the crystal structure. Frenkel defects can equally form in the bulk or near the surface of the crystal, whereas Schottky defects can only form at the surface and diffuse into the bulk [249]. Hence, the type of

Table 3.2: Data on order-disorder transitions in several $Ba(B'_{1/3}B''_{2/3})O_3$

System	$T_{C\ theor.}$ °C	$T_{C\ meas.}$ °C	Reference
$Ba(Mg_{1/3}Ta_{2/3})O_3$	3000...3500	>1650	[245, 18], [217]
$Ba(Zn_{1/3}Ta_{2/3})O_3$	2773	1600...1625	[245], [229, 247]
$Ba(Ni_{1/3}Ta_{2/3})O_3$	654		[245]
$Ba(Mg_{1/3}Nb_{2/3})O_3$	2820	> 1610	[245], [248]
$Ba(Zn_{1/3}Nb_{2/3})O_3$	2200...2470	1350...1500	[244, 245], [248, 240]
$Ba(Ni_{1/3}Nb_{2/3})O_3$	320	1400	[245], [240]

predominant defects in the crystal will determine the kinetics of disordering in $Ba(B'_{1/3}B''_{2/3})O_3$ perovskites [250]. Analysis of the order-disorder phase transition in $Ba(B'_{1/3}B''_{2/3})O_3$ (where B′ = Mg, Zn, Ni and B″ = Nb and Ta) and its effect on the dielectric properties is one of the subjects of the present project.

3.3.2 Dielectric properties of $Ba(B'_{1/3}B''_{2/3})O_3$ perovskites

Dielectric properties (e.g., ε and tan δ) of $Ba(B'_{1/3}B''_{2/3})O_3$ compounds depend on their crystal structure, tolerance factor, the type of the ions occupying the B-site, and the A-site cation radius. The pronounced effect of the A-site cation radius on the dielectric constant can be envisaged when $Ba(B'_{1/3}B''_{2/3})O_3$ perovskites are compared to $Pb(B'_{1/3}B''_{2/3})O_3$ compounds. Lead and barium cation radii in 12-fold coordination are R_{Pb}=0.172 nm and R_{Ba}=0.161 nm. This results in the dielectric constants, for example, of 6500 and 24 for $Pb(Mg_{1/3}Ta_{2/3})O_3$ and $Ba(Mg_{1/3}Ta_{2/3})O_3$, respectively [251]. The tolerance factor and dielectric properties of several $Ba(B'_{1/3}B''_{2/3})O_3$ perovskites are summarized in Table 3.3

As shown in Table 3.3, the dielectric constant of $Ba(B'_{1/3}B''_{2/3})O_3$ compounds has a value of 20 to 40. Niobates possess higher values of dielectric constants than tantalates. Tantalates, in general, have higher Q-factors than niobates. This is because the materials with higher ε have higher anharmonic component of the lattice vibration energy [252]. The Q-factors of BMT and BZT ceramics reach 43,000 and 16,800 at 10 GHz, respectively. These are the highest Q-factors known for $Ba(B'B'')O_3$ compounds. The only two contributions into the dielectric constant of $Ba(B'_{1/3}B''_{2/3})O_3$ compounds come from ionic and electronic polarizations. That is why, no dispersion of ε' is observed up to the frequencies of the optical phonon modes (10^{12} - 10^{13} Hz). The frequency dependence of dielectric loss in $Ba(B'_{1/3}B''_{2/3})O_3$ perovskites has been studied in microwave, submillimeter and far infra-red ranges. In the microwave range (10^9 -10^{11} Hz), the theoretically expected proportionality $\varepsilon'' \propto f$ is observed for BMT and BZT ceramics [194]. In the infra-red range, the dielectric constant shows

Table 3.3: Tolerance factor and dielectric properties of several $Ba(B'_{1/3}B''_{2/3})O_3$ compounds.

System	t	ε	Q×f, THz	τ_f, ppm/K	Ref.
$Ba(Mg_{1/3}Ta_{2/3})O_3$	1.03	23...25	160...430	2...8	[195, 200]
$Ba(Zn_{1/3}Ta_{2/3})O_3$	1.026	29...30	90...168	0	[223, 237]
$Ba(Ni_{1/3}Ta_{2/3})O_3$	1.035	23	50	-18	[182]
$Ba(Co_{1/3}Ta_{2/3})O_3$	1.026	25	46	-16	[182]
$Ba(Mn_{1/3}Ta_{2/3})O_3$	1.012	22	58	+34	[189]
$Ba(Ca_{1/3}Ta_{2/3})O_3$	0.925	30	27	+145	[182]
$Ba(Mg_{1/3}Nb_{2/3})O_3$	1.030	32	55	+33	[182]
$Ba(Zn_{1/3}Nb_{2/3})O_3$	1.026	41	54...72	+31	[180, 189]
$Ba(Ni_{1/3}Nb_{2/3})O_3$	1.035	36	70	+20	[181]
$Ba(Mn_{1/3}Nb_{2/3})O_3$	1.012	39	9.3	+27	[189]

resonant features corresponding to the optical phonon eigenfrequencies [229, 253, 226, 228, 224, 227].

There is a controversial opinion about the effect of ordering on the Q-factor of $Ba(B'_{1/3}B''_{2/3})O_3$ (where $B' =$ Mg, Zn, Ni and $B'' =$ Nb and Ta) [237, 200]. In the case of undoped ceramics, a high degree of ordering is considered to be important for achieving low dielectric loss which is in agreement with the theory of intrinsic losses [193]. Kawashima et al. [237] reported that improvement in the Q-factor corresponds to increased ordering of Zn and Ta in $Ba(Zn_{1/3}Ta_{2/3})O_3$. However, Matsumoto et al. [200] reported improved Q-factor in disordered $Ba(Mg_{1/3}Ta_{2/3})O_3$ (BMT) doped with $BaSnO_3$. Although later investigation performed by Tien et al. [254] confirmed some improvement of the Q-factor of BMT after addition of $BaSnO_3$, the absolute values of the Q-factor turned out to be significantly smaller than that of pure BMT reported by other investigators [235, 255].

3.3.3 Aspects of synthesis of $Ba(B'_{1/3}B''_{2/3})O_3$ perovskites

Obtaining $Ba(B'_{1/3}B''_{2/3})O_3$ ceramics with high Q-factor is a challenging task. According to the literature, a high degree of ordering and high density are the two most important factors determining the dielectric constant and loss. Kinetics of cation ordering depends on the diffusion of B-site cations from one oxygen octahedron to another. This is controlled by temperature, type of B-site cations, stoichiometry and impurities. The rate of ordering and densification of ceramics can be significantly increased with temperature. However, above a critical temperature which is specific to each $Ba(B'_{1/3}B''_{2/3})O_3$ compound (see Table 3.2), the structure starts to disorder. A well ordered phase is obtained by long-term annealing at temperatures below the order-disorder phase transition.

Kawashima [237] reported that it took 120 h at 1350 °C to achieve perfect hexagonally ordered BZT ceramics with Q =16800 at 10 GHz. The time required to sinter BMT ceramics with high Q-factor is in the range of 15 - 20 hours at temperatures of 1600 - 1650 °C [200, 230].

Several additives have been tested in order to accelerate sintering and improve the density of ceramics. Nomura et al. [195] obtained BMT ceramics with a density of 7.52 g/cm^3 (98% of theoretical value) after addition of 1 mol% of Mn. However, the Q-factor of ceramics thus obtained was only 16800 at 10 GHz. Tamura et al. [182] investigated the effect of addition of $BaZrO_3$ in BZT. They reported that both sintering and crystallization of the BZT-$BaZrO_3$ system were accelerated compared to pure BZT. The temperature compensation of the dielectric constant of BZT-$BaZrO_3$ was performed by addition of $Ba(Ni_{1/3}Ta_{2/3})O_3$ to the BZT-$BaZrO_3$ system [182]. Matsumoto and Hiuga [235] employed a fast heating rate (about 500 °C/min) to obtain dense BMT ceramics with ultra low dielectric loss (Q=35000 at 10 GHz). However, as was pointed out by Chen [255], the fast heating rate is not only difficult to realize in industrial furnaces but also introduces sintering flaws into the ceramics. Instead of using traditional ZnO, Ta_2O_5, Nb_2O_5, and $BaCO_3$ precursors, Yanchevsky [256] reported the benefits of $ZnTa_2O_6$ and $ZnNb_2O_6$ precursors which have the tri-rutile structure [257]. Formation of $Ba(Zn_{1/3}Ta_{2/3})O_3$ and $Ba(Zn_{1/3}Nb_{2/3})O_3$ from these precursors required lower temperatures and accelerated ordering of the B-site cations.

Wet chemical preparation routes have several advantages over the solid state reaction method. The former method produces very pure, homogeneous, fine powders with high sinterability. The dense BMT ceramics prepared by the sol-gel method using double Mg-Ta alkoxide and barium hydroxide was obtained at 1400 °C by Renoult et al.[258]. Although their ceramics had 98.5 % theoretical density and showed a high degree of cation ordering, the Q-factors were fairly low (e.g., in the range of 5990 to 6750 at 10 GHz) [258].

The most intensely investigated complex barium perovskites are the BMT and BZT compounds since they have the most important commercial applications. However, aspects of the synthesis of other $Ba(B'_{1/3}B''_{2/3})O_3$ complex perovskites, such as BMN, BZN, BNT, BNN are insufficiently understood. For example, the effect of sintering temperature on dielectric properties of BMN, BZN, BNT, and BNN has not been investigated. Consequently the goals of this project were to perform a thorough analysis of the effect of preparation conditions on ordering and microwave dielectric properties of BMT, BNT, BMN, BZN and BNN compounds.

Chapter 4

Experimental procedure

4.1 Sample preparation

All samples in this study were prepared by the conventional technique from fine powders of metal oxides or metal carbonates. The nominal purity of the initial powders as well as their manufacturers are given in Table 4.1.

Table 4.1: Raw chemicals, purity, and manufacturers

Chemical	Purity, %	Mesh	Powder,μm	Producer
Y_2O_3	99.99	320	1.0	Alfa Products, U.S.A.
$BaCO_3$	99.9	320	2.0	Cerac, U.S.A.
TiO_2 (rutile)	99.9	320	1.5	Cerac, U.S.A.
Ta_2O_5	99.99	320	3.0	Cerac, U.S.A.
MgO	99.95	320	1.0	Cerac, U.S.A.
ZnO	99.99	320	2.0	Cerac, U.S.A.
Nb_2O_5	99.9	320	3.5	Cerac, U.S.A.
NiO	99.9	320	4.0	Inco, Canada

Simplicity and low cost were the governing factors in choosing the synthesis method. That is why the mixed oxide method was preferred over the other synthesis techniques, such as sol-gel, alcoxide, co-precipitation, Pechini, etc. Since in the solid-state reaction regime, the particle size controls the kinetics of reaction, it is important to know the powder size of the starting materials. This was determined by sedimentation technique using a particle size distribution analyzer (CAPA-700, Horiba, Japan) and the average particle size is listed in Table 4.1.

4.1.1 Nominal composition

Yttrium doped $BaTiO_3$

In this work, unless otherwise specified, yttrium was used as a dopant to render $BaTiO_3$ n-type. As was mentioned in Chapter 2, Ba^{2+} can be substituted by Y^{3+}, thus resulting in an extra positive charge in the A-sublattice. At low dopant concentrations (< 0.5 at%), it is assumed that the charge is compensated by the Ti ion whose valence changes from 4+ to 3+. The occupation of the 3d orbital of Ti by an electron is accompanied by the appearance of n-type conductivity in $BaTiO_3$. However, the electronic compensation mechanism of the extra positive lattice charge is not the only one possible. At higher donor-doping levels, cation vacancy compensation begins to dominate and hence, electronic conductivity vanishes. In order to investigate the defect compensation mechanism and its effect on the resistivity of $BaTiO_3$, the chemical compositions with different Y doping levels and different A/B ratios were prepared. These compositions are listed in Table 4.2.

Table 4.2: Nominal compositions of Y doped $BaTiO_3$

Nominal composition	x (at%)
$(Ba_{1-x}Y_x)(Ti^{4+})_{1-x}(Ti^{3+})_xO_3$	0, 0.02, 0.05, 0.1, 0.4
$(Ba_{1-x}Y_x)(Ti^{4+})_{1.01-x}(Ti^{3+})_xO_3$	0.1, 0.2, 0.3, 0.4, 0.6
$(Ba_{1-x}Y_x)(Ti^{4+})_{1.02-x}(Ti^{3+})_xO_3$	0.05, 0.1, 0.2, 0.3, 0.4, 0.6, 0.8
$(Ba_{1-x}Y_x)(Ti^{4+})_{1-x/4}(V_{Ti})_{x/4}O_3$	0.4
$(Ba_{1-1.5x}Y_x)(V_{Ba})_{x/2}TiO_3$	0.4
$(Ba_{1.05-x}Y_x)(Ti^{4+})_{1-x}(Ti^{3+})_xO_3$	0.4

Complex barium tantalates and niobates

In order to investigate the role of precursor powders in the phase formation of BMT, it was prepared by two different solid state methods; *(i)* one-step mixed oxide method and *(ii)* two-step columbite method. It was found that the columbite method yields higher ceramic density and better dielectric properties (i.e., higher Q-factor and higher ε). Hence the rest of the compounds (BNT, BMN, BZN and BNN) were prepared by columbite method. According to the first method, ceramics were synthesized directly from $BaCO_3$, ZnO, MgO, Ta_2O_5 and Nb_2O_5 precursors. The second method involved preparation of $MgTa_2O_6$, $MgNb_2O_6$, $ZnNb_2O_6$, $NiTa_2O_6$ and $NiNb_2O_6$ columbite or tri-rutile type precursors followed by reaction of these compounds with stoichiometric amounts of $BaCO_3$. The nominal chemical compositions of the prepared samples are listed in Table 4.3.

Table 4.3: Nominal compositions of complex barium tantalates and barium niobates

Nominal composition	Preparation method
$Ba(Mg_{1/3}Ta_{2/3})O_3$	mixed oxide & columbite
$Ba(Ni_{1/3}Ta_{2/3})O_3$	columbite
$Ba(Mg_{1/3}Nb_{2/3})O_3$	columbite
$Ba(Zn_{1/3}Nb_{2/3})O_3$	columbite
$Ba(Ni_{1/3}Nb_{2/3})O_3$	columbite

4.1.2 Preparation process

Weighing

After heating the starting powders at 150 °C to remove adsorbed water, the reagents were placed in a vacuum desiccator and allowed to cool down to room temperature. After that, the appropriate amounts of powders were weighed on an analytical balance (Acculab, Canadawide Scientific, Ottawa, Canada) with a relative error not exceeding 0.01 %. For weighing of small amounts of dopants, a more accurate analytical balance (Model R200D, Sartorius Research, Gottingen, Germany) was used. This allowed for keeping the relative error of weighing at 0.01 % for all reagents.

Mixing and milling

To achieve a homogeneous mixture, starting powders were vibromilled in polyethylene bottles with absolute ethanol and yttria stabilized zirconia (YSZ) grinding balls (Tosoh Ceramics). Usually, around 80 grams of the YSZ balls were used for mixing of 30 grams of powder. The duration of mixing was kept constant at 2 hours. After calcination of the powders, a second vibromilling was undertaken. This was done mainly to break up the agglomerated particles and to increase the surface activity of the powders. The duration of milling varied from 2 to 48 hours. During vibromilling, the powder becomes contaminated with small amounts of YSZ and polyethylene. According to the information from the YSZ manufacturers, the maximum wear rate of the YSZ balls does not exceed 0.8 ppm/h. Hence, the total amount of YSZ impurity in the 30 g powder batch can reach 3 mg, or 0.01 % after 48 hours of vibromilling.

Calcination

After mixing, the slurries were placed in porcelain dishes and dried in an oven at 70 °C for 10 hours. The dried mixtures were screened through 60 mesh sieve, pressed into pellets and calcined in alumina crucibles at various temperatures and dwell times. The process of calcination has two major goals: *(i)* to completely release CO_2 from $BaCO_3$ and *(ii)* to achieve a single-phase product. The calcined products were vibromilled in order to obtain fine powders and to increase the powder activity for solid-state sintering. After this step the powders were heated at 700 °C for 4 hours to burn off traces of polyethylene from the vibromilling process.

Pressing

Before pressing, the powders were mixed with 2 wt % of aqueous solution of polyvinyl alcohol and screened through 60 mesh sieve. A uniaxial pressing was performed on a laboratory press (Model K, Fred S. Carver Inc., Summit, N. J. U.S.A.) under pressures not exceeding 1200 kg/cm^2. To compare the effect of preparation conditions, some pellets were isostatically pressed under a pressure of 10 000 kg/cm^2. Since special care has to be taken to avoid contamination of the pellets with iron and other impurities during pressing, a special pressing die was manufactured from heat-treated tool steel in the university machine shop. The traces of iron contamination were removed from the pellet surface with 1200 mesh SiC sandpaper.

Sintering

Different sintering conditions were applied to the samples with different chemical compositions. Y-doped $BaTiO_3$ samples were sintered in air, forming gas (7% H_2 and 93 % Ar) and different mixtures of CO/CO_2 at 1380 °C with dwell time of up to 5 h. The pellets were supported on a zirconia substrate coated with a thin layer of zirconia powder to prevent samples from reacting with the substrate. It was found that alumina substrates or alumina filling powder were not suitable for sintering $BaTiO_3$ due to reaction of the samples with the substrate and powder. Complex barium tantalates and niobates were sintered in alumina crucibles filled with alumina powder. No reaction of samples with powder or crucibles were observed. The samples were sintered in air at temperatures of 1300 °C to 1700 °C with soaking times of up to 60 h. The heating and cooling rates were varied from 15 to 300 °C/h.

Single crystal $BaTiO_3$

Undoped and yttrium doped $BaTiO_3$ single crystals were grown from melts using $BaCl_2$ flux according to Cherepanov [259]. A mixture of $BaCl_2$, $BaCO_3$ and TiO_2 in molar ratios 1:1.4:1 was heated in a closed platinum crucible to 1420 °C in 4 hours, soaked for 0.5 hour, and cooled at a rate of 20 °C/h to 1100 °C. At this temperature the melt was decanted. The crystals remaining in the crucible were then cooled to 800 °C at a rate of 50 °C/h. This method yielded thin triangular plates with a hypotenuse of around 2-3 mm. Some crystals had the shape of butterfly wings as described by Remeika [260]. In addition to the laboratory made single crystals, an undoped $BaTiO_3$

single crystal was kindly provided by Andreia Charos of Deltronic Crystal Industries, Inc. Another undoped single crystal was purchased from MTI Inc.

Density measurements

The densities of the sintered samples were measured by Archimedes method using a pycnometer with distilled water as the immersion liquid. The value of the density was calculated according to:

$$\rho_s = \frac{m_s \rho_w}{m_s + m_w - m_{s+w}} \tag{4.1}$$

where ρ_s is the density of the sample, m_s is the weight of sample, m_w is the weight of water in the pycnometer when no sample present, m_{s+w} is the weight of sample and water when both are in the pycnometer.

4.2 Thermal, crystallographic and microstructure analysis

4.2.1 Thermal analysis

Differential thermal analysis (DTA) and thermogravimetric analysis (TGA) were performed on a NETZSCH STA-409 simultaneous thermal analyzer, from 300 °C to 1400 °C in air at a heating rate of 10 °C/h.

4.2.2 Crystallographic analysis

For X-ray diffraction analysis, the sintered samples were first ground in an agate mortar and pestle. The phase composition, crystallographic parameters and degree of cation ordering of calcined powders and sintered samples were analyzed using two diffractometers: a Rigaku Geigerflex Dmax II diffractometer with cobalt K_α radiation (λ =1.7889 Å) and a DRON-III diffractometer with a copper K_α radiation source (λ =1.54051 Å). Powder diffraction patterns were taken for $10^\circ < 2\theta < 90^\circ$ with a scanning step of 0.02° and count time of 4 sec/step.

4.2.3 Microstructure analysis

SEM and optical analysis

The microstructure and the chemical composition of polished and thermally etched samples were analyzed by scanning electron microscope (Philips 515) equipped with Energy Dispersive X-ray Spectrometer (EDS, Link Analytical). Sections of the samples were polished with diamond pastes stepwise from 6 μm to 1 μm. The final polish was done with alumina powder of 0.25 μm followed by cleaning in acetone. Subsequently, the samples were thermally etched for 1 h at temperatures 100 - 200 °C below the sintering temperature. To avoid charging effects during SEM analysis, the surface of the samples was coated with thin layers of Au (for conventional SEM observations) or carbon (for micro-chemical analysis with EDS). The average grain size of the sintered pellets was measured by a linear intercept method. Optical observation of polished and etched samples was performed on Leitz Wetzlar optical microscope.

TEM and electron diffraction analysis

For TEM observations the samples were mechanically ground using 600 mesh SiC paper to a thickness of 100 μm. They were further thinned to 15 - 20 μm with a Gatan dimpling apparatus. Then the samples were mounted into a Mo holder and placed into a Gatan ion mill equipped with two Ar^+ ion guns. The milling was performed at an accelerating voltage of 3 kV, ion current of 3 mA per gun, and a tilt angle of 10° until perforation of the sample. Transmission electron microscopy (TEM) investigation and electron diffraction were conducted using a Philips CM12 TEM operating at 120 kV and equipped with a double-tilt specimen holder.

4.3 Measurements of electronic and dielectric properties

4.3.1 Electrodes

Electrodes play a crucial role in electrical measurements of semiconductors. Generally two possible situations may arise at the metal-semiconductor interface: either an ohmic contact will form and the contact will have zero resistance, or a Schottky barrier forms and significant part of the applied voltage will drop at the junction resulting in large contact resistance. For DC measurements this problem can be overcome by using a four-probe technique. However, in order to accurately measure AC impedance and I-V characteristics of weakly conducting oxides, it is essential to have a stable ohmic contact over the entire sample area. The contact properties of the $BaTiO_3$-metal junction have been studied many times. It was found that Au, Ag and Pt metals form Schottky barriers with semiconducting $BaTiO_3$. In contrast, In-Ga alloy, Al and Ni metals produce ohmic contacts with $BaTiO_3$. For laboratory research of n-type $BaTiO_3$, the most widely used ohmic electrode is an In-Ga (1:2) [261] alloy. This electrode is easy to fabricate and apply on the surface of the sample. However, the results of this thesis show that the In-Ga electrode does not provide the lowest contact resistance and has a strong tendency to increase electrode resistance with time. As an alternative, an Al electrode grown by Al vapor deposition and a Ni electrode formed by electrolysis were investigated. Among the three types of electrodes, the Ni electrode has shown the lowest contact resistance and excellent stability over time in the 10 K - 700 K temperature range.

4.3.2 Low-field DC conductivity measurements

Low-field DC electronic conductivity of $BaTiO_3$ was investigated in the temperature range of 25 to 350 °C. Both two- and four-probe techniques have been used initially. During the course of the studies, however, it was found that the two-probe technique was sufficient for accurate conductivity measurements of n-doped $BaTiO_3$ ceramics when Ni electrodes were utilized. Measurements of conductivity were performed either in air or in a reducing atmosphere of forming gas (7% H_2 and 93 % Ar) under controlled flow rate. The temperature was monitored with a K-type thermocouple positioned at a distance of 2 mm from the sample. Both temperature and conductivity were measured simultaneously by an HP 3478A multimeter. The data were collected by 286 IBM computer connected through a Scientific Solutions DA board.

4.3.3 Measurements of current-voltage characteristics

Current-voltage (I-V) characteristics of $BaTiO_3$ ceramics were measured by means of a programmable power supply (Keithley 237 High Voltage Source, Keithley Instruments, Inc. U.S.A.) using short voltage pulses of 2 ms to prevent Joule heating of the samples during measurements. I-V characteristics were measured in the temperature range of 145 °C to 330 °C. The temperature of the sample was measured with a K-type thermocouple attached to one of the sample's electrodes. In order to avoid electrical contact between the thermocouple and the sample, the thermocouple was coated with a dielectric film of AREMCO cement.

4.3.4 Complex impedance measurements

The complex impedance was measured as a function of both temperature and frequency under an applied alternating voltage of 50 mV. Measurements in the temperature range of 10 K to 200 K were performed in the closed cycle He cryostat (Displex ADP - Cryostat). A chromel versus Au-0.07% Fe thermocouple was used to monitor the temperature of the sample. For measurements in the temperature range of 25 to 300 °C, samples were placed in a conventional temperature-controlled furnace. The undesirable contribution of coaxial wires to the impedance data was removed by the conventional short-circuit and open-circuit compensation technique. The complex impedance of the sample was measured with a Solartron 1260 Impedance/Gain-Phase Analyzer at 77 frequencies in the range of 1 Hz - 32 MHz. The complex permittivity, ε^*, was calculated from the complex impedance, Z^*, according to:

$$\varepsilon^* = (j\omega C_0 Z^*)^{-1} \tag{4.2}$$

where ω is the angular frequency $2\pi f$, C_0 is the vacuum capacitance of the measuring cell and electrodes with an air gap in place of the sample, $C_0 = \varepsilon_0/k$, where ε_0 is the permittivity of free space (8.854×10^{-14} F/cm) and $k = l/A$, the cell constant where l is the thickness and A the area.

4.3.5 Electron paramagnetic resonance measurements

EPR studies were performed at 77 K and at 300 - 420 K. Two X-band EPR spectrometers, JEOL JES-FA 100 and Bruker EMX 8/2.7 were employed. The JEOL JES-FA 100 spectrometer was equipped with an external Mn^{2+} standard for accurate determination of the giromagnetic constant. The ceramic samples were ground into powder in an agate mortar and pestle. For qualitative analysis, the weight of the samples was kept at 50 ± 1 mg. Subsequent analysis of the resonance spectra was performed with WIN-EPR software provided with the Bruker EPR Spectrometer.

4.3.6 Seebeck coefficient measurements

The Seebeck coefficient (or so-called thermopower) of n-type $BaTiO_3$ was measured between 50 and 320 K. The samples for thermopower measurements were shaped into a rod of 5 mm in diameter and 7 mm in length. In Seebeck coefficient measurements, the temperature gradient, ΔT, applied along the sample results in the corresponding voltage, V. The value of the Seebeck coefficient, S is given by

$$S = \frac{V}{\Delta T} \tag{4.3}$$

The instrument used for thermopower measurements was built at the Brockhouse Institute for Materials Research at McMaster University. A schematic diagram of the sample holder is shown in Fig. 4.1. The sample is clamped between two copper heads A and B that are in thermal contact (but electrically isolated) with base stage C. The base is mounted on the cold end of a CTI Inc. model 21C closed cycle He refrigerator. The copper heads A and B contained a 6 Ω ceramic resistor that serves as a heater, while base C has a Ni-Cr wire wound 25 W cartridge heater. The temperature gradient along the sample can be controlled by varying the power applied to the heaters in heads A and B while keeping the temperature of the base C constant. In order to ensure a uniform voltage distribution at the points of temperature and voltage measurements, two Ni metal bands (1 mm wide) were deposited on the circumference of the sample. The chromel versus Au-0.07% Fe thermocouples for temperature measurement and two copper wires for voltage measurement are attached to the Ni bands with silver paste. The sample holder unit was placed in a vacuum chamber. The base pressure of 10^{-6} Torr in the chamber was maintained with a turbopump.

In order to determine the Seebeck coefficient at various temperatures, the sample is allowed to equilibrate at each temperature setting. One end of the sample is held at a constant temperature T_1, while the temperature of the other end, T_2, is allowed to vary in the range of $T_1 \pm 5$ K in δT (2 K) steps. At each step in the temperature profile, the sample is allowed to reach equilibrium at which point the temperature difference, ΔT, and the voltage, V, are measured several times for statistical averaging. Once the temperature profile ($T_1 \pm 5$ K) has been swept, the sample is heated to the next temperature and the measurement is repeated. The data collection is computer controlled via a standard RS232 serial interface. The Seebeck coefficient, at each temperature, is then calculated

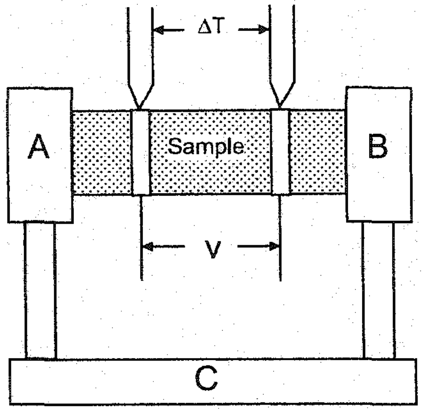

Figure 4.1: Schematic of the sample holder unit for thermopower measurements

from Eq. 4.3 from the gradient of the average voltage *versus* the temperature difference obtained at each δT step.

4.3.7 Dielectric measurements in X-band

Dielectric characterization of the samples in the X-frequency band was performed with an HP 8510 vector network analyzer. Owing to difficulties in determining the Q-factor by the Hakki and Coleman post-resonator technique, as discussed in [262] a simpler and more reliable transmission method [263] was employed in this work. For transmission measurements, a cylindrical dielectric resonator (DR) shaped into $TE_{01\delta}$ resonant mode was centered in the X-band rectangular copper waveguide using a styrofoam holder. In this configuration, the waveguide serves as a band-stop filter at the $TE_{01\delta}$ resonance frequency. To separate the $TE_{01\delta}$ mode from the higher resonance modes, the samples must have an aspect ratio close to 0.45. The diameter and thickness of the samples was 6 mm and 2.7 mm, respectively. The unloaded Q-factor was calculated according to:

$$Q = \frac{Q_L}{1 - 10^{-P/20}} \tag{4.4}$$

where Q_L is the loaded quality factor determined from the full width of the resonance peak at the 3 dB level, and P is the depth of the resonance peak in decibels. As has been pointed out by Zurmühlen *et al.*[262] the rectangular waveguide transmission method gives the same values of Q-factor as the commercially utilized cylindrical cavity method. However, due to the closer proximity of the sample to the waveguide walls, the resonant frequency, f_c, of the transmission method is always higher than that determined by the cylindrical cavity method. This difference is smaller for samples with higher dielectric constant, and can be further minimized to less than 2 % by making the resonator diameter smaller. The accuracy of the transmission method setup has been tested by using two commercially available dielectric resonators, Murata [264] F-series DR and OXIDE [265] barium tetratitanate DR. The results showed that the Q-factor agreed to 0.1 % of that specified and that f_c was higher by 2 % and 0.5 % for Murata and OXIDE DRs, respectively. The real part of the dielectric constant, ε', in the X-band was calculated according to [162]:

$$\varepsilon' = \left[\frac{34}{r\,f_c}\left(\frac{r}{d} + 3.45\right)\right]^2 \tag{4.5}$$

where r is the radius of the DR, d is the thickness of the DR, and f_c is the resonant frequency in GHz. Strictly speaking, Eq. 4.5 is applicable for $30 < \varepsilon' < 50$, and it underestimates ε by 5 - 7 % for materials with $20 < \varepsilon' < 30$. Temperature dependence of the resonance frequency was measured in the range of +20 °C to +95 °C. For measurement of τ_f, the sample was placed in a porous, low-ε' ceramic holder with a small thermal expansion coefficient. The waveguide was wrapped with a resistive heating tape, and the temperature was monitored using a K-type thermocouple attached to the outer surface of the waveguide. The temperature coefficient of the resonant frequency is defined by

$$\tau_f = \frac{\Delta f_0}{f_0 \Delta T} \tag{4.6}$$

where Δf_0 is the shift of the resonant frequency introduced by the temperature change ΔT.

Chapter 5

$BaTiO_3$: Synthesis and low field resistivity

In this chapter, the preparation and analysis of $BaTiO_3$ powders as well as phase composition of Y-doped $BaTiO_3$ samples are described. This is followed by the results of low field electrical conductivity of polycrystalline $BaTiO_3$ sintered at different oxygen partial pressures. Finally, the effect of oxidation on the PTCR properties is discussed in the light of *oxygen chemisorption* and *cation vacancy segregation* models.

5.1 Synthesis

There are different opinions in the literature regarding the process of reaction of $BaCO_3$ and TiO_2. Templeton and Pask [266] considered that barium metatitanate forms directly from reaction of $BaCO_3$ and TiO_2. However, Ishii et al. [267] reported that the first product of reaction between barium carbonate and titanium dioxide is barium orthotitanate (Ba_2TiO_4). The appearance of other intermediate phases, such as $BaTi_3O_7$ and $BaTi_4O_9$ has also been reported in literature [268]. These intermediate phases transform into barium metatitanate only but at temperatures above 1100 - 1200 °C .

$BaTiO_3$ has been modified by a number of elements in order to achieve desirable properties. Yttrium is a common donor dopant used for manufacturing PTCR thermistors [269]. Yttrium was employed in the present study in order to obtain semiconducting $BaTiO_3$. Several sintering additives, such as excess TiO_2, SiO_2 and Al_2O_3 are widely used to reduce the sintering temperature of PTCR $BaTiO_3$ [270, 10]. Although these additives do not modify the electronic properties of the grain bulk, the grain boundary conductivities may be altered. Another concern is that the EPR spectra of $BaTiO_3$ ceramics doped with sintering additives will contain additional signals due to the paramagnetic defects present in SiO_2 and Al_2O_3. That is why no sintering additives were employed in $BaTiO_3$ ceramics studied in this project.

5.1.1 Thermal Analysis

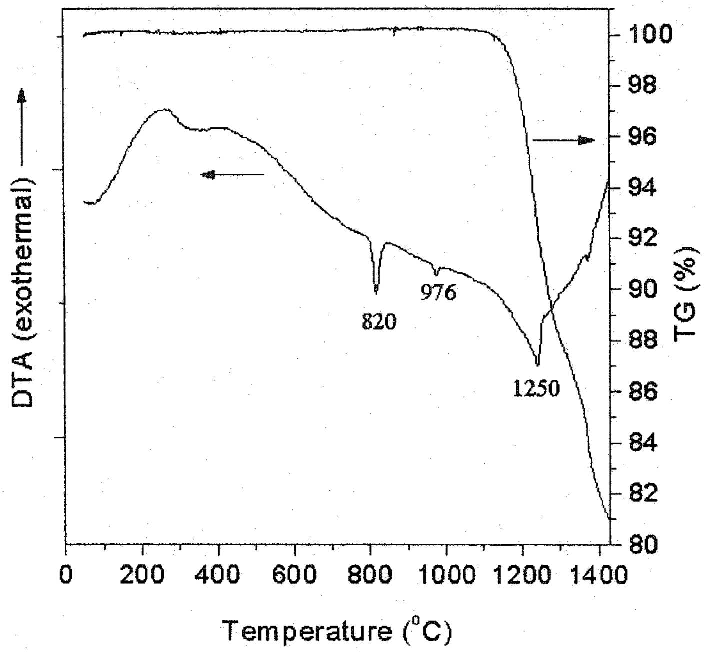

Figure 5.1: DTA and TG curves of $BaCO_3$

DTA and TG were performed on $BaCO_3$ and an equimolar mixture of $BaCO_3$ and TiO_2 after the powders were ball milled for 2 hours. The results are presented in Figs. 5.1 and 5.2. The TG and DTA curves of $BaCO_3$ indicate that below 550 °C there is a small weight loss, corresponding to two broad exothermic peaks at 280 °C and 450 °C, probably due to the pyrolysis of organic impurities from the Nalgene bottle. There are two sharp endothermic peaks on the DTA curve corresponding to the structural transitions of $BaCO_3$ from γ to β phase at 820 °C and from β to α phase at 976 °C [271]. No significant weight loss is observed for $BaCO_3$ up to 1150 °C. A sudden weight loss above 1150 °C is attributed to decomposition of $BaCO_3$. This process is characterized by an endothermic peak at 1250 °C on the DTA curve.

As can be seen in Fig. 5.2, the weight loss in the $BaCO_3$ + TiO_2 system starts at about 800 °C due to reaction of $BaCO_3$ with TiO_2. An endothermic peak due to the $\gamma \rightarrow \beta$ phase transition of $BaCO_3$ [271] is observed at 830 °C. A broad endothermic peak in the temperature range 960 - 1100 °C originates from the overlap of the two endothermic peaks at 976 °C and at 1040 °C. The former one is due to the $\beta \rightarrow \alpha$ transition of $BaCO_3$ [271] and the latter one is due to the decomposition

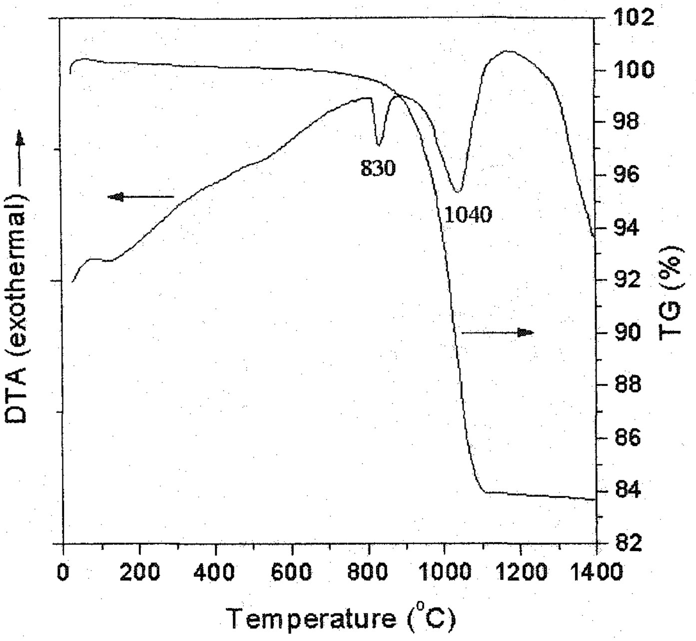

Figure 5.2: DTA and TG curves of $BaCO_3$ +TiO_2

of $BaCO_3$. This is supported by the fact that the weight loss in the $BaCO_3$ + TiO_2 reaction is complete at 1100 °C.

5.1.2 Phase composition

XRD analysis was performed for $BaCO_3$ + TiO_2 mixtures with Ba/Ti ratios of 1:1, 1.05:1, and 1:1.02. The results are presented in Table 5.1. The XRD patterns of 0.4 at% Y-doped $BaTiO_3$ with different Ba:Ti ratios sintered in air at 1300 °C are shown in Fig. 5.3. According to the X-ray analysis, in an equimolar mixture of $BaCO_3$ and TiO_2, barium carbonate decomposes in the temperature range of 900 - 1200 °C. Barium oxide reacts with titanium dioxide to form $BaTiO_3$, $BaTi_3O_7$, $BaTi_4O_9$, and Ba_2TiO_4. In the temperature range of 1000 – 1200 °C, the intermediate phases $BaTi_3O_7$, $BaTi_4O_9$, and Ba_2TiO_4 transform to $BaTiO_3$. As can be concluded from data in Table 5.1, the 5% excess of Ba does not change the sequence of chemical reactions. However, the final product contains a small amount of Ba_2TiO_4 phase. An excess of TiO_2 decreases the temperature of formation of the intermediate phases $BaTi_3O_7$ and $BaTi_4O_9$ by ca. 100 °C compared with the case of Ba/Ti=1:1. Small additions of yttrium oxide (less than 0.8 at%) employed in this project do not change the phase composition of the calcined powders which suggests that yttrium tends to be incorporated into the $BaTiO_3$ lattice rather than form a second phase. This is also confirmed by investigation of the solid solubility of yttrium in Ba and Ti sublattices performed by Jing [272] who found a solid solubility limit of 1.5 at% of yttrium on Ba sites and 12.2 at% on Ti sites [272].

Table 5.1: Phase composition of mixtures of $BaCO_3$ and TiO_2 after 2 h anneal.

T, °C	Ba/Ti =1:1	Ba/Ti=1.05:1	Ba/Ti=1:1.02
800	$BaCO_3$, TiO_2	$BaCO_3$, TiO_2	$BaCO_3$, TiO_2
900	$BaCO_3$, TiO_2	$BaCO_3$, TiO_2, Ba_2TiO_4	$BaCO_3$, TiO_2, $BaTi_3O_7$, $BaTiO_3$
1000	$BaCO_3$, TiO_2, $BaTi_3O_7$, $BaTiO_3$	$BaCO_3$, TiO_2, Ba_2TiO_4 $BaTiO_3$, $BaTi_3O_7$	$BaCO_3$, TiO_2, $BaTiO_3$, $BaTi_4O_9$
1100	$BaCO_3$, TiO_2, $BaTi_4O_9$ $BaTiO_3$	$BaCO_3$, TiO_2, Ba_2TiO_4 $BaTiO_3$	$BaTiO_3$
1200	$BaTiO_3$	$BaTiO_3$, Ba_2TiO_4	$BaTiO_3$
1300	$BaTiO_3$	$BaTiO_3$, Ba_2TiO_4	$BaTiO_3$

5.1.3 Density and microstruture

Since the final goal of this project was investigation of the electronic properties of $BaTiO_3$, it was important to obtain dense ceramics with well defined microstructure and semiconducting properties. It was also important to find the optimum concentration of donor dopant which would result in the highest conductivity of ceramics. $Ba_{1-x}Y_xTiO_3$ ceramics with x = 0, 0.0002, 0.0005, 0.001, 0.002, 0.004, 0.006, 0.008 were prepared and sintered at 1380 °C in air and forming gas for 3 hours. According to Table 5.2, the density of ceramics sintered in air is 3-5 % higher than that sintered in reducing atmosphere. There are two possible factors responsible for that, namely a higher degree of

Table 5.2: The density of $Ba_{1-x}Y_xTiO_3$ ceramics sintered in air and forming gas

x	D_T, g/cm^3	Air		Forming gas	
		D_m, g/cm^3	D_{rel}, %	D_m, g/cm^3	D_{rel}, %
0	6.011	5.71	94.9	5.52	91.8
0.0002	6.0108	5.72	95.1	5.5	91.5
0.0005	6.0105	5.74	95.5	5.48	91.2
0.001	6.0098	5.75	95.7	5.49	91.3
0.002	6.0086	5.661	94.2	5.54	92.2
0.003	6.0073	5.6	93.2	5.51	91.7
0.004	6.0061	5.781	96.2	5.53	92.0
0.006	6.0036	5.871	97.8	5.497	91.6
0.008	6.0011	5.89	98.15	5.53	92.1

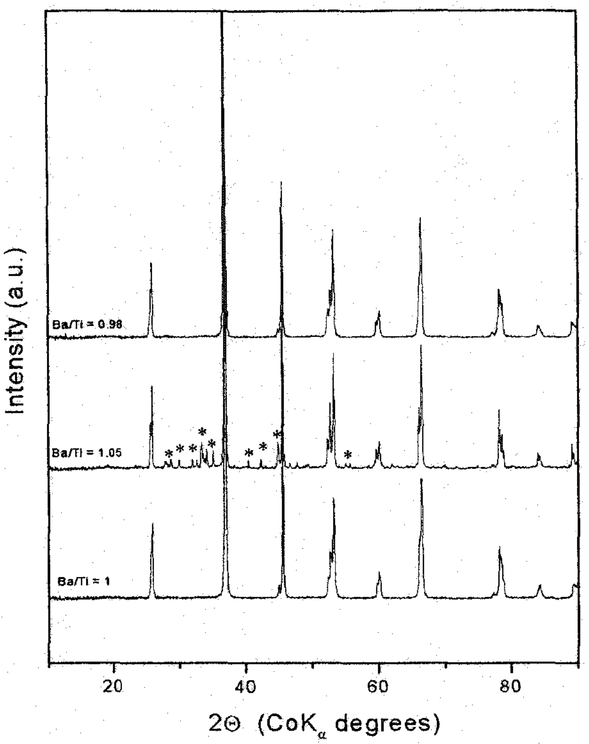

Figure 5.3: XRD patterns of 0.4 at.% Y-doped $BaTiO_3$ samples with different (Ba+Y)/Ti ratio sintered in air at 1300 °C. The Ba_2TiO_4 phase is indicated by $*$.

porosity and a lower concentration of the lattice oxygen in ceramics sintered in forming gas. In order to evaluate the deviation from oxygen stoichiometry, ceramics sintered in forming gas were annealed in air at 1400 °C for 10 hours. However, there was no noticeble change in mass of the samples after annealing. This indicates that the lower densities of samples sintered in reducing atmosphere were due to higher degree of porosity as was confirmed by SEM observations shown in Figs. 5.4 and 5.5. As revealed by Fig. 5.4, the average grain size of undoped $BaTiO_3$ was ca. 2 - 3 μm. With yttrium doping, the grain size increased to 20 - 30 μm [Fig.5.4 (a)-(c)]. However, at a doping level of 0.4 at% [Fig. 5.4 (d)], the microstructure became bimodal with pockets of 3 μm grains coexisting with 20 - 30 μm grains. At Y = 0.6 at% [Fig. 5.4 (e)], the volume fractions of small and large grains are approximately equal. At higher yttrium doping level, the microstructure consists of small grains of ca. 2 - 3 μm. This data is consistent with observations of other authors who reported anomalous grain growth in n-doped $BaTiO_3$ ceramics at donor concentration of 0.1 - 0.4 at% [71].

For ceramics sintered in a reducing atmosphere of forming gas, the effect of donor concentration is not so obvious (see Fig. 5.5). The average grain size of Y-doped ceramics sintered in forming gas was in the range of 30 - 60 μm. As also seen in Fig. 5.5, all ceramics sintered in forming gas have much larger pore size than ceramics sintered in air.

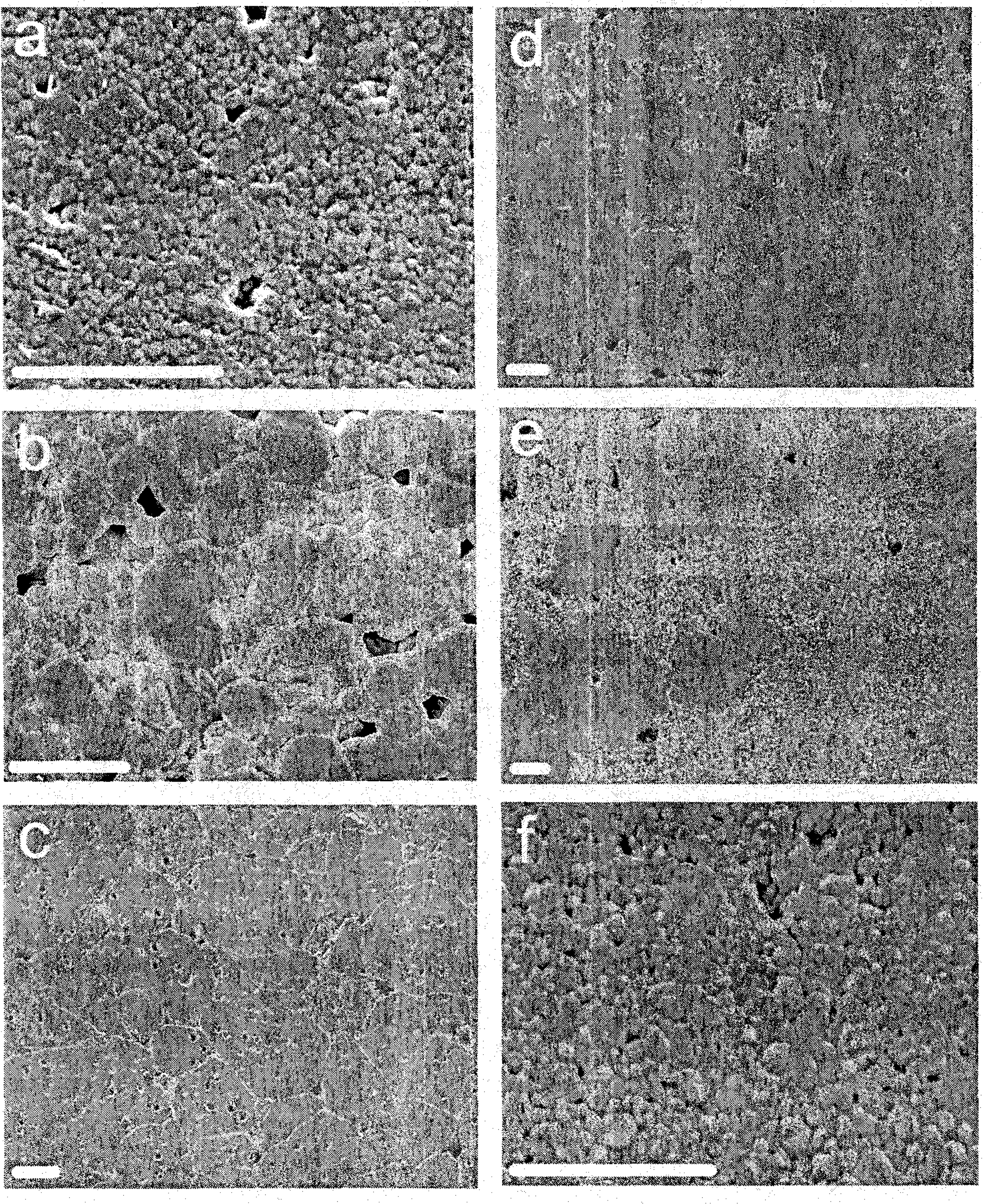

Figure 5.4: Scanning electron micrographs of the polished and thermally etched sections of $Ba_{1-x}Y_xTiO_3$ samples with a) x = 0, b) x = 0.001, c) x = 0.003, d) x = 0.004, e) x = 0.006, and f) x = 0.008 sintered in air at 1380 °C. The white bar represents 20 μm.

5.2 Electrodes

5.2.1 Introduction

Electrodes play an important role in determination of the electronic properties of a semiconductor. For accurate analysis of the electronic conductivity of ceramics an ohmic (non-blocking) electrode

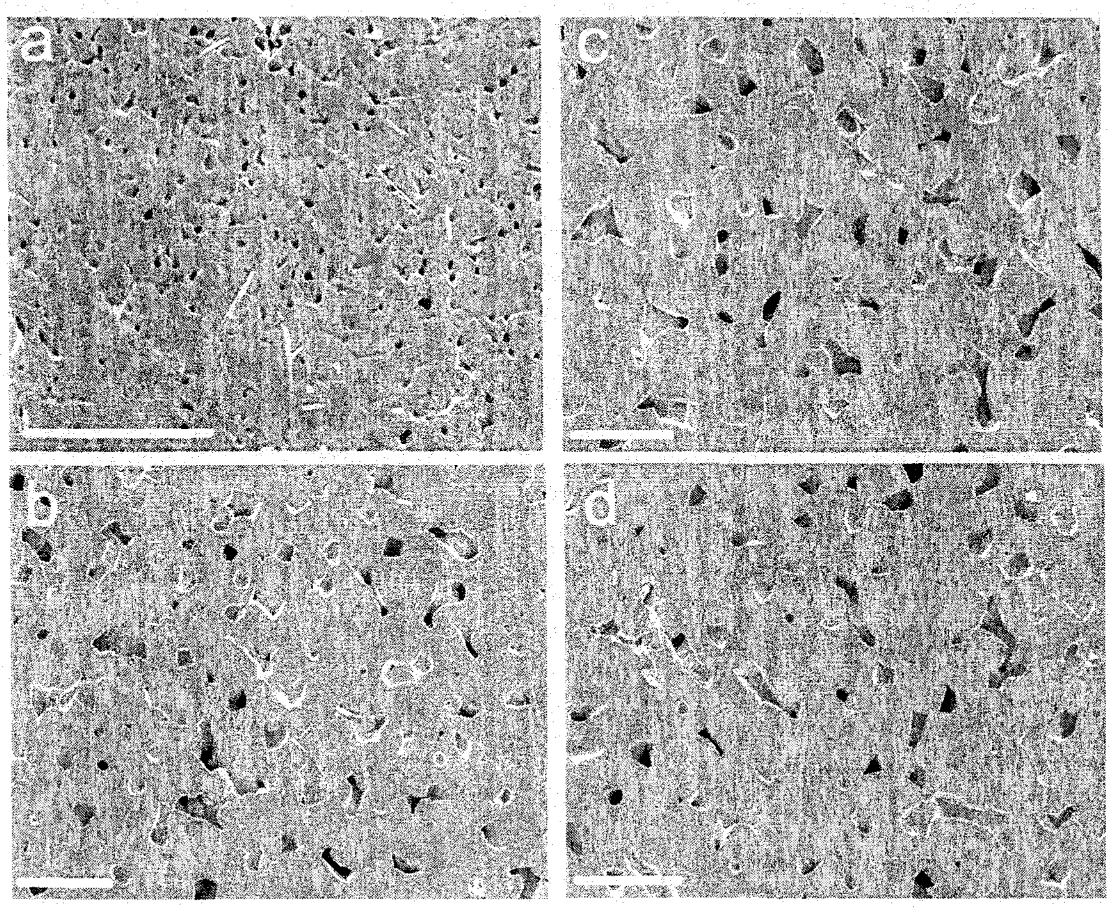

Figure 5.5: Scanning electron micrographs of the polished and thermally etched sections of $Ba_{1-x}Y_xTiO_3$ samples with a) x = 0, b) x = 0.002, c) x = 0.004, and d) x = 0.008, sintered in forming gas at 1380 °C. The white bar represents 50 μm.

is required. Moreover, for consistent measurements, it is neccessary that electrical resistance of the metal-semiconductor interface does not change with time, i.e., no degradation of the electrode properties should occur.

Depending on the type of contact metal, semiconducting $BaTiO_3$ forms ohmic- or Schottky-type contacts. In the latter case, the main part of the applied voltage drop occurs at the metal-semiconductor interface, resulting in very high total resistance of the device. The problem of the metal contacts for n-type $BaTiO_3$ has been addressed by a number of workers. Turner and Sauer [273] found that Ni electrodes formed ohmic contacts with barium titanate. However, Murakami [274], using capacitance measurements, found that the electrode potential barriers for Ni, Cu, Ag, and Au electrodes were 0.72, 0.81, 0.99, and 1.86 eV, respectively, and were related to the work functions of the electrode. Heywang [275] investigated Zn, Sn, Fe, Cd, Ni, Sb, Pb, Cu, Pd, and Au electrodes. He found that $BaTiO_3$-metal contact resistance depends on the reducing strength of the metal, i.e., on the enthalpy of formation of the first oxide step of the contact metal used (e.g., Cu → Cu_2O) compared to the enthalpy of the reaction $Ti_2O_3 \rightarrow TiO_2$. It has been established that indium amalgam [276], In-Ga alloy [277], electroless nickel [278], and aluminum [7], are the electrodes which give a low contact resistance. On the other hand, silver [261], platinum [279] and gold [280] deposited on the surface of n-type $BaTiO_3$ provide Schottky-type contacts.

In the present work the properties of Al, Ni, In-Ga alloy, Ag, Au, and Pt electrodes have been investigated. Al electrodes were obtained by Al vapor deposition on the $BaTiO_3$ surface which was held at room temperature. Ni electrodes were obtained by electrolytic deposition of Ni from aqueous solution. The solution was prepared by dissolving 62.5 g of $NiSO_4{\cdot}6H_2O$, 12.5 g of $NiCl_2{\cdot}6H_2O$ and 10 g of H_3BO_3 in 250 ml of water. The Ni deposition was carried out at the current density of 1-3 A/dm^2. After electrode deposition the samples were annealed in air at 320 °C for 30 minutes.

In the case of other electrode materials, In-Ga 1:1 alloy was rubbed into the surface of $BaTiO_3$ using a paint brush. Silver electrodes were deposited by firing laboratory prepared Ag paste according to Okazaki [281]. Au and Pt electrodes were deposited by RF magnetron sputtering.

5.2.2 Results and discussion

Fig. 5.6 compares the time dependence of the electrical resistivity of $Ba_{.998}Y_{.002}$ TiO_3 with different electrodes. Resistivity, ρ, of ceramics with freshly deposited Ni, In-Ga, and Al electrodes ranges from 3 Ω·cm to 6 Ω·cm with Ni electrodes having the lowest ρ. As revealed from Fig. 5.6, resistiviy of ceramics with Ni electrodes decreased slightly after the first 10 - 20 hours and after that remained constant for more than 2000 hours. Initial decrease of resistivity may be associated with reduction of Ti at the electrode surface at the expense of oxidation of the Ni. This would result in the more conductive surface layer enriched with Ti^{3+} ions. Ni electrodes showed very good stability with time. Later experiments confirmed that samples with two-year old Ni electrodes showed the same values of resistivity as freshly prepared electrodes. The resistivity of ceramics measured with a 4-point probe technique gave similar results as with Ni electrodes. The resistivity of ceramics with Al electrodes was relatively stable in time, but the magnitude of resistivity was ca. 50 % higher than that of Ni electrodes. In contrast to Ni and Al electrodes, resistivity of ceramics with In-Ga alloy electrodes showed significant drift with time (see Fig.5.6). The resistivity of In-Ga electrodes increased by a factor of 4 in 2000 hours. In order to investigate this effect in more detail, complex impedance measurements were performed. The results are presented in Fig. 5.7. The curve labeled "Old In-Ga electrode" was obtained 4 months after applying an electrode. This curve shows two overlapping semicircles, one at high frequency at the origin of the graph with ca. 10 Ω diameter, and another, at lower frequencies, with a diameter of 130 Ω. The curve labeled "Fresh In-Ga electrode" was obtained right after removing the old In-Ga electrode and applying a new one. Only one semicircle is observed in this case. Based on this observation, a conclusion can be drawn, that the first (high frequency) semicircle represents the resistance of the bulk ceramic, whereas the second semicircle

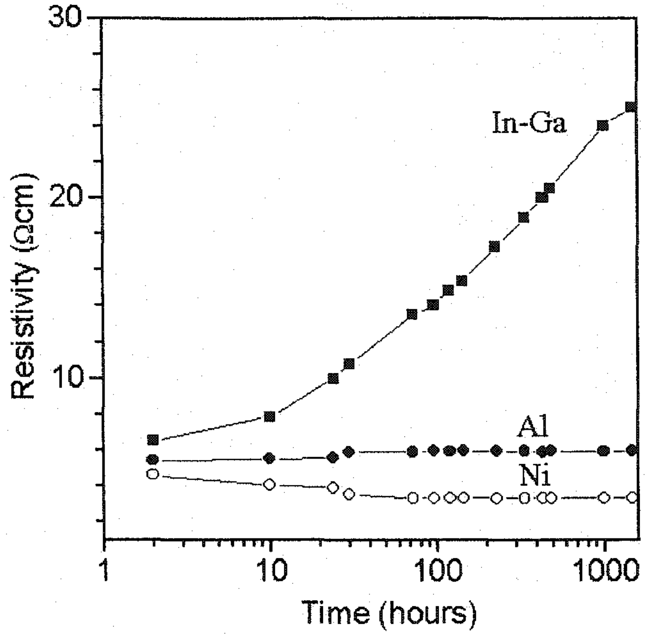

Figure 5.6: Time dependence of the low field electrical resisitivity of $Ba_{0.998}Y_{0.002}TiO_3$ ceramics with In-Ga, Ni, and Al electrodes

is characteristic of the ceramic-electrode interface. It is obvious that In-Ga electrodes cannot be employed in measurements of resistivity of $BaTiO_3$ ceramics due to their unstable behaviour in time and high overall resistance.

In contrast to Ni, Al, and In-Ga electrodes, contacts made of silver, gold and platinum showed values of resistivity of the order of MΩ·cm (see Fig.5.8). These electrodes did not show any appreciable dependence of resistivity with time. The high values of resistivity obtained for these electrodes are associated with the formation of blocking (Schottky-type) contacts at the metal-ceramic interface. According to the classical theory of Schottky-type contacts [282], when an n-type semiconductor comes into contact with a metal, a potential barrier (Schottky barrier) will form, providing that the work function of the semiconductor is less than that of the metal (see Fig. 5.9) The barrier arises because of the contact potential (difference in work functions) between the metal and the semiconductor. In the absence of the surface states, the diffusion potential, V_{d0}, is equal to the difference between the metal, ϕ_m, and semiconductor, ϕ_s, work functions

$$V_{d0} = \phi_m - \phi_s \tag{5.1}$$

and the barrier height, φ_b, seen from the metal is given by the difference between the metal workfunction, ϕ_m, and electron affinity of the semiconductor χ:

$$\varphi_b = \phi_m - \chi \tag{5.2}$$

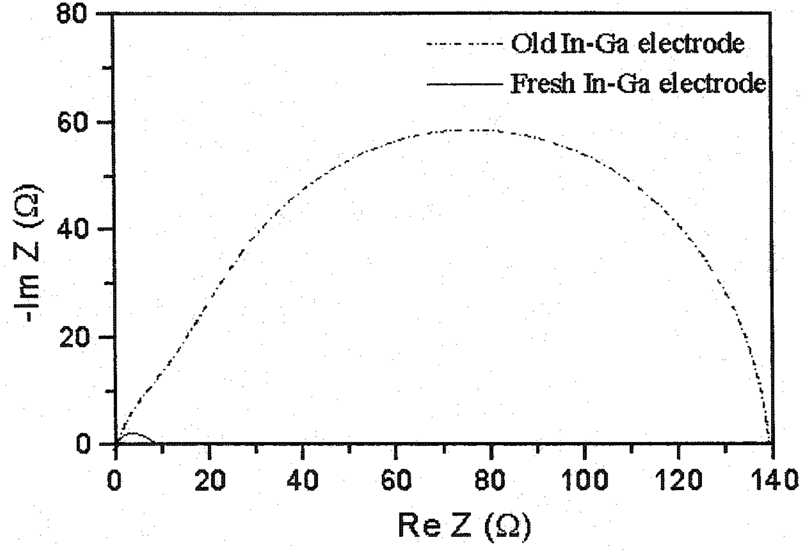

Figure 5.7: Complex impedance of $Ba_{0.998}Y_{0.002}TiO_3$ ceramics with In-Ga electrodes.

where $\chi = \phi_s - \xi$, and ξ is the energy difference between the Fermi level and the bottom of the conduction band. Formation of the Schottky barrier indicates that there must be a negative charge on the surface of the metal balanced by the positive charge in the semiconductor. The negative charge on the metal surface consists of extra electrons contained within the Thomas-Fermi screening distance of ca. 0.5 Å. The charge in the semiconductor arises from the uncompensated positive donor ions in a region depleted by electrons.

According to Eq. 5.2, it can be expected that the Schottky barrier height will increase with increasing metal work function. Pt has the highest work function [283] (ϕ_{Pt}=5.65 eV) among the analyzed electrode materials, and indeed it yields a blocking electrode with $BaTiO_3$. On the other hand, In-Ga alloy (ϕ_{In-Ga}=4.1 eV) has the lowest work function value and it provides an ohmic contact with $BaTiO_3$. The other metals, however, do not fit well into this scheme. While Ni and Au have the same values of ϕ (e.g., ϕ_{Ni}=5.15 eV, ϕ_{Au}=5.1 eV), Ni forms an ohmic contact, whereas Au gives a blocking contact. Surprisingly, silver (ϕ_{Ag}=4.26 eV) produces a blocking contact, although its work function is almost 1 eV smaller than that of nickel. In contrast to silver, aluminum (ϕ_{Al}=4.28 eV) gives an ohmic contact, although the values of the work functions of Al and Ag are approximately the same. The above results indicate that the properties of the metal-$BaTiO_3$ contact deviate from the ideal Schottky barrier model and the formation of the Schottky barrier with $BaTiO_3$ does not always correlate with the magnitude of the metal work function. Based on these results, it can be concluded that noble metals form Schottky barriers with $BaTiO_3$, whereas more electropositive metals form ohmic contacts. It is possible that the ability of the metal to reduce Ti^{4+} to Ti^{3+} is crucial in the formation of the ohmic contact with $BaTiO_3$.

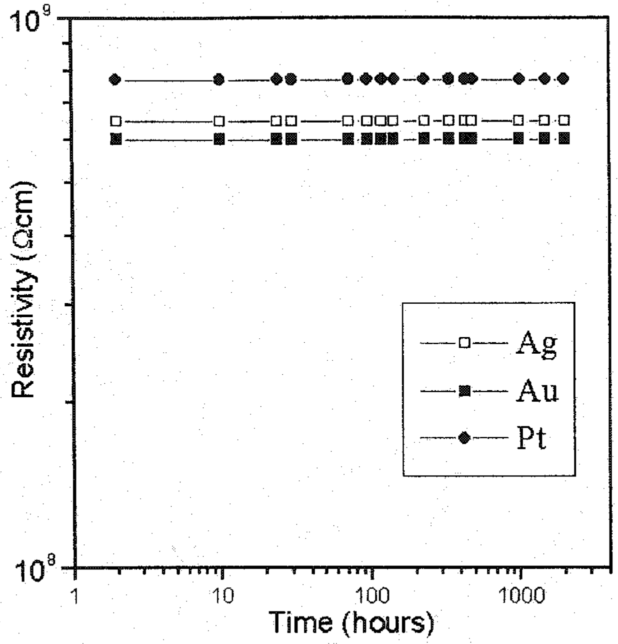

Figure 5.8: Time dependence of the low field electrical resisitivity of $Ba_{0.998}Y_{0.002}TiO_3$ ceramics with Ag, Au, and Pt electrodes

5.3 Room temperature DC resistivity

5.3.1 Introduction

A number of donor dopants have been employed to render $BaTiO_3$ n-type. Saburi [276] investigated the effect of Nb, Ta, Sb, La, Ce, Pr, Sm, and Bi on the resistivity of $BaTiO_3$ ceramics sintered in air. He found that at small dopant levels (below 0.2 at%), the resistivity decreases with increase in dopant concentration. The minimum resistivity was observed at donor doping levels of ca. 0.2 - 0.3 at%, depending on the type of dopant. At higher dopant concentrations (above 0.4 at%) the resistivity increased abruptly reaching values of 10^{10} Ω·cm. Later on, Sauer and Fisher [277] and Tennery and Cook [159] reported similar behaviour for resistivity of $BaTiO_3$ doped with La, Sm, Gd, and Ho. The effect of yttrium as an n-type dopant was investigated by Blanchart et al. [269] who found that $BaTiO_3$ prepared by the conventional mixed oxide route had a minimum resistivity of 6 Ω·cm when doped with 0.4 at% yttrium. However, their $BaTiO_3$ prepared by the alkoxide-hydroxide route showed a minimum resistivity of 5 Ω·cm at 0.2 at% yttrium. Moreover, they demonstrated that the range of yttrium concentration which was yielding the lower resistivity could be expanded to 0.7 at% by addition of 2 at% of SiO_2. Little is known about the effect of donor dopants on resistivity of ceramics sintered at low oxygen partial pressure. This is partially because there is no commercial application yet for this type of material. However, it is interesting to consider the effect

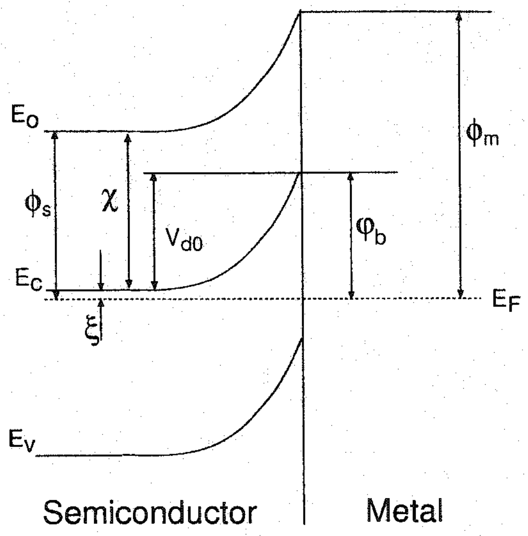

Figure 5.9: Schematic of the band diagram for a Schottky barrier

of donor dopants on the the grain bulk and grain boundary resistivity of ceramics sintered at various values of P_{O_2}.

Recently Tsur et al. [284] investigated the effect of Ba/Ti ratio on the substitution of donor dopants. They found that trivalent ions with a large ion size, $r \geq 0.94$ Å (e.g., Sm, Nd, La), will substitute for Ba independent of Ba/Ti ratio. Small rare-earth ions with $r \leq 0.87$ Å such as Lu and Yb will incorporate into Ti sublattice and will behave as acceptors, since the charge compensation will be via oxygen vacancies. Ions with intermediate radii of 0.87 Å $\leq r \leq$ 0.94 Å, (e.g. Er, Y, Ho, Dy, Gd) show "amphoteric" behaviour. They substitute on the Ba sublattice when Ba/Ti $<$ 1 and behave as donors, whereas when Ba/Ti $>$ 1 they are found in the Ti sublattice and behave as acceptors. In another recent publication, Morrison et al. [285] reported quite surprising results. Based on XRD, electron probe, and EDS analysis, the authors [285] concluded that compensation of the La donor in $BaTiO_3$ occurs exclusively by titanium vacancies independent of the concentration of the La. This finding strongly contradicts the earlier experimental results of Chan et al. [99] who found that only at high (e.g. $\geq$ 0.5 at%) n-dopant concentration does the compensation mechanism change from electronic type to cation vacancy type.

In this thesis the resistivity of yttrium doped $BaTiO_3$ with $0.98 \leq$ Ba/Ti ≤ 1.05 was investigated with special attention to the effect of atmosphere during sintering and postsintering anneal on the grain bulk and grain boundary properties.

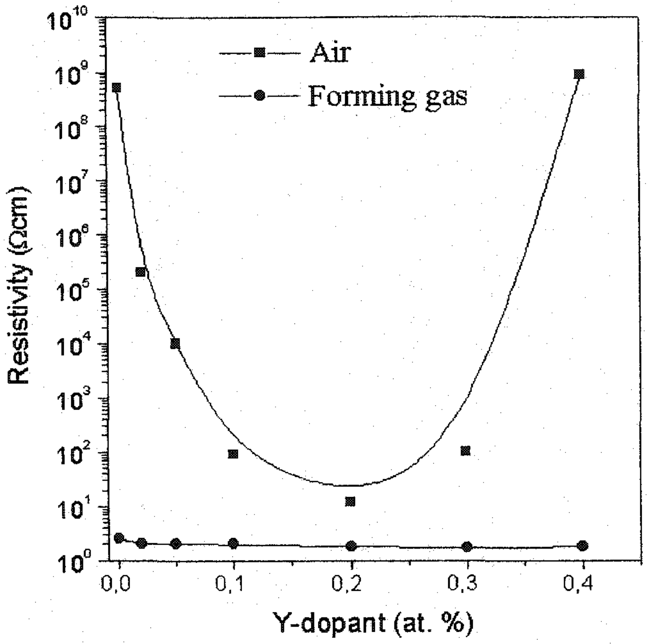

Figure 5.10: Room temperature resistivity of $Ba_{1-x}Y_xTi_{1.0}O_3$ (x=0, 0.0002, 0.0005, 0.001, 0.002, 0.003, 0.004) sintered at 1380 °C in air and forming gas

5.3.2 Results and discussion

Fig. 5.10 demonstrates the resistivity behaviour of Y-doped ceramics with Ba+Y/Ti = 1. The resistivity versus Y-dopant concentration of ceramics sintered in air shows a typical U-shape dependence. The minimum ρ value of 12 Ω·cm is achieved at a yttrium concentration of 0.2 at%. In contrast, the resistivity of $BaTiO_3$ ceramics sintered in forming gas at low oxygen partial pressure ($P_{O_2} \approx 10^{-17}$ atm) has a typical value of 2-3 Ω·cm and does not depend significantly on yttrium concentration. Next the effect of yttrium concentration on room temperature DC resistivity of $Ba_{1-x}Y_xTi_{1.02}O_3$ ceramics with a slight excess of Ti was measured (Fig. 5.11). It can be seen that 2 at% excess of titanium broadens the Y-concentration range which provides ceramics with low resistivity. The minimum resistivity value of 8 Ω·cm is obtained at a yttrium concentration of 0.4 at%. Again, as in the case of ceramics with Ba+Y/Ti=1, no significant ρ versus Y-dopant dependence is observed for ceramics sintered in forming gas. The question of broadening of the yttrium concentration range where low resistivity of ceramics is achieved was addressed by Blanchart et al. [269]. They found a yttrium-rich second phase, $Y_2Ti_2O_7$, in ceramics containing an excess of titania. Hence, in this ceramic, not all yttrium ions perform as effective donor dopants.

As revealed by Figs. 5.10 and 5.11, for ceramics sintered in air, at low yttrium concentration (e.g. $\leq 0.2 - 0.3$ at%) the resistivity decreases with an increase of Y. This would be expected for electronic-type compensation of donor ions. At higher concentration of yttrium, ρ increases by

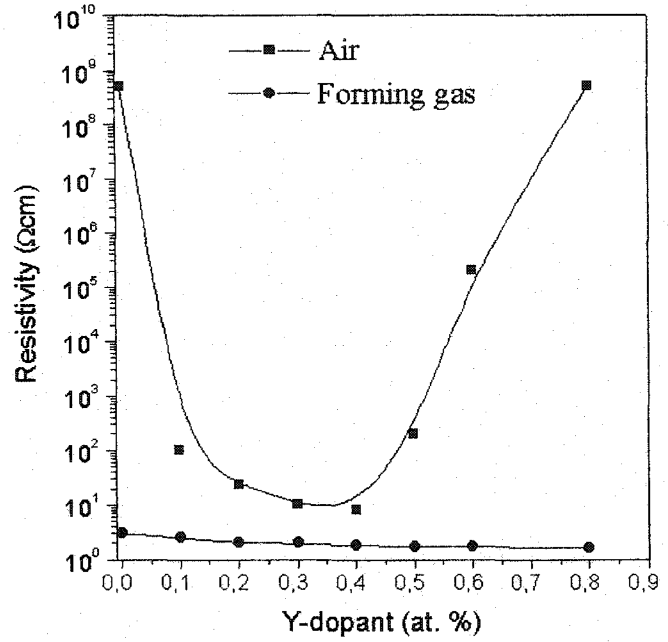

Figure 5.11: Room temperature resistivity of $Ba_{1-x}Y_xTi_{1.02}O_3$ (x=0, 0.001, 0.002, 0.003, 0.004, 0.005, 0.006, 0.008) sintered at 1380 °C in air and forming gas.

8 orders of magnitude. This phenomenon was first explained by Daniels and Härdtl [64]. They suggested that at high P_{O_2}, donor ions are compensated by doubly ionized barium vacancies. Later Chan et al. [101] using X-ray EDS analysis, found that at donor concentration ≥ 0.5 at%, the charge compensation is achieved by Ti vacancies. Hwang and Han [89] using equilibrium conductivity measurements and X-ray analysis suggested that both barium and titanium vacancies participate in charge compensation at donor dopants of ≥ 0.5 at% according to complete Schottky disorder. It is obvious that at high yttrium concentration, the charge compensation mechanism changes from electronic to cation vacancy type. However, at this point the results of the room temperature resistivity of Y-doped ceramics are not sufficient to draw an unequivocal conclusion about the nature of the cation vacancies. However, the EPR analysis of yttrium doped $BaTiO_3$ presented in Chapter 7 suggests that both titanium and barium vacancies participate in the compensation of yttrium ions. In contrast to ceramics sintered in air, Y-doped $BaTiO_3$ sintered at low P_{O_2} does not seem to depend on donor dopant concentration. Both donor ions and oxygen vacancies contribute toward the electronic conductivity of these samples. The compensation mechanism remains electronic-type in the wide donor-dopant range. However, as revealed by Fig. 5.12 a small excess of Ba (1-4 at%) results in a dramatic increase in resistivity for ceramics sintered both in air and in forming gas. This is a manifestation of the "amphoteric" behaviour of the yttrium ion. In $BaTiO_3$ ceramics with barium excess, yttrium substitutes for Ti and behaves as an acceptor ion. This results in an increase

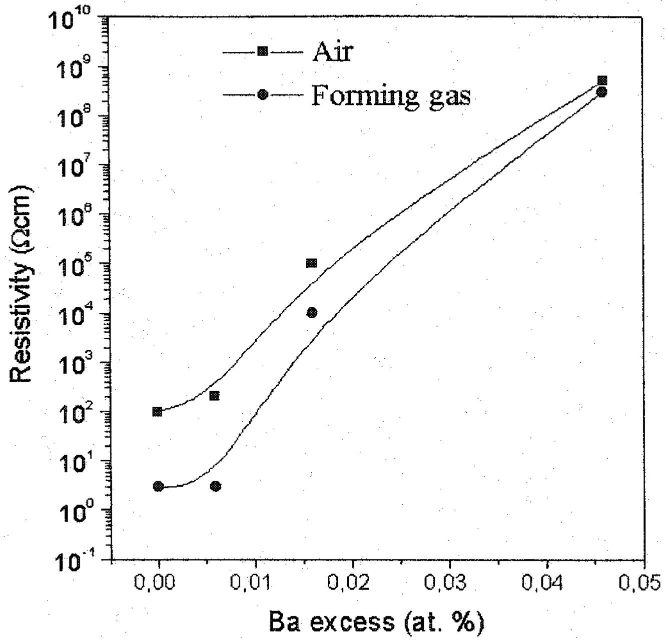

Figure 5.12: Room temperature resistivity of $Ba_{1+x}Y_{0.002}Ti_{1.0}O_3$ (x=0, 0.006, 0.016, 0.046) sintered at 1380 °C in air and forming gas.

of resistivity of $BaTiO_3$ ceramics. Similar behaviour for other "amphoteric" donor ions (e.g., Er, Ho, Dy, and Gd) has been reported by Tsur et al. [284].

5.4 Effect of P_{O_2} on resistivity

5.4.1 Introduction

N-type doped $BaTiO_3$ sintered in air is known to possess a positive temperature coefficient of resistivity (PTCR). However, when $BaTiO_3$ containing n-type dopant is sintered in reducing atmosphere no PTCR effect is observed. It is obvious that the PTCR effect is strongly affected by oxygen partial pressure. Heywang [1] interpreted the PTCR effect in terms of temperature-dependent double Schottky barriers (DSB) located at grain boundaries. In the simplest form, DSB originates from the negatively charged layer of mono-energetic in-gap interface states (electron traps). Several possible sources of the interface states in $BaTiO_3$ have been proposed [152] but a consensus about the nature of these electron traps has yet to be reached. The most frequently discussed sources of interface states in $BaTiO_3$ are either segregated cation vacancies or chemisorbed oxygen. Indeed, chemisorbed oxygen contributes to interface state density in several cases of metal oxide semiconducting ceramics [286, 287]. Oxygen chemisorption was found on the surface of n-type ZnO, and SnO_2 single crystals by UPS, TPD, AES, and EELS techniques [288, 289, 287]. Chemisorption of oxygen on these semiconductors leads to a partial reduction of surface oxygen giving adsorbed O_2^- or O^- and forming a depletion layer at the surface. It is worth mentioning that neither chemisorption of oxygen nor oxygen induced in-gap surface states have been observed on the low index surfaces of $BaTiO_3$ single crystals [70].

Daniels and Wernicke [4] have shown that during sintering of $BaTiO_3$ in an oxidizing atmosphere, ionized barium vacancies segregate to the grain boundaries. They proposed that these defects play the role of the interface states in the Heywang model. Desu and Payne [71] suggested that segregated titanium vacancies can behave as acceptor states in the Heywang model. Other authors [2, 3, 150, 290] have assigned interface states in $BaTiO_3$ to chemisorbed oxygen. Jonker [2] proposed that oxygen chemisorbed at grain boundaries behaves as an electron trap in the DSB model. He found that after annealing the $BaTiO_3$ sample in nitrogen or vacuum at 1000 °C for a few hours, the resistivity jump completely disappears. Kuwabara [3] examined degradation of the PTCR effect in porous barium titanate in reducing atmospheres below 400 °C. He attributed the change in resistivity to the elimination of chemisorbed oxygen from the grain boundaries. Furthermore, by showing that the PTCR effect can be decreased at such low temperatures, Kuwabara ruled out the role of Ba vacancies in the formation of the PTCR properties of his samples. It should be realised, however, that $BaTiO_3$ samples examined by Kuwabara [3] and others [2, 150, 290] had been sintered in air and had initially exhibited the PTCR effect. Heat treatment of $BaTiO_3$ in oxygen deficient atmospheres would introduce oxygen vacancies in the grain boundary region, causing an increase in electron concentration in the grain boundary region and making grain boundaries highly conductive. Thus, reduction of $BaTiO_3$ ceramics would inevitably result in degradation of the PTCR effect irrespective of the nature of the interface states.

An important result in favour of the chemisorption model was reported by Alles et al. [291]. The authors obtained the PTCR effect in undoped $BaTiO_3$ sintered in air, reduced at 1150 °C in a flowing mixture of 80% H_2-20% N_2 and then reoxidized in a mixture containing 1,1,1,3,3,3-hexafluoro-2-propanol. The authors [291] assumed that the reason for the PTCR effect in their samples was chemisorption of fluorine gas, since, according to the defect chemistry, no cation vacancies were supposed to exist in undoped $BaTiO_3$ [99]. However, EPR analysis of $BaTiO_3$ reported in Chapter 7 suggests that barium and titanium vacancies do exist in undoped $BaTiO_3$ sintered in air.

The effect of P_{O_2} on grain bulk and grain boundary resistivity of $BaTiO_3$ in light of oxygen chemisorption and cation vacancy segregation models is reported below.

5.4.2 Results and discussion

Low temperature complex impedance spectroscopy ($1 - 3.2{\cdot}10^7$ Hz) was used to characterize the electrical properties of $BaTiO_3$ samples. For electrically inhomogeneous samples (i.e., for a sample with a large difference in the grain bulk and grain boundary resistance and capacitance) the total impedance is given by [292]

$$Z^* = \sum \frac{R_i}{1 + j\omega R_i C_i} \tag{5.3}$$

where i stands for grain bulk or grain boundary. According to Blanchart et al. [269] and Sinclair and West [292], in order to observe grain bulk and grain boundary electrical properties, they have to possess the time constants $\tau = R_i C_i$ of at least two orders of magnitude difference. In addition to this requirement, the samples for impedance spectroscopy analysis should not be too conductive; otherwise the spectrum features will collapse into the origin of the complex impedance plot. Earlier studies of semiconductive PTCR $BaTiO_3$ were focused on the temperature range of 20 - 400 °C. At these temperatures, in most cases, only grain boundary characterisics can be resolved, since the grain bulk conductivity is too high. In order to overcome this drawback, the samples in this study were measured at liquid nitrogen temperature (i.e., 77 K) where both grain bulk and grain boundary impedances were clearly resolved. Fig. 5.13 shows complex impedance spectra of $Ba_{0.998}Y_{0.002}Ti_{1.0}O_3$ ceramic sintered in the P_{O_2} range of 10^{-17} atm $\leq P_{O_2} \leq 0.2$ atm. The samples were measured at 77 K. At room temperature, the resistivity of all samples was too low to be able to be measured with an impedance analyzer even when rigorous "short" and "open" circuit compensations were employed. All spectra except the one for the sample sintered at $P_{O_2} = 10^{-17}$ atm show two distinct semicircles on the complex impedance plot. The high-frequency semicircle of the sample sintered at $P_{O_2} = 0.2$ atm is too small to be resolved in Fig. 5.13. However, two semicircles are clearly revealed when the data is presented in a double logarithmic scale in Fig. 5.14. As can be seen from Fig. 5.13, the resistivity of the samples increases with increase in the oxygen content of the sintering atmosphere. It is also realized from the complex impedance data that the samples are not electrically homogeneous, since at least two semicircles are observed. It can be assumed with a high degree of confidence that the two semicircles in the complex impedance plot represent grain bulk and grain boundary resistances of the samples. In order to present additional evidence that the observed features in Fig. 5.13 are grain bulk and grain boundary impedances, the dielectric constant of the samples was calculated by

$$\varepsilon^* = (j\omega C_0 Z^*)^{-1} \tag{5.4}$$

where ω is the angular frequency $2\pi f$, C_0 is the vacuum capacitance of the measuring cell and electrodes with an air gap in place of the sample, $C_0 = \varepsilon_0/k$, where ε_0 is the permittivity of free space (8.854×10^{-14} F/cm) and $k = l/A$ is the cell constant with thickness l and area A. Frequency dependence of the real part of the dielectric constant, ε', of the samples sintered at various P_{O_2} is shown in Fig. 5.15. As revealed by Fig. 5.15 the dielectric constant of the samples is quite high. It exceeds the ε' of undoped dielectric $BaTiO_3$ by 2-3 orders of magnitude [293]. These high values of ε' are attributed to the thin grain boundary layers with high resistance. The value of ε' at low frequencies decreases with increase of the P_{O_2}. This can be attributed to the increase in the thickness of the grain boundary layer. At high frequency, the dielectric constant of all samples

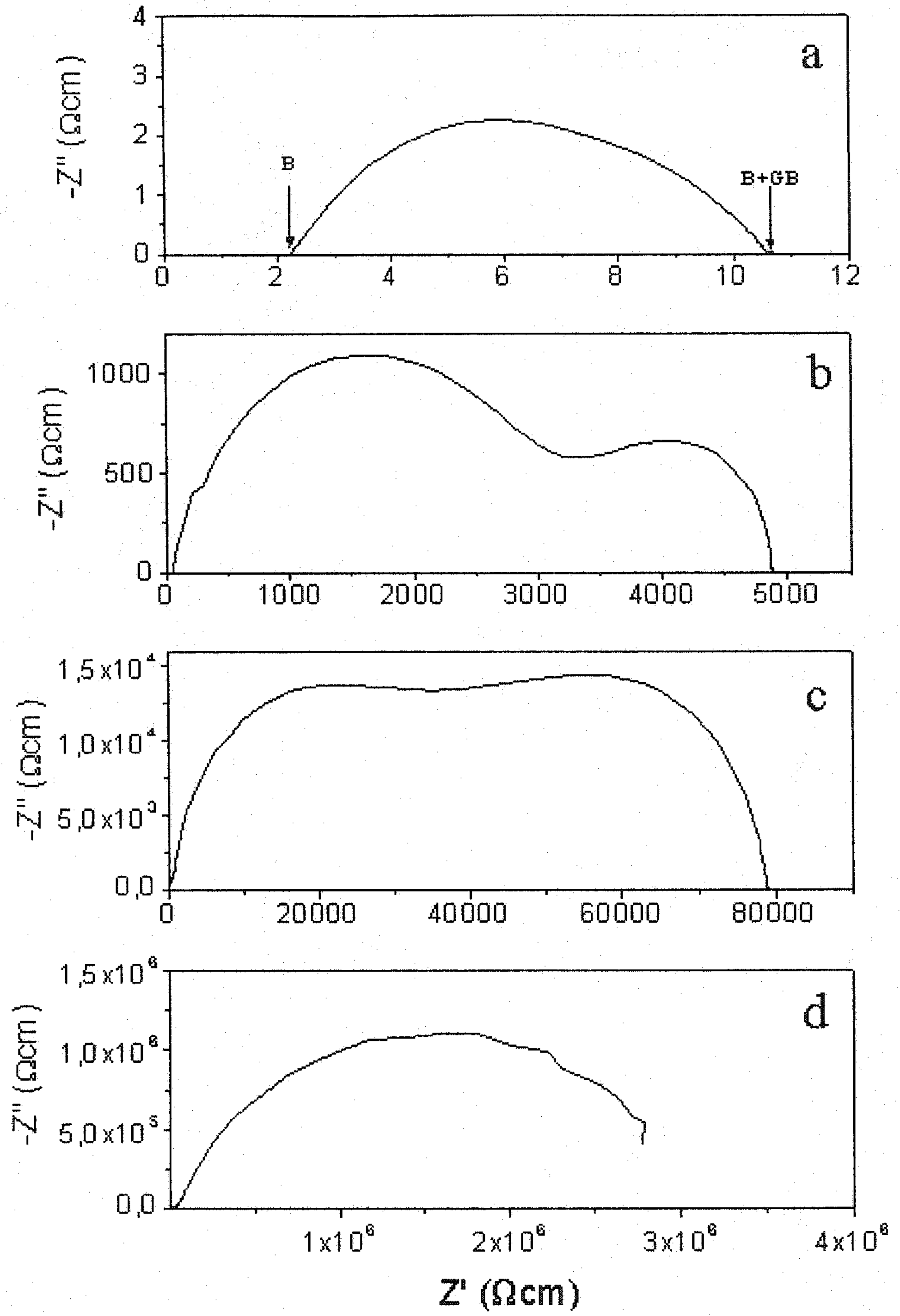

Figure 5.13: Complex impedance of $Ba_{0.998}Y_{0.002}Ti_{1.0}O_3$ sintered at a) $P_{O_2} = 10^{-17}$ atm, b) $P_{O_2}= 10^{-15}$ atm, c) $P_{O_2}= 10^{-12}$ atm, d) $P_{O_2}= 0.2$ atm at 1380 °C. All spectra were measured at 77 K. The letters B and GB indicate grain bulk and grain boundary.

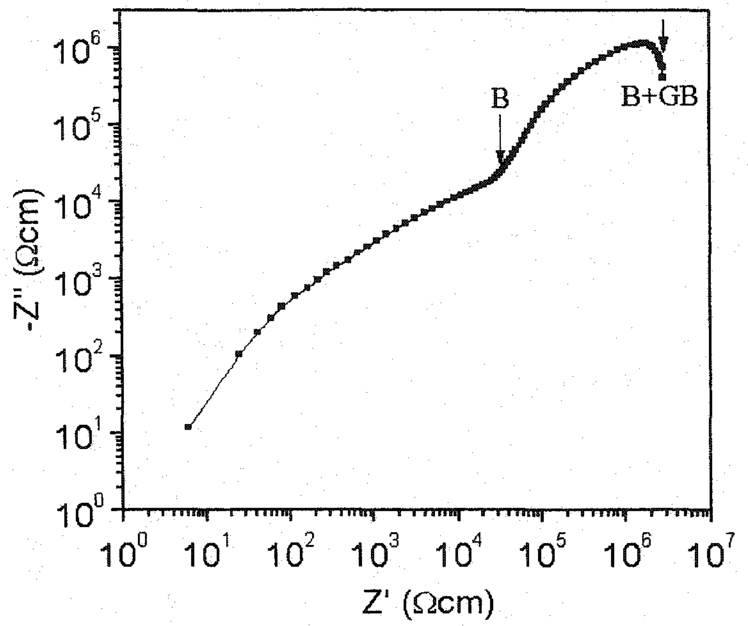

Figure 5.14: Complex impedance of $Ba_{0.998}Y_{0.002}Ti_{1.0}O_3$ sintered at P_{O_2}= 0.2 atm and measured at 77 K. The letters B and GB indicate grain bulk and grain boundary resistivity.

decreases, approaching the ε' of undoped dielectric $BaTiO_3$ represented by the solid line in Fig. 5.15. In fact, as revealed by Fig. 5.15, ε' of the $Ba_{0.998}Y_{0.002}Ti_{1.0}O_3$ sample sintered in air (i.e., at P_{O_2}=0.2 atm) equals 450, which coincides with the ε' of undoped dielectric $BaTiO_3$ at $f \geq 2 \cdot 10^6$ Hz. Hence, it can be concluded that the complex impedance data shown in Figs. 5.13 and 5.14 represent the grain bulk and grain boundary impedances of semiconducting $BaTiO_3$.

Fig. 5.16 shows the grain bulk conductivity, σ_B, of $Ba_{0.998}Y_{0.002}Ti_{1.0}O_3$ samples obtained from the complex impedance data. The conductivity decreases from 0.5 $\Omega^{-1} \cdot$ cm^{-1} for samples sintered at $P_{O_2} = 10^{-17}$ atm to $2 \cdot 10^{-5}$ $\Omega^{-1} \cdot cm^{-1}$ for samples sintered at P_{O_2} = 0.2 atm. At higher oxygen partial pressures, the grain bulk conductivity increases slowly from $5 \cdot 10^{-5}$ $\Omega^{-1} \cdot$ cm^{-1} at P_{O_2} = 10^{-14} atm to $2 \cdot 10^{-5}$ $\Omega^{-1} \cdot$ cm^{-1} at P_{O_2} = 0.2 atm. It is interesting that the results obtained at 77 K show the same trend as high temperature equilibrium conductivity of Nb doped $BaTiO_3$ reported by Chan and Smyth [99]. The grain bulk conductivity of our yttrium doped samples is nearly independent of the oxygen partial pressure in the range of 10^{-14} atm $\leq P_{O_2} \leq$ 0.2 atm. According to Chan and Smyth [99], at oxygen partial pressure where oxygen vacancy concentration is lower than donor dopant concentration, the conductivity is independent of P_{O_2}. Only at very low P_{O_2} (e.g., $P_{O_2} < 10^{-14}$ atm in our case), the conductivity is pressure sensitive, since the concentration of oxygen vacancies exceeds the donor ion concentration. However, as can be seen from Fig. 5.16, the increase of conductivity with decreasing pressure at $P_{O_2} < 10^{-15}$ atm does not obey $\sigma \propto P_{O_2}^{-1/6}$ dependence as would be expected in the case of $V_O^{\cdot\cdot}$ as the major compensation mechanism. In

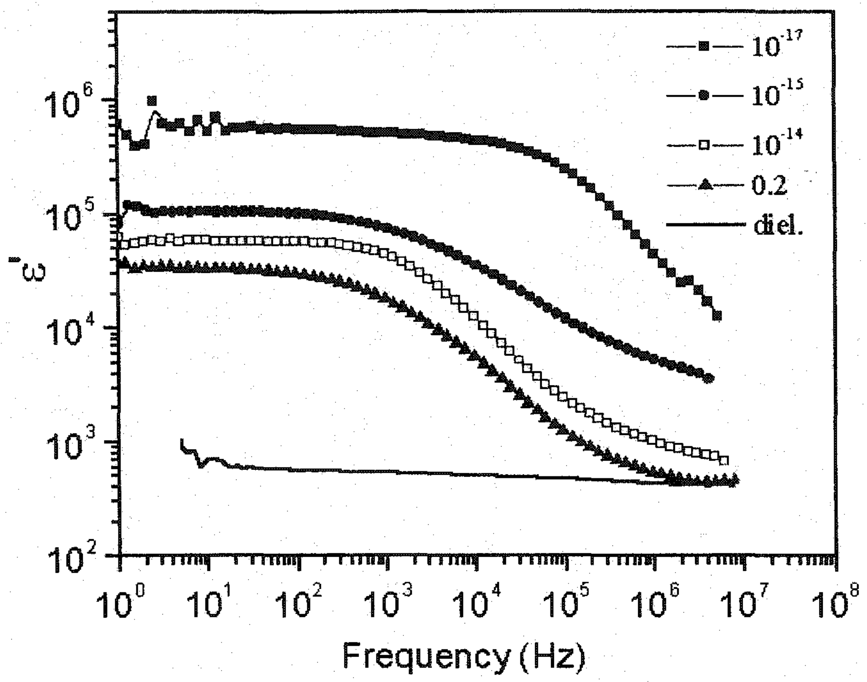

Figure 5.15: Frequency dependence of the real part of dielectric constant of $Ba_{0.998}Y_{0.002}Ti_{1.0}O_3$ sintered at various P_{O_2}. The solid line represents the ε' of undoped $BaTiO_3$ sintered in air at 1380 °C. All spectra were measured at 77 K.

fact, the conductivity of the samples increases more steeply with P_{O_2}. One of the reasons for this anomalous σ versus P_{O_2} behaviour is nonactivated mobility which is observed in samples sintered at very low P_{O_2}. The conductivity of these samples does not decrease with temperature and sometimes exhibits metallic-like behaviour. These results are discussed Chapter 6.

Let us now examine the effect of oxygen on the PTCR anomaly in $BaTiO_3$. According to Heywang [1], the height of the potential barrier φ at the grain boundary is defined as

$$\varphi = \frac{eN_t^2}{8\varepsilon\varepsilon_0 N_d} \tag{5.5}$$

where e is the elementary charge, ε_0 the permittivity of free space, ε the dielectric constant of $BaTiO_3$, N_d the concentration of ionized donors, and N_t is the density of occupied interface states. In the 'chemisorption' assumption, the value N_t is equal to the density of chemisorbed oxygen at the grain boundary. Oxygen chemisorption occurs by trapping of conduction band electrons by initially physically adsorbed oxygen molecules. A negative charge from chemisorbed oxygen results in the formation of a depletion layer and a negative interface potential barrier φ. The rate of chemisorption is proportional to the concentration of the conduction electrons, which decreases as the depletion layer forms. The process of chemisorption reaches an equilibrium when the energy of interface states E_t approaches the Fermi level E_F, i.e., $E_t = E_F + \varphi$. At this point the number of trapped and

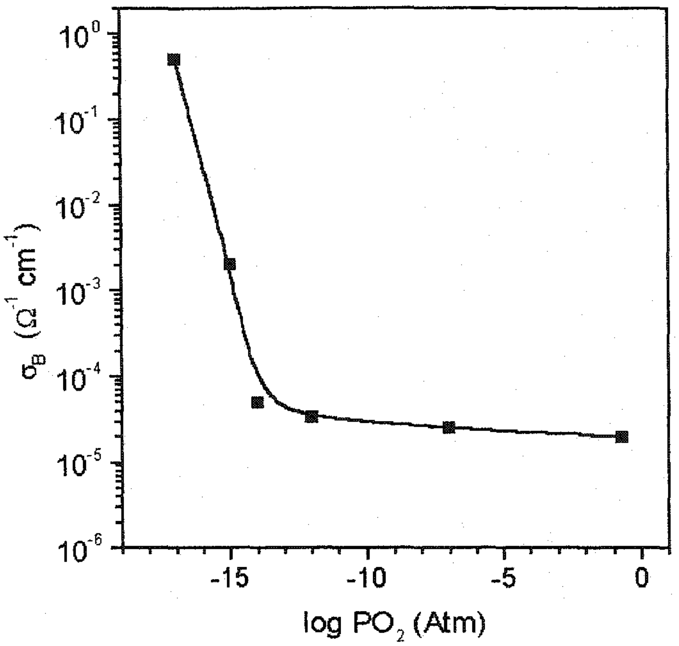

Figure 5.16: Grain bulk conductivity of $Ba_{0.998}Y_{0.002}Ti_{1.0}O_3$ sintered at vaious P_{O_2} and measured at 77 K.

released electrons at the interface are equal. In light of the chemisorption model, the substantial PTCR effect requires that chemisorbed oxygen be uniformly distributed over the surface of the $BaTiO_3$ grains. Since electron trapping is a fast process, the rate-determining step in the formation of the PTCR properties is the diffusion of oxygen along the grain boundaries into the sample. The question is what minimum temperature and soaking time are required to ensure that oxygen has completely diffused into the grain boundary regions of the sample of known geometry. Unfortunately, the oxygen diffusion coefficient along the grain boundary of $BaTiO_3$ is not known. Most studies of n-type $BaTiO_3$ and $SrTiO_3$ focused on the grain bulk oxygen diffusion [69, 294]. Shirasaki et al. [69] have found $D_O \approx 10^{-13}$ cm^2/sec for the self-diffusion coefficient of oxygen in La-doped $BaTiO_3$ at 1000 °C. Helmbold et al. [294] using ^{18}O tracer diffusion technique found the oxygen diffusion coefficient in Nb and La doped $SrTiO_3$ single crystals to be on the order of 10^{-11} - 10^{-14} cm^2/sec at 1050 °C. It can be expected, however, that the activation energy of oxygen diffusion along the grain boundary is much lower than that for lattice diffusion [249]. This would result in a much higher diffusion coefficient. As a rough estimate for this calculation, the oxygen diffusion coefficient of $D_O = 5.7 \cdot 10^3 exp(-2.05eV/kT)$ cm^2/sec derived by Wernicke [93] for lattice diffusion of oxygen vacancies in undoped $BaTiO_3$ was assumed. Moreover, as is shown below, this value is justified by the experimental results. It was also assumed that the surface of the sample is an infinite source of oxygen. The concentration of the chemisorbed oxygen in the sample sintered at low P_{O_2} is negligibly small. Upon heat treatment in air, chemisorbed oxygen will start to diffuse into the sample along the grain boundaries. After sufficient time, the concentration of chemisorbed oxygen at the grain boundaries located at the middle of the sample will be equal to the concentration of the oxygen at the surface. For samples with a diameter exceeding the thickness by at least one order of magnitude, the problem can be treated as diffusion into an infinite plane. A solution for diffusion into a plane is given by Crank [295]:

$$\frac{C(t,x)}{C_1} = 1 - \frac{4}{\pi}\sum_{n=0}^{\infty}\frac{(-1)^n}{2n+1} exp\left(\frac{-D(2n+1)^2\pi^2 t}{4l^2}\right) cos\frac{(2n+1)\pi x}{2l} \tag{5.6}$$

where C_1 is the surface concentration of oxygen, D is the diffusion coefficient, l is the half thickness of the plane sheet, t is time in sec, and x is the distance from the center of the plane sheet. When solving Eq. 5.6, the following boundary conditions were applied:

$C = 0, -l < x < +l, t = 0;$

$C(x = -l) = C(x = +l) = C_1, t \geq 0.$

Solutions of Eq. 5.6 at $x = 0$ (i.e., at the center of the plane sheet of 1.2 mm thickness) for various temperatures are plotted in Fig. 5.17. It can be reasonably assumed that equilibrium between the

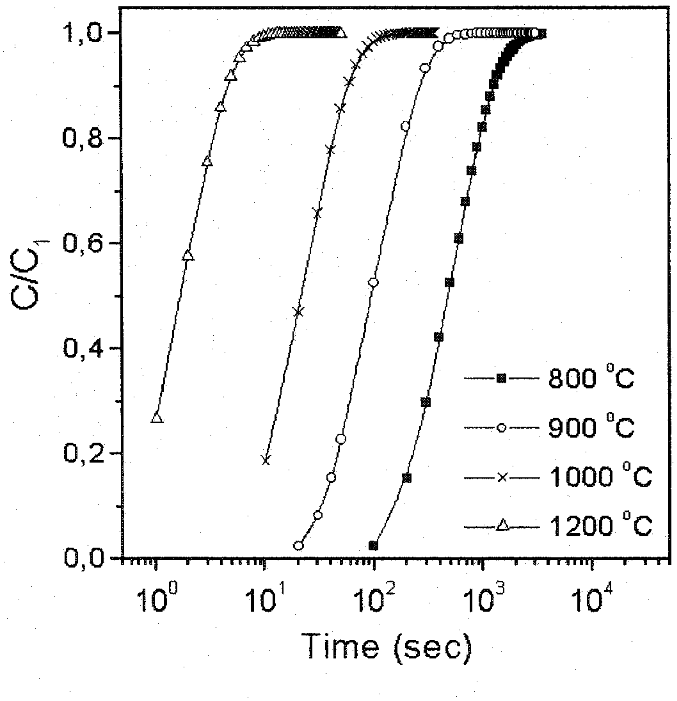

Figure 5.17: Time dependence of the ratio of the concentration of chemisorbed oxygen at the center of the plane sheet of thickness 1.2 mm to the concentration at the surface, calculated according to Eq. 5.6 for different temperatures.

surface of the sample and the grain boundary located at the middle of the pellet is attained when the difference in density of chemisorbed oxygen at the surface and at the center of the pellet is less than ca. 1 %, i.e., $C/C_1 > 0.99$. Fig. 5.17 shows that these conditions require 40 minutes of treatment in air at 800 °C but are met after 10 seconds of treatment at 1200 °C.

However, in order to justify these calculations one needs to obtain an experimental estimate of the grain boundary oxygen diffusion in $BaTiO_3$. For this purpose, a sample of $Ba_{0.996}Y_{0.004}TiO_3$ was sintered at 1380 °C and an oxygen partial pressure of 10^{-17} atm. The sample had a diameter of 16 mm and relative density of 92 %. Two pellets of thickness 1 mm and 5 mm were prepared from the original sample by slicing it with a diamond saw. These two pellets were annealed in air at 800 °C for 2 hours and slowly cooled to room temperature. Ohmic Ni electrodes were applied by electrolytic deposition of Ni from aqueous solution followed by annealing in air at 320 °C. Complex impedance of the pellets was measured at 77 K. The results are presented in Figs. 5.18 and 5.19.

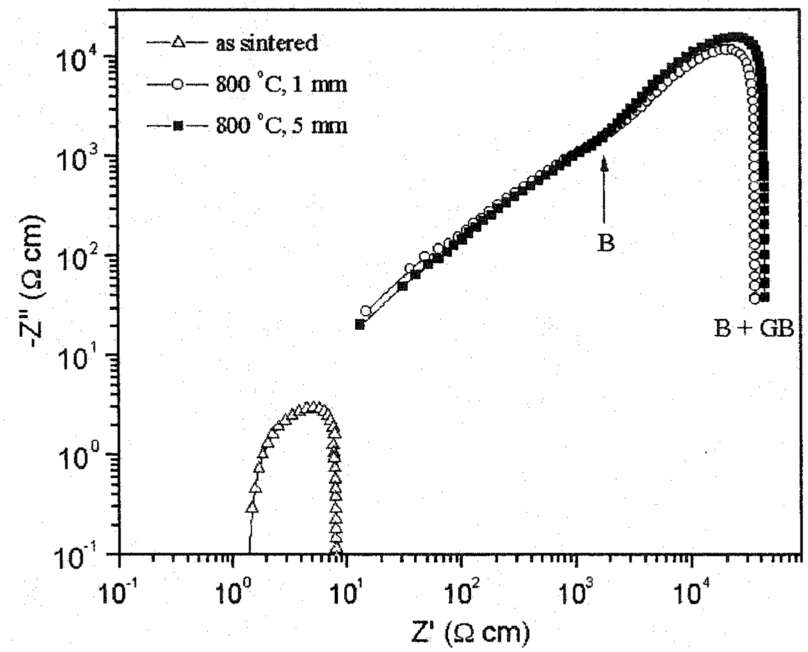

Figure 5.18: Complex impedance of the $Ba_{0.996}Y_{0.004}TiO_3$ samples sintered at $P_{O_2}=10^{-17}$ atm and annealed at 800 °C in air for 2 hours. The spectra were measured at 77 K.

From Fig. 5.18 it can be seen that the resistivity of the pellets annealed in air at 800 °C for 2 hours is 3 orders of magnitude higher than that of original sample sintered at an oxygen partial pressure of 10^{-17} atm. An important result is that both samples (i.e., 1 mm and 5 mm thickness) showed the GB+B resistivity values which differ by less than 5 %. Their grain bulk resistivity indicated by the arrow in Fig. 5.18 also showed similar values of ca. 20 000 Ω·cm. This confirms that the grain boundary regions of both samples were equally oxidized. This conclusion is also supported by measurements of the dielectric constant shown in Fig. 5.19. Compared with the as- sintered sample, which has $\varepsilon' = 5 \cdot 10^5$ at 5 Hz, both samples of 1 mm and 5 mm thickness showed similar values of

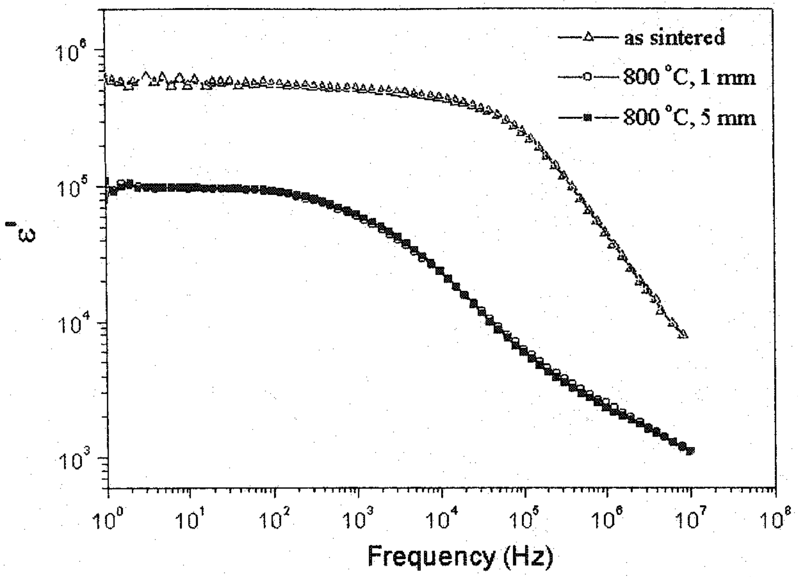

Figure 5.19: Frequency dependence of dielectric constant of the $Ba_{0.996}Y_{0.004}TiO_3$ samples sintered at P_{O_2}=10^{-17} atm and annealed at 800 °C in air for 2 hours. The measurements were performed at 77 K.

dielectric constant (e.g., ε'= $1 \cdot 10^5$ at 5 Hz) which indicates an increase of the thickness of the grain boundary layer by a factor of 5. The above experimental results suggest that the grain boundary layers of the samples of chosen geometry are uniformly oxidized after heat treatment in air at 800 °C for 2 hours. This also justifies the magnitude of the grain boundary diffusion coefficient of oxygen employed in our calculations. It is important, however, that the samples sintered at P_{O_2}=10^{-17} atm and oxidized at 800 °C for 2 hours did not show the PTCR effect.

According to Eq. 5.5, the height of the grain boundary potential barrier, φ, is inversely proportional to the concentration of the charge carriers provided by ionized donors, N_d. Thus, it can be argued, that the PTCR effect in ceramics sintered in reducing atmosphere and annealed in air, is absent because φ is small due to the high concentration of the charge carriers rather than the low density of chemisorbed oxygen. To clarify this argument, ceramics sintered at P_{O_2}=10^{-12} atm and annealed in air at different temperatures were investigated. As revealed by complex impedance analysis at 77 K presented in Figs. 5.13 and 5.14, the grain bulk resistivity of ceramics sintered at P_{O_2}=10^{-12} atm and at P_{O_2}=0.2 atm equals $3.6 \cdot 10^4$ Ω·cm and $4.9 \cdot 10^4$ Ω·cm, respectively. Hence, the density of the charge carriers in these ceramics differ only by a factor of 1.36. Fig. 5.20 shows the temperature dependence of resistivity of ceramic samples of 1 mm thickness sintered at P_{O_2}=10^{-12} atm and annealed in air at 800 °C, 1000 °C, and 1250 °C for 2 hours. According to Fig. 5.20, a weak PTCR effect is detected in ceramics annealed at 800 °C. Annealing at 1000 °C and 1250 °C resulted in resistivity jumps of 1.8 and 3.5 orders of magnitude respectively. The samples reported

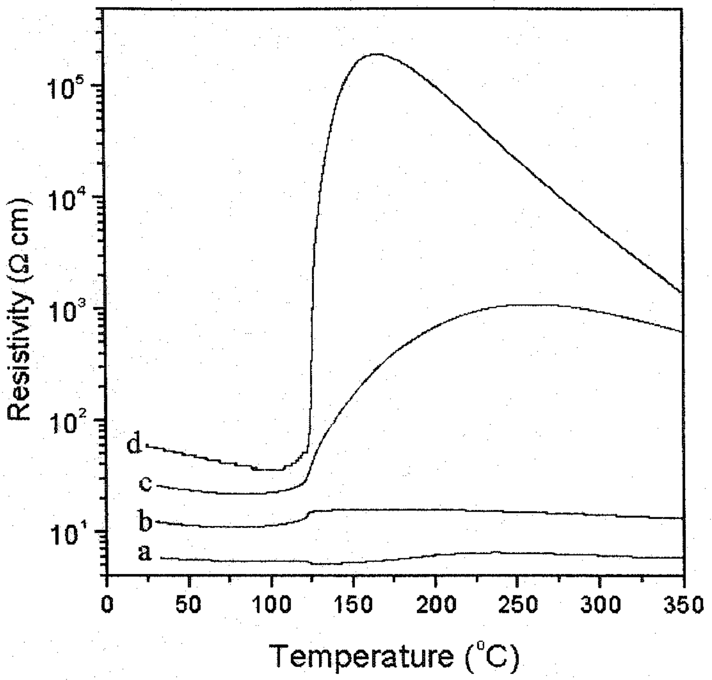

Figure 5.20: Temperature dependence of resistivity of the $Ba_{0.996}Y_{0.004}TiO_3$ samples of 1 mm thickness sintered at $P_{O_2}=10^{-12}$ atm and annealed at different temperatures in air for 2 hours: a) as sintered, b) 800 °C, c) 1000 °C, d) 1250 °C.

in Fig. 5.20 were annealed for 1 h in forming gas (7 % H_2, 93 % Ar) at 400 °C. Their resistivity was measured as a function of temperature under forming gas atmosphere. As shown in Fig. 5.21, heat treatment in the reducing atmosphere decreases the resistivity of $BaTiO_3$ as well as the PTCR effect. Significant reduction of the PTCR effect in reducing atmosphere is observed for samples annealed in air at 1000 °C and 1250 °C. These samples are labelled "c" and "d" in Fig. 5.21. Sample "c" shows only 60% increase in ρ in the vicinity of 120 °C, the Curie temperature. The resistivity jump of sample "d" decreased from 3.5 orders of magnitude in Fig. 5.20 to a factor of 4 in Fig. 5.21. Annealing of the samples in the reducing atmosphere also caused an overall decrease in their room temperature resistivity when compared with Fig. 5.20. This reduction of the total resistivity of the samples occurs at the expense of the grain boundary resistivity as revealed by complex impedance analysis. Hence, it is not surpising that on subsequent oxidation in air for 1 h at 400 °C, the resistivity of the reduced samples changed to the original values shown in Fig. 5.20. Our results demonstrate that pronounced PTCR effect appears in ceramics annealed at temperatures much higher than that required to promote grain boundary diffusion of oxygen. These observations suggest that the PTCR effect in n-type $BaTiO_3$ is weakly, if at all, affected by oxygen chemisorption at the grain boundaries.

It is obvious, that another defect formation mechanism, which requires much higher temperatures, is involved in formation of the PTCR effect. It has long been known that cation vacancies play an

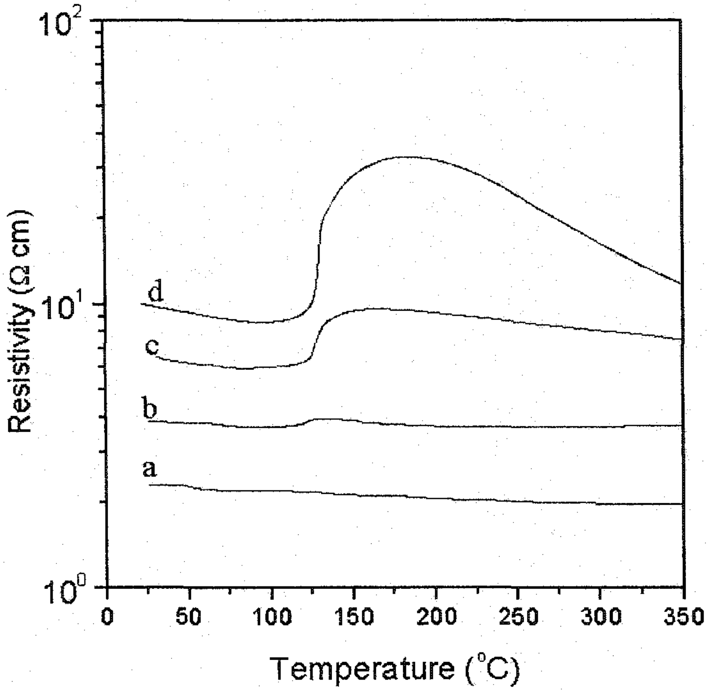

Figure 5.21: Temperature dependence of resistivity of the $Ba_{0.996}Y_{0.004}TiO_3$ samples reported in Fig.5.20 after 1 hour annealing in forming gas at 400 °C.

important role in the defect equilibrium of $BaTiO_3$. Daniels and Härdtl [64] have suggested that ionized donors, $D^{\cdot}$, are compensated by the doubly ionized barium vacancies, V''_{Ba}, and the electrical neutrality condition at oxygen partial pressures higher than 10^{-5} atm requires that $D^{\cdot} = 2V''_{Ba}$. Lewis and Catlow [79], on the other hand, proposed a titanium vacancy compensation mechanism $D^{\cdot} = 4V''''_{Ti}$, which is based on their calculation of defect energies for $BaTiO_3$. Chan et al. [101] reported that for donor concentrations greater than 0.5 mol% in $BaTiO_3$, charge compensation is achieved solely by titanium vacancies. Cation vacancies become predominant defects in $BaTiO_3$ under oxidizing conditions at high temperatures. Since the lattice diffusion coefficients of these defects are orders of magnitude lower than those for oxygen, higher temperatures and prolonged soaking time are required to obtain a uniform grain boundary layer enriched in cation vacancies. Our results on the effect of oxygen partial pressure on the resistivity of $BaTiO_3$ suggest that the PTCR effect in $BaTiO_3$ is associated with the formation of titanium and barium vacancies and oxidation of the grain boundaries rather than grain boundary chemisorption of oxygen. Moreover, the proposed interpretation is not inconsistent with the decrease of the PTCR effect in reducing atmospheres. Treatment of PTCR $BaTiO_3$ in reducing atmosphere at moderate temperatures (e.g., 300 - 700 °C) does not cause changes in the concentration or spatial distribution of cation vacancies.

However, it causes incorporation of the oxygen vacancies in the grain boundary region, rendering it conductive and reducing the overall resistivity of ceramics. Changing from a reducing to an oxidizing atmosphere reinstates the PTCR effect due to the oxidation of the grain boundaries.

In conclusion, annealing of n-type $BaTiO_3$ ceramics in vacuum or reducing atmosphere causes degradation of the PTCR effect. This observation has prompted several authors [3, 2, 150, 290] to attribute the in-gap interface electron states of the Heywang model to chemisorbed oxygen. To clarify this hypothesis, we studied the effect of atmosphere on n-doped $BaTiO_3$ sintered at various P_{O_2} followed by annealing in air. Our results show that formation of the PTCR properties occurs at much higher temperatures than expected in the frame of the oxygen chemisorption model. A substantial PTCR effect is achieved in ceramics sintered in reducing atmosphere only after prolonged annealing in air at temperatures as high as 1200 – 1250 °C. This observation suggests that the PTCR effect in $BaTiO_3$ ceramics is associated with grain boundary segregation of cation vacancies and oxidation rather than chemisorption of oxygen.

Chapter 6

Thermoelectric power, Hall effect and mobility

6.1 Introduction

Although n-type $BaTiO_3$ has been studied for more than four decades [276], there are still a number of questions which require explanation. Among them are the chemistry of intrinsic and extrinsic defects [296, 76, 71, 284], valence band structure [107, 110], electron transport [146], and the PTCR effect [152]. The most comprehensive investigations of the electronic properties of $BaTiO_3$ were performed at temperatures $T > 25$ °C, being inspired by the challenges of the resistivity anomaly or PTCR (positive temperature coefficient of resistivity) effect [1, 155, 3, 297, 298]. One of the fundamental questions regarding the electron transport is whether the charge carriers in $BaTiO_3$ are small polarons or conduction band electrons [146]. Despite the accumulating evidence of the small polaron transport in $BaTiO_3$ [299], the most accepted model of the PTCR effect employs the conduction band electron formalism [1]. Few papers have addressed the electron transport properties of low temperature phases of $BaTiO_3$. Table 2.1 summarizes the data about the drift and Hall mobilities, as well as the thermal activation energies of mobility and conductivity in $BaTiO_3$.

Gillot et al. [130] studied the conductivity of the Nb-doped $BaTiO_3$ single crystal in the temperature range 40 - 420 K. The authors found that the conductivity behaviour of the rhombohedral phase (below 200 K) obeys the polaronic-type mechanism with the overall activation energy of conductivity of E_σ=0.092 eV. Iguchi et al. [129] investigated La and Gd doped $BaTiO_3$ ceramics. They reported an activation energy for conductivity of 0.070 ±0.002 eV in the rhombohedral phase. The authors [129] observed an absorption peak in the dielectric loss tangent at temperatures below 100 K. This peak was attributed to dielectric relaxation due to small polaron hopping. Based on these data, Iguchi et al. [129] proposed that the dominant conduction in n-type $BaTiO_3$ is due to hopping of non-adiabatic small polarons.

Thermoelectric power is an important complementary technique to conductivity measurements. It allows us to evaluate the concentration of the charge carriers and their drift mobility. This technique has been employed for n-type $BaTiO_3$ single crystals above room temperature [78, 144, 139]. Anomalous behaviour of thermopower in PTCR $BaTiO_3$ was reported by Tennery and Cook [159] and Michenaud et al. [160] who observed a change from n- to p-type conductivity at the Curie temperature, T_C. In contrast to previous authors, the thermoelectric power of PTCR $BaTiO_3$ measured by Saburi [276] showed n-type conductivity above and below T_C.

Berglund and Baer [14] measured the Hall effect and thermoelectric power of single domain $BaTiO_3$ single crystal in the 20 - 126 °C range. They explained the electron transport properties of $BaTiO_3$ in terms of conduction band electrons with a large electron-phonon coupling. To the best of our knowledge, there are no data on low temperature measurements of thermopower and Hall effect in $BaTiO_3$ single crystals or polycrystalline ceramics.

In this section the study of the Hall effect, thermoelectric power, and resistivity of $BaTiO_3$ in the temperature range of 40 – 300 K is reported. It was found that except for heavily reduced ceramics, the activation energies of conductivity of single crystal and polycrystalline grain bulk have similar values (i.e., $E_\sigma \approx 0.092$ eV) in the rhombohedral phase. Oxidation leads to an increase in the activation energy of grain boundary conductivity, while grain bulk values remain unchanged. There is a significant difference in temperature dependence of thermoelectric power of single crystal and polycrystals. Anomalous behaviour of thermopower at the rhombohedral to orthorhombic phase transition of $BaTiO_3$ polycrystals is reported for the first time. A correlation between the Hall constant and conductivity suggests that below room temperature, the conductivity follows the change in the concentration of the mobile charge carriers. It was found that drift and Hall mobilities in rhombohedral and orthorhombic phases decrease with temperature which cannot be explained in the frame of the the small polaron model.

6.2 Experimental

Two nominally undoped $BaTiO_3$ single crystals provided by Deltronic Crystal Industries, Inc. and MTI were used in this study. These crystals were annealed at $P_{O_2}=10^{-15}$ atm and 1380 °C for 2 hours. Polycrystalline samples of $Ba_{0.996}Y_{0.004}TiO_3$ were prepared according to the mixed oxide method. No sintering additives such as SiO_2, Al_2O_3 or excess TiO_2 were used. Samples were sintered at 1380 °C and oxygen partial pressures of 10^{-17} and 10^{-15} atm. The oxygen partial pressure was fixed by a controlled ratio of flowing CO/CO_2 gas. The density of the polycrystalline sample was about 92% and the average grain size was 50 μm. X-ray analysis confirmed the existence of a single-phase $BaTiO_3$. In order to investigate the effect of oxidation on the activation energy of conductivity, the samples sintered at 10^{-15} atm were annealed in air at 800 °C, 1000 °C, and

1200 °C for 2 hours. The complex impedance of ceramics was measured with a Solartron 1260 Impedance/Gain-Phase Analyzer in the frequency range of 1 Hz - 32 MHz. Detailed information about impedance measurements can be found in Chapter 4.1. The resistivity of the single crystal and the low-resistivity polycrystalline samples were measured using a four-probe technique. The thermoelectric power was measured in the 40-320 K range using an apparatus described in Chapter 4.1. Hall effect was measured in the magnetic field of 5 Tesla using a Quantum Design PPMS apparatus.

6.3 Results and discussion

6.3.1 Single crystal

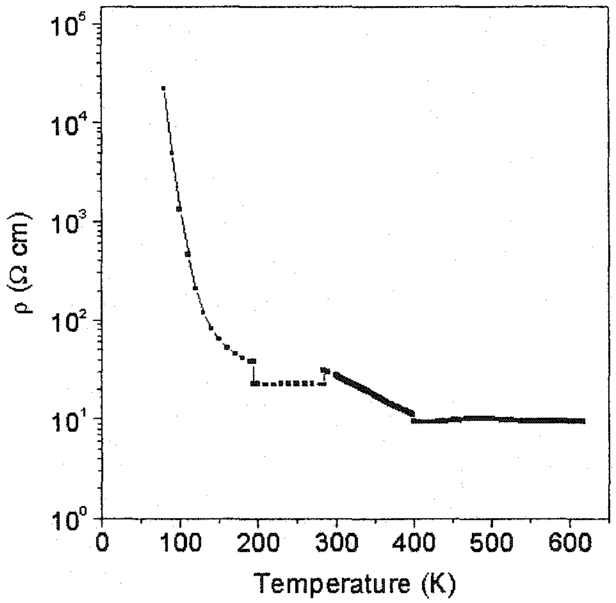

Figure 6.1: Temperature dependence of resistivity of $BaTiO_3$ single crystal

The temperature dependence of resistivity of single crystal $BaTiO_3$ is shown in Fig. 6.1. The features of the ρ versus T plot are very similar to those reported by Gillot et al. [130]. In the rhombohedral phase ($T \leq 200$ K), resistivity decreases with temperature with an activation energy of 0.093 eV. In the orthorhombic phase, ($200 \text{ K} < T < 285$ K), the resistivity is independent of temperature. In the tetragonal phase, ($285 \text{ K} < T < 395$ K), ρ decreases with temperature with activation energy of 0.100 eV. The cubic phase, ($T > 395$ K), shows nearly temperature independent resistivity. At the rhombohedral to orthorhombic phase transition ($T=190$ K), a sharp decrease of ρ by a factor of 2 is observed similar to the results of Gillot et al. [130]. At 285 K, ρ increases step-like by a factor of 1.5, again in agreement with the results of the previous authors [130]. In the cubic phase, resistivity is nearly independent of temperature up to 600 K.

In trying to explain the temperature dependence of conductivity in the rhombohedral phase at 60 - 200 K, Iguchi et al. [129] and Gillot et al. [130] invoked the small polaron model. In this model, the main contribution to conductivity which is given by

$$\sigma = ne\mu \tag{6.1}$$

comes from the temperature activated mobility of free small polarons:

$$\mu = \frac{ea^2J^2}{\hbar k_BT\sqrt{4E_Ak_BT/\pi}}exp\left(-\frac{E_A}{k_BT}\right) \tag{6.2}$$

where a is the distance between two adjacent Ti ions, E_A is the thermal activation energy of a small polaron hop, and J is the overlap integral of the wavefunctions of the Ti ions. In fact, E_A is the sum of the hopping energy E_H, disorder energy E_D, and the small polaron activation energy E_0 (not to be confused with the activation energy of small polaron hopping).

When the small polaron model is applied to low temperature conductivity, it is important to know whether the activation of conductivity is due to the mobility term or due to the increase in concentration of the charge carriers. As was found by Iguchi [129], the small polaron activation energy, E_0 is of the order of 0.002 eV which implies that the small polarons are already unbound at temperatures above 20 - 30 K. To clarify this finding, we measured the Seebeck coefficient, S, in the 90 - 270 K range. The results (Fig. 6.2) show that the Seebeck coefficient is temperature independent in the orthorhombic phase. However, in the rhombohedral phase, the thermopower increases with decreasing temperature. Neglecting the spin degeneracy, the Seebeck coefficient within the small polaron model is related to the concentration of the charge carriers via Heikes formula [300]

$$s = -\frac{k_B}{e}\left(ln\frac{1-c}{c} + A\right) \tag{6.3}$$

where c and (1-c) are the relative proportions of the two different oxidation states present, namely Ti^{3+} and Ti^{4+} and A is the transport term which depends on the mechanism of chage transport. Using the Austin and Mott estimate of A (i.e., $A \approx E_H/20k_BT$, where E_H is the thermal hopping energy of the small polaron [146]), the concentration of free small polarons, n, in rhombohedral and orthorhombic phases was calculated assuming E_H=0.09 eV. The results are presented in Fig. 6.3. There is a general agreement between $\sigma(T)$ and $n(T)$ dependencies. One can observe a step-like increase in $n(T)$ at T = 190 K which is reflected in a similar step-like increase of conductivity. However, there is significant difference in the activation energy of small polaron concentration, E_0 = 0.278 eV and conductivity, E_σ = 0.093 eV. It may be assumed that thermoelectric power measurements overestimate the value of charge carrier concentration mainly due to the uncertainty in the A term at low temperatures. It can be speculated that the Seebeck coefficient could be enhanced in the rhombohedral phase by carrier-induced vibrational softening similar to that proposed by Emin

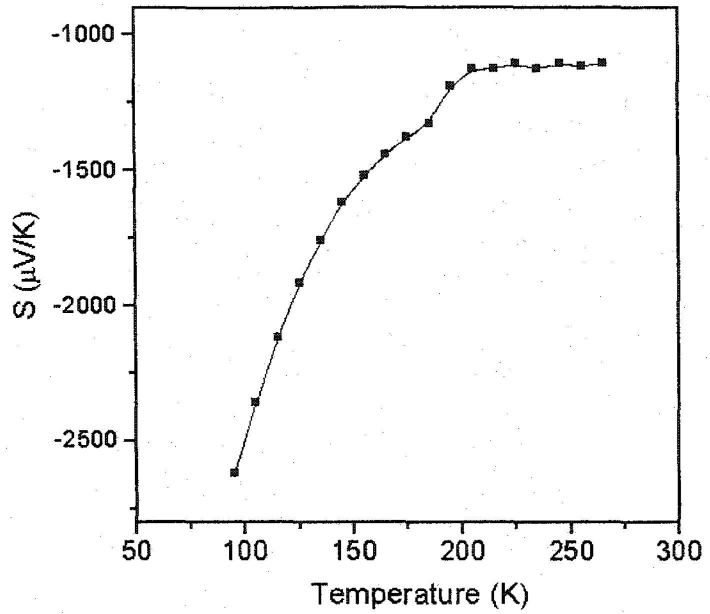

Figure 6.2: Temperature dependence of thermoelectric power of a $BaTiO_3$ single crystal

for boron carbides [301]. As a result, the drift mobility (Fig. 6.4) estimated from Eq. 6.2 decreases with temperature and shows anomalously high values at low temperatures which disagree with a small polaron-type behaviour. In the orthorhombic phase, both conductivity and drift mobility are nearly independent of temperature. The value of the drift mobility calculated from the Seebeck coefficient approaches 5 $cm^2V^{-1}s^{-1}$ at 250 K. This value, however, might be considered too high for small polaron hopping. Other authors reported μ_D in the range of 0.1 to 0.6 $cm^2V^{-1}s^{-1}$ at 300 K [146]. Recently Bernasconi et al. [16] reported large anisotropy of drift mobility in $BaTiO_3$ and $KNbO_3$. In $BaTiO_3$, they found for holes $\mu_a/\mu_c = 19.6$, where μ_a and μ_c are drift mobilities in a and c directions in tetragonal $BaTiO_3$. It is possible that significant spread of the drift mobility values in $BaTiO_3$ reported in literature can be partially explained by the anisotropy of μ_D.

Hall effect was measured on a single crystal purchased from MTI. For this crystal, the activation energy of conductivity in rhombohedral phase was similar to the crystal from Deltronic Crystal Industries, Inc. (i.e., $E_\sigma = 0.090$ eV). We performed Hall effect measurements of this crystal in the 120 K - 300 K temperature range. The data are presented in Figs. 6.5 and 6.6. Due to the low signal to noise ratio, the only reliable data were obtained on the rhombohedral phase. Fig. 6.5 shows that the Hall constant decreases with temperature in the rhombohedral phase, indicating an increase in concentration of the charge carriers with an activation energy of 0.130 eV.

The temperature dependence of the Hall mobility calculated from the resistivity and Hall constant is presented in Fig. 6.6. Hall mobility decreases with temperature in rhombohedral phase. At 120 K and 220 K, Hall mobility equals ca. 9 cm^2/Vs and 2 cm^2/Vs respectively. This is in rather good

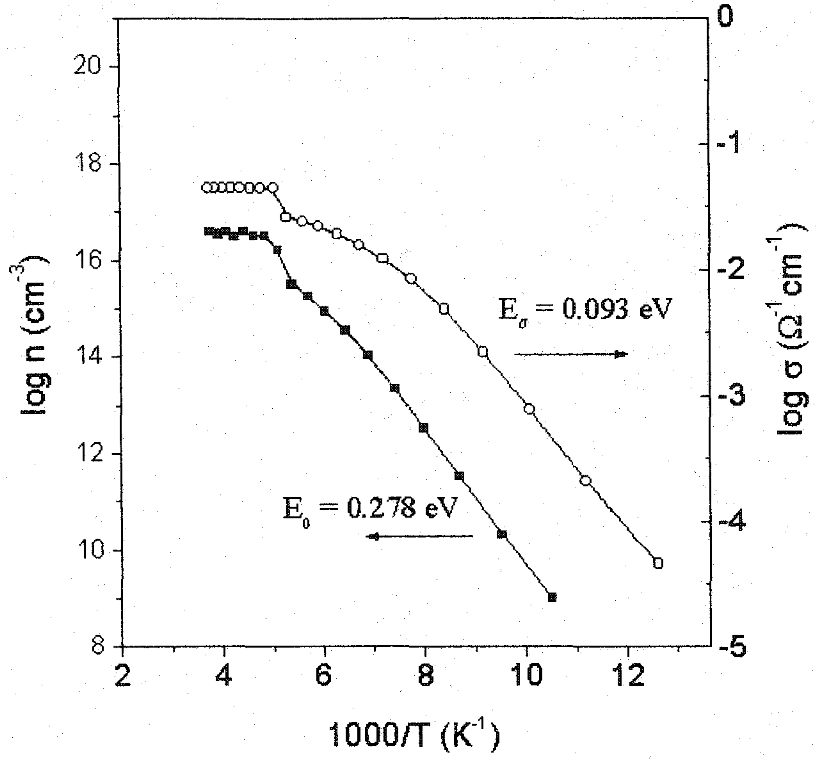

Figure 6.3: Temperature dependence of n and σ in rhombohedral and orthorhombic phases

agreement with the room temperature value of 1.2 cm^2/Vs reported by Berglund and Baer [14]. Both Hall effect and thermoelectric power measurements suggest that concentration of the charge carriers increases with temperature in the rhombohedral phase. This increase may be attributed to the thermal ionization of oxygen vacancies which behave as donor impurities in reduced, undoped $BaTiO_3$. As compared with thermoelectric power, Hall effect provides better agreement between the activation energy of conductivity and charge carrier concentration.

Hence, one may conclude that in single crystal $BaTiO_3$, the increase in conductivity in the rhombohedral phase occurs due to the increase in concentration of charge carriers rather than temperature activation of drift mobility. In other words, the electron transport occurs via a conduction band rather than by a small polaron hopping. However, in the wake of the conduction band model, it is unclear why the conductivity increases with temperature in the tetragonal phase, where all charge carriers are already activated. It can be proposed that the change from conduction band transport to small polaron hopping occurs at the orthorhombic to tetragonal phase transition due to the slight increase in the lattice constants of $BaTiO_3$.

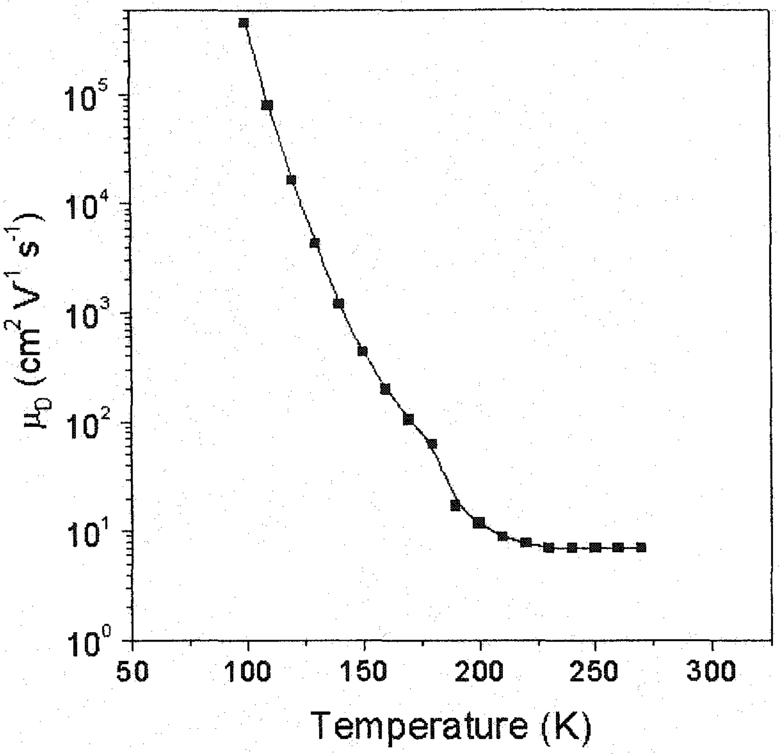

Figure 6.4: Temperature dependence of drift mobility in rhombohedral and orthorhombic phases of single crystal $BaTiO_3$.

6.3.2 $BaTiO_3$ sintered at $P_{O_2}=10^{-17}$ atm

Fig. 6.7 shows the temperature dependence of resistivity of $Ba_{0.996}Y_{0.004}TiO_3$ sintered at $P_{O_2}= 10^{-17}$ atm. The resistivity of this sample was measured with a four-probe technique. Due to its low resistivity, it was imposible to measure the complex impedance of this sample in a wide temperature range. Only one spectrum was obtained at 77 K where the total resistivity of the sample had a value of 11 Ω cm (see Fig. 5.13). As revealed in Fig. 6.7, the resistivity of the sample sintered in strongly reducing conditions demonstrates a number of interesting features. First of all, ρ versus T dependence shows a hysteresis associated with the rhombohedral-to-orthorhombic phase transition at 190 K. The resistivity exhibits metallic-type behaviour (i.e., ρ rising with temperature) at temperatures below 100 K. In the temperature interval of 100 - 190 K, ρ gradually decreases by an order of magnitude reaching a minimum of 1 Ω cm at 200 K. An increase of resistivity by a factor of 3 is observed upon passing through the phase transition at 190-200 K. Finally, a small resistivity drop is observed at the orthorhombic-to-tetragonal phase transition at 260 K. Abrupt changes in ρ at the 190 K and 260 K phase transitions in $BaTiO_3$ have been reported earlier by several authors [140, 159, 130]; however, a change from semiconducting to metallic-type behaviour in n-type $BaTiO_3$

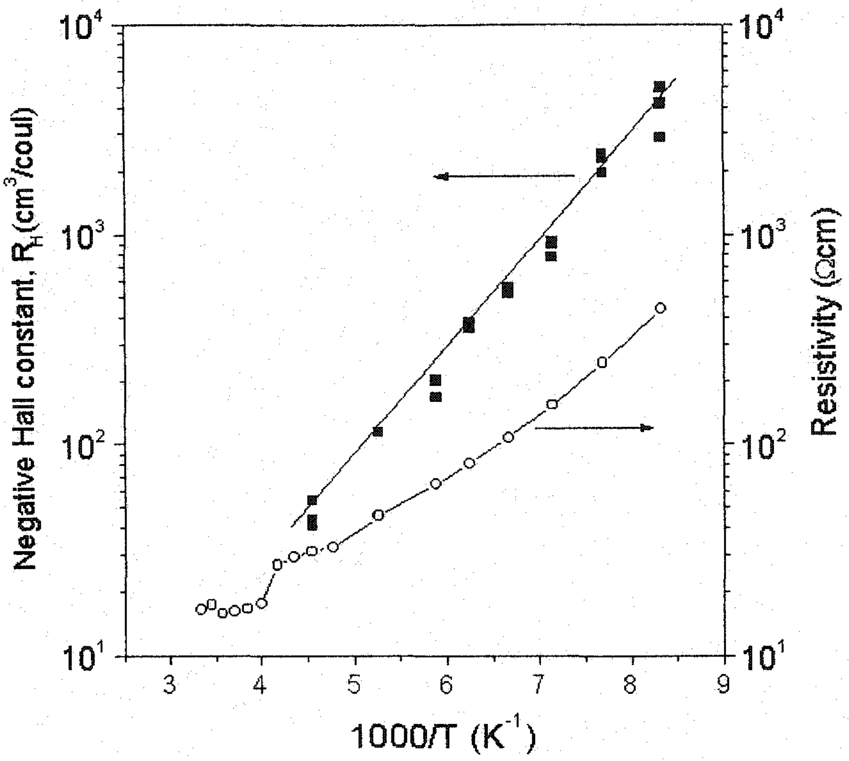

Figure 6.5: Temperature dependence of Hall constant and resistivity of single crystal $BaTiO_3$.

below 100 K has not been observed before. This indeed, is quite unusual behaviour which is difficult to explain in terms of a small polaron model. Normally, for small polaron hopping transport, one would expect an increase in ρ with decreasing temperature. We consider that this metallic-like ρ versus T behaviour is a result of the high concentration of the charge carriers in heavily reduced $BaTiO_3$. Theoretical treatment of the problem of polarons in heavily doped semiconductors was given by Mahan [302]. It was shown that in a many electron system interacting with a phonon system, the electron-electron interactions screen the electron-phonon interactions. At a certain concentration of charge carriers, this screening considerably weakens the polaron binding energy, E_p, which is twice the polaron hopping energy, E_H [133]. It was suggested by Mahan [302] that metallic-like electrical properties may be observed in such heavily doped crystals at low temperatures. The mobility of polarons in such a system is no longer an activated process. In fact, this system no longer behaves as a polaron model, but rather as a degenerate free electron gas. It is quite possible that this scenario is realized in the strongly reduced sample in Fig. 6.7.

The thermoelectric power of $Ba_{0.996}Y_{0.004}TiO_3$ sintered at $P_{O_2}= 10^{-17}$ atm is shown in Fig. 6.8. The negative Seebeck coefficient indicates that the major charge carriers are electrons. At temperatures below 100 K, the thermopower demonstrates metallic-type behaviour with a Seebeck coefficient slowly approaching zero as the entropy of the crystal decreases. An anomalous increase

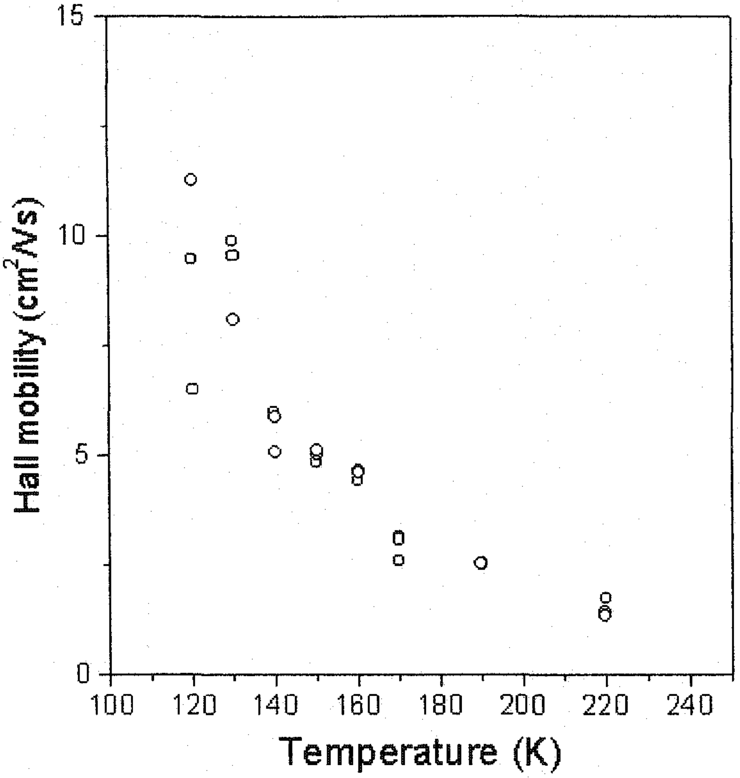

Figure 6.6: Temperature dependence of Hall mobility of single crystal $BaTiO_3$.

in Seebeck coefficient by a factor of 5 is observed in the interval of 190 - 250 K. Using Eq. 6.3 and assuming $A = 0$, the value of Ti^{3+} at 200 K and 250 K was estimated to be 1.4×10^{21} cm^{-3} and 2.6×10^{19} cm^{-3} respectively. Although this corresponds to a decrease in electron concentration by a factor of 50, the resistivity of the sample increased only by a factor of 3 (see Fig. 6.7). Obviously, this disagreement cannot be explained only in terms of conductivity change, unless an increase in the drift mobility is assumed at the rhombohedral to orthorhombic phase transition. One wonders if such a large change in concentration of the charge carriers at T=200 K could be confirmed by other techniques, for example, by a change of the polaron plasmon frequency in the electron energy loss spectrum. At this point it is difficult to explain the reason for the decrease in electron concentration with increasing temperature. It is interesting that an anomalous increase in Seebeck coefficient at 200 - 250 K was observed only in polycrystals and not in reduced $BaTiO_3$ single crystals (see Fig. 6.2). At this stage, one can only speculate whether specific point defects with fairly large concentrations could be responsible for trapping of electrons at the temperature of the phase transition.

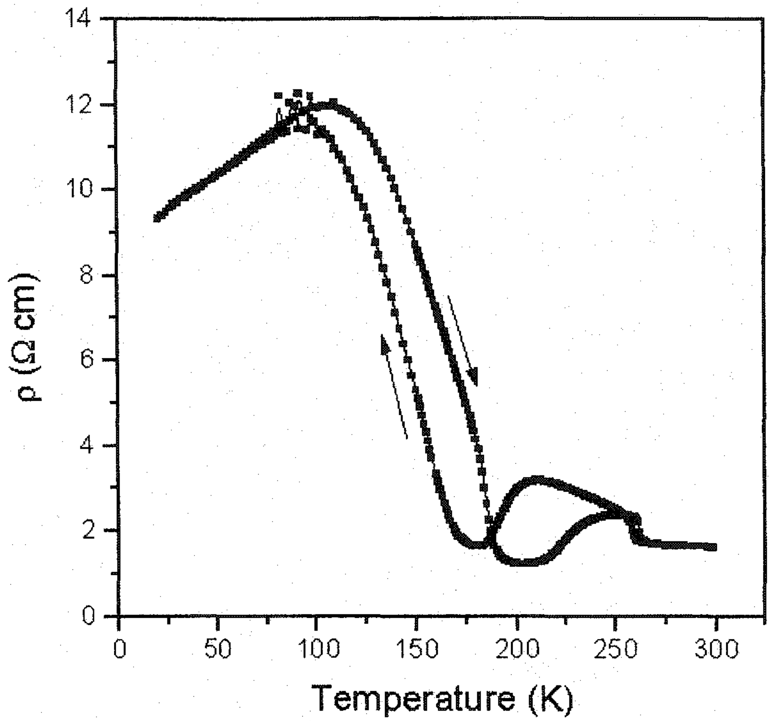

Figure 6.7: Temperature dependence of resistivity of the $Ba_{0.996}Y_{0.004}TiO_3$ sample sintered at P_{O_2}= 10^{-17} atm. The resistivity was measured in both cooling and heating directions. These directions are indicated by arrows.

6.3.3 $BaTiO_3$ sintered at $P_{O_2}=10^{-15}$ atm

Ceramics sintered at higher oxygen pressure e.g., $P_{O_2}=10^{-15}$ atm showed resistivity dependence typical of semiconductors (Fig. 6.9). The resistivity gradually decreases with temperature and no discontinous changes of resistivity were observed at the phase transitions. Thermoelectric power of the sample sintered at $P_{O_2}=10^{-15}$ atm is shown in Fig. 6.10. Similar to the heavily reduced sample, thermoelectric power increased by a factor of 3.5 in the temperature interval of 200 - 240 K corresponding to the temperature of the rhombohedral-orthorhombic phase transition. However, as shown in Fig. 6.9, the resistivity of the sample did not respond to an increase in the thermopower. In the temperature range of 80 - 150 K, thermoelectric power decreases with temperature, indicating an increase in the concentration of the mobile charge carriers. In the 250 - 300 K range, the thermopower slightly decreases, which again suggests an increase in the electron concentration. From resistivity and thermopower data, the drift mobility of this sample was calculated. The results are shown in Fig. 6.11. Providing that thermopower gives the correct estimate of the charge carrier concentration above 240 K, the drift mobility is calculated to be in the range of 0.15 - 0.22 $cm^2V^{-1}s^{-1}$. At lower temperatures, μ_D decreases significantly because of the drastic change in thermopower, which leaves

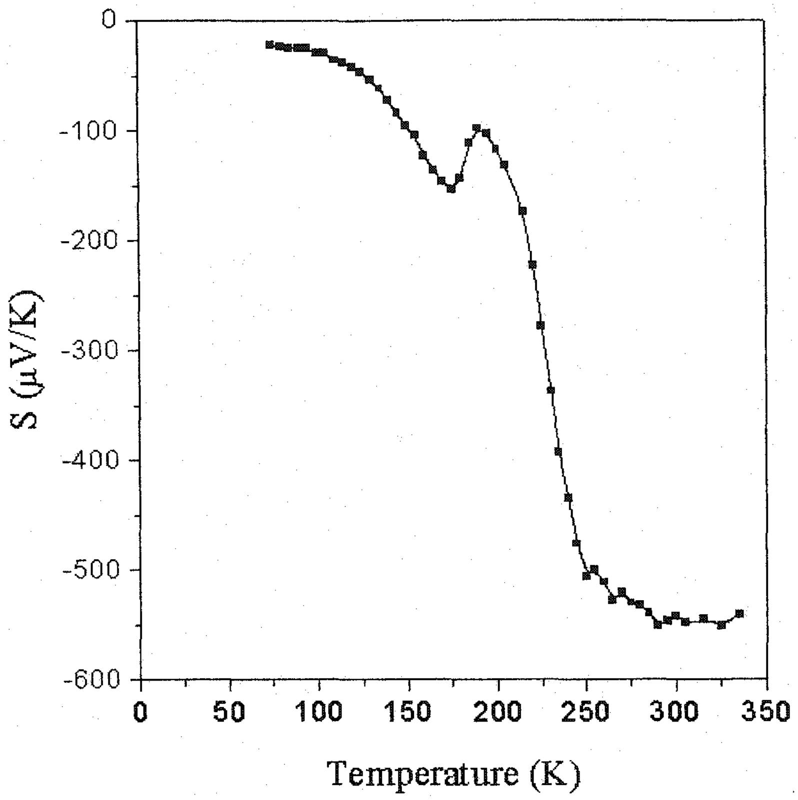

Figure 6.8: Temperature dependence of thermoelectric power of the $Ba_{0.996}Y_{0.004}TiO_3$ sample sintered at $P_{O_2}= 10^{-17}$ atm.

our values of μ_D below 240 K in doubt. Nevertheless, based on the thermopower data, the drift mobility is temperature activated, which seems to be in agreement with the small polaron model. However, measurements of the Hall effect presented below, provided quite different results.

Fig. 6.12 shows temperature dependence of the Hall constant, R_H, and resistivity. A very important result is that the temperature dependence of these two variables is very similar. According to Seeger [303], the Hall constant is given by

$$R_H = \frac{r_H}{en} \tag{6.4}$$

where $r_H \approx 1$ is the Hall factor and n is the concentration of the free charge carriers. Hence, it is obvious from Fig. 6.12 that the change in resistivity at 100-300 K is attributed to the change in the concentration of the charge carriers. Another important result is that Hall measurements do not reveal any drastic change in the concentration of the charge carriers at 200 - 240 K, in contrast to thermopower data. From the Hall and resistivity data the temperature dependence of the Hall mobility was calculated. The results are shown in Fig. 6.13. The room temperature value of the Hall mobility ($\mu_H \approx 0.3$ cm^{2}V^{-1}s^{-1}) is in good agreement with earlier published data $0.2 \leq \mu_H \leq$

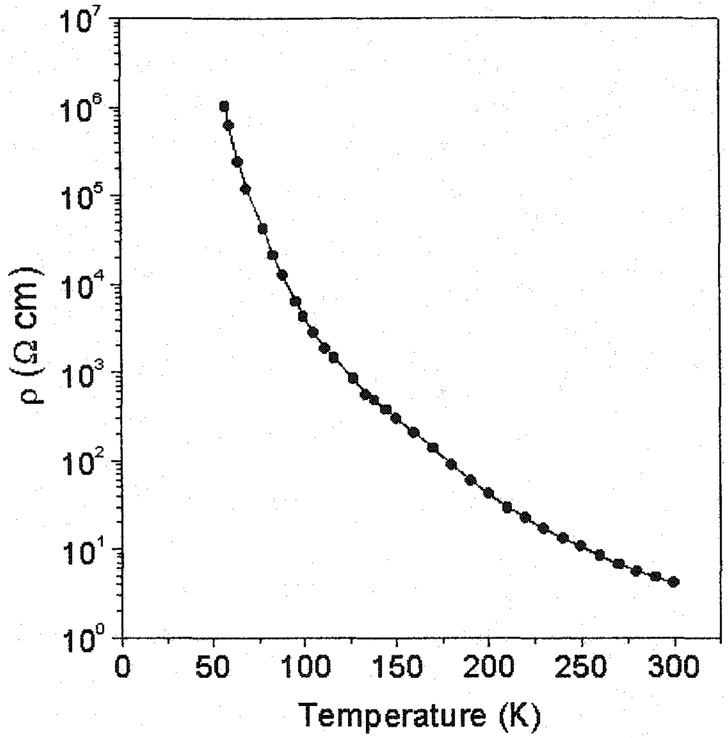

Figure 6.9: Temperature dependence of resistivity of the $Ba_{0.996}Y_{0.004}TiO_3$ sample sintered at $P_{O_2}=10^{-15}$ atm.

1.2 [14]. The temperature dependence of the Hall mobility below room temperature has not been studied before. Our results show that below room temperature, Hall mobility increases to 0.8 - 1.2 $cm^2V^{-1}s^{-1}$ at 170 K and than decreases to 0.6 $cm^2V^{-1}s^{-1}$ at 100 K.

It is worth mentioning that similar values of the Hall and drift mobilities were one of the strongest arguments for the band conduction model in $BaTiO_3$ [14, 146]. This has been resolved by Emin's 'correlated small polaron hopping' model [147] in which drift and Hall mobilities do not have to differ significantly. A close correlation of the Hall constant and conductivity reported in this work obviously casts new doubts about applicability of the small polaron model in $BaTiO_3$ below 300 K. Additional investigation of the Hall and Seebeck effects in high quality $BaTiO_3$ single crystals would be neccessary to draw an unequivocal conclusion about small polaron transport below 300 K. Certainly a better understanding of the kinetic transport term, A, is required in order to properly interpret the low temperature thermopower data.

In conclusion, conductivity, Seebeck and Hall effects suggest that temperature activated conductivity in $BaTiO_3$ below 300 K is due to the change in electron concentration rather than temperature activated mobility.

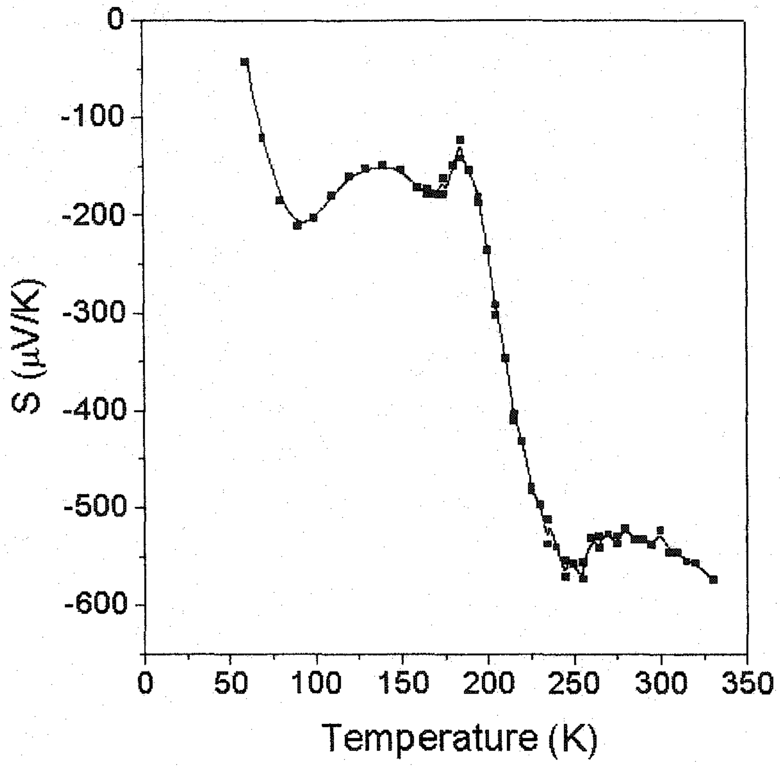

Figure 6.10: Temperature dependence of thermoelectric power of the $Ba_{0.996}Y_{0.004}TiO_3$ sample sintered at $P_{O_2}= 10^{-15}$ atm.

6.3.4 Activation energy of grain bulk and grain boundary resistance

Due to the higher resistivity of samples sintered at $P_{O_2} = 10^{-15}$ atm, it was possible to apply complex impedance analysis to investigate the grain bulk and grain boundary properties. Fig. 6.14 shows an example of complex impedance spectra obtained at different temperatures for a sample sintered at $P_{O_2} = 10^{-15}$ atm. It is obvious from Fig. 6.14 that $BaTiO_3$ sintered at low P_{O_2} is electrically inhomogeneous. Two arcs representing grain bulk and grain boundary impedances are clearly resolved in the spectra. Assignment of the high frequency arc to the grain bulk impedance is confirmed by dielectric constant measurements shown in Fig. 5.15. The real part of the dielectric constant at high frequencies approaches ε' of undoped $BaTiO_3$ (Fig. 5.15). These are the first measurements of grain bulk and grain boundary impedances of $BaTiO_3$ sintered at low P_{O_2}. It has long been accepted that n-doped $BaTiO_3$ polycrystals sintered in reducing atmosphere have low grain boundary resistance since no PTCR effect is observed for these type of ceramics. As revealed by Fig. 6.14, this is not the case, i.e., the ceramic does contain resistive grain boundaries. Assuming that the grain boundary (GB) layer consists of $BaTiO_3$ (i.e., no second phase present), the thickness

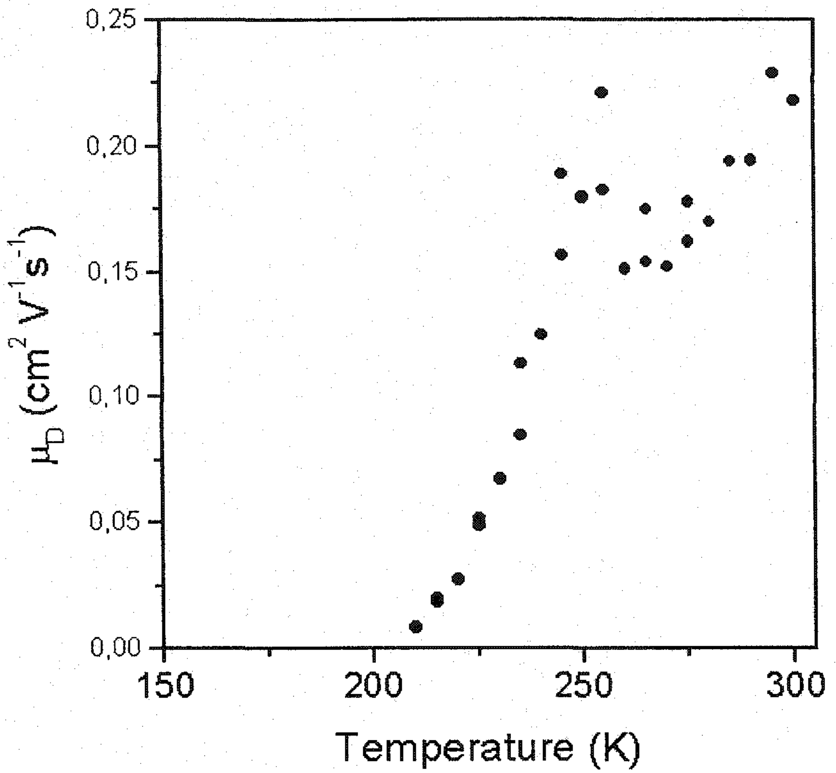

Figure 6.11: Temperature dependence of the drift mobility of the $Ba_{0.996}Y_{0.004}TiO_3$ sample sintered at $P_{O_2} = 10^{-15}$ atm.

of the GB layer, d_{GB} can be calculated as follows. The GB capacitance, C_{GB} is given by

$$C_{GB} = \frac{1}{2\pi R_{GB} f_{max}} \tag{6.5}$$

where f_{max} is the frequency of the impedance arc maxima and R_{GB} is the resistance of the GB. Then, assuming a simple brick model, d_{GB} is given by

$$d_{GB} = \frac{\varepsilon\varepsilon_0 A}{C_{GB} n} \tag{6.6}$$

where A is the area of the sample, ε is the dielectric constant of undoped $BaTiO_3$ (e.g., $\varepsilon = 400$ at 77 K), and $n = l/d$ (where l is the thickness of the sample and d is the average grain diameter). From Eq. 6.6, the thickness of the grain boundary layer, d_{GB}, of high resistance at 77 K equals 85 ± 5 nm. Regarding the nature of the grain boundary resistive layer, one should recall the defect chemistry of $BaTiO_3$ under reducing conditions [76, 71]. According to Chiang and Takagi [76], at low P_{O_2}, defects of the negative effective charge (e.g., acceptor impurities) will accumulate in the space charge region at the grain boundary. This would result in the formation of a resistive layer in the grain boundary region.

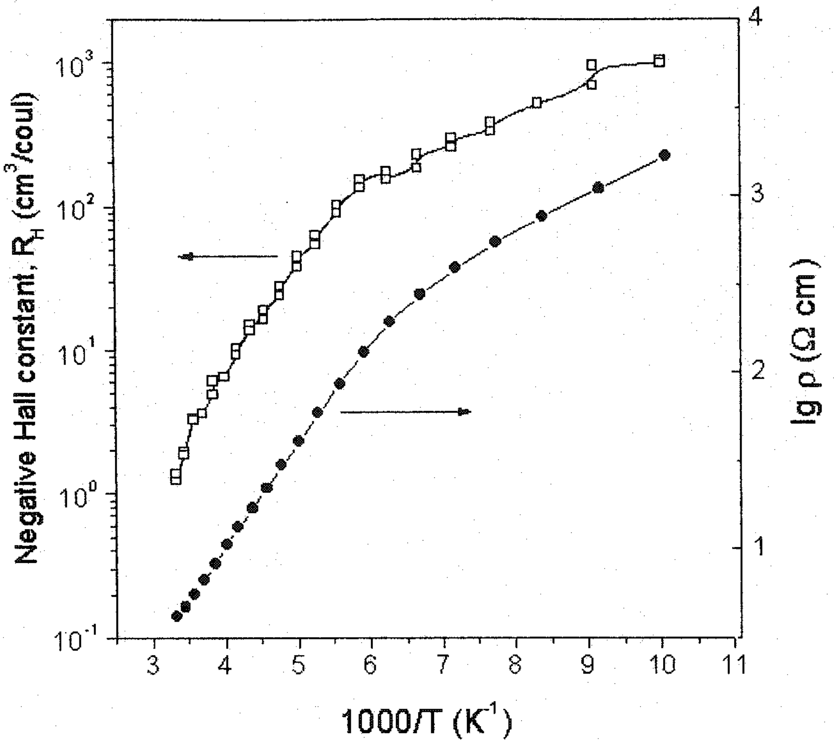

Figure 6.12: Temperature dependence of the Hall constant and resistivity of the $Ba_{.996}$ $Y_{.004}TiO_3$ sample sintered at $P_{O_2}= 10^{-15}$ atm.

The effect of oxidative annealing at 800 , 1100 , and 1200 °C on the grain bulk and grain boundary resistance of $BaTiO_3$ ceramics was investigated. The temperature dependences of the grain bulk and grain boundary resistance were obtained from the complex impedance spectra measured at different temperatures. Figs. 6.15 - 6.18 show Arrhenius behaviour of grain bulk and grain boundary resistance of the as-sintered sample and samples post-annealed in air at 800, 1100, and 1200 °C for 5 h. According to Figs. 6.15 - 6.18, both grain boundary and grain bulk resistance increases with temperature of oxidation. After the oxidation at 1100 °C, R_{GB} exceeds that of R_G in the whole temperature range of measurements. There is also another important trend in the Arrhenius plot, i.e., the activation energy of the grain bulk resistance remains essentially the same (e.g., 0.090 eV) independent of the postsinter treatment, but, the activation energy of the grain boundary resistance increases from 0.064 ± 0.002 eV for the as-sintered sample to 0.113 ± 0.002 eV for the sample oxidized at 1200 °C. The effect of oxidation on the grain bulk and grain boundary activation energies is summarized in Table 6.1.

In conclusion, $BaTiO_3$ sintered at low P_{O_2} is electrically inhomogeneous. However, due to the high conductivity of this ceramic, it was possible to resolve the grain bulk and grain boundary properties only below 200 K (i.e., in the rhombohedral phase). It was found that the activation

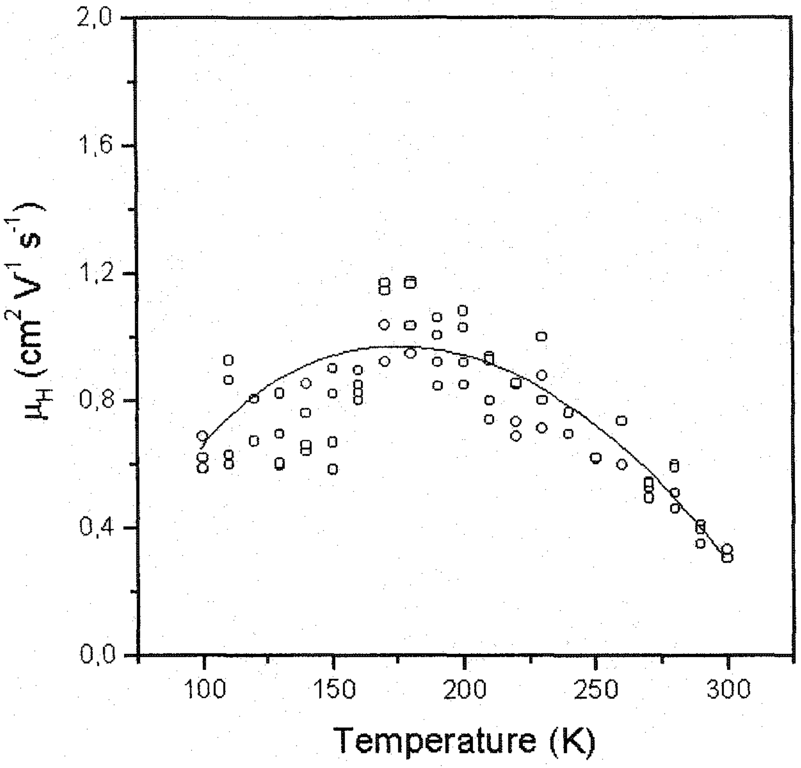

Figure 6.13: Temperature dependence of Hall mobility of the $Ba_{0.996}Y_{0.004}TiO_3$ sample sintered at $P_{O_2} = 10^{-15}$ atm.

energy of the grain bulk resistance, E_B is very close to that of the single crystal, whereas E_{GB} is sensitive to the oxidation treatment and increases from 0.064 ± 0.002 eV for the as-sintered sample to 0.113 ± 0.002 eV for the sample annealed in air at 1200 °C. It is this grain boundary resistive layer which is responsible for the PTCR effect at 120 °C.

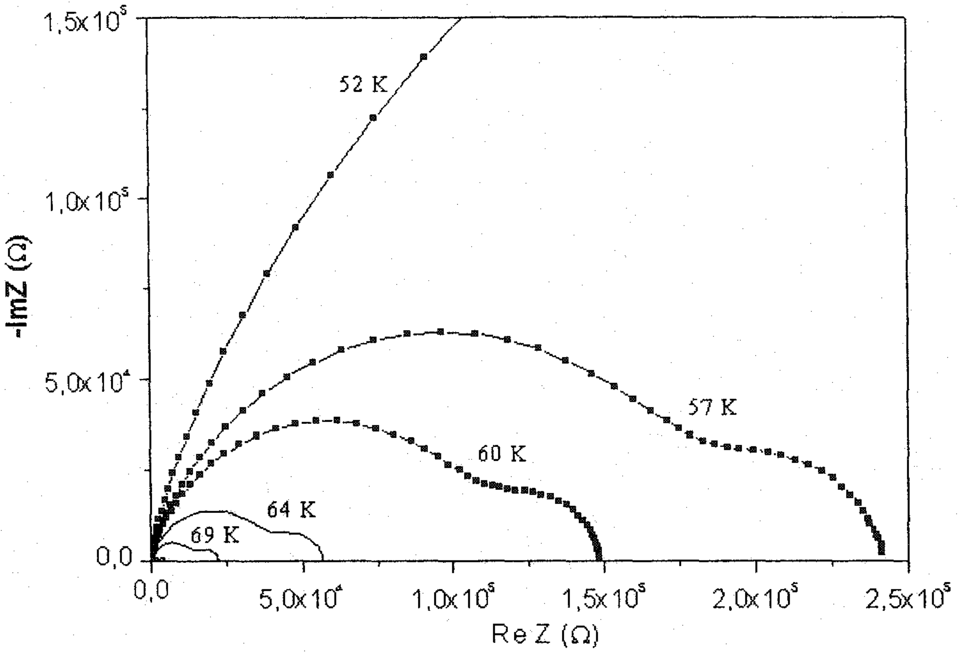

Figure 6.14: Complex impedance measured at different temperatures of $Ba_{0.996}Y_{0.004}TiO_3$ sintered at $P_{O_2}= 10^{-15}$ atm.

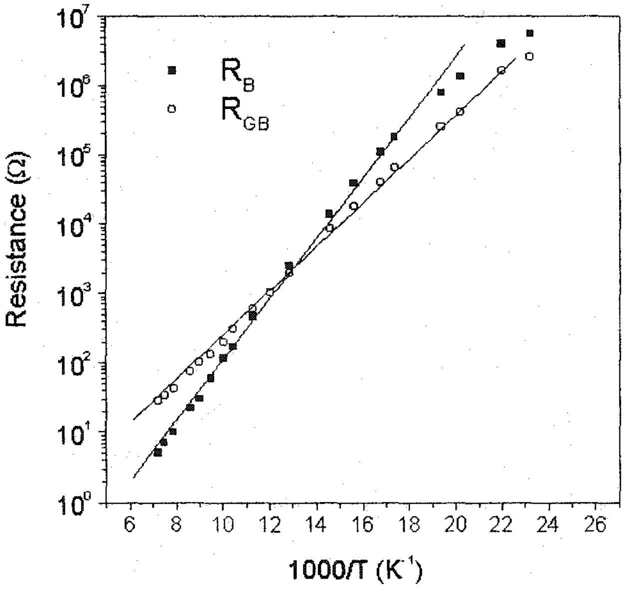

Figure 6.15: Arrhenius plot of grain and grain boundary resistivity of $Ba_{0.996}Y_{0.004}TiO_3$ sintered at $P_{O_2}= 10^{-15}$ atm.

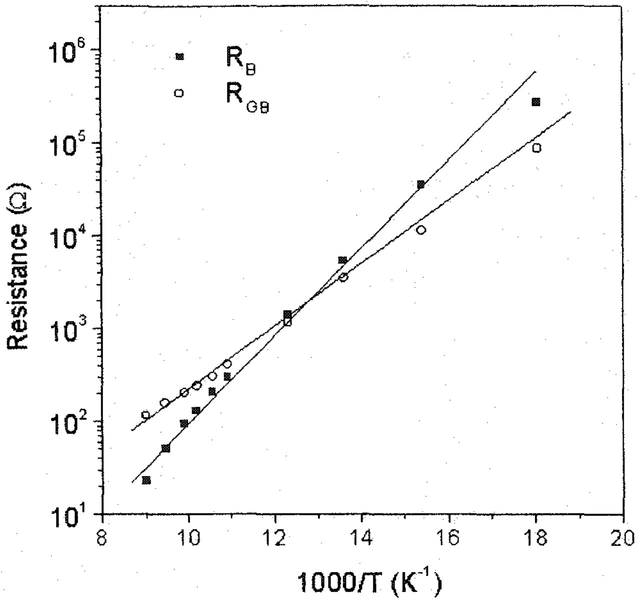

Figure 6.16: Arrhenius plot of grain and grain boundary resistivity of $Ba_{0.996}Y_{0.004}TiO_3$ sintered at $P_{O_2} = 10^{-15}$ atm and oxidized in air at 800 °C for 5 hours.

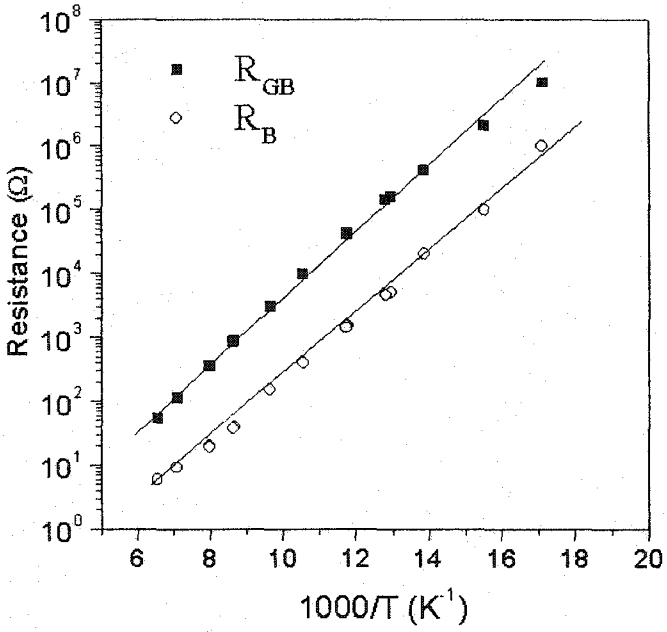

Figure 6.17: Arrhenius plot of grain and grain boundary resistivity of $Ba_{0.996}Y_{0.004}TiO_3$ sintered at $P_{O_2} = 10^{-15}$ atm and oxidized in air at 1100 °C for 5 hours.

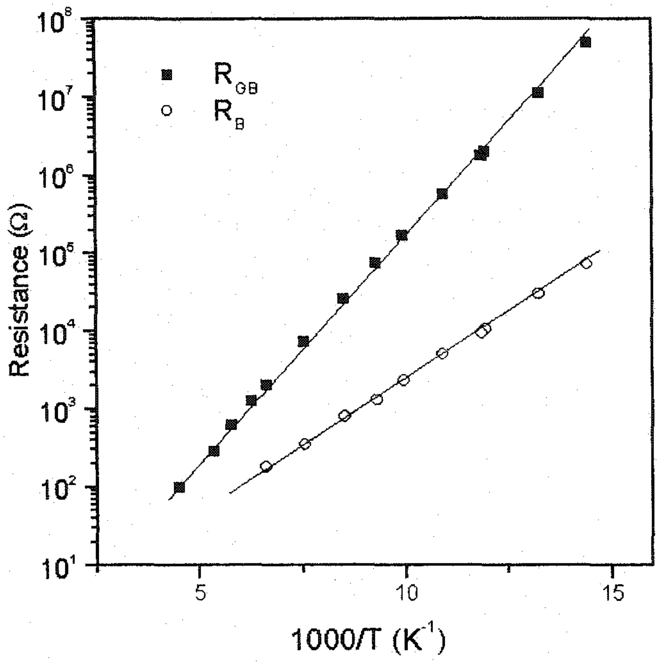

Figure 6.18: Arrhenius plot of grain and grain boundary resistivity of $Ba_{0.996}Y_{0.004}TiO_3$ sintered at $P_{O_2}= 10^{-15}$ atm and oxidized in air at 1200 °C for 5 hours.

Table 6.1: Grain bulk and grain boundary activation energy of resistance of the $BaTiO_3$ rhombohedral phase

Treatment	E_B, eV	E_{GB}, eV	Single crystal, eV
As-sintered	0.089 ± 0.002	0.064 ± 0.002	0.092 ± 0.002
800 °C	0.090 ± 0.002	0.084 ± 0.002	
1100 °C	0.090 ± 0.002	0.093 ± 0.002	
1200 °C	0.091 ± 0.002	0.113 ± 0.002	

Chapter 7

Electron paramagnetic resonance of $BaTiO_3$

7.1 Introduction

A number of paramagnetic defects and defect complexes have been found in $BaTiO_3$ by the EPR technique. In addition to understanding the foundamental defect chemistry of $BaTiO_3$, investigation of these defect centers has also been driven by applications of $BaTiO_3$ such as in photorefractive devices [304] and positive temperature coefficient of resistivity (PTCR) ceramics [5, 6].

According to the widely accepted Heywang model [1], the PTCR effect requires the presence of in-gap electron states at the grain interfaces or near the grain boundary [4]. Some of these electronic states, having unpaired spin and apparently related to the PTCR effect, have been detected and analyzed by EPR [5, 98, 6, 7]. However, the correlation of EPR features to particular defect centers is not without controversy. Table 7.1 summarizes information about several paramagnetic centers observed in single crystal and polycrystalline $BaTiO_3$.

In addition to the Mn^{2+} signal which is often observed in $BaTiO_3$ ceramics, Kutty et al. [5] and Hari et al. [98] detected EPR signals with giromagnetic constants of 1.997 – 2.00 and 1.963 – 1.97. Kutty et al. [5] assigned the g=1.997 feature to a barium vacancy and g=1.963 to a shallow donor center (e.g., Ti^{3+} associated with an oxygen vacancy). Kutty et al. [5] also observed an asymmetric signal with g=1.931 below 180 K, but did not comment on the origin of this signal. In contrast to Kutty et al., Er et al. [6] attributed the g=1.997...2.00 signal to iron impurities rather than V'_{Ba} and the g=1.963...1.97 signal to Ti^{3+} centers. Er et al. [6] have also reported that both Ti^{3+} and Fe^{3+} signals increased above T_C = 120 °C. However, observation of Ti^{3+} and Ti^{3+}-V_O signals at room temperature and above [5, 6] strongly contradicts the reports of German authors [305, 306, 94, 307]. Although, the latter investigations [305, 306, 94, 307] were performed on single

Table 7.1: g-Values of several paramagnetic centers in $BaTiO_3$

g-Value	Defect center	Temperature, K	Reference
1.907...1.936	Ti^{3+}	4.2...80	[305, 306, 94]
1.899...1.938	Ti^{3+}-V_O-K(Na)	4.2...80	[94, 307]
1.920...1.937	Ti^{3+}-V_O	10...80	[94]
1.963...1.97	Ti^{3+}	300...423	[6]
	Ti^{3+}-V_O	200...400	[5, 98]
	Ti^{3+}-Ln^{3+}	300...400	[7]
1.997...2.0043	V'_{Ba}	70...423	[5, 98]
	Fe^{3+}	300...420	[6]

crystals, the g-values of Ti^{3+} and Ti^{3+} related centers were much lower (e.g., g = 1.899...1.938) than that reported by Kutty et al. [5] and Er et al. [6]. Moreover, according to a number of authors [130, 308, 305, 306, 94, 307], EPR signals of Ti^{3+} related defects could only be observed at low temperatures (typically 4.2 – 80 K) due to the short spin-lattice relaxation time.

In the present work, the paramagnetic centers in polycrystals and single crystals prepared under oxidizing and reducing conditions were investigated.

7.2 Experimental

Samples of $Ba_{1-x}Y_xTiO_3$ with doping levels up to $x = 0.008$ and cation ratios of $0.98 \leq Ba/Ti \leq 1.05$ were prepared by conventional mixed oxide method. High purity starting reagents ($BaCO_3 >$ 99.9 %, $TiO_2 >$ 99.99 %, $Y_2O_3 >$ 99.99 % from Cerac, USA) were utilized. No sintering additives such as Al_2O_3 or SiO_2 were used. The mixtures were calcined at 1150 °C. Special care was taken to avoid contamination of the pellets with iron during pressing. For this purpose, the circumference of the pellets was cleaned from iron residue using a fine sandpaper. The pellets were sintered either in air or in a reducing atmosphere of forming gas (7% H_2 and 93 % Ar) at 1380 °C for 3 h. The phase composition was examined by a Rigaku Geigerflex Dmax II diffractometer. In order to investigate the effect of oxidation on the chemistry of paramagnetic defects, several samples sintered in reducing atmosphere were oxidized in air at 800 °C, 1000 °C, 1200 °C and 1400 °C for 5 hours. In addition to the polycrystalline samples, an undoped $BaTiO_3$ single crystal was donated by Deltronic Crystal Industries, Inc. This crystal was reduced in forming gas at 1380 °C for 2 hours. After this treatment the coloration of the crystal changed from clear transparent to blue transparent. A thin surface layer of dark blue colour was removed with fine sandpaper.

EPR studies were performed at 77 K and at 295 – 430 K. Two X-band EPR spectrometers, JEOL JES-FA 100 and Bruker EMX 8/2.7 were used. The JEOL spectrometer was equipped with Mn^{2+} standard for accurate determination of giromagnetic constant. Ceramic samples were ground into powders. For quantitative analysis, the weight of the powdered samples was kept at 50 ± 1 mg. Measurements were performed in the frequency range of 9.4 – 9.8 GHz and at the constant microwave power of 2 mW. Analysis of the resonance spectra was conducted with WIN-EPR software.

Briefly, the EPR resonance signal arises when the energy of the electromagnetic wave, $h\nu$, passing through the sample is equal to the Zeeman splitting, ΔE, of the electron levels with high and low spin configurations,

$$\Delta E = h\nu = g\mu_0 H, \tag{7.1}$$

where μ_0 is the Bohr magneton, H is a magnitude of the magnetic field, and g is the giromagnetic constant. It is this constant that is specific for each paramagnetic defect. If the sample contains atoms with nonzero nuclear magnetic spin, then additional energy splitting may occur due to their interaction with unpaired electrons.

7.3 Results and discussion

7.3.1 Signal associated with n-type conductivity in $BaTiO_3$

Polycrystalline samples sintered in a reducing atmosphere of forming gas had room temperature resistivity of ca. 2 Ω·cm. They did not show any PTCR effect at 120 °C. The EPR spectra of Y-doped $BaTiO_3$ is shown in Fig. 7.1. The EPR spectrum of undoped $BaTiO_3$ sintered in reducing atmosphere was identical to that of the Y-doped sample at 77 K and 295 K. As revealed by Fig. 7.1, the room temperature EPR spectrum of ceramics sintered in reducing atmosphere is featureless. Several paramagnetic defects are observed in the spectrum obtained at 77 K. Six sharp resonance peaks are due to the hyperfine splitting of the ^{55}Mn isotope having a nuclear spin of 5/2. A weak signal with $g = 1.974$ is associated with an intrinsic point defect which is present in undoped and donor doped $BaTiO_3$. The features of this defect and its identification are described in the next section. A broad asymmetric signal with giromagnetic constant of 1.932 is observed at 77 K only in conducting ceramics (either reduced or donor-doped). The signal with $g=1.932$ is absent in insulating ceramics sintered in air, which was either undoped or doped with more than 0.5 at% yttrium. Intensity of the $g=1.932$ signal decreases with oxidation of ceramics at high temperature in air (Fig. 7.5). It is obvious that a broad signal with $g=1.932$ is associated with n-type conductivity in $BaTiO_3$ ceramics. This signal most likely originates from several Ti^{3+}-related paramagnetic defects, such as Ti^{3+}, Ti^{3+}-V_O, Ti^{3+}-V_O-K(Na), etc. These defects, having g-value in the range of 1.899 to 1.938, have been observed and identified in single crystal $BaTiO_3$ [305, 306, 94, 307].

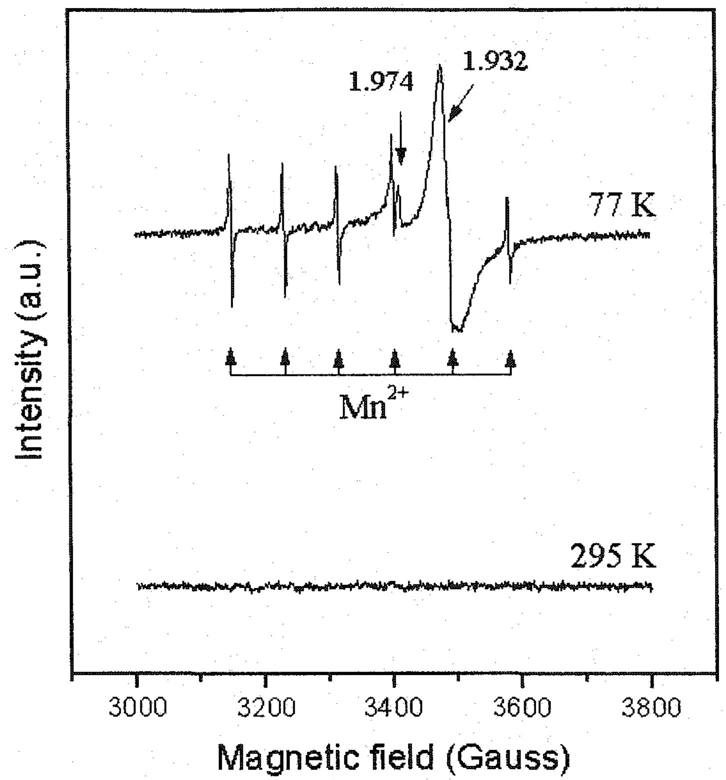

Figure 7.1: EPR spectra of $Ba_{0.996}Y_{0.004}TiO_3$ sintered in reducing atmosphere of forming gas and acquired at 77 K and at 295 K.

An analysis of the paramagnetic defects in reduced undoped single crystal was also performed in this study. In order to access the whole range of g-values, the sample was oriented with a magnetic field parallel to the [100] direction. The sample was then rotated by 360° while acquiring signals in 5° increments. This approximated the situation which occurs in polycrystals where g-values are averaged over all possible orientations. As illustrated in Fig. 7.2, several intense signals with $g \leq 2.0$ appeared in the $BaTiO_3$ EPR spectra after reduction. Also a strong, high symmetry $g = 2.006$ signal, observed in the unreduced crystal, disappeared after reduction. The g-values for several strong EPR signals observed in reduced single crystals are plotted with respect to the angle of rotation in Fig. 7.3. For two of the signals, the g-values varied in the range of 1.904 to 1.958 and for the third signal, the g-value varied in the range of 1.903 to 2.001. The latter signal is most likely attributed to the Fe - V_O or Pt-V_O complexes reported by Possenriede et al. [309]. The former two signals with averaged g-value of 1.931 are attributed to Ti^{3+} related complexes (e.g., Ti^{3+}, Ti^{3+}-Y, Ti^{3+}-V_O, Ti^{3+}-V_O-K(Na)) since their g-values are close to those reported by Scharfschwerdt et al. [94].

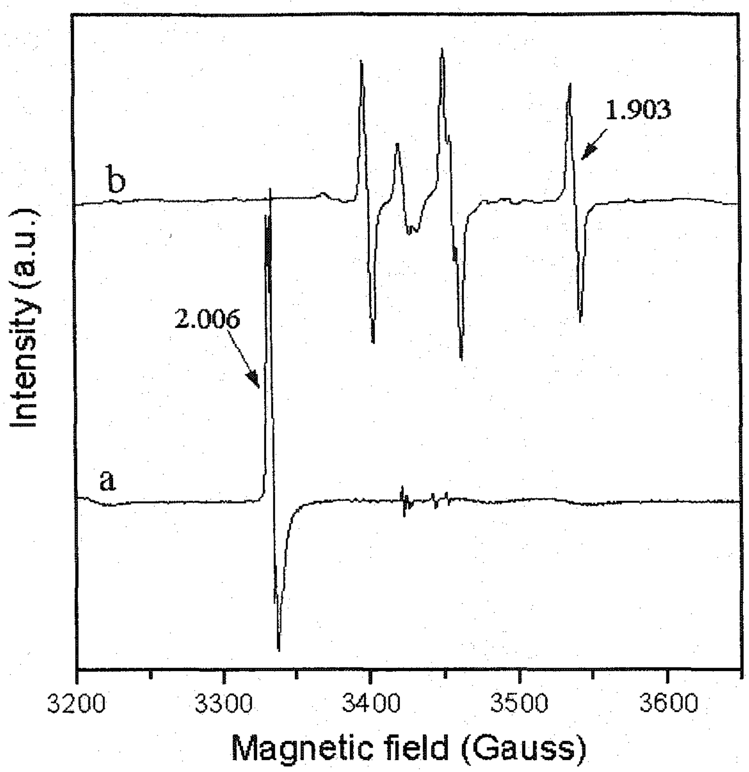

Figure 7.2: An example of EPR spectra of a) unreduced and b) reduced $BaTiO_3$ single crystals measured at 77 K. The spectra shown are only for one orientation of the crystal.

7.3.2 EPR signals with g = 1.974 and g = 2.004

In $BaTiO_3$ sintered at low oxygen partial pressure, the g = 2.004 signal is absent. A weak signal with g = 1.974 can be seen at 77 K. However, this signal is not detected in the spectra obtained above 295 K (see Fig. 7.1). Fig. 7.4 shows that the intensity of both g = 2.004 and g = 1.974 signals increases with oxidation of reduced $BaTiO_3$ ceramics in air at high temperatures. Kutty et al. [5] and Er et al. [6] assigned the g = 1.974 signal to Ti^{3+} and Ti^{3+}-V_O, respectively. If this were the case, then ceramics sintered in reducing atmosphere, having the largest concentration of Ti^{3+} and Ti^{3+}-V_O, would have the strongest intensity of the g = 1.974 signal. This is in contrast to what is observed in our samples; the g = 1.974 signal is absent from the room temperature EPR spectrum in Fig. 7.1. It only appears after oxidation of ceramics in air. Moreover, signals with g = 2.004 and 1.974 have been detected in undoped, insulating $BaTiO_3$ as will be discussed below. Hence, it can be concluded that neither g =1.974 nor g =2.004 signals are associated with the Ti^{3+} center.

The effect of oxidation on the EPR features of the polycrystalline $BaTiO_3$ rhombohedral phase is shown in Fig. 7.5. It is found that the intensity of the g = 1.932 signal decreases with oxidation temperature, whereas the intensity of the g = 1.974 and g = 2.004 signals increases with oxidation.

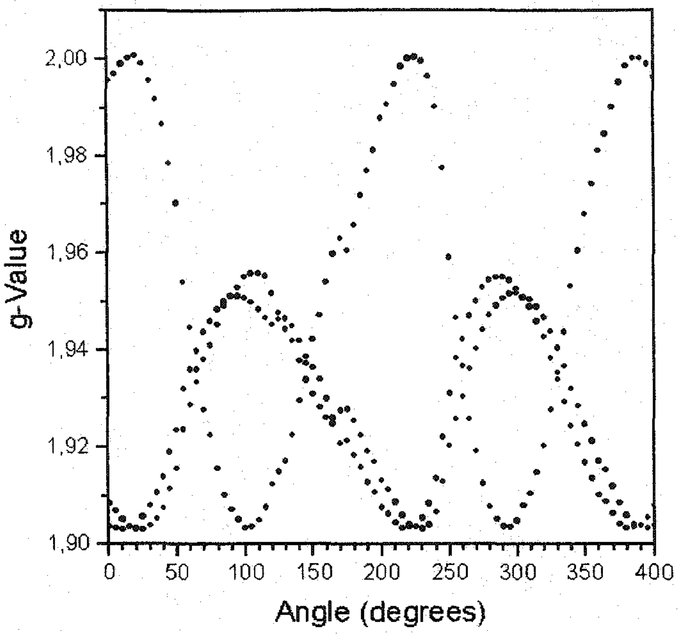

Figure 7.3: Dependence of the g-values of several paramagnetic defects of reduced $BaTiO_3$ single crystal measured at 77 K.

As revealed by Fig. 7.5, the g = 1.932 signal disappears in Y-doped ceramics oxidized at 1400 °C for 5 hours. The effect of donor dopant concentration on the intensity of EPR signals at g = 1.932, g = 1.974 and g = 2.004 was further investigated. Fig. 7.6 shows the EPR spectra of $Ba_{1-x}Y_xTi_{1.01}O_3$ ceramics with x = 0.0005, 0.002, 0.004, 0.006, 0.008 sintered in air. At low donor dopant concentration ($x \leq 0.004$), the intensity of the g = 1.932 signal increases and the intensity of the g = 1.974 and g = 2.004 signals decreases. However, at higher donor dopant concentrations, the g = 1.932 signal disappears while the g = 2.004 signal achieves the highest intensity in the rhombohedral phase.

According to the defect chemistry of $BaTiO_3$ [64], at low P_{O_2} the donor dopants and oxygen vacancies are compensated by electrons, whereas at high P_{O_2}, the excess positive charge of donor ions is compensated by cation vacancies. Subbarao and Shirane [100] and Hwang and Ho [89] suggested that both barium and titanium vacancies compensated the donors. Daniels and Härdtl [64] favored barium vacancy compensation, whereas Jonker and Havinga [95], Chan et al. [101], Millet et al. [102], and Makovec [97] proposed that at high doping levels (above 1 at%), donors were compensated by titanium vacancies.

In order to find out whether the g = 1.974 and g = 2.004 signals are related to cation vacancies, the effect of Ba/Ti ratio was studied. It was found that the g = 1.974 signal is sensitive to deviations from Ba/Ti stoichiometry. As revealed by Fig. 7.7, the g = 1.974 signal is completely suppressed

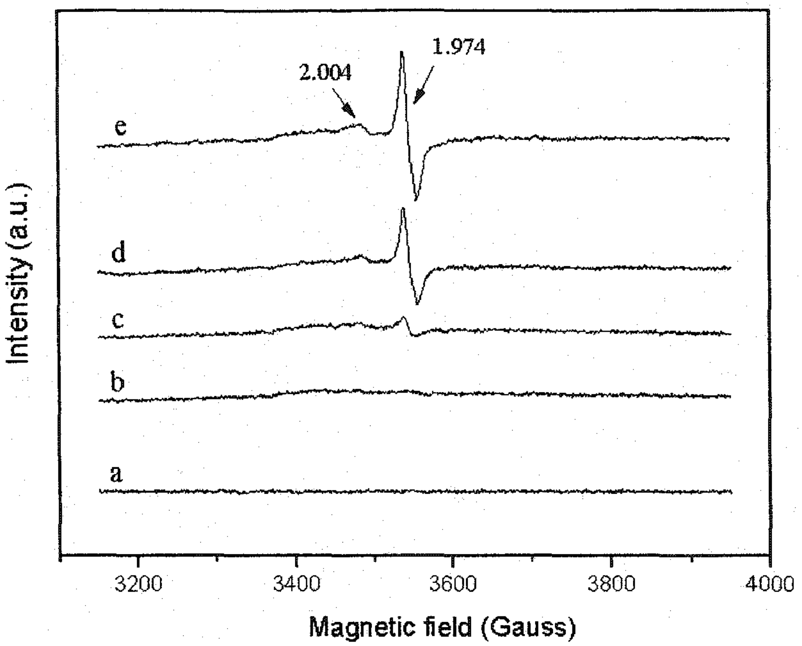

Figure 7.4: Room temperature EPR spectra of a) $Ba_{0.996}Y_{0.004}TiO_3$ sintered in a reducing atmosphere of forming gas and annealed in air at b) 1000 °C, c) 1200 °C, d) 1300 °C, and e) 1400 °C for 5 hours.

at Ba+Y/Ti $\geq$ 1.03. The XRD analysis of Ba+Y/Ti = 1.03 sample revealed the presence of a barium-rich second phase (i.e., Ba_2TiO_4). No g = 1.974 signal was detected either in rhombohedral, or in tetragonal and cubic phases. Hence, it can be concluded that at ratios of Ba+Y/Ti $\geq$ 1.03, the defect associated with the g = 1.974 signal is absent in $BaTiO_3$ ceramics. These observations are in contrast to those of Kutty et al. [5], who reported that the g = 1.974 signal is insensitive to Ba/Ti ratio whereas the g = 2.004 signal can be suppressed at Ba/Ti = 1.07. In fact, the present results have shown that the g = 2.004 signal is nearly independent of Ba/Ti ratio (Fig. 7.7). At this point we cannot explain these differences. However, based on our results, the g = 1.974 signal can be assigned to the singly ionized barium vacancy and the g = 2.004 signal can be tentatively assigned to the titanium vacancy, although Er et al. [6] attributed g = 2.004 to Fe^{3+}. Indeed, iron impurities in $BaTiO_3$ have g-values close to 2.00 [309]. However, as was recently revised by Glinchuk et al. [7], Fe^{3+} and Fe^{3+}-V_O also demonstrate resonances at g = 6.26, 5.549, 2.47, 2.00, 1.62. We observed iron in several of our samples which were accidentally contaminated with iron from the steel pressing die. An example of the EPR spectrum of $BaTiO_3$ containing Fe^{3+} and Fe^{3+}-V_O complex defects is shown in Fig. 7.8. Thus, we agree with Kutty et al. [5] in that the g = 2.004 center is not an Fe^{3+} impurity, but an intrinsic defect which develops in $BaTiO_3$ at high P_{O_2} to compensate for donor dopants. Based on the defect chemistry of $BaTiO_3$, it is most probable that the g=2.004 signal originates from a titanium vacancy with unpaired electron spin, e.g., V_{Ti}' or V_{Ti}'''.

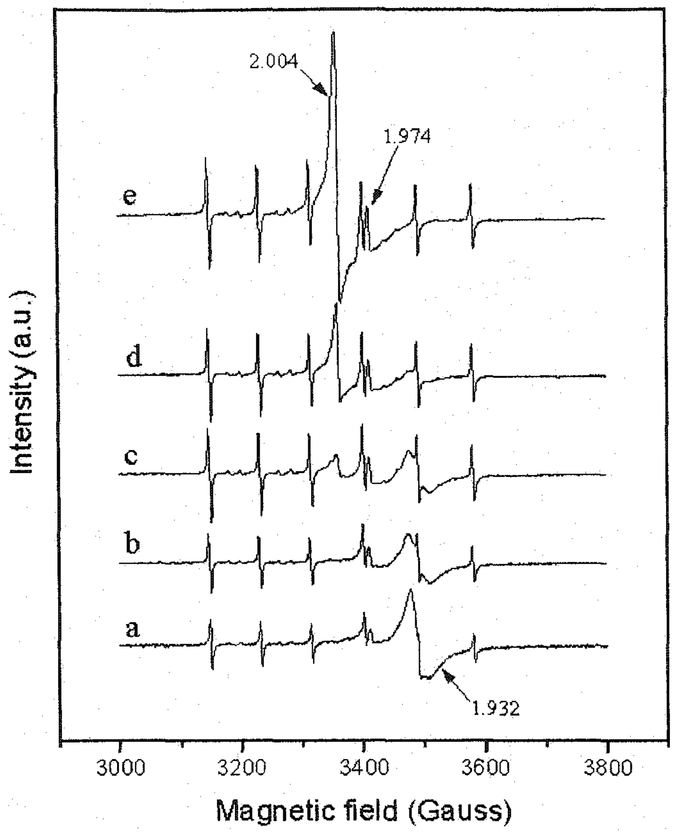

Figure 7.5: EPR spectra of a) $Ba_{0.996}Y_{0.006}TiO_3$ ceramics sintered in reducing atmosphere of forming gas and annealed in air at b) 1000 °C, c) 1200 °C, d) 1300 °C, and e) 1400 °C for 5 hours. All spectra were taken at 77 K.

7.3.3 Temperature dependence of EPR features

The temperature dependence of paramagnetic defects provides additional insight into the point defect chemistry of $BaTiO_3$. Normally one would expect the decrease in intensity of the EPR signal with temperature due to the decrease in the difference of the high and low spin populations [310]. However, $BaTiO_3$ undergoes several phase transitions at which the change in spin-lattice (or spin-spin) relaxation time, oxidation state, or low-to-high spin configuration may occur. These changes may affect the EPR intensity of the point defects present in $BaTiO_3$. The experimental setup used in this study did not allow us to measure the temperature dependence of EPR spectra in the rhombohedral phase. These spectra were measured only at 77 K. At this temperature, the paramagnetic defects with g-values of 2.004, 1.974, 1.932, as well as the Mn^{2+} sextet were detected. At 295 K, the EPR spectrum of yttrium doped $BaTiO_3$ sintered in air contains the $g = 1.974$ signal and a weak asymmetric signal at $g = 2.004$ as shown in Fig. 7.4. The EPR spectrum of nominally undoped, insulating $BaTiO_3$ contains weak signals with giromagnetic constants of 2.004

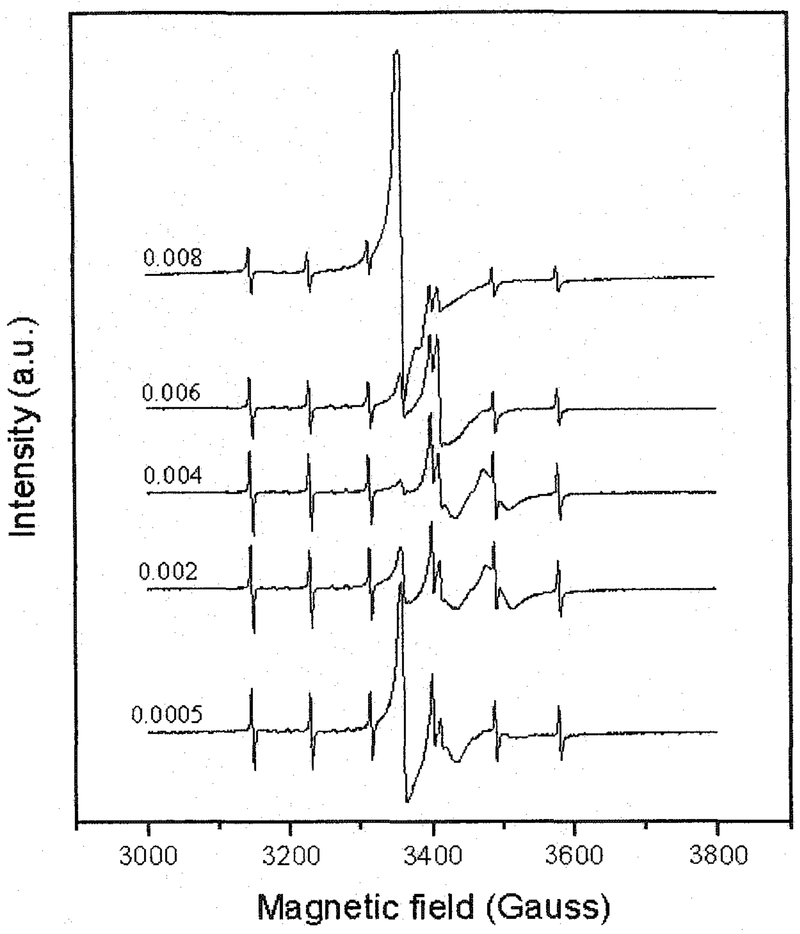

Figure 7.6: EPR spectra of $Ba_{1-x}Y_xTi_{1.01}O_3$ ceramics with x = 0.0005, 0.002, 0.004, 0.006, 0.008 sintered in air. All spectra were obtained at 77 K.

and 1.974. At T= 393 K, an anomalous increase of the g = 2.004 and Mn^{2+} signals are observed in both undoped and yttrium doped ceramics as shown in Figs. 7.9 and 7.10. As revealed by Figs. 7.9 and 7.10, in the cubic phase, the g = 2.004 signal becomes symmetric. The intensity of the g = 1.974 signal at the phase transition slightly increases, and the signal becomes narrower. The change in intensity of the g = 2.004, g = 1.974, and Mn^{2+} signals at 390 - 420 K occurred reversibly, indicating that they are associated with tetragonal-to-cubic phase transition at T_C = 393 K. The main question is why the intensity of these signals increases in the cubic phase and whether it is related to the PTCR effect. There are at least three possible reasons for the change in intensity at phase transition, namely

- Change in the oxidation state of the defect
- Change in the electron spin configuration from low to high.

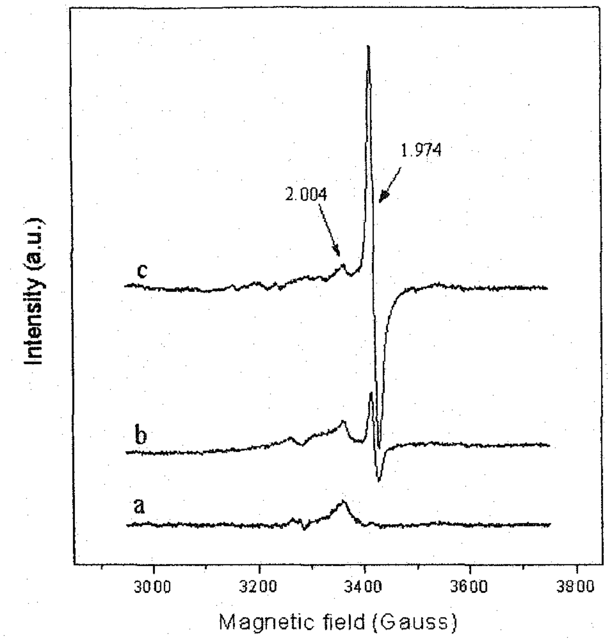

Figure 7.7: Room temperature EPR spectra of $BaY_{0.004}TiO_3$ ceramics for a) Ba+Y/Ti = 1.03, b) Ba+Y/Ti = 1.02, and c) Ba+Y/Ti = 1.00. The samples were sintered in air.

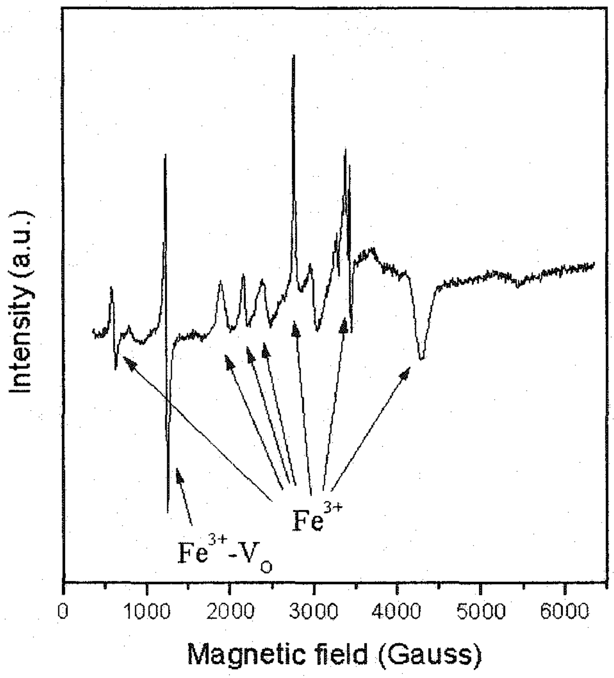

Figure 7.8: Room temperature EPR spectra of $BaY_{0.004}TiO_3$ ceramics containing Fe^{3+} impurity.

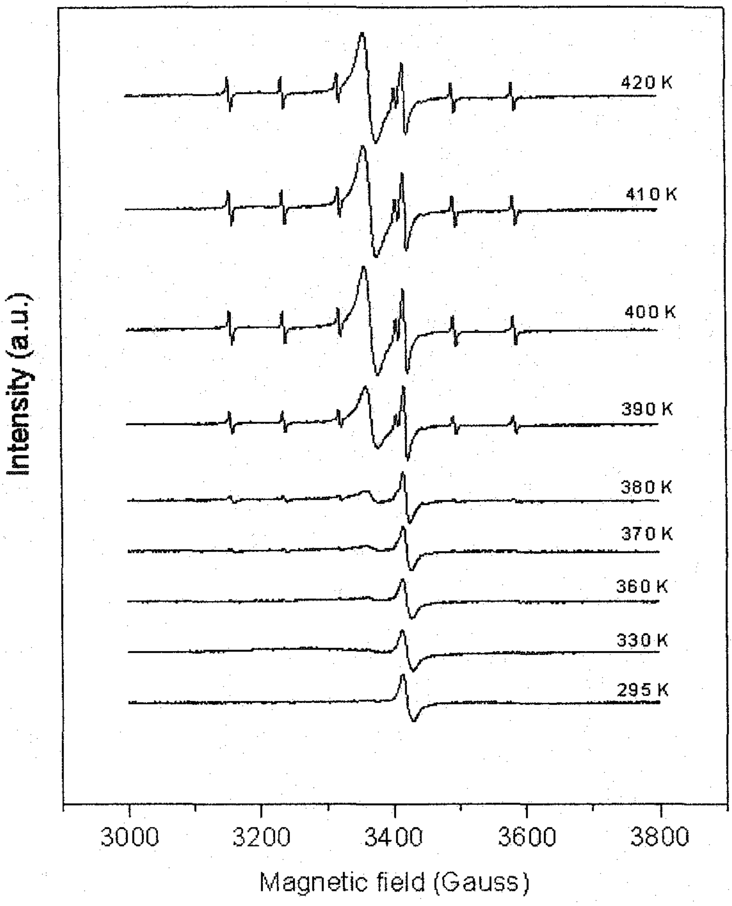

Figure 7.9: Temperature dependence of EPR spectra of $BaY_{0.004}TiO_3$ ceramics in tetragonal and cubic phases.

- Change in the spin-lattice relaxation time.

Kutty et al. [5] and Hari et al. [98] proposed that the increase in the intensity of the g = 2.004 signal occurs due to the change in the ionization state of the barium vacancy according to $V_{Ba}^{\times} + e = V_{Ba}'$. Similar arguments were applied to explain an increase in Mn^{2+} signal. It was assumed [98] that in the tetragonal phase, Mn exists in Mn^{3+} form which is EPR silent. In the cubic phase, a change in oxidation state from Mn^{3+} to Mn^{2+} was proposed, according to $Mn^{3+} + e = Mn^{2+}$. It has been further elaborated that these changes are responsible for the PTCR effect in $BaTiO_3$ ceramics [5, 98].

On the other hand, Er et al. [6] proposed that the change in Mn^{2+} intensity is associated with a transition from the low spin $(t_{2g})^5$ configuration in the tetragonal phase to the high spin $(t_{2g})^3(e_g)^2$ configuration in the cubic phase. However, according to Cox [311], in metal halides and oxides, the intra-atomic exchange interaction is more important than the ligand field splitting, and therefore

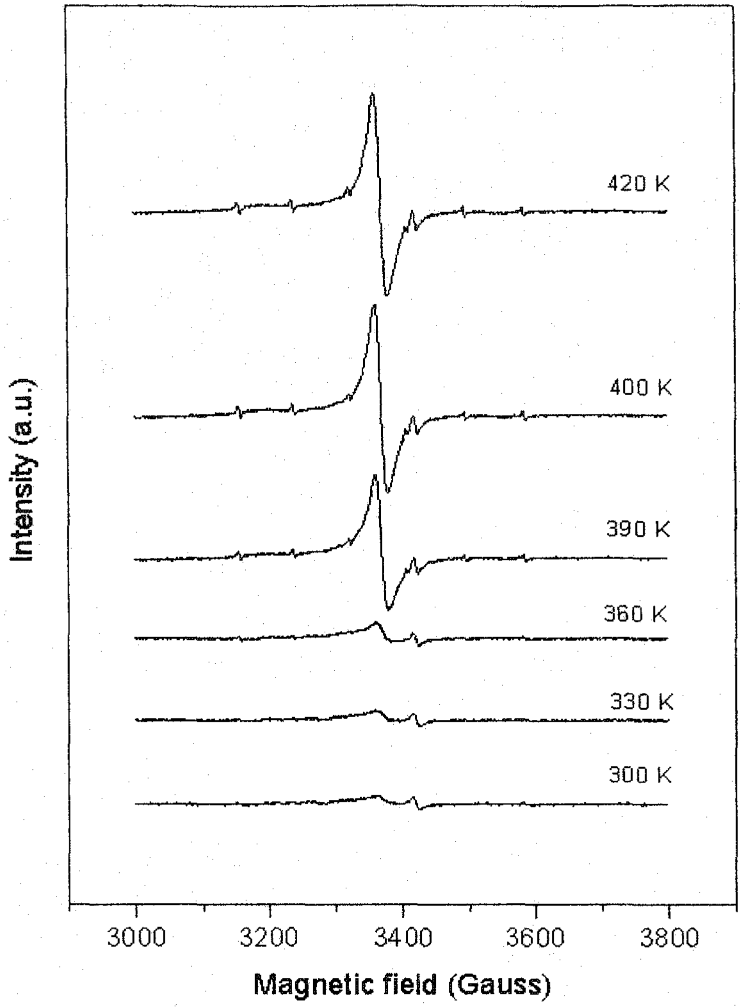

Figure 7.10: Temperature dependence of EPR spectra of undoped polycrystalline $BaTiO_3$ sintered in air at 1380 °C.

electrons will always occupy the high-spin configuration. If, however, an increase in the Mn^{2+} signal was indeed associated with the low-to-high spin transition, then this effect would be observed in ceramics sintered at both low and high P_{O_2}. As demonstrated in Fig. 7.11, ceramics sintered at low P_{O_2} do not show an increase in the Mn^{2+} signal above $T_C = 393$ K. This does not seem to be due to the difference in concentration of Mn^{2+} ions since, as revealed by Fig. 7.5, at 77 K an intensity of the Mn^{2+} signal is nearly the same for ceramics sintered in forming gas as that oxidized at 1400 °C. Thus the hypothesis of a transition of Mn^{2+} from low-to-high spin configuration at T_C has to be ruled out.

Similar experimental arguments apply against the hypothesis of Hari et al. [98] who proposed that the change from high to low oxidation state of the manganese ion is responsible for an increase

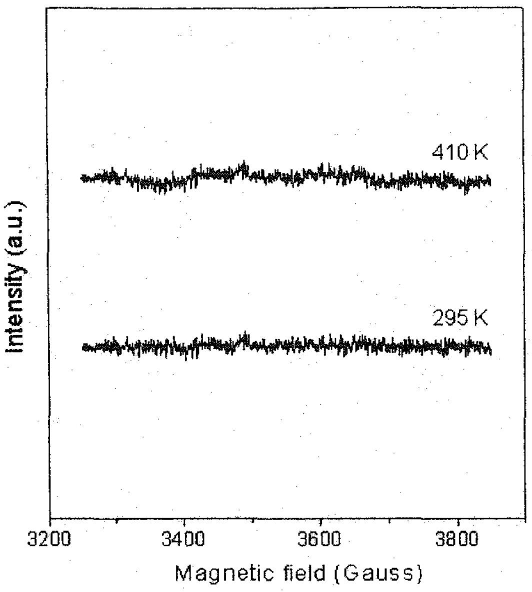

Figure 7.11: EPR spectra of tetragonal and cubic $BaY_{0.004}TiO_3$ polycrystal sintered in reducing atmosphere.

of the Mn^{2+} signal above 393 K. It seems reasonable to expect that the ceramic sintered at low P_{O_2} has the highest concentration of Mn^{2+}, yet we don't observe a Mn^{2+} signal in this ceramic above 393 K (see Fig. 7.11).

Thus it is proposed that the Mn^{2+} signal observed above 393 K originates from a complex defect such as Mn^{2+} - V_{Ti}'' or Mn^{2+} - V_{Ba}''. This defect is formed in $BaTiO_3$ ceramics at high P_{O_2}. The spin-lattice relaxation time of this defect must be different from that of a single Mn^{2+} defect. A change in the spin-lattice relaxation time at the tetragonal-to-cubic phase transition may be responsible for an increase in the EPR intensity of this defect above 393 K.

As for the change in intensity of the g = 2.004 signal above 393 K, Er et al. [6] proposed that this is due to the vanishing of spontaneous polarization. In order to investigate the effect of spontaneous polarization on the intensity of EPR signals, several $BaTiO_3$ single crystals which were either insulating or n-type semiconducting were examined. None of the crystals showed an increase in the EPR signals above T_C. In fact, all EPR signals demonstrated the usual behaviour, i.e., their intensity decreased with temperature as demonstrated in Fig. 7.12 which also shows the shift of the EPR signals towards g = 2.00 value due to the decrease in the effect of the tetragonal crystal field splitting. It can be concluded that paramagnetic defects present in polycrystalline $BaTiO_3$ have a different nature than that observed in a single crystal. If spontaneous polarization was the only reason responsible for a change in intensity of the EPR signals, then similar behaviour would be expected in both. The reason for an increase in the g=2.004 signal in the cubic phase might be the same as in case of Mn^{2+}, namely the change in the spin-lattice relaxation time. However, the change in the population of the defect with the g=2.004 signal cannot be excluded completely.

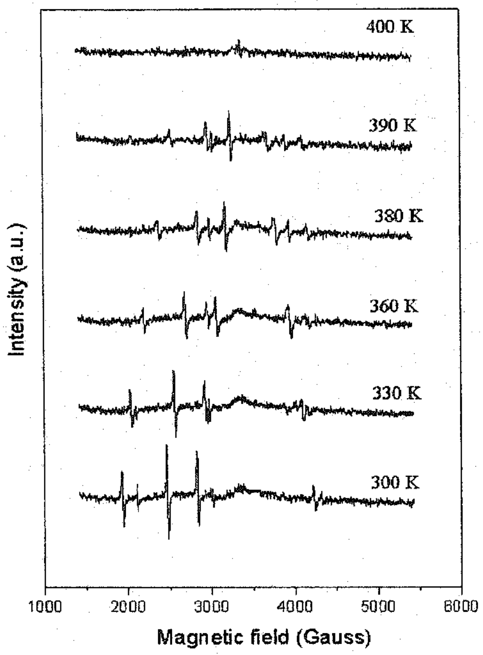

Figure 7.12: EPR spectra of undoped single crystal $BaTiO_3$.

Finally, let us examine the possible relation between the change in intensity of the g=2.004 and Mn^{2+} signals and the PTCR effect. Figs. 7.13 and 7.14 show the temperature dependence of the double integrated intensity of the g=2.004 and Mn^{2+} signals plotted together with the resistivity of Y-doped ceramics sintered in air at 1380 °C. A sharp increase in the intensity of the g=2.004 and Mn^{2+} signals occurs at ca. 100 °C. At 120 °C, the intensity of these signals reaches the maximum value. An increase in the resistivity of polycrystalline samples starts near 95 °C and has the steepest slope at 125 °C. As was mentioned above, Kutty et al. [5] attributed the change in the g=2.004 signal to the ionization of a neutral barium vacancy by trapping an electron according to

$$V_{Ba}^{\times} + e = V_{Ba}' \tag{7.2}$$

This process would yield a decrease in the concentration of the charge carriers above T_C manifested by the PTCR effect. However, as revealed in Fig. 7.10, a similar increase of the g=2.004 as well as Mn^{2+} signals occurs in undoped, insulating $BaTiO_3$ with a specific resistivity of ca. $1\times10^{10}\Omega\cdot$cm. Owing to a very low concentration of electrons in insulating ceramics (e.g., $n \approx 10^{10}$ cm^{-3}), the change in the concentration of the ionized barium vacancies in undoped $BaTiO_3$ according to Eq. 7.2 would not be high enough to be detected by the EPR technique. Moreover, the change in the EPR intensity does not seem to correlate well with the change in resistivity. As demonstrated in

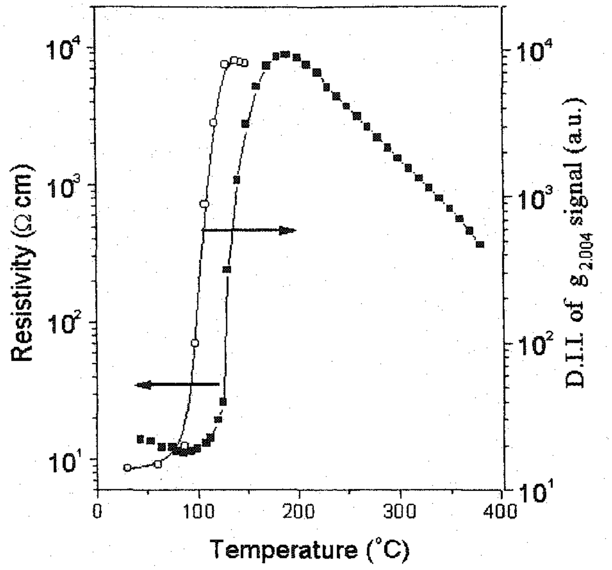

Figure 7.13: Temperature dependence of the double integrated intensity of the g=2.004 signal and resistivity of $BaY_{0.004}Ti_{1.01}O_3$ sample

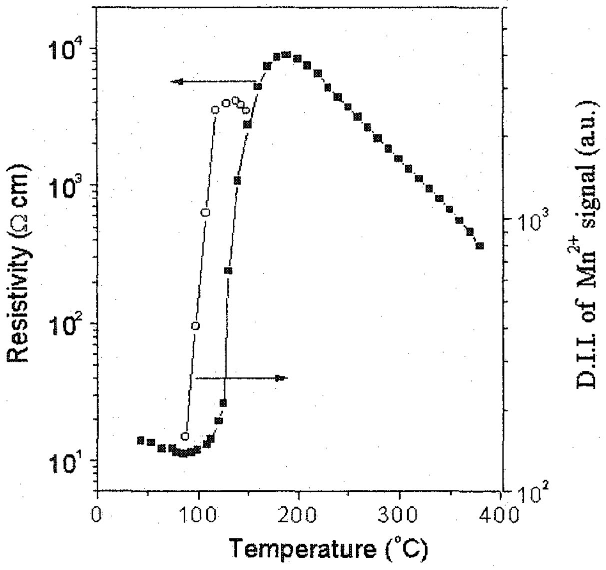

Figure 7.14: Temperature dependence of the double integrated intensity of the Mn^{2+} complex center and resistivity of polycrystalline $BaY_{0.004}Ti_{1.01}O_3$

Figs. 7.13 and 7.14, an increase in intensity of the EPR signals occurs 20 °C below an increase in the resistivity of ceramics. Thus, although point defects such as, V_{Ba}', V_{Ti}'''', Mn^{2+} play a crucial role in the PTCR effect, there is no sufficient evidence for a change in oxidation state of V_{Ba}, V_{Ti}, and Mn^{2+} above T_C.

7.4 Conclusions

In conclusion, several paramagnetic point defects in $BaTiO_3$ polycrystals were detected and identified using the electron paramagnetic resonance technique. Polycrystals sintered in reducing atmosphere showed a strong broad signal with giromagnetic constant of 1.932 – 1.934. This signal, observed only in conducting ceramics, was assigned to Ti^{3+} and Ti^{3+} related complexes. Signals with g=1.974 and g=2.004 were attributed to intrinsic point defects (V_{Ba} and V_{Ti}). The EPR intensity of these defects increases with oxidation of ceramics at $T > 1000$ °C. Formation of the V_{Ba} and V_{Ti} signals in EPR spectra of oxidized ceramics correlates with appearance of the PTCR effect. Hence, it is justified that these defects are the source of the in-gap electron traps in PTCR ceramics. At donor dopant levels of $\geq$0.3 at%, the concentrations of V_{Ba} and V_{Ti} defects show a good agreement with the defect compensation mechanism of donor doped $BaTiO_3$ [101, 89, 64, 95]. However, small amounts of V_{Ba}, and V_{Ti} defects were detected in undoped $BaTiO_3$ ceramics. This observation is contrary to the generally accepted model of undoped $BaTiO_3$ where only oxygen vacancies were allowed to compensate the acceptor impurities at high P_{O_2} [99].

Chapter 8

Current-voltage dependence of n-doped $BaTiO_3$

8.1 Introduction

Although $BaTiO_3$ based positive temperature coefficient (PTC) thermistors have been widely used for a number of years [312], the nature of the positive temperature coefficient of resistivity (PTCR) effect in n-type $BaTiO_3$ is not altogether clear [152]. One of the open questions about PTCR behavior is a satisfactory interpretation of the current-voltage, $j(V)$, characteristics of this material. This issue has been addressed by a number of authors. However, their conclusions have been rather contradictory. Heywang [1] explained the $j(V)$ dependence in light of thermionic emission of electrons over the double-Schottky barrier (DSB). According to Heywang, the current density in the paraelectric phase should obey the exponential dependence:

$$j \propto exp\left(\frac{eV}{2k_BT}\right) \tag{8.1}$$

However, the experimental $j(V)$ dependence has turned out to be less steep than given by Eq. 8.1 [313]. Failure to observe exponential $j(V)$ dependence has prompted a search for alternative models. By taking into account the low mobility of electrons in BaTiO3, Mallick and Emtage [11], and later Kulwicki and Purdes [8] suggested diffusion current through the grain boundary (GB) as an explanation of $j(V)$. Space-charge-limited-current (SCLC) in PTCR $BaTiO_3$ was reported by MacChesney and Potter [314] and later by Nemoto and Oda [10]. Kvaskov and Valeev [9], on the other hand, explained $j(V)$ characteristics of Ce-doped $BaTiO_3$ in terms of the Frenkel-Poole emission model [315]. The interest in $j(V)$ behaviour of PTCR $BaTiO_3$ has been revived recently by Kuwabara et al. [151]. They proposed that electron transport through the grain boundary is controlled by a trap-filled-limited-current (TFLC).

In this Chapter, the current-voltage characteristics will be analyzed in terms of existing models of electron transport in PTCR $BaTiO_3$. Special attention is given to the electric field dependence of the population of the interface electron states. It is shown that interface states cause pinning of the Fermi level at the grain boundary. This leads to partial stabilization of the interface potential barrier and, consequently, alters the shape of the $j(V)$ curves considerably.

8.2 Experiment

Two samples of approximately similar grain size were used in this experiment. Sample A of composition $Ba_{0.996}Y_{0.004}Ti_{1.01}O_3$ was prepared as follows. Reagent-grade powders of $BaCO_3$, TiO_2, and Y_2O_3 were weighed in appropriate proportions, vibromilled in Nalgene bottles with alcohol and ZrO_2 grinding balls. The dried mixture was then calcined at 1300 °C in forming gas (5% H2 / 95% Ar) for 2 hours, pressed into pellets and sintered in air at 1320 °C for 0.5 hour. Sample B, of composition $Ba_{0.69}Sr_{0.3}Y_{0.004}Ti_{1.01}O_3$ doped with 0.03 mol % MnO was provided by Prof. A.G. Belous from the Institute of General and Inorganic Chemistry in Kyiv, Ukraine. For grain size determination, the samples were polished and thermally etched. The SEM images of samples A and B are shown in Fig. 8.1. The average grain size, determined by the linear intercept method, was 3.81 and 3.42 μ m for samples A and B, respectively. Stable ohmic contacts were obtained by electroplated Ni electrodes, annealed at 350 °C in air. Current-voltage characteristics were measured by means of a programmable power supply (Keithley 237 High Voltage Source, Keithley Instruments, Inc.) using

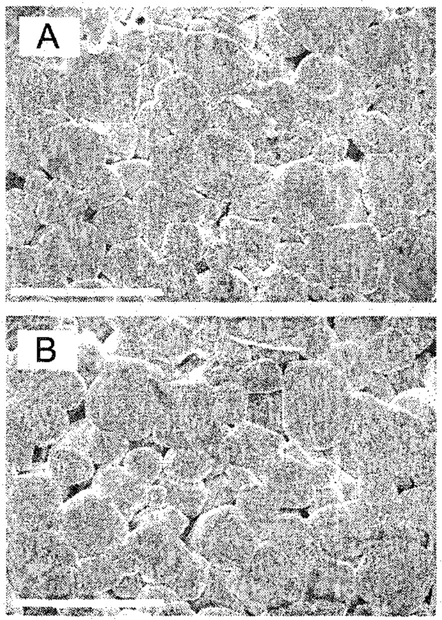

Figure 8.1: SEM images of samples A and B. The white bar indicates 10 μ m.

short voltage pulses of 2 ms to prevent Joule heating of the samples during measurements. The temperature was accurate to within ± 1 °C and the resistivity to within 1 %.

8.3 Results and discussion

The low electric field resistivity of samples A and B is plotted against temperature in Fig. 8.2. Both samples show a typical PTCR effect with a resistivity increase of 3 orders of magnitude for sample A and 6 orders of magnitude for sample B which contains Mn. The significant increase in resistivity jump is attributed to doping with Mn, as found by others [316]. According to the Heywang model [1], such an increase is explained by the deeper localization of grain boundary (GB) electron states in the band gap of $BaTiO_3$. This is consistent with an observed increase in the activation energy, E_a, of resistivity above $T_{\rho_{max}}$. The E_a values were obtained from the Arrhenius dependence of the resistivity data in the high-temperature NTCR region in Fig. 8.2. These are 0.40 eV and 0.87 eV for samples A and B, respectively. The $j(V)$ dependencies were measured above and below $T_{\rho_{max}}$ in the temperature range 145 - 330 °C with the temperature of measurement indicated by arrows in Fig. 8.2. A double logarithmic plot of the current density against the voltage drop per GB is shown in Fig. 8.3. When the voltage drop is below 0.04 V per GB, both samples satisfy Ohm's law. At

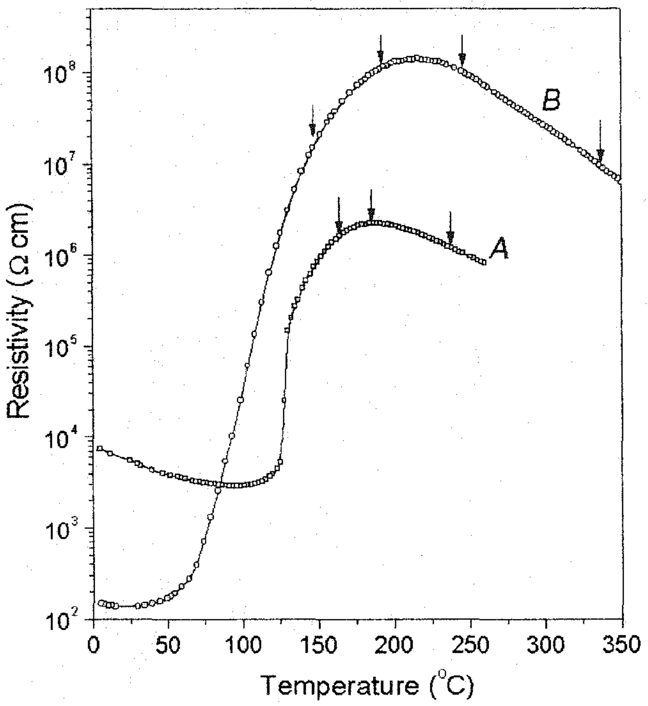

Figure 8.2: Temperature dependence of resistivity of samples A and B. Arrows indicate the temperatures where $j(V)$ characteristics were measured.

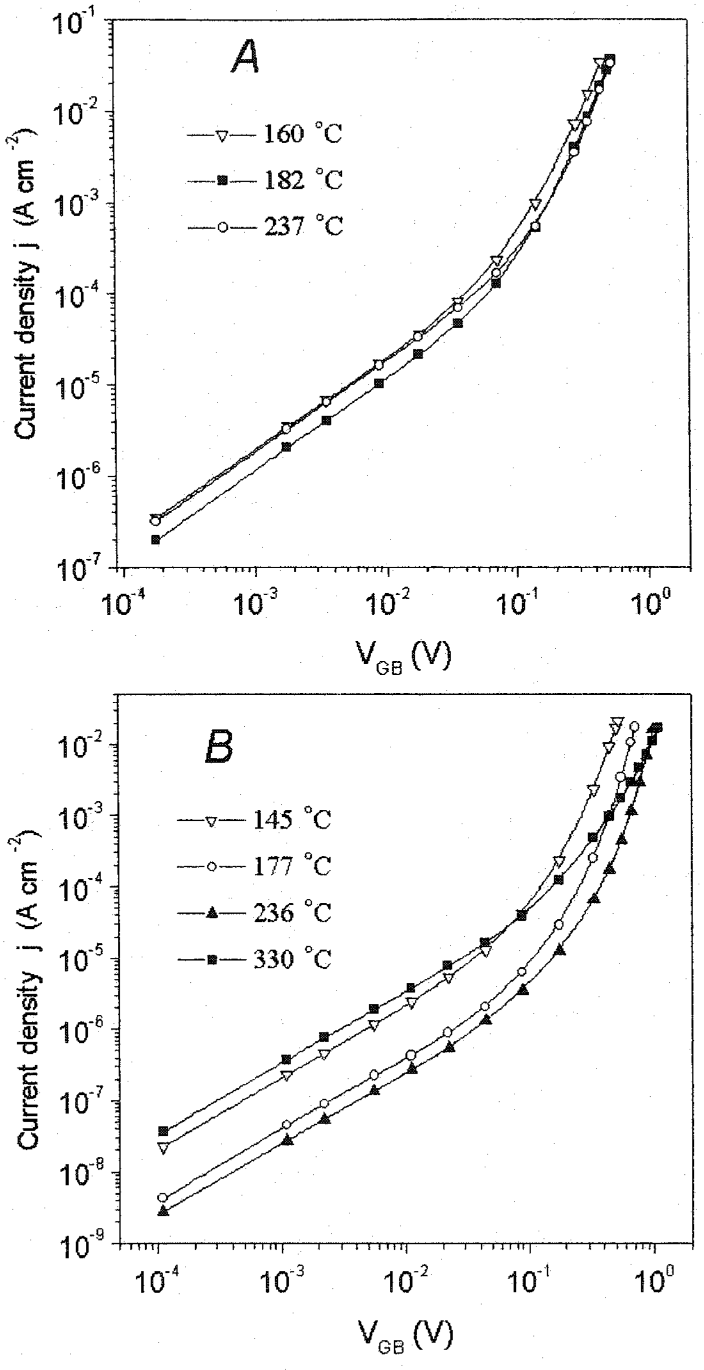

Figure 8.3: The $j(V)$ characteristics of samples A and B measured at various temperatures.

higher values of V_{GB}, the current increases progressively more with increase in voltage. In the high V_{GB} region, the current increases more steeply with decreasing temperature for both samples A and B except at 145 °C for sample B. The last may be due to unavoidable overheating of the sample at low temperatures. The results are now discussed in the light of various electron transport models.

8.3.1 Space charge limited current model

According to the space charge limited current (SCLC) model for an insulator without traps, the current density obeys Child's law [317]

$$j = \frac{9}{8}\frac{\varepsilon\mu}{w^3}V^2 \tag{8.2}$$

where ε is the dielectric permittivity, μ the drift mobility of electrons, w the thickness of insulator layer, and V the voltage drop across the layer. According to the SCLC model, as given by Eq. 8.2, j is proportional to V^2. The experimental data in Fig. 8.3 show that j is not proportional to V^2 over any significant range of voltage. Moreover, the slope of the $j(V)$ plot in Fig. 8.3 in the nonohmic region is not the same at different temperatures. However, from Eq. 8.2, it is obvious that temperature should not affect the slope of the $j(V)$ dependence plotted in a log-log scale. Yet, a distinct effect of temperature on the slope of $j(V)$ characteristics is still observed when plotted in this way, which seems to conflict with the consequences of the SCLC model. Jonker [157] pointed out a futher limitation of the SCLC model without traps, namely that it results in an extremely large Debye length, L_D, in $n-i-n$ BaTiO$_3$. For an i layer in BaTiO$_3$, the value of the L_D may easily extend to the length scale of a meter, unless a low-ε interphase layer is present between BaTiO$_3$ grains.

An already known alternative to the simple SCLC model for n-type BaTiO$_3$ is the trap-filled limited current (TFLC) model [10], which is a specific case of SCLC model influenced by electron traps. The presence of the negative space charge in GB layer due to the trapped electrons will decrease the Debye length, making the $n-i-n$ structure in PTCR BaTiO3 possible. In general, both shallow and deep electron traps can give rise to the TFL current [317]. However, the $j(V)$ behaviour preceding the onset of TFLC is found to be different for these two types of traps. In the case of shallow traps (i.e., trap energy, E_t, lying above the Fermi level E_F) the current density follows the modified square law [317]:

$$j = \frac{9}{8}\frac{\varepsilon\mu}{w^3}\Theta V^2 \tag{8.3}$$

before the onset of the TFLC. The parameter $\Theta = n/n_t$, in Eq. 8.3, designates the ratio of the free electron concentration, n, in the i layer to the concentration of electrons trapped in shallow traps, n_t. As the voltage increases, the Fermi level would cross the energy of the shallow traps which would result in a rapid increase of TFLC. At higher voltages, as soon as all traps are filled, the current again obeys the square law as given by Eq. 8.3 but with a finite and constant value of Θ. Fig. 8.3 did not demonstrate square law dependence over the significant voltage range prior to the rapid rise in current. Thus it can be concluded that the TFLC model controlled by shallow traps does not adequately describe the $j(V)$ characteristics of the PTCR BaTiO$_3$. If deep traps were to form, i.e., when E_t is below E_F, two situations may occur. Since only unoccupied electron traps can contribute to TFLC, no TFLC will result if the traps are several k_BT below the Fermi level. In this case the current will be proportional to V^2 as in Eq. 8.2. If, however, E_t is close to E_F, the remaining concentration of unoccupied electron traps will give rise to TFLC. The TFLC region in this case should appear immediately after the ohmic region. At higher voltages, TFLC is expected to be followed by the square law dependence after all traps are filled. In the PTCR region below $\mathrm{T}_{\rho_{max}}$, all deep traps are populated and thus $j \propto V^2$ should be observed. Around $\mathrm{T}_{\rho_{max}}$, the Fermi level at the grain boundary approaches E_t and, according to the Fermi-Dirac statistics, a certain population of the traps becomes unoccupied. This creates favorable conditions for the appearance of TFLC. Accordingly, for the TFLC model with deep traps, we expect $j \propto V^2$ at $\mathrm{T} < \mathrm{T}_{\rho_{max}}$ and TFLC to dominate at $\mathrm{T} \geq \mathrm{T}_{\rho_{max}}$. The data in Fig. 8.3, however, do not confirm this behavior, i.e., at $\mathrm{T} < \mathrm{T}_{\rho_{max}}$ the current does not increase with V^2 and the slope of the $j - V$ curve is much higher. When the temperature exceeds $\mathrm{T}_{\rho_{max}}$, the slope becomes less, thus implying no effect of unoccupied electron traps on the TFLC above $\mathrm{T}_{\rho_{max}}$. This analysis of the data in terms of the SCLC and TFLC models fails to explain nonlinear $j(V)$ characteristics in samples A and B. It may be argued that the variation of the parameters w, n_t, and ε of Eq. 8.3 for individual GB layers can hinder the $j \propto V^2$ dependence in polycrystalline samples. However, the known $j(V)$ measurements on individual GB in PTCR $\mathrm{BaTiO_3}$ [10, 151, 149] have also been found to contradict the above mentioned behaviour.

8.3.2 Frenkel-Poole effect

. Kvaskov and Valeev [9] reported another interesting type of $j(V)$ behaviour in PTCR $\mathrm{BaTiO_3}$. Their high-field conductivity data obeyed the Frenkel-Poole dependence in both PTCR and high temperature NTCR regions. In case of Frenkel-Poole dependence [315], the conductivity increases as a result of the electric-field-assisted thermal ionization of a Coulombic center. Based on a simple one-dimensional model, the field effect on conductivity is described by [315]

$$\sigma = \sigma_0 exp\left(\beta\frac{\sqrt{E}}{k_BT}\right) \tag{8.4}$$

and

$$\sigma = \sigma_0 exp\left(\frac{\beta\sqrt{V_{GB}}}{k_BT\sqrt{w}}\right), \tag{8.5}$$

where

$$\beta = \sqrt{\frac{e^3}{\pi\varepsilon\varepsilon_0}} \tag{8.6}$$

and σ_0 is the low-field conductivity, E is the electric field in the GB layer of thickness w, e is the electronic charge, ε is the dielectric permittivity of the sample and ε_0 that of the vacuum. The low temperature conductivities of several materials e.g. Si, $\mathrm{SiO_2}$, $\mathrm{Al_2O_3}$ and $\mathrm{Ta_2O_5}$ [318, 319] have been successfully described by Eq. 8.4. However, as seen from Fig. 8.4, the normalized conductivity of our samples in the measured voltage range does not follow a straight line when plotted against

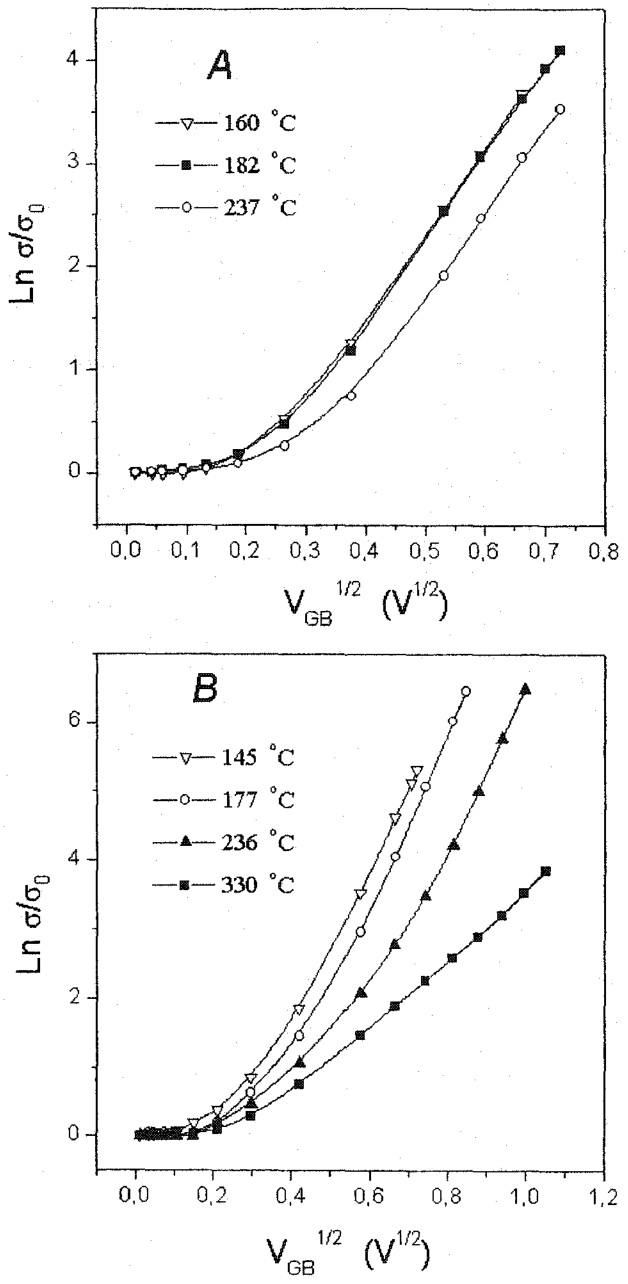

Figure 8.4: Voltage dependence of normalized conductivity σ/σ_0 for samples A and B measured at various temperatures.

$\sqrt{V_{GB}}$. Hence the Frenkel-Poole effect in our PTCR samples may not be present or is hindered by other effects.

8.3.3 Small radii polaron transport in $BaTiO_3$

Observation of low electron mobility and an optical-absorption maximum at 0.6 eV has led a long-standing discussion regarding the nature of electron transport in n-doped $BaTiO_3$. In particular, the question of whether the charge carriers in n-doped $BaTiO_3$ are small polarons [78] or conduction band electrons [14]. In the polaronic scheme, the conductivity results from electron hopping between the titanium ions whose valence may change from site to site according to the formula: $Ti^{4+} + e^- = Ti^{3+}$. The temperature dependence of zero-bias polaronic-type conductivity is given by

$$\sigma = T^{-3/2} en\mu_0 exp\left(-\frac{E_A}{k_B T}\right), \tag{8.7}$$

where μ_0 is the polaron mobility and E_A is the thermal activation energy of a small polaron hop. To analyse $j(V)$ data according to the polaron model, the formalism proposed by Böttger and Bryksin [320] for small polaron transport in a strong electric field was employed. The electron current is given by the difference in the hopping probabilities forward, P_+, and backward, P_-, in the electric field E

$$j = ena(P_+ - P_-), \tag{8.8}$$

where a is the nearest-neighbour distance (a = 4.01 Å) for $BaTiO_3$ above 120 °C, and n is the small polaron density. The activation energy, E_A, for hopping probability decreases in the electric field according to,

$$E_A(E) = E_A\left(1 - \frac{eaE}{4E_A}\right)^2 \tag{8.9}$$

and, following Efros [321] the final expression for the current density has a form

$$j = 2\frac{en}{a} Dexp\left(-\frac{(eaE)^2}{16E_A k_B T}\right) sinh\left(\frac{eaE}{2k_B T}\right), \tag{8.10}$$

where D is the diffusion coefficient of small polarons. The limits of applicability of Eq. 8.10 are determined by the exponential term. At high field ($eaE \approx 4E_A$), the polaron well collapses and one may not refer to polaron localisation at a lattice site. Since one may assume that the entire voltage drop occurs at GB in the PTCR range, the electric field, E, may be expressed as $E = V_{GB}/w$ where V_{GB} is voltage drop per single GB and w is a thickness of depletion layer. Hence, for hopping conductivity, a plot of j against $\sinh(\alpha V_{GB})$ where $\alpha = ea/2wk_B T$, should be a straight line. Fig. 8.5 shows an attempt to fit $j(V)$ data to the polaronic model for sample B at 330 °C. Although a good fit is observed for almost two decades of j, it was achieved at the expense of an unrealistically high value of $\alpha = 3.9$ at which the whole GB voltage drops at a distance of ca. 7.5 Å. This value, however, is at least two orders of magnitude smaller than typical depletion layer widths for PTCR ceramics reported from capacitance measurements [270]. Analysis of Eq. 8.10 for real values of depletion layer widths (e.g., 100 nm - 400 nm) suggests that polaronic-type behaviour of the $j(V)$ characteristics will not be observed until a voltage drop of ca. 60 V per GB is reached.

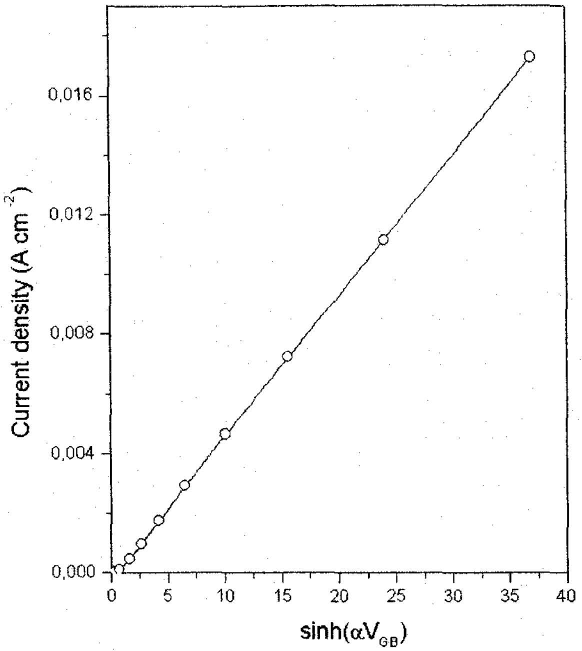

Figure 8.5: Polaronic fit of $j(V)$ dependence of sample B at 300 °C, $\alpha = 3.9$.

8.3.4 Double-Schottky barrier model

In his original model, Heywang [1] explained the PTCR effect in terms of temperature dependent double-Schottky barriers formed at the grain boundaries of $BaTiO_3$ ceramics. These barriers are seen to originate from the negative charge of the interface electron states.

Depending on the thickness of the DSB depletion layer, w, and electron mean free path, l, two different models of electron transport have been put forth: (i) the ***diffusion*** model, which is for the condition, $l \ll w$, and (ii) the *thermionic emission* model for the condition, $l \geq w$. The current densities through the single DSB are given by [8]

$$j = \frac{\mu ne\varphi(V)}{w} exp\left(-\frac{e\varphi(V)}{k_B T}\right)\left[1 - exp\left(-\frac{eV}{k_B T}\right)\right] \tag{8.11}$$

for the diffusion model, and [13]

$$j = A^* T^2 exp\left(-\frac{e\varphi(V) + E_F}{k_B T}\right)\left[1 - exp\left(-\frac{eV}{k_B T}\right)\right] \tag{8.12}$$

for the thermionic emission model, where A* is the effective Richardson constant, T the absolute temperature, μ the drift mobility of electrons, n the free electron concentration, E_F the Fermi energy, V the voltage drop across a single GB, and $\varphi(V)$ the voltage dependent height of DSB. Both models predict a thermally activated current through GB. Even though the diffusion model gives similar results, it is instructive to analyze the data in terms of a thermionic emission model as follows.

For the DSB model at $V = 0$, the barrier height, φ_0, at the interface is given by

$$\varphi_0 = \frac{Q_0^2}{8\varepsilon\varepsilon_0 en}, \tag{8.13}$$

where Q_0 is the zero voltage interface charge. The interface charge is related to the density of the occupied interface states by

$$Q = e\int_{E_v}^{\infty} N_t(E)f(E)dE, \tag{8.14}$$

where E_v is the energy at the top of the valence band, $f(E)$ is the Fermi-Dirac distribution function and $N_t(E)$ is the density of the interface states (DOS) function. In general, to take into account the intrinsic electron states present at the neutral interface, the integration in Eq. 8.14 should proceed from the Fermi level of the neutral interface [13]. In case of the single energy interface states with energy E_t below the conduction band, the DOS function in Eq. 8.14 becomes

$$N_t(E) = N_t\delta(E - E_t), \tag{8.15}$$

where N_t is the total density of the interface states and $\delta(E)$ is the Dirac δ-function. The result for the interface charge is

$$Q = eN_t\left[1 + exp\left(\frac{E_{F,int} - E_t}{k_BT}\right)\right]^{-1}, \tag{8.16}$$

where $E_{F,int}$ is the energy of the Fermi level at the interface. Hence, to obtain the values of Q and φ, the exact value of the $E_{F,int}$ should be known. For zero voltage, the Fermi level at the interface coincides with that in the bulk

$$E_{F,int} = k_BTln\frac{n}{N_c} - e\varphi_0, \tag{8.17}$$

where $k_BTln(n/N_c)$ is the energy of the Fermi level in the bulk, E_F, and N_c is the electron density of states in the conduction band ($N_c = 1.56 \times 10^{22}$ cm^{-3} for BaTiO$_3$ [322]). As illustrated in Fig. 8.6 for nonzero voltage, the quasi-Fermi-level at the interface, $E_{F,int}$, is lowered with respect to that of the bulk by an amount of $\Delta E_F(V)$ so that

$$E_{F,int} = k_BTln\frac{n}{N_c} - e\varphi(V) - \Delta E_F(V). \tag{8.18}$$

The value of $\Delta E_F(V)$ is determined by the detailed balance between electrons emitted and electrons trapped at the interface. For thermionic emission, it is given by [323]

$$\Delta E_F = k_BTln\frac{2}{1 + exp\left(-\frac{eV}{k_BT}\right)}. \tag{8.19}$$

According to Eq. 8.19, $\Delta E_F = 0$ at zero voltage and $\Delta E_F = k_BT\text{ln}2$ when $eV/k_BT \gg 1$. In view of ΔE_F being small irrespective of the voltage magnitude, electrons localized on the interface remain in quasi-equilibrium with electrons on the negatively biased side of the DSB. Finally, the dependence of the potential barrier, φ, on V, which includes the effect of the interface charge is found from [324]

$$\varphi(V) = \varphi_0\gamma^2\left[1 - \frac{V}{4\varphi_0\gamma^2}\right]^2, \tag{8.20}$$

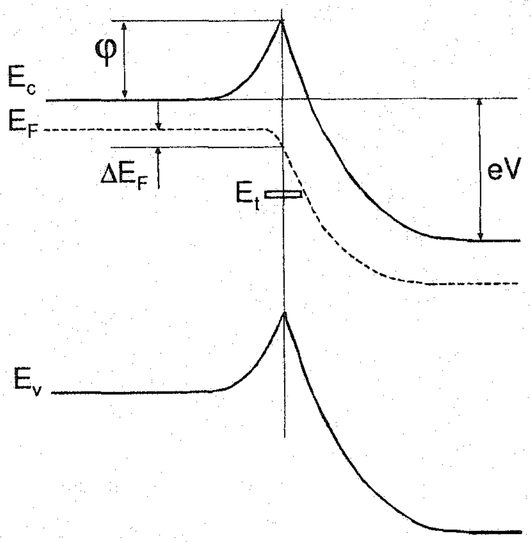

Figure 8.6: An illustration of the double-Schottky barrier at nonzero voltage.

where γ is the ratio of the interface charge at nonzero and zero voltages:

$$\gamma = \frac{Q(V)}{Q_0}. \tag{8.21}$$

The above formalism from Eqs. 8.12-8.21 was used in analyzing the data here. The drift mobility of electrons, μ, was taken to be 0.5 cm^{2}V/s. The values of E_t, N_t and n were obtained from the best fit of $T_{\rho_{max}}$ and the resistivity by the method proposed by Ihrig and Puschert [322]. These values are $E_t = 0.8$ eV, $N_t = 7 \times 10^{13}$ cm^{-2} and n = 1×10^{18} cm^{-3} for sample A and $E_t = 1.3$ eV, $N_t = 9 \times 10^{13}$ cm^{-2} and n = 4×10^{18} cm^{-3} for sample B. The concentration of free electrons, n, was taken to be higher than that obtained from the room temperature resistivity. This was done in order to take into account the residual potential barrier in the ferroelectric phase which increases ρ and therefore yields a lower value of n.

The calculated temperature dependence of φ_0, and N_t, for samples A and B are shown in Fig. 8.7.

In the paraelectric phase, the potential barrier increases gradually with temperature until E_F approaches E_t. A further increase in temperature causes a reduction of the interface charge as a result of the depopulation of the interface states. At some temperature, the φ_0 stops increasing and begins to decrease slowly together with E_F according to

$$e\varphi_0 = k_B T ln \frac{n}{N_c} - E_t. \tag{8.22}$$

The effect of non-zero voltage conditions on the φ and γ factor is shown in Fig. 8.8. At low temperatures, almost all interface states are occupied and therefore $\gamma \approx 1$ at all V, and when V

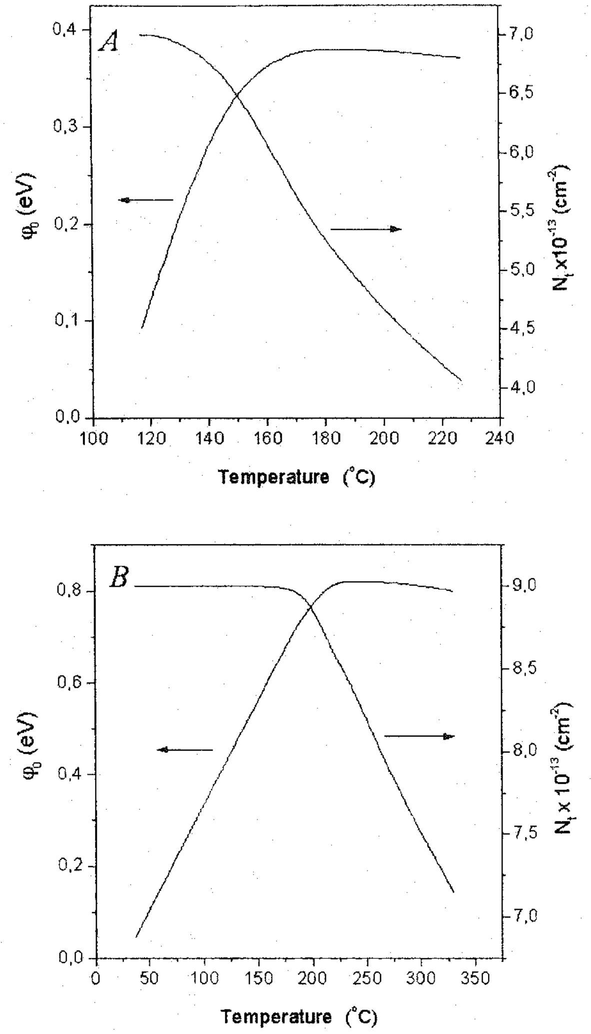

Figure 8.7: Calculated temperature dependence of φ_0 and N_t for samples A and B.

reaches $4\varphi_0$ the GB barrier vanishes. At higher temperatures, the effect of interface charge on the potential barrier becomes pronounced. Since the density of interface states is fixed with respect to the conduction band edge, the $N_t(E)$ shifts with respect to $E_{F,int}$ as the barrier height is changed (see Fig. 8.6). Increase in V causes the empty interface states to become filled, and consequently, the interface charge, $Q(V)$, increases. Hence, reduction of the interface barrier in an external electric field is partly compensated by increase of the trapped charge as long as some unoccupied traps remain at GB. As seen from Fig. 8.8, such partial stabilization of $\varphi(V)$ is expected for both samples at high temperatures. At higher voltages, all traps are filled and the barrier decays rapidly according to Eq. 8.22 for a constant value of γ.

The $j(V)$ curves calculated within the thermionic emission model are compared with experimental curves obtained at different temperatures, in Figs. 8.9 and 8.10. As can be seen for sample A, the

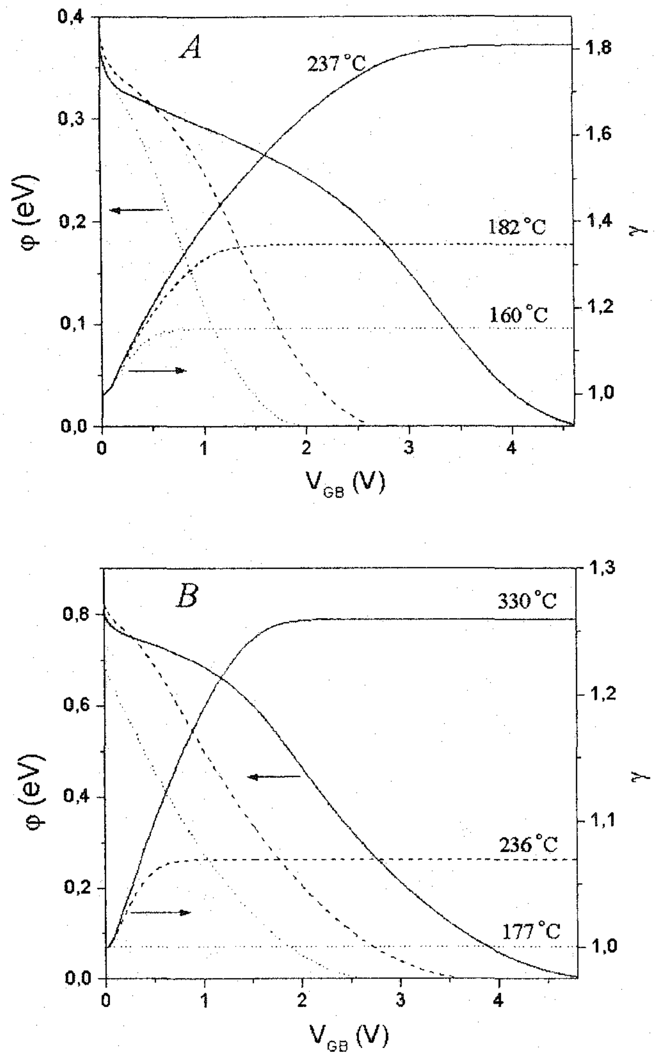

Figure 8.8: Dependence of φ and γ on applied voltage for samples A and B at various temperatures.

effect of the interface charge is already noticeable at 22 °C below $T_{\rho_{max}}$ of 182 °C. For sample B at 71 °C and 41 °C below $T_{\rho_{max}}$ of 218 °C, the effect of the trapped charge is still small because the traps are completely occupied at these temperatures. At higher temperatures, the calculated $j(V)$ curves show three distinct regions. At low voltage, when $eV \ll k_B T$, the $j(V)$ dependence is ohmic as the barrier does not change appreciably. At higher voltages, two processes, (*i*) the decrease in $\varphi(V)$ and (*ii*) the increase in $Q(V)$ counteract each other. For partially stabilized barrier, this leads to subohmic $j(V)$ dependence. Finally, as the interface states are filled up completely, the barrier collapses and j increases rapidly by several orders of magnitude. The measured $j(V)$ curves in Figs. 8.9 and 8.10, however, do not agree well with the calculated ones. At high temperatures, j increases nonlinearly at voltages much lower than those predicted by Eq. 8.12. There may be

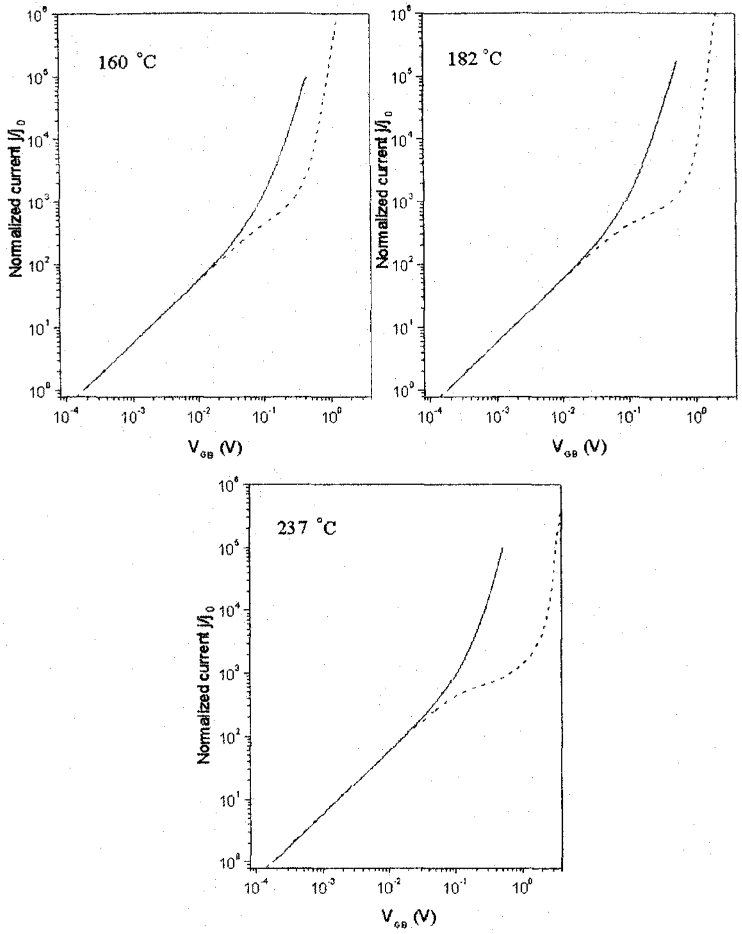

Figure 8.9: Normalized $j(V)$ characteristics for sample A at various temperatures. Solid line, measured$j(V)$; dashed line, calculated $j(V)$.

several possible reasons for this behaviour. In our calculations we assumed a single energy DOS. A certain $j(V)$ improvement may be achieved by considering a more sophisticated DOS function with interface states spread over a narrow energy range. Also, the electron-hole recombination process in the DSB region may become significant at high temperatures. This will increase a total current over the DSB. We also assumed that all grain boundaries have the same density of the interface states. This may not necessarily be true as was revealed by $\rho(T)$ and $j(V)$ measurements on single grain boundaries in $BaTiO_3$ [151, 325]. Finally, as was found by others [151], some grain boundaries in $BaTiO_3$ show no PTCR effect. Consequently, the voltage drop on the remaining GB will increase. This will result in the shift of the $j(V)$ dependence towards lower voltages. Thus, in the framework of the Heywang model [1], the current-voltage characteristics will show far more complex behavior than an exponential dependence in Eq. 8.1 and the DSB model may still be applicable for explanation of the $j(V)$ dependence in PTCR $BaTiO_3$.

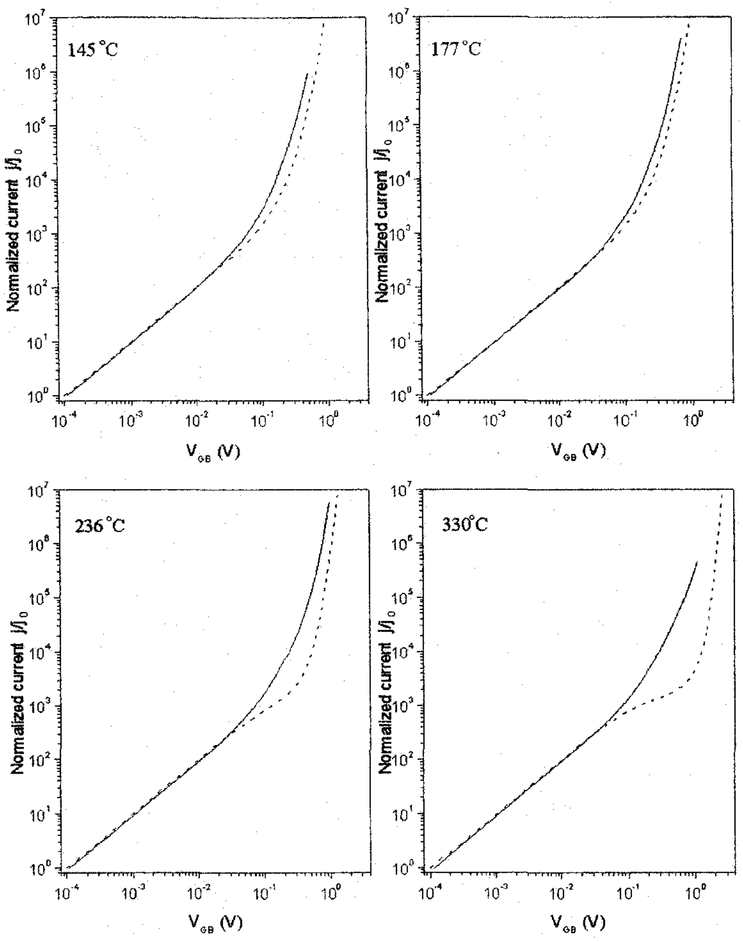

Figure 8.10: Normalized $j(V)$ characteristics for sample B at various temperatures. Solid line, measured$j(V)$; dashed line, calculated $j(V)$.

8.4 Conclusions

In conclusion, the $j(V)$ characteristics of two types of the PTCR $BaTiO_3$ ceramics were analyzed in light of SCLC, TFLC, Frenkel-Poole, small polaron, and DSB models. It was shown that for the DSB model a partial stabilisation of the potential barrier is expected when the Fermi level is pinned at GB by a high density of the interface states. This will result in an ohmic or even subohmic $j(V)$ dependence at moderate voltages, e.g. $V_{GB} < 1$ V. The DSB model predicts a drastic increase of the current only after all interface states are filled up. The voltage corresponding to the onset of this current is expected to shift towards higher values with increasing temperature. The possible reasons for disagreement between measured and calculated $j(V)$ characteristics within DSB model were also discussed. Among them might be uncertainty in the DOS function, electron-hole recombination at high temperatures, and variation of the GB barrier height at individual grain boundaries.

Chapter 9

Synthesis and dielectric properties of $Ba(Mg_{1/3}Ta_{2/3})O_3$

9.1 Introduction

The dielectric ceramic, $Ba(Mg_{1/3}Ta_{2/3})O_3$ or BMT, has found wide application in X (8-12 GHz), Ku (12-18 GHz), and K (18-27 GHz) frequency bands. Owing to its exceptionally low dielectric loss (high Q-factor) and temperature stable coefficient of resonance frequency, it has been utilized as a dielectric resonator in output multiplexers of communication satellites [170]. This has considerably decreased insertion losses and hence increased the output microwave power of the satellite. BMT-based dielectric resonators have also been used in microwave oscillators, base stations, radar detectors, etc.

Obtaining BMT ceramic with a high Q-factor is a technologically challenging task. BMT with its melting temperature of ca. 3000 °C [326], is considered one of the most refractory oxides. Several papers have addressed the preparation of high Q BMT ceramics [195, 235, 200, 199]. Nomura et al. [195] obtained high-density (98 %) BMT with $Q \times f$ = 168 THz by doping with 1 mol% of Mn. Matsumoto et al. [235] found that fast heating rates of up to 500 °C/min produce BMT ceramics with $Q \times f$ = 400 THz. Another group, Matsumoto et al. [200] obtained BMT of $Q \times f$ = 430 THz after sintering for 20 hours at 1640 °C. The latter group has also claimed that $BaSnO_3$ is an effective dopant for tuning the temperature coefficient of the resonance frequency, τ_f, in the range of -0.5 to +5.4 ppm/°C.

It is considered that both the high density of the ceramic and the high degree of 1:2 ordering of B-site cations are responsible for low dielectric loss of BMT at microwave frequencies. Although densification of ceramics increases with sintering temperature, the 1:2 ordered phase remains thermodynamically stable below a certain temperature, T_C, and becomes disordered above this temperature. Until now, however, neither the temperature T_C nor the mechanism of the order-disorder phase transition in BMT has been known unambiguously. Several recent papers have reported a theoretical analysis of a high temperature order-disorder transition in perovskite compounds [242, 243]. Takahashi et al. [18] used first-principles calculations to predict that the order-disorder transition in BMT should occur at T_C = 3500 °C which is above the melting point. In view of this high value of apparent T_C, the authors [18] proposed that it is beneficial to sinter BMT at higher temperatures and longer times to increase the degree of cation ordering. In contrast to this prediction, Guo et al. [326] obtained completely disordered BMT single crystals grown by the laser heated pedestal technique at 2960 - 3100 °C. Annealing of these crystals at 1600 °C for 3 hours did not result in increase in the degree of ordering. While analyzing cation ordering transformations in $Ba(Mg_{1/3}Ta_{2/3})O_3$ - $BaZrO_3$ perovskite solid solutions, Chai et al. [217] reported that in pure BMT the 1:2 ordered phase remained stable up to 1650 °C. The sintering temperatures of the BMT ceramics range from 1400 °C to 1650 °C. However, no detailed analysis of the effect of the sintering temperature on the dielectric properties of BMT has been published so far. This chapter reports on the study of the effect of preparation conditions on the degree of 1:2 ordering and its subsequent effect on dielectric properties of BMT ceramics.

9.2 Experimental procedure

In order to investigate the role of precursors, BMT was prepared by two different solid state methods. The first one was a conventional method (referred to as method I) which can be described by the reaction:

$$3BaCO_3 + MgO + Ta_2O_5 \rightarrow 3Ba(Mg_{1/3}Ta_{2/3})O_3 + 3CO_2.$$

In the second method (method II) a $MgTa_2O_6$ precursor was prepared first and then reacted with $BaCO_3$, according to:

$$3BaCO_3 + MgTa_2O_6 \rightarrow 3Ba(Mg_{1/3}Ta_{2/3})O_3 + 3CO_2.$$

The choice of method II was governed by its successful application in preparation of $Pb(Mg_{1/3}Nb_{2/3})O_3$ [327] and $Ba(Zn_{1/3}Ta_{2/3})O_3$ [256] ceramics. High purity (> 99.9%) metal oxides and carbonates (MgO, Ta_2O_5, $BaCO_3$ Cerac) were used for both methods. For method II, $MgTa_2O_6$ precursor was prepared by heating MgO and Ta_2O_5 at 1300 °C for 10 hours. Stoichiometric amounts of the required powders were milled for 2 hours in a Nalgene bottle with ethanol and zirconia grinding balls. The dried powders were pressed into pellets and calcined at 800 - 1400 °C for 2 - 10 hours. For preparation of ceramic samples, the powders calcined at 1400 °C were ground and vibromilled for 10 hours. After addition of a small amount of polyvinyl alcohol binder, the powders were uniaxially pressed into pellets at 800 kg/cm^2 pressure. The pellets were sintered in air at a temperature range between 1550 and 1650 °C for 20 h. The heating and cooling rates were varied from 15 °C/h to 200 °C/h. Phase identification was performed on Rigaku Geigerflex Dmax II diffractometer with Co K_α radiation source (λ =1.7889 Å), a step size of 0.02 ° and a count time of 4 s/step. The microstructure of polished samples was studied by SEM (Philips 515) and optical microscopy (Leitz Wetzlar). Thermally etched samples were analyzed by SEM equipped with EDS (Link Analytical). Samples for TEM (Philips CM12, 120 keV) and electron diffraction were prepared by mechanical grinding followed by dimpling and ion-beam milling until perforation. Details about dielectric measurements at microwave frequencies can be found in Section 4.3.7.

9.3 Synthesis

9.3.1 Thermal analysis

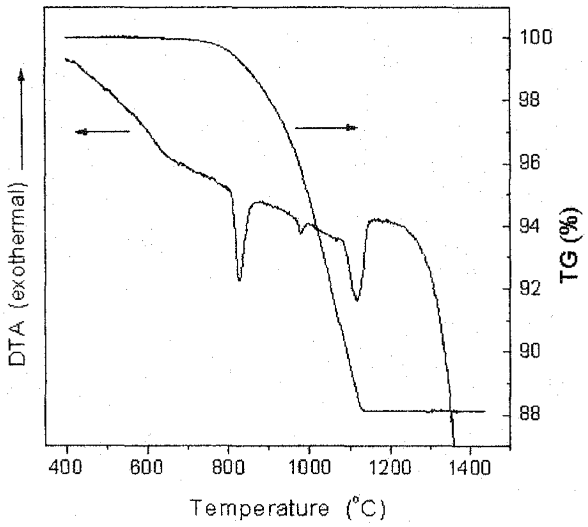

Figure 9.1: DTA and TG of $Ba(Mg_{1/3}Ta_{2/3})O_3$

DTA and TG analysis was performed on stoichiometric mixtures of $MgO + Ta_2O_5 + BaCO_3$ and $MgTa_2O_6 + BaCO_3$. No substantial difference was observed in DTA and TG of method I and II samples. As an example, the DTA and TG for method II BMT are shown in Fig. 9.1. The DTA curve showed endothermal effects at 820...830 °C and 970...980 °C due to the $\gamma \rightarrow \beta$ and $\beta \rightarrow \alpha$ structural phase transitions of $BaCO_3$. The major weight loss in BMT sample occurs in the 800 - 1100 °C range and is attributed to the release of CO_2 from $BaCO_3$. This is manifested by a broad endothermal effect at 1090 - 1130°C.

9.3.2 Phase composition

The XRD patterns of samples calcined at various temperatures and times are presented in Figs. 9.2 and 9.3. The phases in each sample identified from JCPDS files are summarized in Table 9.1. As revealed by XRD analysis, the process of formation of BMT phase is different for the two different methods. In method I, single-phase BMT is completely formed only after heating at 1400 °C for 10

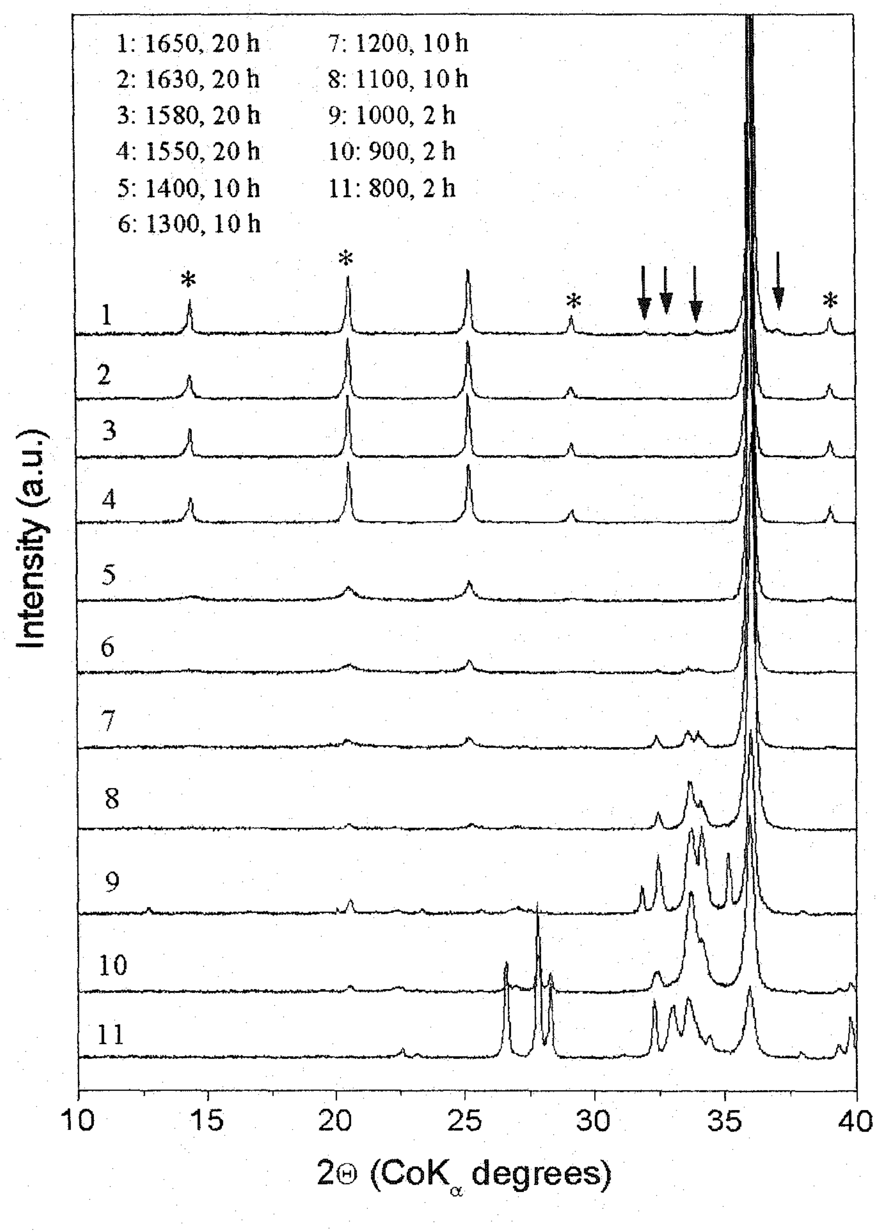

Figure 9.2: XRD patterns of method I BMT calcined at different temperatures. Superstructure reflectios from 1:2 ordered domains are indicated by $*$. The arrows show the traces of the second phase.

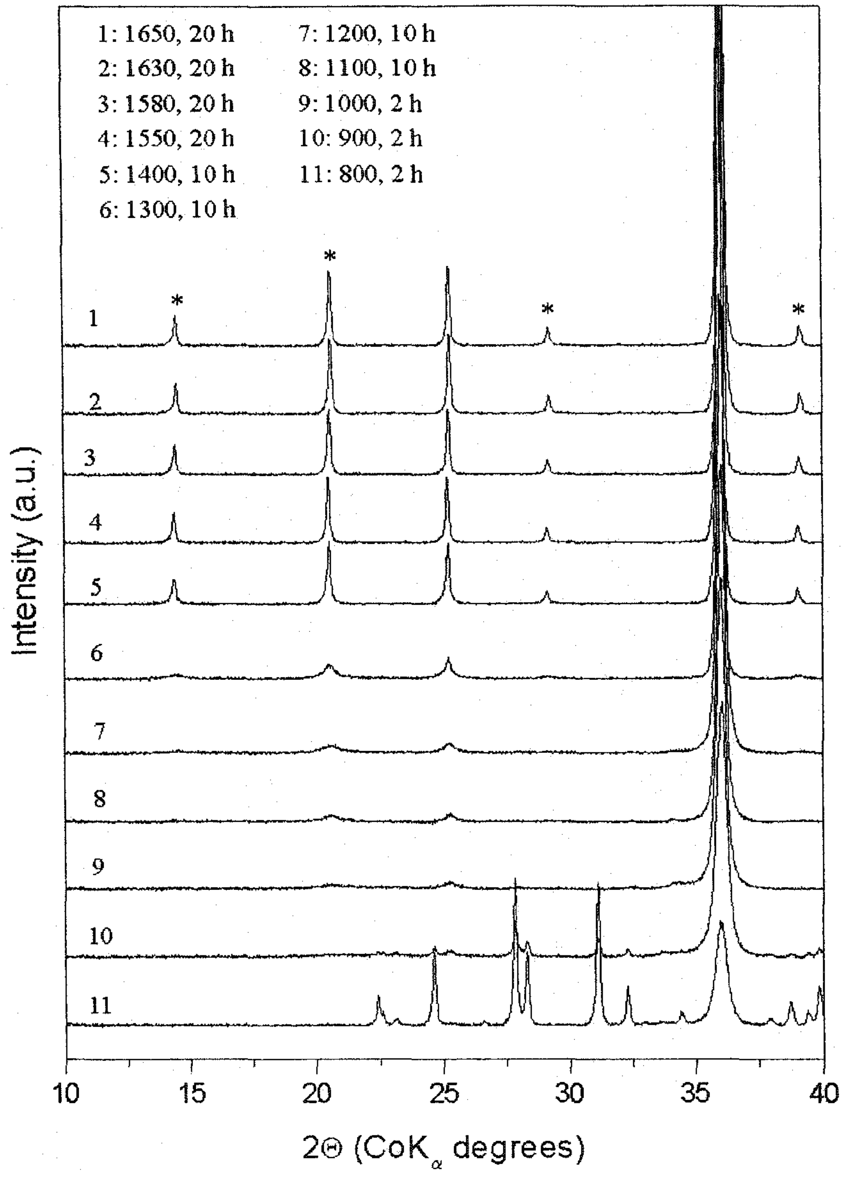

Figure 9.3: XRD patterns of method II BMT calcined at different temperatures. Superstructure reflections from 1:2 ordered domains are indicated by $*$.

hours. In contrast, method II yields nearly pure BMT phase after a 2-hour treatment at 1000 °C. According to Table 9.1, the major difference between the two preparation methods is the presence of undesirable intermediate second phases (i.e., $Ba_4Ta_2O_9$, $Ba_5Ta_4O_{15}$) in method I. These phases, being quite stable at 800 - 1300 °C, impede the formation of single-phase BMT below 1400 °C. Based on our XRD results, formation of BMT in a single-step method can be tentatively described

Table 9.1: Phases comprising method I and II BMT samples prepared at different temperatures and soaking.

Treatment	Method I BMT		Method II BMT	
	Major phases	Minor phases	Major phases	Minor phases
800 °C, 2 h	$BaCO_3$, Ta_2O_5, MgO, $Ba_5Ta_4O_{15}$	$Ba(Mg_{1/3}Ta_{2/3})O_3$	$BaCO_3$, $MgTa_2O_6$, $Ba(Mg_{1/3}Ta_{2/3})O_3$	Ta_2O_5 traces, MgO traces
900 °C, 2 h	$Ba(Mg_{1/3}Ta_{2/3})O_3$, Ta_2O_5, MgO, $Ba_5Ta_4O_{15}$	$Ba_4Ta_2O_9$, $BaCO_3$	$Ba(Mg_{1/3}Ta_{2/3})O_3$	$BaCO_3$, $MgTa_2O_6$
1000 °C, 2 h	$Ba(Mg_{1/3}Ta_{2/3})O_3$, $Ba_4Ta_2O_9$, $Ba_5Ta_4O_{15}$	Unidentified phase, MgO traces	$Ba(Mg_{1/3}Ta_{2/3})O_3$	
1100 °C, 5 h	$Ba(Mg_{1/3}Ta_{2/3})O_3$, $Ba_5Ta_4O_{15}$	$Ba_4Ta_2O_9$, MgO traces	$Ba(Mg_{1/3}Ta_{2/3})O_3$	
1200 °C, 10 h	$Ba(Mg_{1/3}Ta_{2/3})O_3$	$Ba_4Ta_2O_9$, $Ba_5Ta_4O_{15}$	$Ba(Mg_{1/3}Ta_{2/3})O_3$	
1300 °C, 10 h	$Ba(Mg_{1/3}Ta_{2/3})O_3$	$Ba_4Ta_2O_9$ traces $Ba_5Ta_4O_{15}$ traces	$Ba(Mg_{1/3}Ta_{2/3})O_3$	
1400 °C, 10 h	$Ba(Mg_{1/3}Ta_{2/3})O_3$		$Ba(Mg_{1/3}Ta_{2/3})O_3$	
1630 °C, 10 h	$Ba(Mg_{1/3}Ta_{2/3})O_3$	$Ba_3Ta_5O_{15}$ traces	$Ba(Mg_{1/3}Ta_{2/3})O_3$	
1650 °C, 10 h	$Ba(Mg_{1/3}Ta_{2/3})O_3$	$Ba_3Ta_5O_{15}$ traces	$Ba(Mg_{1/3}Ta_{2/3})O_3$	$Ba_3Ta_5O_{15}$ traces

by the following sequence of chemical reactions:

$$x\mathrm{MgO} + x\mathrm{Ta_2O_5} \rightarrow x\mathrm{MgTa_2O_6} \tag{9.1}$$

$$x\mathrm{MgTa_2O_6} + 3x\mathrm{BaO} \rightarrow 3x\mathrm{Ba(Mg_{1/3}Ta_{2/3})O_3} \tag{9.2}$$

$$\frac{5}{2}(1-x)\mathrm{BaO} + (1-x)\mathrm{Ta_2O_5} \rightarrow \frac{1}{2}(1-x)\mathrm{Ba_5Ta_4O_{15}} \tag{9.3}$$

$$\frac{1}{2}(1-x)\mathrm{BaO} + \frac{1}{6}(1-x)\mathrm{Ba_5Ta_4O_{15}} \rightarrow \frac{1}{3}(1-x)\mathrm{Ba_4Ta_2O_9} \tag{9.4}$$

$$\frac{1}{6}(1-x)\mathrm{Ba_5Ta_4O_{15}} + \frac{1}{3}(1-x)\mathrm{Ba_4Ta_2O_9} \rightarrow (1-x)\mathrm{Ba_3Ta_2O_8} \tag{9.5}$$

$$(1-x)\mathrm{Ba_3Ta_2O_8} + (1-x)\mathrm{MgO} \rightarrow 3(1-x)\mathrm{Ba(Mg_{1/3}Ta_{2/3})O_3} \tag{9.6}$$

According to Eqs. 9.1 - 9.6, the perovskite phase is formed by at least two different chemical routes due to the possible reactions of Ta_2O_5 with MgO as well as with BaO. In the first case [Eqs. 9.1- 9.2], the perovskite phase forms at temperatures below 1000 °C. However, the amount of the perovskite phase thus formed is small. In the temperature range of 900 - 1300 °C the two major phases besides BMT are $Ba_4Ta_2O_9$, and $Ba_5Ta_4O_{15}$. One of the mechanisms of their transformation into BMT is described by Eqs. 9.3 - 9.6. The absence of $Ba_3Ta_2O_8$ in calcined powders suggests that this phase has a labile character (i.e., upon formation it immediately reacts with MgO). An unidentified phase was detected in the powders calcined at 1000 °C. This leads to the conclusion that there exists one more chemical route of formation of BMT besides those described in Eqs. 9.1 - 9.6. The powders prepared by method II contained traces of MgO and Ta_2O_5 phases due to incomplete synthesis of $MgTa_2O_6$ precursor. These phases disappeared after heat treatment at 900

°C. No additional second phases were detected during heat treatment of the method II powders. This indicates that the perovskite phase in method II forms directly by reaction of $MgTa_2O_6$ with BaO:

$$3BaO + MgTa_2O_6 \rightarrow 3Ba(Mg_{1/3}Ta_{2/3})O_3 \tag{9.7}$$

Within the XRD accuracy of 2-3%, BMT samples obtained by both method I and method II in the temperature range of 1400 to 1620 °C do not contain any other phases. However, the XRD analysis of method I samples sintered at 1630 °C and 1650 °C reveals the presence of a small amount of a second phase, identified as $Ba_3Ta_5O_{15}$ [328]. Traces of the $Ba_3Ta_5O_{15}$ phase were also detected in the method II BMT sintered at 1650 °C as seen in Fig. 9.4

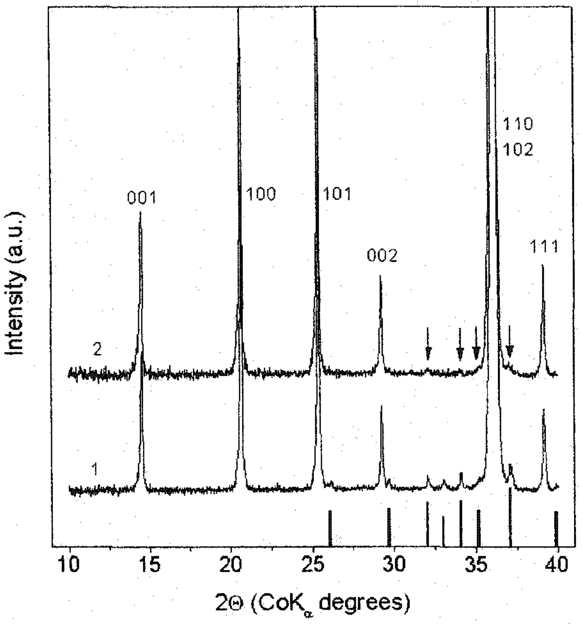

Figure 9.4: XRD patterns of method I (1) and method II (2) BMT sintered at 1650 °C for 20 h. Vertical bars represent the relative intensity of reflections from $Ba_3Ta_5O_{15}$ phase. The arrows indicate traces of $Ba_3Ta_5O_{15}$ phase in method II BMT.

9.3.3 1:2 cation ordering

It is known that BMT can exist in ordered and disordered forms [326]. In the low-temperature ordered form (space group $P\bar{3}m1$) the Mg^{2+} and Ta^{5+} cations are distributed on individual (111) planes of the perovskite subcell with alternating {Mg, Ta, Ta} layers. This is the 1:2 ordered configuration with the ordered phase having a hexagonal crystal structure. In the high-temperature disordered phase, the Mg^{2+} and Ta^{5+} cations are randomly distributed on octahedral sites of the perovskite subcell which raises the symmetry of the system to cubic (space group $Pm3m$). According to Figs. 9.2 and 9.3, weak reflections from 1:2 ordered BMT domains begin to become visible for powders treated at a temperature as low as 1000 °C. The ordering increases with the annealing temperature. To quantitatively examine the degree of 1:2 ordering in BMT, one has to determine the ordering parameter, S,

$$S = \sqrt{\frac{(I_{100}/I_{110,012,102})_{obs}}{(I_{100}/I_{110,012,102})_{calc}}} \tag{9.8}$$

where $(I_{100}/I_{110,012,102})_{obs}$ is the ratio of the observed intensity of the (100) superlattice reflection to that of (110,012,102) main reflection, and $(I_{100}/I_{110,012,102})_{calc}$ is the calculated value for completely ordered structure.

According to calculations presented in Section 10.2.3, the ordering parameter for a completely ordered BMT structure is 0.0842 for Co K_α radiation. The values of the observed intensities, I_{100} and $I_{110,012,102}$, were found from the area of the corresponding XRD peaks. The ordering parameter, S, for ceramics sintered at different temperatures for 20 hours and cooled down to 1400 °C at a rate of 20 °C/h is plotted in Fig. 9.5. For both method I and method II ceramics the value of

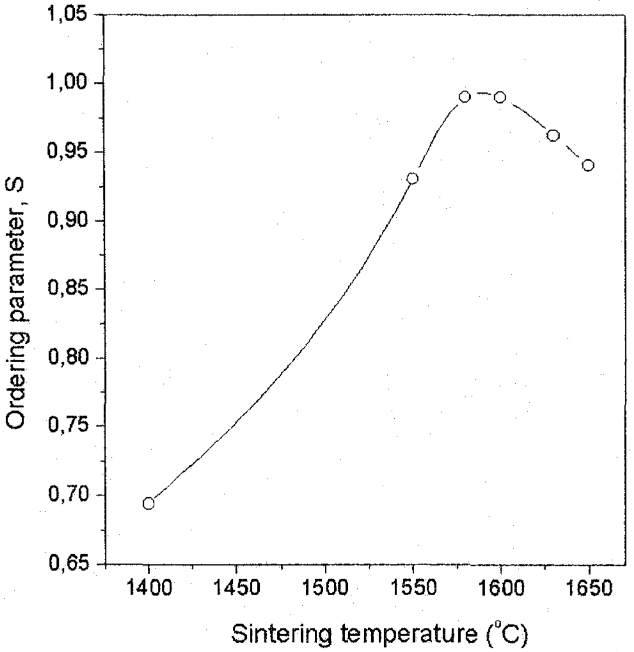

Figure 9.5: Dependence of the ordering parameter on the sintering temperature of the method II BMT.

S increases with sintering temperature, goes through a maximum of 0.995 at 1580 °C, and then decreases to 0.948 at 1650 °C. To examine the possibility of increasing the degree of ordering by postsinter annealing, ceramics sintered at 1630 °C and 1650 °C were annealed at 1580 °C for 20 hours. However, the value of S did not change.

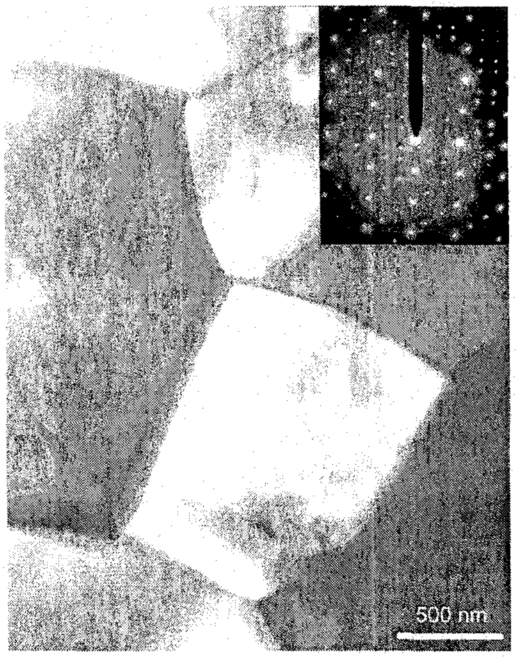

Figure 9.6: Bright field TEM image of BMT sample sintered at 1580 °C for 20 h. The inset shows the SAD pattern from 1:2 ordered domains.

Fig. 9.6 shows a bright-field TEM image of BMT sintered at 1580 °C. A selected area electron diffraction (SAD) pattern taken along the [011] main zone axis is shown in the inset of Fig. 9.6. Extra electron diffraction spots at $\{ h \pm \frac{1}{3},\ k \pm \frac{1}{3},\ l \pm \frac{1}{3}, \}$ from 1:2 ordered domains are observed on SAD pattern. It was found that all BMT ceramic samples sintered in the 1570 - 1650 °C temperature range consist of large (> 200 nm) 1:2 ordered domains. However, due to the relatively small electron-transparent area of the samples and large size of the 1:2 domains, it was impossible to perform any statistical analysis of the size of those domains by the electron diffraction technique.

9.3.4 Microstructure and density

Microstructural observations of the samples revealed a gradual increase of the grain size from 2.5 to 15 μ m for ceramics sintered at 1570 - 1650 °C. The average grain size is listed in Table 9.2. The second phase was observed on the surface of the thermally etched BMT samples. Fig. 9.7 shows SEM images of method I and II BMT samples sintered at 1650 °C and thermally etched at 1450 °C for 2 hours. The EDS chemical analysis of the matrix phase and second-phase has revealed that the ratio of the Ba to Ta major peaks equals 0.888 for the matrix and 0.357 for the second-phase. This agrees well with the chemical composition of the second phase of $Ba_3Ta_5O_{15}$. Regarding the formation of this phase the following mechanism is proposed. Owing to the close-packed perovskite structure of BMT and tolerance factor close to unity, it is most likely that Schottky defects predominate in BMT

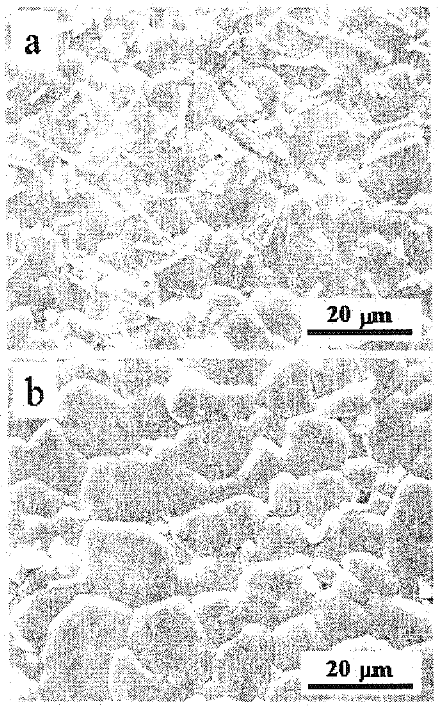

Figure 9.7: SEM images of a) method I and b) method II BMT sintered at 1650 °C for 20 h.

at sintering temperatures. While the equilibrium point defect chemistry of the BMT grain bulk is governed by the mass action relationships, the interfacial concentration of defects is determined by their formation energy. In case of Schottky defects, the interface performs as an ideal source or sink of defects, in other words, defect formation occurs at the interface. The difference in the individual defect formation energies leads to preferential enrichment of the interface in the ion of lower vacancy formation energy. This ion will be predominant in the second phase formed at the interface and in the voids of the matrix grains. Based on our XRD and EDS results, it can be assumed that the Ta ion has the lowest defect formation energy in the BMT compound. Fig. 9.8 shows the dependence

Table 9.2: Grain size, d, temperature coefficient of resonance frequency, τ_f and dielectric constant, ε' of BMT ceramics prepared by 2 different methods and sintered for 20 hours.

T_{sint}	Method I BMT			Method II BMT		
	d, μm	τ_f, ppm/K	ε'	d, μm	τ_f, ppm/K	ε'
1580 °C	3.1	0.2	22.0	3.5	-0.3	22.5
1600 °C	5.0	1.8	23.0	6.4	1.2	23.7
1630 °C	10.0	2.9	23.0	10.2	2.5	23.9
1650 °C	15.0	4.1	22.8	15.0	3.5	23.9

of the relative density on sintering temperature. A relative density was calculated from

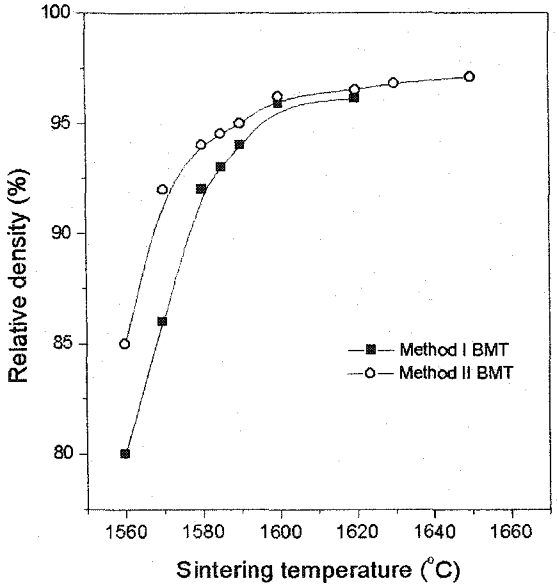

Figure 9.8: Dependence of the density of the BMT samples on sintering temperature. The samples were sintered for 20 h.

$$\rho = \frac{\rho_m}{\rho_{th}} \times 100\% \tag{9.9}$$

where ρ_m is the measured density and $\rho_{th} = 7.657\ \mathrm{g \cdot cm^{-3}}$ is the theoretical density of BMT [212]. A meaningful calculation of the density of method I ceramics sintered above 1620 °C was not possible due to the presence of the second phase. However, the microstructural observations of ceramics sintered at 1630 °C and 1650 °C revealed that method I BMT has a larger proportion of voids than method II ceramics sintered at the same temperatures. We may conclude that over the whole range of sintering temperatures, method II ceramics have a higher density than that of method I. In general, the density of ceramics increases with sintering temperature. Method II ceramic sintered at 1650 °C has the highest density of 97.3 %.

9.4 Dielectric properties

According to Fig. 9.9, method II ceramics have higher values of dielectric constant, which can be explained by their higher density. In addition, method I ceramics sintered above 1620 °C show a slight decrease of the dielectric constant with sintering temperature, T_{sint}. The possible reason for such behavior might be the presence of the $Ba_3Ta_5O_{15}$ second phase with apparently low ε'. For method II ceramics, the value of ε' levels off at 24 ± 0.5 for $T_{sint} > 1600$ °C. This value agrees well with the dielectric constant of BMT sintered at 1650 °C reported by Youn et al. [236]. We cannot

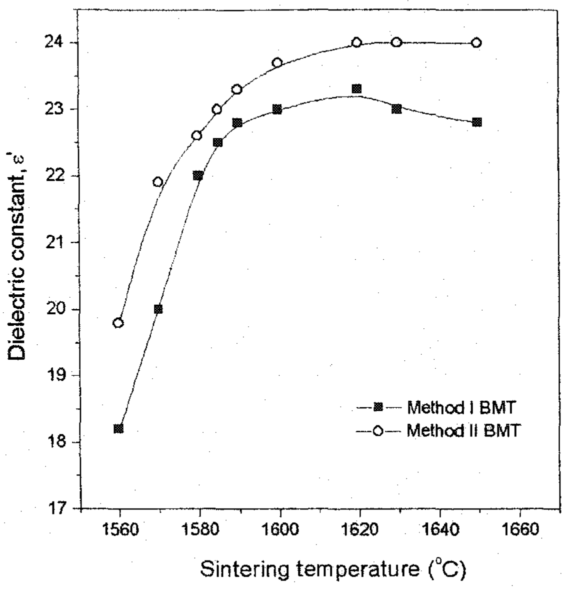

Figure 9.9: Dependence of the dielectric constant at 10 GHz on sintering temperature of the BMT ceramics.

explain the anomalously high dielectric constant ($\varepsilon' = 37$) obtained by Tien et al. [254] in BMT sintered at 1600 °C. According to Fig. 9.10, the dependence of dielectric constant on the porosity of ceramics obeys the Maxwell-Wagner relation [329]

$$\varepsilon' = \varepsilon_1' \left\{ 1 + \frac{3\gamma(\varepsilon_2' - \varepsilon_1')}{2\varepsilon_1' + \varepsilon_2'} \right\} \tag{9.10}$$

where $\varepsilon' = 25$ for completely dense BMT ceramics, ε_2' is the permittivity of vacuum, and γ is the porosity of ceramics.

Fig. 9.11 shows the dependence of $Q \times f$ on sintering temperature with the bars showing the range of variation of $Q \times f$. The curves show a maximum at $T_{sint} = 1590$ °C for method I BMT and at $T_{sint} = 1580$ °C for method II BMT. As also evident from Fig. 9.11, the maximum values of $Q \times f$ obtained for method I and II ceramics were 200 THz and 280 THz, respectively. The value of $Q \times f$ decreases appreciably for samples sintered both above and below 1585 ± 5 °C. It is worth noting that the density of ceramics exhibiting the highest value of $Q \times f$ was approximately 94 %. For samples sintered below 1580 °C, the low value of $Q \times f$ can be attributed both to poor densification and insufficient ordering on the B-sublattice. For samples sintered above 1590 °C, although the density continues to increase, $Q \times f$ decreases and reaches a value of 80 - 130 THz at $T_{sint} = 1650$ °C.

Measurement of the temperature coefficient of the resonant frequency, τ_f, of BMT DRs, which was performed by using a rectangular copper waveguide, gives a total temperature coefficient of the

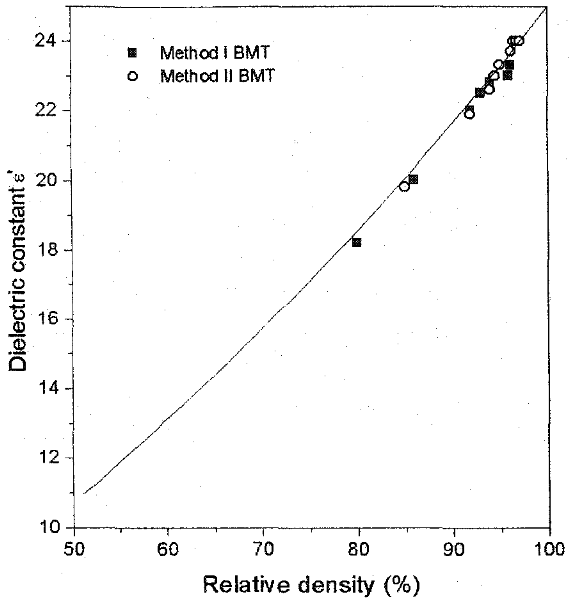

Figure 9.10: Dependence of the dielectric constant on the density of BMT samples. The solid line was calculated from Eq. 9.10.

resonance frequency,τ_f^t, of the whole *waveguide and DR* system by the equation:

$$\tau_f^t = \tau_f^w + \tau_f \tag{9.11}$$

where τ_f^w is a temperature coefficient of the resonance frequency of the waveguide, and τ_f is the temperature coefficient of the resonance frequency of the DR without enclosure. According to O'Bryan et al. [330] is given by

$$\tau_f = -\alpha - \frac{1}{2}\tau_\varepsilon \tag{9.12}$$

where α is the linear thermal expansion coefficient of the DR ($\alpha = \frac{dlnl}{dT}$), and τ_ε is the temperature coefficient of the dielectric constant. The value of τ_f^w is specific to the thermal expansion coefficient of the waveguide material and to the spacing between the waveguide walls and the DR, which makes its accurate determination difficult. In order to obtain an approximate value of τ_f in Eq. 9.11, the value of τ_f^w was calculated by using a similar size dielectric resonator with known τ_f [264]. It was found that our copper waveguide had $\tau_f^w \approx$ -1.2 ± 0.5 ppm/K. The shift of the resonant frequency, Δf_c, of the whole *waveguide and DR* system with increase in temperature is shown in Fig. 9.11. The values for BMT ceramics sintered at different temperatures were determined from Eq. 9.11, and are listed in Table 9.2. Both the data in Table 9.2 and curves in Fig. 9.12 show that τ_f increases with sintering temperature.

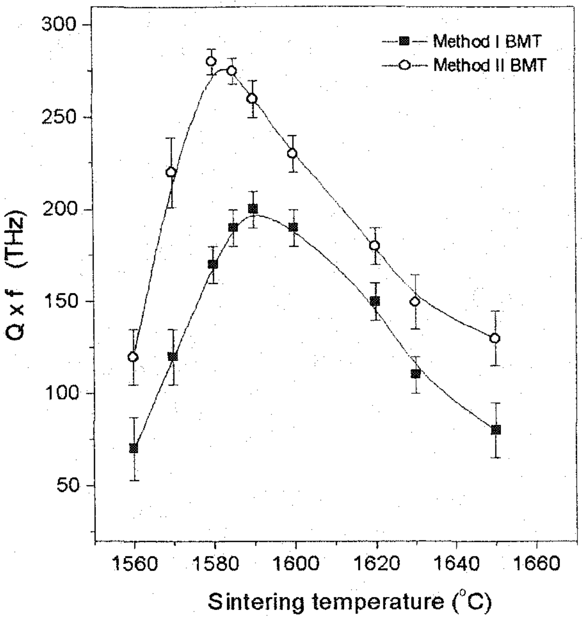

Figure 9.11: Dependence of $Q \times f$ on the sintering temperature of BMT samples. The samples were sintered for 20 h.

9.5 Discussion

Since ε' of the BMT crystal is entirely determined by the polar phonon contribution, no dielectric dispersion is expected below the submillimeter range. The behavior of ε'', however, is more complex. According to Tagantsev et al. [252] two frequency regimes of ε'' variation should be distinguished: (i) at frequencies between γ_T and Ω_i where Ω_i is the eigenfrequency of the i-th phonon mode, and γ_T is the averaged damping of thermally populated phonons, the frequency dependence of ε'' is given by $\varepsilon''(\omega) \propto T\omega^2$, (ii) at ω below γ_T, ε'' is linearly proportional to frequency, i.e., $\varepsilon''(\omega) \propto T^2\omega$. In the microwave range, the energy of photons is much lower than that of optical phonons. Thus, due to the energy conservation requirements, the incident photons cannot be absorbed by the excitation of the transverse optical (TO) phonons. Hence, at temperatures of the order of the Debye temperature or higher, the major dielectric loss comes from the two-phonon difference absorption [193] (three-quantum process). In this process, an incident photon couples to an intermediate TO phonon which in turn couples to two other phonons. One phonon is absorbed and another created with the energy difference being equal to the energy of the incident photon. Due to the small energy of the incident photon in the microwave range, this process occurs close to the lines of degeneracy of the phonon branches in the Brillouin zone. High-temperature order-disorder transition of BMT from low to high crystal symmetry increases the number of degeneracies of the phonon modes. This in turn will increase the dielectric loss due to the increased probability of the three-quantum process. Experimental results presented in Figs. 9.5 and 9.11 confirm this assumption. The decrease of the

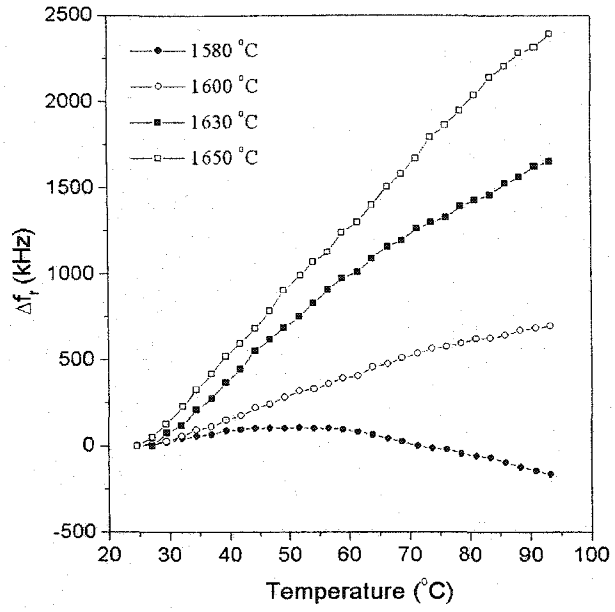

Figure 9.12: Temperature dependence of the shift of the resonance frequency of method I BMT dielectric resonators sintered at different temperatures.

$Q \times f$ follows the decrease of the ordering parameter, S, for samples sintered above 1590 °C.

In addition to purely intrinsic dielectric loss, extrinsic loss due to defects, impurities, porosity, second phase, and grain boundaries will also contribute to the lowering of the Q-factor. It is found that ceramics prepared by method I have higher porosity and lower $Q \times f$ value compared with method II BMT. The $Ba_3Ta_5O_{15}$ second phase is found by EDS and XRD in BMT sintered above 1630 °C. The second phase was mostly concentrated on the internal surface of the voids. Formation of Ta-rich second phase will change the stoichiometric composition of BMT grains by introducing tantalum vacancies into the BMT matrix. Since the process of disordering involves interdiffusion of and cations it will be significantly facilitated in the region of high vacancy concentration.

As mentioned above, experimental results have shown that the degree of 1:2 ordering in BMT starts to decrease for samples sintered above 1585 ± 5 °C. This temperature, however, is much lower than that obtained in the theoretical work of Takahashi et al. [18]. It can be suggested that this difference may originate from the fact that in the cluster calculations of Takahashi et al. [18] vacancies were not taken into account. The presence of vacancies in the BMT structure at sintering temperatures will significantly lower the temperature of the order-disorder phase transition. Similar arguments were proposed by Hong et al. [240] who studied the order-disorder transition in $Ba(Ni_{1/3}Nb_{2/3})O_3$ and $Ba(Zn_{1/3}Nb_{2/3})O_3$. They reported formation of appreciable amounts of a Nb-rich liquid phase in samples sintered near and above the order-disorder phase transition (T_C = 1300 - 1350 °C). The temperature of order-disorder phase transition in $Ba(Zn_{1/3}Nb_{2/3})O_3$ was found to be also much lower than that calculated by Takahashi et al. [18]. It was found in this work that neither slow cooling nor postsinter annealing at 1580 °C for 20 hours could reinstate the high degree of ordering in BMT ceramics sintered at 1630 °C and 1650 °C. This suggests that upon cooling from sintering temperature, the high-temperature disordered phase in BMT becomes thermoelastically arrested. Thus, in order to obtain low-loss BMT ceramics, it is crucial to preserve a high degree of B-site cation ordering starting from the earliest stages of sintering. This can be done by both reducing the sintering temperature at the expense of sintering time and by reducing the heating rate to avoid a fast mass transport during nucleation and growth of the 1:2 ordered phase.

9.6 Conclusions

It was shown that in the conventional synthesis method, intermediate phases (e.g. $Ba_4Ta_2O_9$, $Ba_5Ta_4O_{15}$) inhibit formation of single-phase $Ba(Mg_{1/3}Ta_{2/3})O_3$ up to 1400 °C, whereas utilization of a $MgTa_2O_6$ precursor produces the nearly pure perovskite phase after treatment at 1000 °C. In the temperature range of 1400-1620 °C, the $Ba(Mg_{1/3}Ta_{2/3})O_3$ ceramic remains single phase. Traces of the $Ba_3Ta_5O_{15}$ phase were detected by XRD and EDS in samples sintered above 1630 °C. As revealed by XRD and microwave dielectric measurements, the highest degree of B-site cation ordering in BMT was achieved for samples sintered at $T_{sint} = 1585 \pm 5$ °C. Both the decrease in ordering and formation of the second phase at high sintering temperatures are responsible for an increase in dielectric loss and increase in the temperature coefficient of the resonance frequency. For samples sintered above this temperature, the high degree of ordering cannot be recovered by prolonged postsinter annealing or by slow cooling.

Chapter 10

Synthesis and dielectric properties of $Ba(Mg_{1/3}Nb_{2/3})O_3$, $Ba(Zn_{1/3}Nb_{2/3})O_3$, $Ba(Ni_{1/3}Nb_{2/3})O_3$, and $Ba(Ni_{1/3}Ta_{2/3})O_3$

10.1 Introduction

In Chapter 9 the effect of preparation conditions and dielectric properties of $Ba(Mg_{1/3}\ Ta_{2/3})O_3$, or BMT, ceramics have been reported. It was found that above a critical temperature T_C (T_C = 1585 °C), the BMT starts to disorder. The process of disordering in BMT is accompanied by the appearance of the $Ba_3Ta_5O_{15}$ second phase. In contrast to the order-disorder phase transition in $Pb(B'_{1/3}B''_{2/3})O_3$ complex perovskites, the process of disordering in BMT is irreversible i.e., the degree of ordering does not change significantly after annealing at lower temperatures. It was also found that BMT sintered above T_C possesses higher dielectric loss in agreement with the theory of intrinsic loss in dielectrics [193]. Until now, most research efforts were restricted to investigation of the BMT compound owing to its wide commercial utilization [331]. It is important to find out whether other $Ba(B'_{1/3}B''_{2/3})O_3$ complex perovskites show similar dependence of their dielectric properties on sintering conditions. Several complex perovskites including $Ba(Mg_{1/3}Nb_{2/3})O_3$, $Ba(Zn_{1/3}Nb_{2/3})O_3$, $Ba(Ni_{1/3}Nb_{2/3})O_3$, and $Ba(Ni_{1/3}Ta_{2/3})O_3$, further abbreviated as BMN, BZN, BNN, and BNT were chosen for this study. The data about their dielectric properties are rather contradictory (see Table

10.1). BZN and BNN were initially considered disordered perovskites [239, 333, 334], until Yoshioka [248] and Akbas and Davies [219] showed that BZN can be prepared with 1:2 cation ordering when sintered at 1350 °C. Hong et al. [240] also reported that below 1400 °C, BNN has an ordered 1:2 perovskite structure. One can also find a major discrepancy between experimental and theoretical values of T_C for $Ba(B'_{1/3}B''_{2/3})O_3$ compounds. Usually, experimental temperatures of the order disorder phase transition are ca. 1000 °C lower than calculated ones [244, 245]. This chapter focuses on the effect of preparation conditions on the degree of cation ordering and dielectric properties of BMN, BZN, BNN, and BNT complex perovskites.

Table 10.1: Delectric properties of several $Ba(B'_{1/3}B''_{2/3})O_3$ compounds.

System	ε	Q×f, THz	τ_f, ppm/K	Ref.
$Ba(Ni_{1/3}Ta_{2/3})O_3$	23	50	-18	[182]
	22	95.5	-10.5...-13.5	this work
$Ba(Mg_{1/3}Nb_{2/3})O_3$	32	55	+33	[189]
	31...34	40	+ 21	[203]
	32	71	+ 30	[332]
	32	65	+ 18.8	[233]
	31.4	160	+14.2...+34	this work
$Ba(Zn_{1/3}Nb_{2/3})O_3$	41	55	+31	[180]
	41	87	+31	[189]
	40	69	+20.7...+23	this work
$Ba(Ni_{1/3}Nb_{2/3})O_3$	36	70	+20	[181]
	35.4	35	-4.9...+5	this work

10.2 Synthesis of BMN, BZN, BNN, and BNT

BMN, BZN, BNN, and BNT powders were prepared by the solid state method using $MgNb_2O_6$, $ZnNb_2O_6$, $NiNb_2O_6$, $NiTa_2O_6$, and $BaCO_3$ precursors. As was reported in Chapter 9, this method offers several advantages over using simple metal oxide precursors. For example, it yields single-phase ceramics at lower sintering temperatures. It also results in higher density and lower dielectric loss. Following ball milling in an alcohol slurry for 2 hours, the milled powders were dried, then calcined at 1000 - 1200 °C for 5 hours. The calcined powders were reground and vibromilled for 10 hours, then dried, mixed with polyvinyl alcohol binder and pressed into pellets at 800 kg/cm^2

pressure. The pellets were sintered in air at temperatures of 1300 - 1620 °C for 20 hours. The heating and cooling rates were varied from 15 to 200 °C/h.

10.2.1 Thermal analysis

DTA and TG analysis was performed on stoichiometric mixtures of $MgNb_2O_6$ + $BaCO_3$, $ZnNb_2O_6$ + $BaCO_3$, $NiNb_2O_6$ + $BaCO_3$, and $NiTa_2O_6$ + $BaCO_3$. The results are shown in Figs. 10.1, 10.2, 10.3, and 10.4. All DTA curves show similar endothermic effects at 820 – 830 °C and 970 – 980 °C due to the $\gamma \rightarrow \beta$ and $\beta \rightarrow \alpha$ structural phase transitions of $BaCO_3$. The major weight loss in BMN, BZN, BNN, and BNT samples occurs in the 800 - 1200 °C range and is attributed to the release of CO_2 from $BaCO_3$. This is manifested by a broad endothermic effect at 1100 - 1150°C in BZN, BNN, and BNT samples. In the BMN sample, the endothermic effect at 1100°C is hindered by a strong exothermic effect at 1200°C which is apparently associated with grain growth.

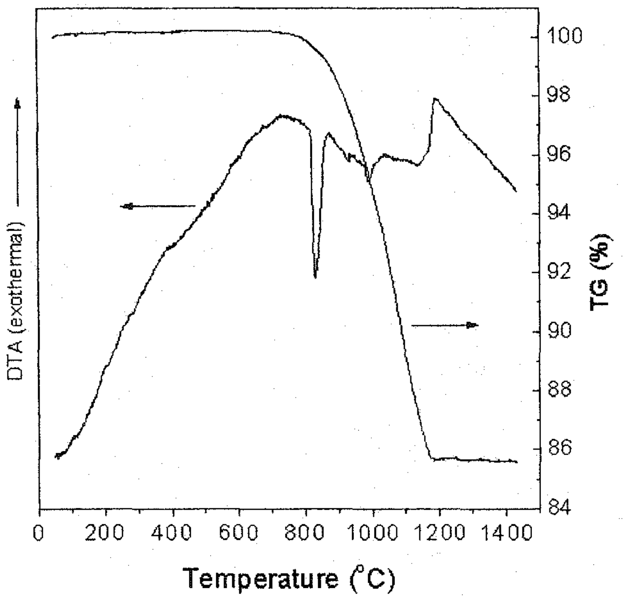

Figure 10.1: DTA and TG of $MgNb_2O_6$ + $BaCO_3$

10.2.2 Phase composition

The XRD patterns of BMN, BZN, BNN, and BNT samples calcined at various temperatures are shown in Figs. 10.5, 10.6, 10.7, and 10.8. Phase compositions of samples calcined at different temperatures and times were identified from JCPDS files and are listed in Tables 10.2, 10.3, 10.4, and 10.5. In contrast to the conventional single-oxide method wich results in several undesirable

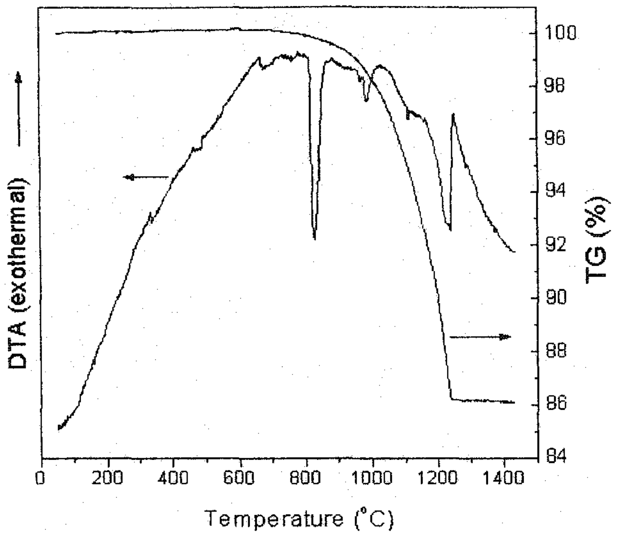

Figure 10.2: DTA and TG of $ZnNb_2O_6 + BaCO_3$

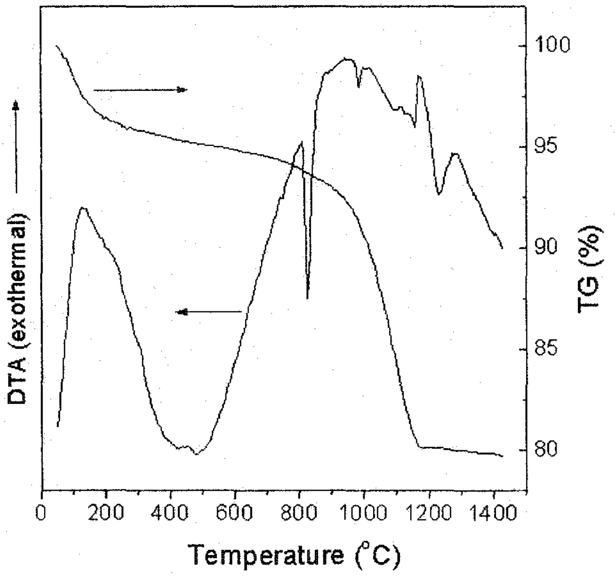

Figure 10.3: DTA and TG of $NiNb_2O_6 + BaCO_3$

second phases (see Chapter 9), the double-oxide method employed in this work gives single-phase complex perovskites formed according to the following reaction:

$$B'B''_2O_6 + BaO \rightarrow Ba(B'_{1/3}B''_{2/3})O_3 \tag{10.1}$$

Within the XRD accuracy of 2%, BMN, BZN, BNN, and BNT powders formed a single phase perovskite compound at 1000°C, 950°C, 1000°C, and 950°C respectively. As revealed by XRD

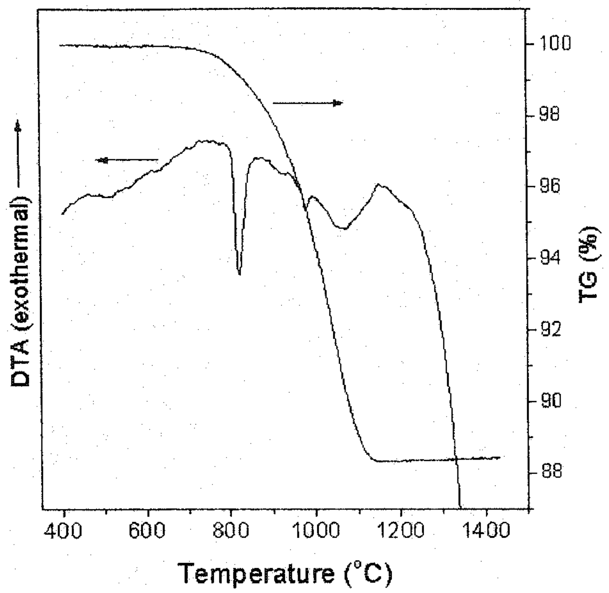

Figure 10.4: DTA and TG of $NiTa_2O_6$ + $BaCO_3$

analysis, up to a critical temperature, BMN, BZN, BNN compounds remained single phase. However, above a critical temperature, which is unique to each compound (see Tables 10.2, 10.3, and 10.4), a second phase (e.g., $Ba_3Nb_5O_{15}$ in case of BMN and BNN and an unidentified phase in case of BZN) appeared. The BNT compound remained in a single phase form above 950°C and no second phase could be detected up to 1610°C.

Table 10.2: Phase composition of calcined powders of $BaCO_3$ + $MgNb_2O_6$

T, °C	Major phases	Minor phases
800	$BaCO_3$, $MgNb_2O_6$	$Ba(Mg_{1/3}Nb_{2/3})O_3$-cubic, MgO traces, Nb_2O_5 traces
900	$Ba(Mg_{1/3}Nb_{2/3})O_3$-cubic	$MgNb_2O_6$, $BaCO_3$
1000	$Ba(Mg_{1/3}Nb_{2/3})O_3$-cubic	
1100	$Ba(Mg_{1/3}Nb_{2/3})O_3$-hex	
1200	$Ba(Mg_{1/3}Nb_{2/3})O_3$-hex	
1500	$Ba(Mg_{1/3}Nb_{2/3})O_3$-hex	
1620	$Ba(Mg_{1/3}Nb_{2/3})O_3$-hex	$Ba_3Nb_5O_{15}$ traces

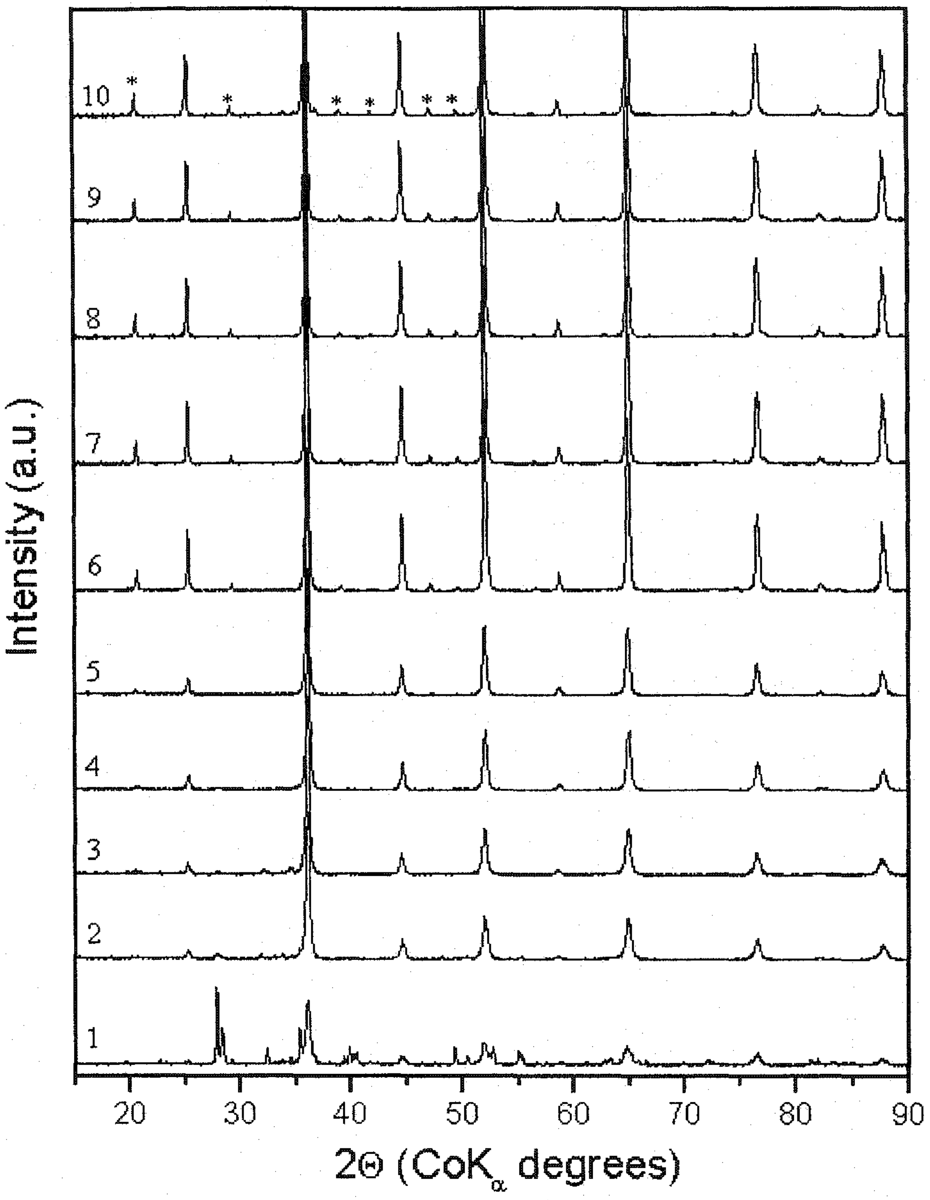

Figure 10.5: XRD patterns of $Ba(Mg_{1/3}Nb_{2/3})O_3$ samples calcined at 1) 800°C, 2) 900°C, 3) 1000°C, 4) 1100°C, 5) 1200°C, 6) 1360°C, 7) 1400°C, 8) 1445°C, 9) 1500°C, 10) 1620°C. Superstructure reflections from 1:2 ordered phase are indicated by $*$.

10.2.3 1:2 cation ordering

Several $Ba(B'_{1/3}B''_{2/3})O_3$ perovskites can exist in disordered or 1:2 ordered phases. The ability of $Ba(B'_{1/3}B''_{2/3})O_3$ to order depends on the size, valence and mass of the B-site cations. The degree of 1:2 order also depends on sample preparation. From a crystallographic point of view, the ordering parameter S can be defined by the difference between on-site and off-site ions occupying B′ and B″

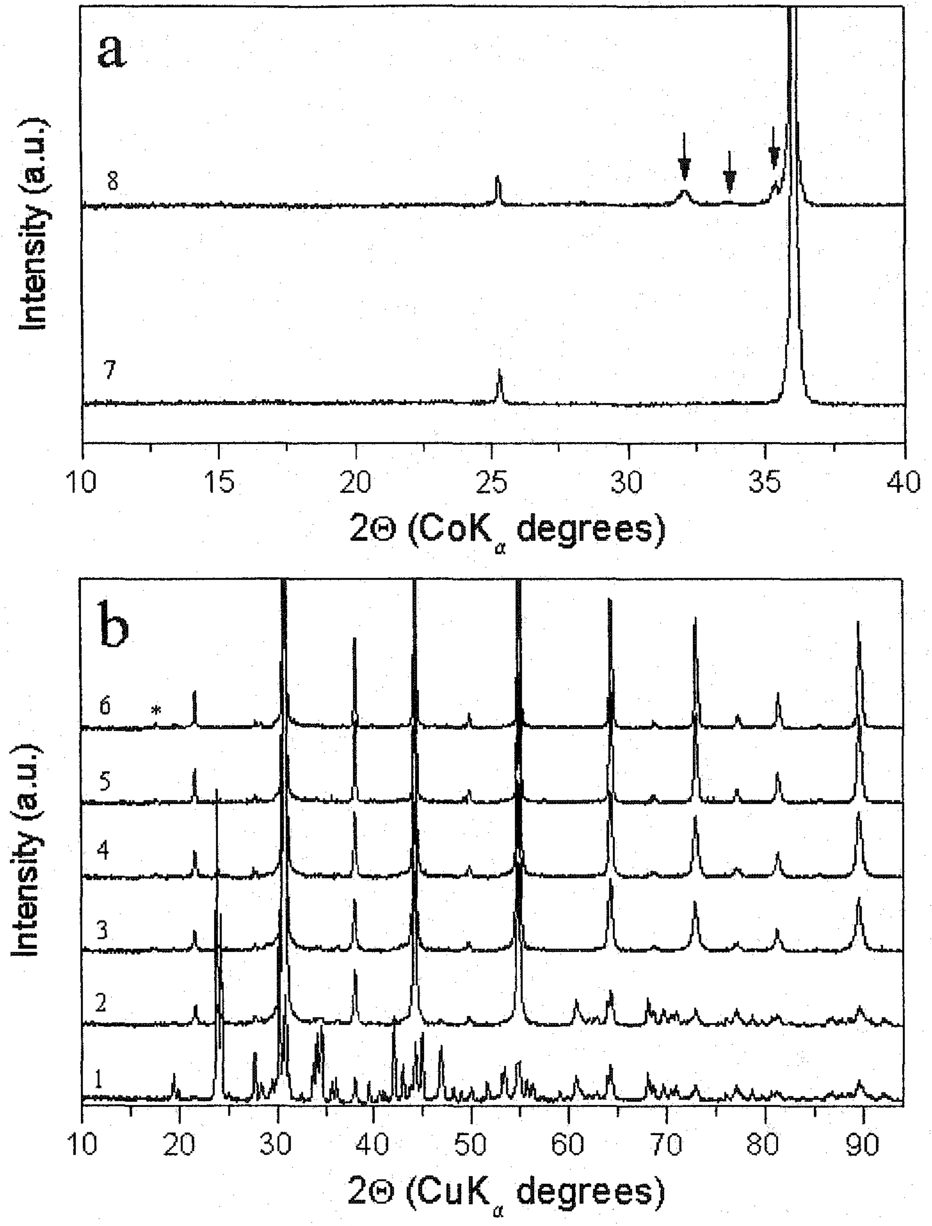

Figure 10.6: XRD patterns obtained with a) Co K_α source and b) Cu K_α source of $Ba(Zn_{1/3}Nb_{2/3})O_3$ samples calcined at 1) 800°C, 2) 850°C, 3) 900°C, 4) 1000°C, 5) 1100°C, 6) 1200°C, 7) 1380°C, 8) 1460°C. Superstructure reflections from 1:2 ordered phase are indicated by $*$. High temperature second phase is indicated by arrows.

sites:

$$S = B''_{B''} - B''_{B'} = B'_{B'} - B'_{B''} \tag{10.2}$$

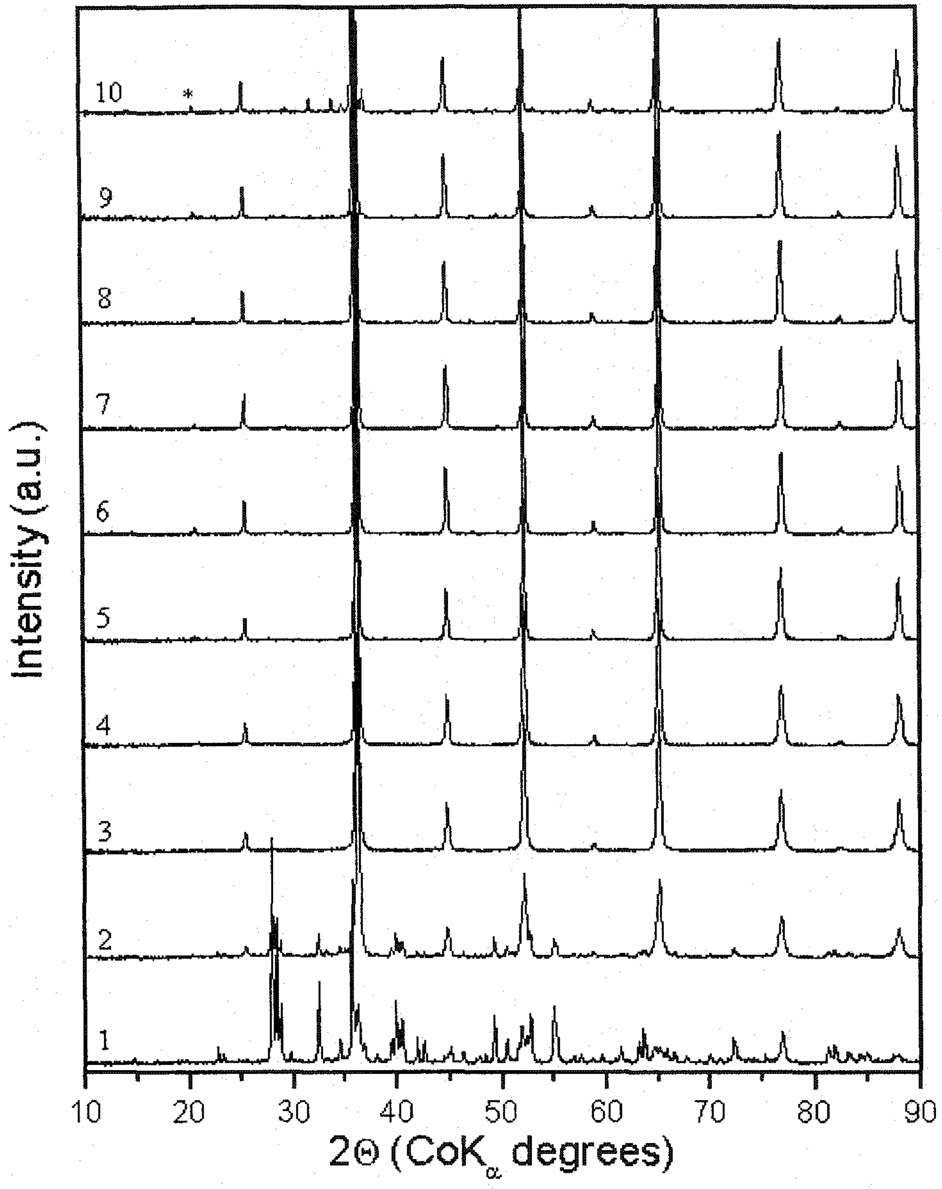

Figure 10.7: XRD patterns of $Ba(Ni_{1/3}Nb_{2/3})O_3$ samples calcined at 1) 800°C, 2) 900°C, 3) 1000°C, 4) 1100°C, 5) 1200°C, 6) 1320°C, 7) 1360°C, 8) 1400°C, 9) 1450°C, 10) 1500°C. Superstructure reflections from 1:2 ordered phase are indicated by $*$.

where $B''_{B''}$ is the fraction of B'' ions in B''-sites, $B''_{B'}$ is the fraction of B' ions in B''-sites, and so on. Although, counting atoms in the crystal is not feasible, the ordering parameter can be deduced from the ratio of the X-ray intensities of the diffraction peaks associated with cation ordering. In $Ba(B'_{1/3}B''_{2/3})O_3$ perovskites, the ordering parameter, S, is determined by the ratio of the intensity of the strongest supperlattice reflection, (100), to the strongest peak of the $Ba(B'_{1/3}B''_{2/3})O_3$

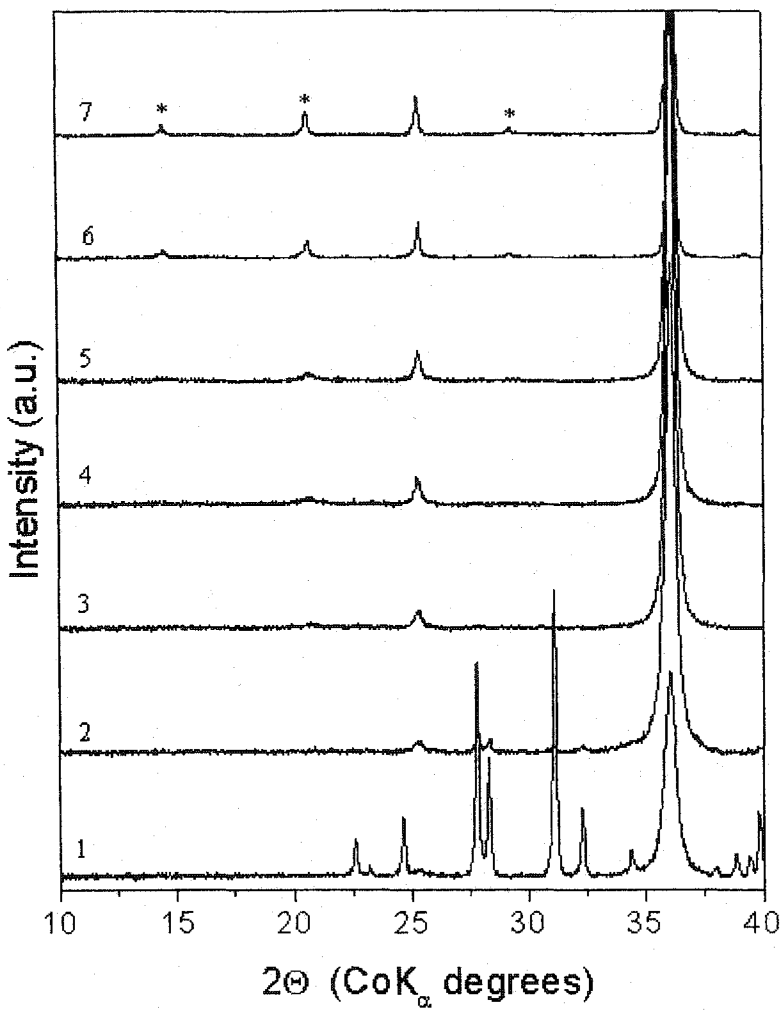

Figure 10.8: XRD patterns of Ba($Ni_{1/3}Ta_{2/3}$)O_3 samples calcined at 1) 800°C, 2) 900°C, 3) 1000°C, 4) 1100°C, 5) 1200°C, 6) 1570°C, 7) 1610°C. Superstructure reflections from 1:2 ordered phase are indicated by $*$.

structure, (110). Since the (012) and (102) peaks are very close to (110) they also should be taken into account in the calculations. Thus, ordering parameter is given by

$$S = \sqrt{\frac{(I_{100}/I_{110,012,102})_{obs}}{(I_{100}/I_{110,012,102})_{calc}}} \tag{10.3}$$

where $(I_{100}/I_{110,012,102})_{obs}$ is the ratio of the observed intensity of the (100) superlattice reflection to that of (110,012,102) main reflection, and $(I_{100}/I_{110,012,102})_{calc}$ is the calculated value for a completely ordered structure. The intensity of an X-ray diffraction peak with Miller indexes (hkl) is calculated by [335]

$$I_{hkl} = kM|F_{hkl}|^2 L_p \tag{10.4}$$

Table 10.3: Phase composition of calcined powders of $BaCO_3$ + $ZnNb_2O_6$

T, °C	Major phases	Minor phases
800	$BaCO_3$, $ZnNb_2O_6$	$Ba(Zn_{1/3}Nb_{2/3})O_3$-cubic,
900	$Ba(Zn_{1/3}Nb_{2/3})O_3$-cubic	$ZnNb_2O_6$, $BaCO_3$
1000	$Ba(Zn_{1/3}Nb_{2/3})O_3$-cubic	
1100	$Ba(Zn_{1/3}Nb_{2/3})O_3$-hex	
1200	$Ba(Zn_{1/3}Nb_{2/3})O_3$-hex	
1380	$Ba(Zn_{1/3}Nb_{2/3})O_3$-cubic	
1460	$Ba(Zn_{1/3}Nb_{2/3})O_3$-cubic	unidentified phase

Table 10.4: Phase composition of calcined powders of $BaCO_3$ + $NiNb_2O_6$

T, °C	Major phases	Minor phases
800	$BaCO_3$, $NiNb_2O_6$	$Ba(Ni_{1/3}Nb_{2/3})O_3$-cubic, NiO traces, Nb_2O_5 traces
900	$Ba(Ni_{1/3}Nb_{2/3})O_3$-cubic	$NiNb_2O_6$, $BaCO_3$
1000	$Ba(Ni_{1/3}Nb_{2/3})O_3$-cubic	
1100	$Ba(Ni_{1/3}Nb_{2/3})O_3$-cubic	
1360	$Ba(Ni_{1/3}Nb_{2/3})O_3$-hex	
1400	$Ba(Ni_{1/3}Nb_{2/3})O_3$-hex	$Ba_3Nb_5O_{15}$ traces
1500	$Ba(Ni_{1/3}Nb_{2/3})O_3$-hex	$Ba_3Nb_5O_{15}$ traces

where k is a constant, F_{hkl} is the structure factor for (hkl) reflection, M is the multiplicity factor for (hkl) reflection, and L_p is the Lorentz polarization factor. The structure factor F_{hkl} is a function of position of ions in the crystal structure. In the case of $Ba(B'_{1/3}B''_{2/3})O_3$, F_{hkl} can be expressed as

$$\begin{aligned} F_{hkl} &= \sum f_O exp[2\pi i(hx_i + ky_i + lz_i)] \\ &+ \sum f_{Ba} exp[2\pi i(hx_i + ky_i + lz_i)] \\ &+ \sum (B'_{B'} f_{B'} + B''_{B'} f_{B''}) exp[2\pi i(hx_i + ky_i + lz_i)] \\ &+ \sum (B'_{B''} f_{B'} + B''_{B''} f_{B''}) exp[2\pi i(hx_i + ky_i + lz_i)] \end{aligned} \tag{10.5}$$

where $x_i y_i z_i$ are the positions of each ion in the unit cell, f_i is the atomic scattering factor for species i, and $B'_{B'}$, $B'_{B''}$, $B''_{B'}$, $B''_{B''}$ bear the same meaning as in Eq. 10.2. The Lorentz-polarization factor depends on the geometry of the X-ray apparatus. For the Debye-Scherrer powder diffraction

Table 10.5: Phase composition of calcined powders of $BaCO_3$ + $NiTa_2O_6$

T, °C	Major phases	Minor phases
800	$BaCO_3$, $NiTa_2O_6$	$Ba(Ni_{1/3}Ta_{2/3})O_3$-cubic,
900	$Ba(Ni_{1/3}Ta_{2/3})O_3$-cubic	$NiTa_2O_6$, $BaCO_3$
1000	$Ba(Ni_{1/3}Ta_{2/3})O_3$-cubic	
1100	$Ba(Ni_{1/3}Ta_{2/3})O_3$-hex	
1360	$Ba(Ni_{1/3}Ta_{2/3})O_3$-hex	
1500	$Ba(Ni_{1/3}Ta_{2/3})O_3$-hex	
1610	$Ba(Ni_{1/3}Ta_{2/3})O_3$-hex	

method, it is defined as

$$L_p = \frac{1 + cos^2 2\Theta}{sin^2\Theta \cdot cos\Theta} \tag{10.6}$$

By putting the values of the structure factors, multiplicity factors and Lorentz polarization factors for each diffraction peak into Eq. 10.4, the intensity of I_{hkl} peak can be deduced.

The theoretical values of $I_{100}/I_{110,012,102}$ for several $Ba(B'_{1/3}B''_{2/3})O_3$ compounds having completely ordered 1:2 structure are listed in Table 10.6 for CuK_α and CoK_α X-ray radiation sources. These values were used to determine the degree of 1:2 ordering in BMN, BNT and BNN compounds according to Eq. 10.3. As revealed by Figs. 10.5 and 10.8, (100) superlattice reflection associated with 1:2 cation ordering in BMN and BNT compounds start to appear in samples calcined at 1000 - 1100 °C. In BZN and BNN compounds, the (100) reflections are very weak, yet still visible (see Figs. 10.6 and 10.7). In contrast to other compounds, the temperature range of stability of the 1:2

Table 10.6: Theoretical values of structure factors and $I_{100}/I_{110,012,102}$ for several $Ba(B'_{1/3}\ B''_{2/3})O_3$ compounds with ordered 1:2 structure

Compound	F_{100}	F_{110}	F_{102}	F_{012}	$I_{100}/I_{110,012,102}$	
					Cu K_α	Co K_α
$Ba(Mg_{1/3}Ta_{2/3})O_3$	-58.31	256.90	-54.43	257.01	0.0827	0.0842
$Ba(Ni_{1/3}Ta_{2/3})O_3$	-42.98	270.89	-40.43	271.01	0.0404	0.0412
$Ba(Zn_{1/3}Ta_{2/3})O_3$	-40.86	273.04	-38.28	273.16	0.0359	0.0366
$Ba(Mg_{1/3}Nb_{2/3})O_3$	-27.15	197.14	-24.54	197.24	0.0304	0.0310
$Ba(Ni_{1/3}Nb_{2/3})O_3$	-11.82	211.13	-10.54	211.24	0.00503	0.00512
$Ba(Zn_{1/3}Nb_{2/3})O_3$	-9.69	213.28	-8.40	213.39	0.00331	0.00337

ordered phase in BZN is quite narrow. Figs. 10.6 (a) and (b) show that BZN remains ordered up to 1250 - 1300 °C. At 1380 °C and above, the BZN forms a disordered perovskite phase in agreement with the results of Yoshioka [248] and Hong et al. [240]. The ordering parameter, S, for BMN, BZN, BNN, and BNT samples sintered at different temperatures is shown in Fig. 10.9. The degree of 1:2 cation ordering in the samples increases with sintering temperature. This is attributed to the enhancement of the rate of ordering with increasing temperature. In BMN samples, the complete ordering (100%) was achieved upon treatment at 1620 °C. The BNT samples showed a maximum degree of ordering of 95% after sintering at 1610 °C. The BZN samples were completely ordered at 1200 °C. However, after treatment at 1380 °C and above, the BZN possessed the disordered cubic perovskite structure. The ordering behaviour of the BNN sample in this study was quite different from that reported by Hong et al. [240]. Although in both cases it showed a high degree of 1:2 ordering, in this study, the BNN sample remained ordered up to 1500 °C, whereas, in the work of Hong et al. [240], the BNN sample underwent an order-disorder phase transition above 1350 °C. This suggests that the mechanism of disordering in BNN depends not only on thermodynamic factors, but also on the preparation history and microstructure of the sample. Indeed, as reported by Hong et al. [240], the grain size of the BNN sample sintered at 1400 ° was of the order of 1 μm. The BNN sample sintered at 1500 ° in this study had an average grain size of 5 μm (see Fig. 10.16). The process of disordering in $Ba(B'_{1/3}B''_{2/3})O_3$ perovskites involves interdiffusion of the B' and B'' ions. This process is facilitated (and apparently originated) in regions of high defect concentration, such as grain boundaries, dislocations, etc. The order-disorder transformation is then controlled by the diffusion of the disordered phase into the grain bulk. Hence, it may be expected that the process

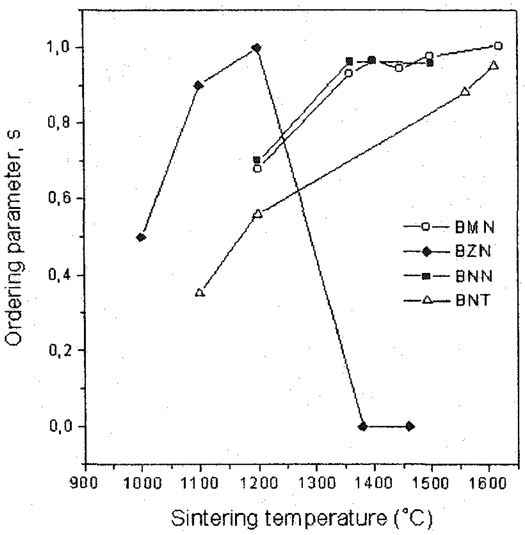

Figure 10.9: Ordering parameter for BMN, BZN, BNN, and BNT samples sintered at different temperatures

of disordering will be much slower in the coarse-grain ceramics. The situation is somewhat different in BZN, where the loss of Zn due to evaporation occurs at high temperatures [223]. Zn vacancies left in the matrix phase will facilitate disordering due to the diffusion of Nb ions into Zn-sublattice.

10.3 Density and microstructure

A number of investigations indicated that both the low dielectric loss and high dielectric constant could be only realized in ceramics having a relative density of higher than 94% [195, 235, 223, 237]. That is why one of the purposes of this study was to find the optimal sintering conditions to achieve dense ceramics with high degree of 1:2 ordering. Fig. 10.10 shows the dependence of the ceramic density on sintering temperature. All samples were held at specified sintering temperatures for 20 hours. As can be seen from Fig. 10.10, the density of BMN, BZN and BNN samples increased with sintering temperature to a maximum and decreased at higher sintering temperature. The maximum relative densities obtained for BMN, BZN and BNN samples were 99.1%, 98.2% and 96.3%, respectively. The maximum density of BNT samples sintered at 1610 °C was 97.1%. The relative densities were calculated from

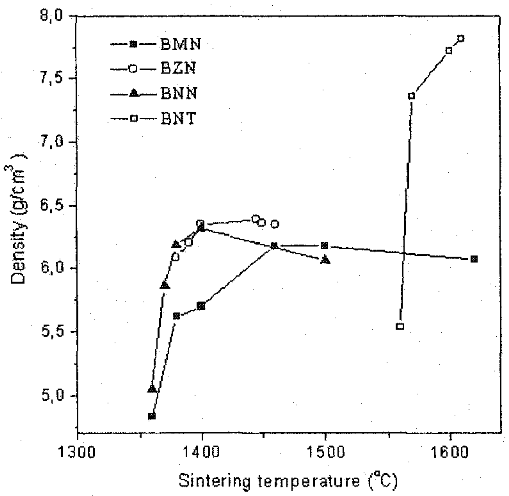

Figure 10.10: Density of BMN, BZN, BNN, and BNT samples sintered at different temperatures for 20 h.

$$\rho = \frac{\rho_m}{\rho_{th}} \times 100\% \tag{10.7}$$

where ρ_m is the measured density and ρ_{th} = 6.236 g/cm^3, 6.511 g/cm^3, 6.554 g/cm^3, and 8.017 g/cm^3, is the theoretical density of BMN, BZN, BNN, and BNT respectively.

The microstructure of ceramics was examined on polished and thermally etched surfaces. Thermal etching was performed at 100-200 degrees below the sintering temperature. In case of BZN, however, a second phase formed on the surface during thermal etching impeded the observation of the matrix grains (see Fig. 10.11). The fractured surface of the BZN shown in Fig. 10.12 provided a better view of the matrix grains. The average grain size of BZN ceramics increased gradually from 5 to 20 μm for ceramics sintered at 1380 - 1460 °C. The EDS chemical analysis of the BZN matrix and the second phase formed at the surface can be compared in Figs. 10.13 and 10.14. It was found that the second phase formed on the surface during thermal etching is depleted of Zn ions.

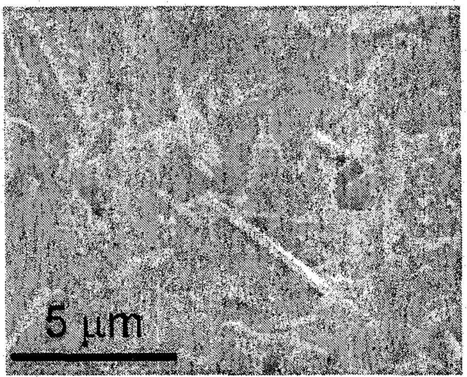

Figure 10.11: SEM image of thermally etched surface of BZN sample sintered at 1380 °C.

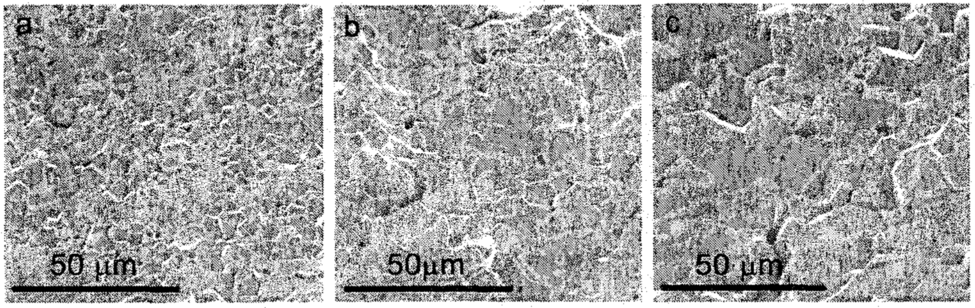

Figure 10.12: SEM image of fractured surface of BZN samples sintered at a) 1380 °C, b) 1420°C, and c) 1460 °C

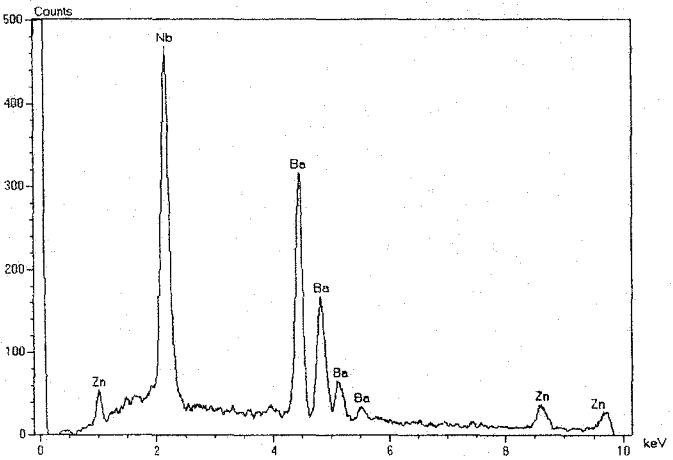

Figure 10.13: EDS spectrum of fractured surface of BZN sample sintered at 1380 °C

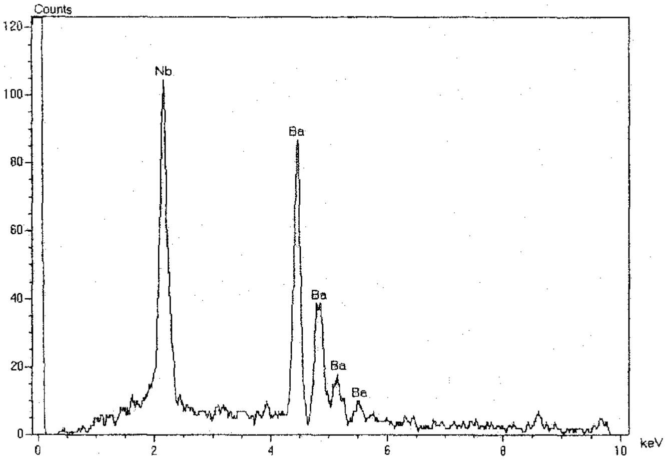

Figure 10.14: EDS spectrum of the second phase formed during thermal etching of BZN sample sintered at 1380 °C

The SEM micrographs of BMN, BNN and BNT samples sintered at different temperatures are shown in Figs. 10.15, 10.16, and 10.17.

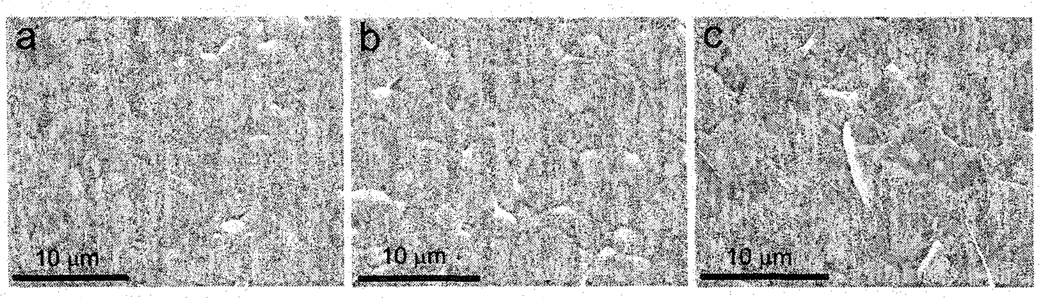

Figure 10.15: SEM image of polished surface of BMN samples sintered at a) 1400 °C, b) 1460°C, and c) 1620 °C

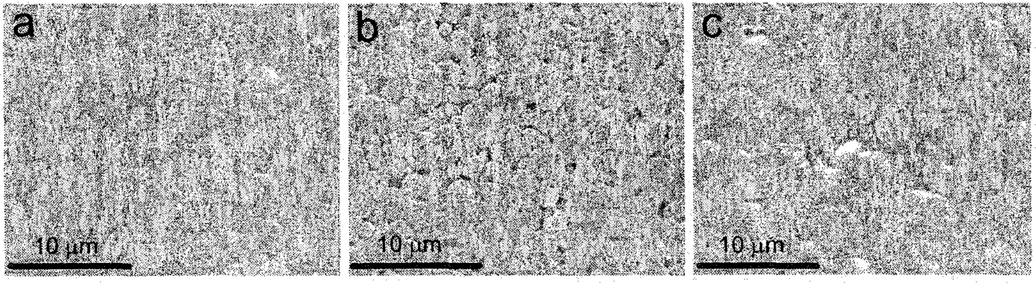

Figure 10.16: SEM image of polished surface of BNN samples sintered at a) 1400 °C, b) 1420°C, and c) 1500 °C

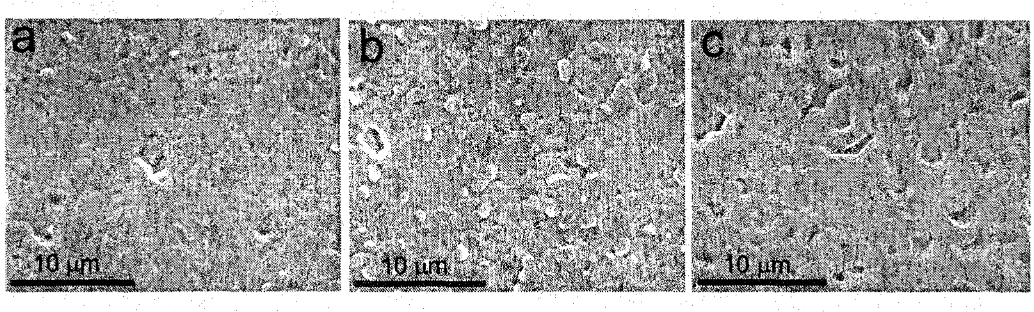

Figure 10.17: SEM image of polished surface of BNT samples sintered at a) 1570 °C, b) 1600°C, and c) 1610 °C

As can be observed in Fig. 10.15, the average grain size of BMN ceramics increased from 3.5 μm to 7 - 8 μm for samples sintered at 1400 - 1620 °C. Second phase is visible in micrographs of ceramics sintered at 1620 °C (Fig. 10.15 (c)). As revealed by EDS analysis, this second phase was enriched with Nb and depleted of Mg. The BNN ceramic showed a gradual increase in the grain size from 1.5 μm to 4.5 μm for samples sintered in the temperature interval from 1400 °C to 1500 °C. The averaged grain size of BNT samples sintered at 1570 - 1610 °C was in the range of 2.5 - 3.5 μm. Ta-rich second phase was observed on the surface of thermally etched samples.

10.4 Dielectric properties

10.4.1 Dielectric constant

The effect of sintering temperature on the dielectric constant of BMN, BZN, BNN, and BNT ceramics is shown in Fig. 10.18. The dielectric constant increases with sintering temperature for BMN, BNN, and BNT samples. The increase in ε' correlates with an increase in ceramic density shown in Fig. 5.2. In the case of the BZN sample, however, ε' initially increases until it reaches maximum of 40 for a sintering temperature, T_{sint}, of 1440 °C. At higher T_{sint}, the dielectric constant slightly decreases. The maximum values of ε' obtained for BMN, BZN, BNN, and BNT were 31.4, 40, 35.4, and 21.5, respectively.

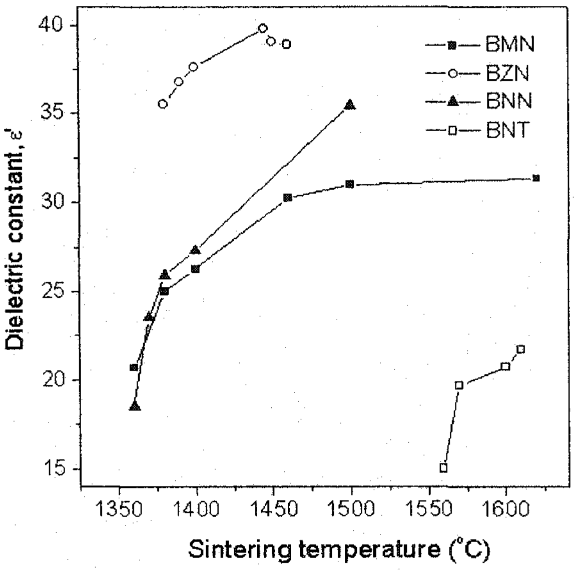

Figure 10.18: Effect of sintering temperature on dielectric constant of BMN, BZN, BNN, and BNT ceramics.

10.4.2 Q-factor

In nonpolar dielectrics well below the phonon eigenfrequencies, the Q-factor (Q = 1/tan δ) is proportional to the reciprocal of frequency. Therefore, the value $Q \times f$ is independent of frequency and provides a useful figure of merit for comparison of dielectric loss in different types of ceramics.

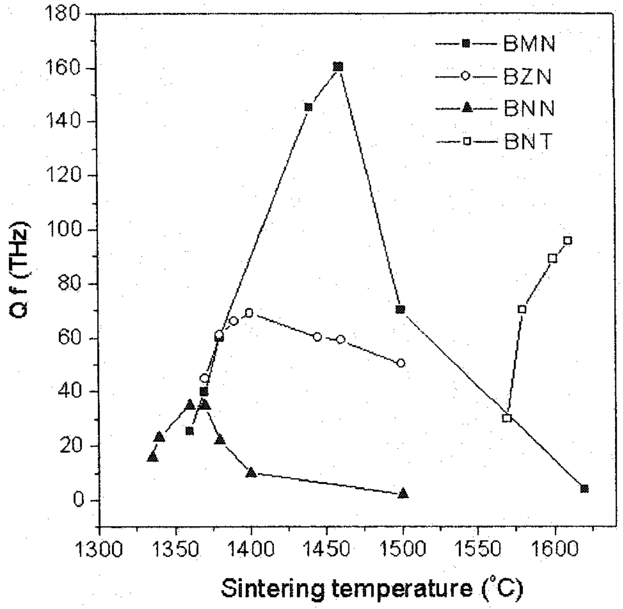

Figure 10.19: Effect of sintering temperature on $Q \times f$ of BMN, BZN, BNN, and BNT ceramics.

Fig. 10.19 demonstrates the dependence of $Q \times f$ on sintering temperature for BMN, BZN, BNN, and BNT ceramics. It is evident from Fig. 10.19 that the dielectric loss of the samples studied is very sensitive to the sintering temperature. Except for BNT, the $Q \times f$ exhibits a maximum as a function of T_{sint}. The decrease of $Q \times f$ following the maximum is especially pronounced in BMN and BNN samples. It is interesting that the decrease of $Q \times f$ cannot be explained by the intrinsic source of dielectric loss (i.e., decrease in the ordering parameter), since, according to Fig. 10.9, both BMN and BNN remained perfectly ordered up to 1620 °C and 1500 °C, respectively. Hence, an extrinsic source is responsible for the decrease in $Q \times f$. Extrinsic dielectric loss may originate from the defects, porosity, second phase, grain boundaries, etc. However, the significant drop in $Q \times f$ cannot be attributed to high porosity, since ceramics sintered at the highest temperatures still possess a relative density of 95 - 97% as shown in Fig. 5.2. Hence one may conclude that the major source of the decay in $Q \times f$ is the formation of a second phase with high dielectric loss. Indeed, the XRD analysis has detected $Ba_3Nb_5O_{15}$ second phase in both BMN and BNN sintered at 1620 °C and 1400°C (see Tables 10.2 and 10.4). This phase is a structural analog of the $Ba_3Ta_5O_{15}$ phase observed in BMT sintered above 1630 °C as reported in Chapter 9.

Similar to BMN and BNN, formation of a second phase was observed in BZN ceramics sintered above 1440 °C. The crystallographic structure of this phase was different from $Ba_3Nb_5O_{15}$, but it was not possible to identify this phase using the JCPDS database. However, since the $Q \times f$ of BZN did not decrease significantly at high T_{sint}, it could be concluded that the unidentified second phase had relatively low dielectric loss. It should also be emphasised that all BZN samples analyzed at 10 GHz were disordered. This may partially explain the lower values of $Q \times f$ compared to literature data summarized in Table 10.1

The BNT sample showed a sharp increase of $Q \times f$ with sintering temperature. This is mainly attributed to the elimination of porosity in BNT ceramics and an increase in the ordering parameter as demonstrated in Figs. 5.2 and 10.9. The XRD analysis did not reveal any second phase in BNT sintered at 1000 - 1610 °C.

Another contribution to dielectric loss is from point defects (e.g., impurities, vacancies, interstitials). Interaction of these defects with electromagnetic waves will result in absorption of part of the electromagnetic energy which otherwise would be stored in the resonator. Some of the point defects having unpaired electron spin can be detected using electron paramagnetic resonance (EPR) technique. Fig. 10.20 demonstrates the room temperature EPR spectra of BMN, BNN, BZN and BNT dielectrics showing characteristic resonance peaks originating from the paramagnetic centers.

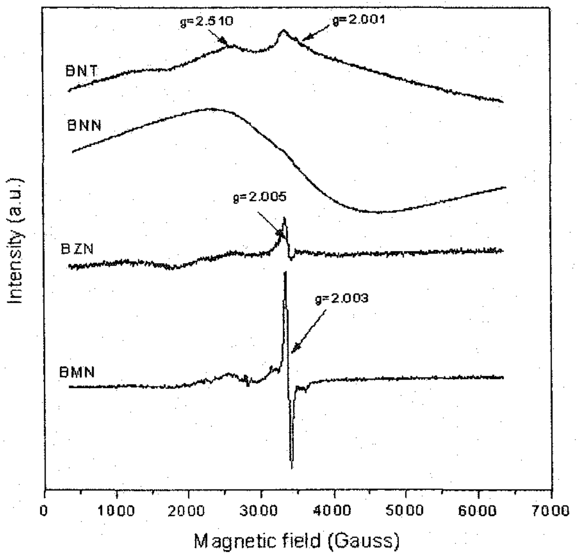

Figure 10.20: Room temperature EPR spectra of BMN, BZN, BNN, and BNT ceramics.

As revealed by Fig. 10.20, the giromagnetic constant, g, of EPR peaks of the BMN and BZN samples is very close to that of the unbound electron (i.e., g_e =2.0023), indicating that the EPR signals originate from the trapped holes [336]. Apparently, holes in these perovskites compensate for the accidental acceptor impurities, or the deviation from the stoichiometric composition. The BNT and BNN compounds show very broad EPR signals. These may originate from the Ni ions having different oxidation states. However, a detailed study of the defect chemistry of $Ba(B'_{1/3}B''_{2/3})O_3$ perovskites is required in order to unambiguously identify the EPR signals presented in Fig. 10.20. At this point it is important to emphasise that $Ba(B'_{1/3}B''_{2/3})O_3$ perovskites sintered in this work are not free from charged point defects which contribute to the extrinsic dielectric loss.

10.4.3 Temperature coefficient of the resonance frequency

Measurements of the temperature coefficient of the resonance frequency, τ_f of BMN, BZN, BNN, and BNT dielectric resonators were performed by using a rectangular copper waveguide in the temperature range of 25 to 90 °C. Using the test dielectric resonator, the waveguide contribution to the τ_f was found to be -1.2 ± 0.5 ppm/K. Fig. 10.21 shows the effect of sintering temperature on the τ_f of the BMN, BZN, BNN, and BNT dielectric resonators. It is evident from Fig. 10.21 that τ_f of BMN, BZN, BNN, and BNT is sensitive to the sintering temperature. In the case of the BMN sample, $\tau_f = +14 \pm 1$ at $T_{sint} < 1470$ °C. At higher sintering temperatures, τ_f increases, reaching + 33.9 ppm/K at $T_{sint} = 1620$ °C. A very important finding is that the τ_f of BNN obtained in this study differs significantly from that reported in the literature (e.g., $\tau_f = +20$ ppm/K [181]). As shown in Fig. 10.21, the value of τ_f of BNN increases from - 4.9 ppm/K at $T_{sint} = 1360$ °C to + 5 ppm/K at $T_{sint} = 1500$ °C. The relatively high value of ε' and nearly zero value of τ_f, make BNN compound promising for technical application. However, more work is required to improve its Q-factor. The temperature coefficient of resonance frequency of BZN compound varied in the range of + 20.7 to + 23 ppm/K. The BNT sample showed the decrease of τ_f with increasing sintering temperature from - 10.5 to - 13.5 ppm/K. The most significant effect of T_{sint} on τ_f was observed for BMN ann BNN compounds. It is most likely that this effect is associated with an increase of the

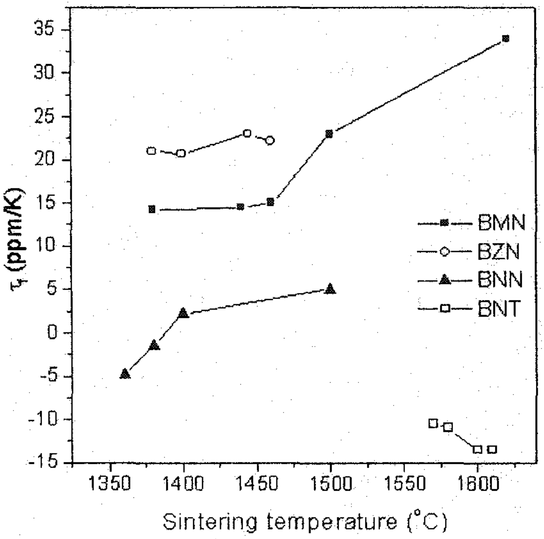

Figure 10.21: Effect of sintering temperature on τ_f of BMN, BZN, BNN, and BNT ceramics.

volume of $Ba_3Nb_5O_{15}$ in the samples. This phase apparently has a negative temperature coefficient of the dielectric constant which causes an increase of the τ_f of the BMN and BNN resonators.

10.5 Conclusions

In conclusion, the effect of preparation conditions on B-site cation ordering and dielectric properties of BMN, BZN, BNN, and BNT complex perovskites was investigated. It was found that all studied perovskites attained a high degree of 1:2 ordering at temperatures specific for each composition. A high temperature order-disorder phase transition in BZN occurs below 1380 °C in agreement with the results of Hong et al. [240]. However, coarse-grained BNN remained well ordered at temperatures as high as 1500 ° in contrast to the report of Hong et al. [240]. One of the most important results is that the second phase ($Ba_3Nb_5O_{15}$) formed at high sintering temperatures (i.e., $T_{sint} > 1400$ - 1500 °C) plays a major role in the decrease in Q-factor of BMN and BNN samples. An increase in τ_f of the BMN and BNN resonators may also be attributed to the increasing amount of the second phase at high sintering temperatures. It was also revealed by EPR that all samples studied contain a substantial amount of charged point defects. These defects contribute to the extrinsic dielectric loss at microwave frequencies [194], thus degrading the Q-factor. The chemical nature and precise identification of these defects requires further investigation.

Chapter 11

Summary

Several important results were obtained during the investigation of $BaTiO_3$:

1. Complex impedance analysis at cryogenic temperatures has revealed that the grain bulk and grain boundary properties of $BaTiO_3$ polycrystals are very sensitive to the oxygen partial pressure during sintering. It was shown that at P_{O_2} as low as 10^{-15} atm, polycrystals were already electrically inhomogeneous (i.e., they consisted of conducting grains and less conductive grain boundaries). The difference in the grain bulk and grain boundary resistance increases with P_{O_2}. The activation energy of the grain bulk resistance in rhombohedral phase was found to be equal to that of single crystal (i.e., 0.090 eV). The activation energy of the grain boundary resistance increases with the temperature of the post-sinter oxidation treatment from 0.064 eV to 0.113 eV.

2. Analysis of the polycrystalline $BaTiO_3$ sintered at $P_{O_2}= 10^{-12}$ atm and then annealed at $P_{O_2} = 0.2$ atm has shown that formation of the PTCR properties occurs at much higher temperatures than expected in the frame of the oxygen chemisorption model. A substantial PTCR effect is achieved only after prolonged annealing in air at temperatures as high as 1200 - 1250 °C. This result suggests that the PTCR effect in polycrystalline $BaTiO_3$ is associated with interfacial segregation of cation vacancies during oxidation of the grain boundaries.

3. Several paramagnetic point defects in $BaTiO_3$ polycrystals were detected and identified using the electron paramagnetic resonance technique. Polycrystals sintered in reducing atmosphere showed a strong signal with a giromagnetic constant of 1.932. This signal, observed only in conducting ceramics, was assigned to Ti^{3+} and Ti^{3+} related complexes. The dependence of the intensity of the g = 1.932 signal on donor dopant concentration was in good agreement with a defect compensation mechanism of donor doped $BaTiO_3$. V_{Ba} and V_{Ti} defects were found at giromagetic constants of 1.974 and 2.004, respectively. The EPR intensity of these

defects increases with oxidation of ceramics at T > 1000 °C. It should be stressed that the appearance of the V_{Ba} and V_{Ti} signals in EPR spectra of oxidized ceramics correlates with onset of the PTCR effect. Hence, it is justified that these defects are the source of the in-gap electron traps in PTCR ceramics. At donor dopant levels of $\geq$0.3 at%, the concentration of V_{Ba} and V_{Ti} defects shows good agreement with the defect compensation mechanism of donor doped $BaTiO_3$ [101, 89, 64, 95]. However, small amounts of V_{Ba}, and V_{Ti} defects are present in undoped $BaTiO_3$ ceramics. This observation is contrary to the generally accepted model of undoped $BaTiO_3$ where only oxygen vacancies were allowed to compensate the acceptor impurities at high P_{O_2} [99].

4. The current-voltage characteristics of two PTCR samples ($Ba_{0.996}Y_{0.004}Ti_{1.01}O_3$ and $Ba_{0.69}Sr_{0.3}Y_{0.004}Ti_{1.01}O_3$ doped with 0.03 mol % MnO) were analyzed in light of SCLC, TFLC, Frenkel-Poole, small polaron, and DSB models. It was shown that the double-Schottky barrier model provides a better fit with experimental $I-V$ curves when the effect of the applied voltage on the population of the interfacial electron states was taken into account. Within the DSB model, a partial stabilisation of the potential barrier is expected when the Fermi level is pinned at GB by a high density of interface states. This will result in an ohmic or even subohmic $I-V$ dependence at moderate voltages, e.g. $V_{GB} < 1$ V. The DSB model predicts a significant increase in the current only after all interface states are filled up. The voltage corresponding to the onset of this current is expected to shift towards higher values with increasing temperature. The possible reasons for disagreement between measured and calculated $I-V$ characteristics within the DSB model were discussed. Among them are uncertainty in the DOS function, electron-hole recombination at high temperatures, and variation of the GB barrier height at individual grain boundaries.

5. In order to distinguish between small polaron and conduction band electron transport in $BaTiO_3$, the Hall and Seebeck effects were studied in the rhombohedral and orthorhombic phases (i.e., in the 100 - 300 K interval) on polycrystalline and single crystal samples. Based on the results of the Hall effect, it was found that at 100 - 300 K, the drift mobility of electrons is thermally activated, which is in general agreement with the model of conduction band electron transport. This was also confirmed by Seebeck effect measurements on a single crystal sample. However, the activation energy of concentration of the charge carriers derived from the Seebeck effect was three times higher than the activation energy of conductivity (i.e., 0.278 eV and 0.093 eV, respectively). This difference was tentatively explained by uncertainty in determination of the transport term A in the Seebeck coefficient. For the first time, a sharp decrease in Seebeck coefficient at 200 - 230 K (i.e., at the temperature of the rhombohedral-orthorhombic phase transition) was observed in polycrystalline samples. This anomalous decrease in thermoelectric power could not be associated with the change in the concentration of the charge carriers, since the Hall constant does not undergo any significant change in this temperature range. The

proper explanation of this anomaly is awaiting further research. In general, the results obtained suggest that the mechanism of electron transport in $BaTiO_3$ follows the conduction band model in the 100 - 300 K interval. However, it should be stressed that these results were obtained for reduced undoped $BaTiO_3$ single crystals and for Y-doped polycrystals. The presence of the charged point defects may cause localization of the charge carriers and eventually alter the conduction mechanism. It is important to perform similar studies in a wider temperature range on high quality n-doped $BaTiO_3$ single crystals to draw unequivocal conclusions about the charge transport mechanism in $BaTiO_3$.

The most important results of the study of $Ba(B'_{1/3}B''_{2/3})O_3$ compounds are summarized as follows:

1. It was found that all the studied complex perovskites attained high degrees of 1:2 cation ordering at temperatures specific for each composition. In the case of $Ba(Mg_{1/3}\ Ta_{2/3})O_3$ it was shown that in the conventional synthesis method from $BaCO_3$, MgO, Ta_2O_5, intermediate phases (e.g., $Ba_4Ta_2O_9$, $Ba_5Ta_4O_{15}$) inhibit formation of single-phase $Ba(Mg_{1/3}Ta_{2/3})O_3$ up to 1400 °C, whereas utilization of a $MgTa_2O_6$ precursor produces the nearly pure perovskite phase after treatment at 1000 °C. In the temperature range of 1400-1620 °C, the $Ba(Mg_{1/3}Ta_{2/3})O_3$ ceramic remains single phase. At higher sintering temperatures, the $Ba_3Ta_5O_{15}$ phase appears in the samples. As revealed by XRD and microwave dielectric measurements, the highest degree of B-site cation ordering in BMT was achieved for samples sintered at $T_{sint} = 1585 \pm 5$ °C. Both the decrease in ordering and formation of the second phase at higher sintering temperatures are responsible for an increase in dielectric loss. For samples sintered above $T_{sint} = 1585 \pm 5$ °C, the high degree of ordering cannot be recovered by prolonged post-sinter annealing or by slow cooling.

2. A high temperature order-disorder phase transition in BZN occurs below 1380 °C in agreement with the results of Hong et al. [240]. BNN and BMN perovskites remained 100 % ordered at temperatures as high as 1500 and 1620 °C, respectively. However, $Ba_3Nb_5O_{15}$ second phase started to form at $T_{sint} = 1400$ and 1620 °C for BNN and BMN, respectively. It is this second phase that plays a major contribution in the decrease in Q-factor of BMN and BNN samples. An increase in τ_f of the BMN and BNN resonators may also be attributed to the increasing amount of the second phase at high sintering temperatures. It was also revealed by EPR that all samples studied contain a substantial amount of charged point defects. These defects contribute to the extrinsic dielectric loss at microwave frequencies, thus degrading the Q-factor. The chemical nature and precise identification of these defects requires further investigation.

3. From the technological point of view, in order to obtain low-loss $Ba(B'_{1/3}\ B''_{2/3})O_3$ ceramics, it is crucial to preserve a high degree of B-site cation ordering and avoid formation of the second phase. This can be done by reducing the sintering temperature at the expense of sintering time. By following this procedure it was possible to obtain the $Ba(Mg_{1/3}Nb_{2/3})O_3$

and $Ba(Ni_{1/3}Ta_{2/3})O_3$ ceramics with the highest ever reported values of $Q \times f$ (i.e., 160 THz and 95.5 THz for BMN and BNT, respectively).

Bibliography

[1] W. Heywang. Resistivity anomaly in doped barium titanate. *J. Am. Ceram. Soc.*, 47:484, 1964.

[2] G.H. Jonker. Halogen treatment of barium titanate semiconductors. *Mater. Res. Bull.*, 2:401, 1967.

[3] M. Kuwabara. Determination of the potential barrier height in barium titanate ceramics. *Solid St. Electron.*, 27:929, 1984.

[4] J. Daniels and R. Wernicke. Part V. new aspects of an improved PTC model. *Philips Res. Repts.*, 31:544, 1976.

[5] T.R.N. Kutty, P. Murugaraj, and N.S. Gajbhiye. Activation of trap centers in PTC $BaTiO_3$. *Materials Letters*, 2:396, 1984.

[6] G. Er, S. Ishida, and N. Takeuchi. Investigations of the electrical property, diffuse reflectance and ESR spectra of the La-(Fe, Mn)-codoped PTCR $BaTiO_3$ annealed in reducing atmosphere. *J. Mater. Sci.*, 34:4265, 1999.

[7] M.D. Glinchuk, I.P. Bykov, S.M. Kornienko, V.V. Laguta, A.M. Slipenyuk, A. G. Bilous, O.I. V'yunov, and O.Z. Yanchevskii. Influence of impurities on the properties of rare-earth-doped barium titanate ceramics. *J. Mater. Chem.*, 10:941, 2000.

[8] B.M. Kulwicki and A.J. Purdes. Diffusion potentials in $BaTiO_3$ and the theory of PTC materials. *Ferroelectrics*, 1:253, 1970.

[9] V.V.Kvaskov and K.H.Valeev. Model for the posistor effect in conducting barium titanate. *Izvestiya Akademii Nauk SSSR, Seriya Fizicheskaya*, 39:166, 1975.

[10] H. Nemoto and I. Oda. Direct examination of PTC action of single grain boundaries in semiconducting $BaTiO_3$ ceramics. *J. Am. Ceram. Soc.*, 63:398, 1980.

[11] G.T. Mallick Jr and P.R. Emtage. Current-voltage characteristics of semiconducting barium titanate ceramic. *J. Appl. Phys.*, 39:3088, 1968.

[12] G.E. Pike. Semiconductor grain-boundary admittance: Theory. *Phys. Rev. B*, 30:795, 1984.

[13] G. Blatter and F. Greuter. Carrier transport through grain boundaries in semiconductors. *Phys. Rev. B*, 33:3952, 1986.

[14] C.N. Berglund and W.S. Baer. Electron transport in single-domain, ferroelectric barium titanate. *Phys. Rev.*, 157:358, 1967.

[15] D. Mahgerefteh, D. Kirillov, R.S. Cudney, G.D. Bacher, R.M. Pierce, and J. Feinberg. Anisotropy of the hole drift mobility in barium titanate. *Phys. Rev. B*, 53:7094, 1996.

[16] P. Bernasconi, I. Biaggio, M. Zgonik, and P. Günter. Anisotropy of the electron and hole drift mobility in $KNbO_3$ and $BaTiO_3$. *Phys. Rev. Letters*, 78:106, 1997.

[17] C. Vittoria. *Elements of Microwave Networks.* World Scientific, Singapore, 1998.

[18] T. Takahashi, E.J. Wu, A. Van Der Ven, and G. Ceder. First-principles investigation of B-site ordering in $Ba(Mg_xTa_{1-x})O_3$ microwave dielectrics with complex perovskite structure. *Jpn. J. Appl. Phys.*, 39:1241, 2000.

[19] S-H. Ra and P.P. Phule. Processing and microwave dielectric properties of barium magnesium tantalate ceramics for high-quality-factor personal communication service filters. *J. Mater. Res.*, 14:4259, 1999.

[20] G. Rong, N. Newman, B. Shaw, and D. Cronin. Role of ni and zr doping on the electrical, optical, magnetic, and structural properties of barium zinc tantalate ceramics. *J. Mater. Res.*, 14:4011, 1999.

[21] V.M. Goldschmidt. *Skrifter Norske Videnskaps-Acad. Oslo, I. Mat.-Naturv. Kl*, page 8, 1926.

[22] H.E. Kay and P. Vousden. *Phil. Mag.*, 40:1019, 1949.

[23] K.W. Kirby and B.A. Wechsler. Phase relations in the barium titanate-titanium oxide system. *J. Am. Ceram. Soc.*, 74:1841, 1991.

[24] W.Känzig. *Helv. Phys. Acta*, 24:175, 1951.

[25] H.T. Evans. Technical Report 58, Laboratory for Insulation Research, Massachusetts Institute of Technology, 1953.

[26] B.C. Frazer, H. Danner, and R. Pepinsky. *Phys. Rev.*, 100:745, 1955.

[27] W. Känzig and R. Meier. *Helv. Phys. Acta*, 21:585, 1949.

[28] W.J. Merz. *Phys. Rev.*, 91:513, 1953.

[29] J.A. Hooton and W.J. Merz. *Phys. Rev.*, 98:409, 1955.

[30] H.B. Haanstra and H. Ihrig. Transmission electron microscopy at grain boundaries of ptc-type batio$_3$ ceramics. *J. Am. Ceram. Soc.*, 63:288, 1980.

[31] W.J. Merz. *Phys. Rev.*, 76:1221, 1949.

[32] H. Neumann and G. Arlt. *Ferroelectrics*, 69:179, 1986.

[33] F. Chu, H.T. Sun, L.Y. Zhang, and X. Yao. *J. Am. Ceram. Soc.*, 75:2939, 1992.

[34] Y.M. Poplavko. *Soviet Phys.-Solid State (English Transl.)*, 6:45, 1964.

[35] Y.M. Poplavko. *Soviet Phys.-Solid State (English Transl.)*, 10:2780, 1969.

[36] P.L. Janega. Hypothesis to explain pressure effects on resistivity in semiconductive barium titanate ceramics. *Solid-State Electronics*, 29:59, 1986.

[37] Y.M. Poplavko. Hypothesis to explain pressure effects on resistivity in semiconductive barium titanate ceramics. *Soviet Phys.-Solid State (English Transl.)*, 4:787, 1962.

[38] F. Jona and G. Shirane. *Ferroelectric crystals.* Pergamon Press, New York, 1962.

[39] K. Kinoshita and A. Yamaji. *J. Appl. Phys.*, 47:371, 1976.

[40] D. Hennings. *Int. J. High Technology Ceramics*, 3:91, 1987.

[41] N. Golego, S.A. Studenikin, and M. Cocivera. Properties of dielectric $BaTiO_3$ thin films prepared by spray pyrolysis. *Chem. Mater.*, 10:2000, 1998.

[42] Dr. J. Preston. Private communication.

[43] W.R. Buessem, L.E. Cross, and A.K. Goswami. *J. Am. Ceram. Soc.*, 49:33, 1966.

[44] G. Arlt, D. Hennings, and G. deWith. *J. Appl. Phys.*, 58:1619, 1985.

[45] M.H. Frey and D.A. Payne. Grain-size effect on structure and phase transformations for barium titanate. *Phys. Rev. B*, 54:3158, 1996.

[46] V. Tura, L. Mitoseriu, C. Papusoi, T. Osaka, and M. Okuyama. Investigation of grain-size influence on the ferroelectric-to-paraelectric phase transition in $BaTiO_3$ ceramics by means of AC calorimetry. *Jpn. J. Appl. Phys.*, 37:1950, 1998.

[47] N. Yasuda, H. Ohwa, and S. Asano. *Jpn. J. Appl. Phys.*, 35:5099, 1996.

[48] D. Hennings, A. Schnell, and G. Simon. *J. Am. Ceram. Soc.*, 65:539, 1982.

[49] Z.Q. Zhuang, M.P. Harmer, and D.M. Smyth. *Mater. Res. Bull.*, 22:1329, 1987.

[50] G.A. Smolensky and V.A. Isupov. *Zhurnal Technicheskoj Fiziki*, 24:1375, 1954.

[51] G.A. Smolensky and K.I. Rozgachev. *Zhurnal Technicheskoj Fiziki*, 24:1751, 1954.

[52] K.A. Müller and H. Burkard. $SrTiO_3$: An intrinsic quantum paraelectric below 4 K. *Phys. Rev. B*, 19:3593, 1979.

[53] W. Zhong and D. Wanderbilt. Effect of quantum fluctuations on phase transitions in $SrTiO_3$ and $BaTiO_3$. *Phys. Rev. B*, 53:5047, 1996.

[54] Y. Luspin, J.L. Servoin, and F. Gervais. Soft mode spectroscopy of barium titanate. *J. Phys. C*, 13:3761, 1980.

[55] K.A. Müller and W. Berlinger. Microscopic probing of odrder-disorder versus displacive behaviour in $BaTiO_3$ by Fe^{3+} EPR. *Phys. Rev. B*, 34:6130, 1986.

[56] K.A. Müller, W. Berlinger, and K.W. Blazey. Electron paramagnetic resonance of Mn^{4+} in $BaTiO_3$. *Solid State Communication*, 61:21, 1987.

[57] F. Gervais. Displacive order-disorder crossover in ferroelectrics. *Ferroelectrics*, 53:91, 1984.

[58] S. Wada, T. Suzuki, M. Osada, M. Kakihana, and T. Noma. Change of macroscopic and microscopic symmetry of barium titanate single crystal around Curie temperature. *Jpn. J. Appl. Phys.*, 37:5385, 1998.

[59] K. Itoh, L.Z. Zeng, E. Nakamura, and N. Mishima. Crystal structure of $BaTiO_3$ in the cubic phase. *Ferroelectrics*, 63:29, 1985.

[60] K.A. Müller. Microscopic investigations of the ferroelectric phase transitions in $BaTiO_3$ by paramagnetic resonance. *Helv. Phys. Acta*, 59:874, 1986.

[61] S.A. Long and R.N. Blumenthal. Ti-rich nonstoichiometric $BaTiO_3$: I, High-temperature electrical conductivity measurements. *J. Am. Ceram. Soc.*, 54:515, 1971.

[62] M. Didomenico and S.H. Wemple. *Phys. Rev.*, 166:565, 1968.

[63] N.H. Chan and D.M. Smyth. Defect chemistry of $BaTiO_3$. *J. Electrochem. Soc.*, 123:1584, 1976.

[64] J. Daniels and K.H. Härdtl. Part I. electrical conductivity at high temperatures of donor-doped barium titanate. *Philips Res. Repts.*, 31:489, 1976.

[65] J. Daniels. Part II. defect equilibria in acceptor-doped barium titanate. *Philips Res. Repts.*, 31:505, 1976.

[66] N.G. Eror and D.M. Smyth. Nonstoichiometric disorder in single-crystalline $BaTiO_3$ at elevated temperatures. *J. Solid State Chem.*, 24:235, 1978.

[67] D. Hennings. Part III. Thermogravimetric investigations. *Philips Res. Repts.*, 31:516, 1976.

[68] H.J. Hagemann and D. Hennings. Reversible weight change of acceptor-doped $BaTiO_3$. *J. Am. Ceram. Soc.*, 64:590, 1981.

[69] S. Shirasaki, H. Yamamura, H. Haneda, K. Kakegawa, and J. Moori. Defect structure and oxygen diffusion in undoped and La-doped polycrystalline barium titanate. *J. Chem. Phys.*, 73:4640, 1980.

[70] R. Courths. Ultraviolet photoelectron spectroscopy (UPS) and LEED studies of $BaTiO_3$ (001) and $SrTiO_3$ (100) surfaces. *Phys. Stat. Sol. (B)*, 100:135, 1980.

[71] S.B. Desu and D.A. Payne. Interfacial segregation in perovskites I-IV. *J. Am. Ceram. Soc.*, 73:3391, 1990.

[72] R. Courths, H. Hochst, P. Steiner, and S. Hufner. X-ray and UV photoemission from defects in $LiNbO_3$ and $BaTiO_3$ surfaces. *Ferroelectrics*, 26:745, 1980.

[73] B. Cord and R. Courths. Photoemission study of $BaTiO_3$ (100) surfaces. *Surface Science*, 152/153:1141, 1985.

[74] S.M. Mukhopadhyay and T.C.S. Chen. Surface chemical states of barium titanate: Influence of sample processing. *J. Mater. Res.*, 10:1502, 1995.

[75] H. Bando, T. Shimitzu, Y. Aiura, Y. Haruyama, K. Oka, and Y. Nishihara. Structure and electronic states on reduced $BaTiO_3$ (100) surface observed by scanning tunneling microscopy and spectroscopy. *J. Vac. Sci. Technol. B*, 14:1060, 1996.

[76] Y-M. Chiang and T. Takagi. Grain-boundary chemistry of barium titanate and strontium titanate I-II. *J. Am. Ceram. Soc.*, 73:3278, 1990.

[77] E. Possenriede, P. Jacobs, and O.F. Schirmer. Paramagnetic defects in $BaTiO_3$ and their role in light-induced charge transport: I. ESR studies. *J. Phys.: Condens. Matter*, 4:4719, 1992.

[78] E.V. Bursian, Ya.G. Girshberg, and E.N. Starov. Small polarons in conducting barium titanate crystals. *Phys. Stat. Sol. (B)*, 46:529, 1971.

[79] G.V. Lewis and C.R.A. Catlow. Defect studies of doped and undoped barium titanate using computer simulation techniques. *J. Phys. Chem. Solids*, 47:89, 1986.

[80] W.O. Stratton. Phase diagram of the BaO–TiO_2 system. *J. Chem. Phys.*, 19:33, 1951.

[81] D.E. Rase and R. Roy. Phase equilibria in the system BaO–TiO_2. *J. Am. Ceram. Soc.*, 38:102, 1955.

[82] T. Negas, R.S. Roth, H.S. Parker, and D. Minor. Subsolidus phase relations in the $BaTiO_3$–TiO_2 system. *J. Solid State Chem.*, 9:297, 1974.

[83] H.M. O'Bryan and J. Thomson. Phase equilibria in the TiO_2- rich region of the system BaO–TiO_2. *J. Am. Ceram. Soc.*, 57:522, 1974.

[84] Y.H. Hu, M.P. Harmer, and D.M. Smyth. Solubility of BaO in $BaTiO_3$. *J. Am. Ceram. Soc.*, 68:372, 1985.

[85] J. Nowotny and M. Rekas. Defect chemistry of $BaTiO_3$. *Solid State Ionics*, 49:135, 1991.

[86] S.N. Ruddlesden and P. Popper. The compound $Sr_3Ti_3O_7$ and its structure. *Acta Crystallogr.*, 11:54, 1958.

[87] F.A. Kröger and H.J. Vink. Solid state physics. volume 3, page 307. Academic Press, New York, 1956.

[88] R. Dieckmann. Point defects and transport in non-stoichiometric oxides: Solved and unsolved problems. *J. Phys. Chem. Solids*, 59:507, 1998.

[89] J.H. Hwang and Y.H. Han. Electrical properties of cerium-doped $BaTiO_3$. *J. Am. Ceram. Soc.*, 84:1750, 2001.

[90] N.H. Chan, R.K. Sharma, and D.M. Smyth. Nonstoichiometry in acceptor-doped $BaTiO_3$. *J. Am. Ceram. Soc.*, 65:167, 1982.

[91] J. Nowotny and M. Rekas. Defect structure, electrical properties and transport in barium titanate. III. Electrical conductivity, thermopower and transport in single crystalline $BaTiO_3$. *Ceramics International*, 20:225, 1994.

[92] N.H. Chan, R.K. Sharma, and D.M. Smyth. Nonstoichiometry in undoped $BaTiO_3$. *J. Am. Ceram. Soc.*, 64:556, 1981.

[93] R. Wernicke. Part IV. The kinetics of equilibrium restoration in barium titanate ceramics. *Philips Res. Repts.*, 31:521, 1976.

[94] R. Scharfschwerdt, A. Mazur, O.F. Schirmer, H. Hesse, and S. Mendricks. Oxygen vacancies in $BaTiO_3$. *Phys. Rev. B*, 54:15284, 1996.

[95] G.H. Jonker and E.E. Havinga. The influence of foreign ions on the crystal lattice of barium titanate. *Mat. Res. Bull.*, 17:345, 1982.

[96] A.S. Shaikh and R.W. Vest. Defect structure and dielectric properties of Nd_2O_3-modified $BaTiO_3$. *J. Am. Ceram. Soc.*, 69:689, 1986.

[97] D. Makovec, Z. Samardzija, U. Delalut, and D. Kolar. Defect structure and phase relations of highly lanthanum-doped barium titanate. *J. Am. Ceram. Soc.*, 78:2193, 1995.

[98] N.S. Hari, P. Padmini, and T.R.N. Kutty. Complex impedance analyses of n-$BaTiO_3$ ceramics showing positive temperature coefficient of resistance. *J. Mater. Sci. - Materials in Electronics*, 8:15, 1997.

[99] N.H. Chan and D.M. Smyth. Defect chemistry of donor-doped $BaTiO_3$. *J. Am. Ceram. Soc.*, 67:285, 1984.

[100] E.C. Subbarao and G. Shirane. Dielectric and structural studies in the systems $Ba(Ti,Nb)O_3$ and $Ba(Ti,Ta)O_3$. *J. Am. Ceram. Soc.*, 42:279, 1959.

[101] N.H. Chan, M.P. Harmer, and D.M. Smyth. Compensating defects in highly donor-doped $BaTiO_3$. *J. Am. Ceram. Soc.*, 69:507, 1986.

[102] J.M. Millet, R.S. Roth, L.T. Ettlinger, and H.S. Parker. Phase equilibria and crystal chemistry in ternary system BaO- TiO_2-Nb_2O_5. *J. Solid State Chem.*, 67:257, 1987.

[103] R. Wernicke. The influence of kinetic processes on the electrical conductivity of donor-doped $BaTiO_3$ ceramics. *Phys. Stat. Sol. (a)*, 47:139, 1978.

[104] J. Frenkel. *Kinetic Theory of Liquids.* Oxford University Press, New York, 1946.

[105] A. Fujishima and K. Honda. *Nature*, 238:37, 1972.

[106] J. Padilla and D. Vanderbilt. Ab initio study of $SrTiO_3$ surfaces. *Surface Science*, 418:64, 1998.

[107] J. Padilla and D. Vanderbilt. Ab initio study of $BaTiO_3$ surfaces. *Phys. Rev. B*, 56:1625, 1998.

[108] A.H. Kahn and A.J. Leyendecker. Electronic energy bands in strontium titanate. *Phys. Rev.*, 135:A1321, 1964.

[109] T. Wolfram. Two-dimensional character of the conduction bands of d-band perovskites. *Phys. Rev. Letters*, 29:1383, 1972.

[110] R.E. Cohen. Periodic slab LAPW computations for ferroelectric $BaTiO_3$. *J. Phys. Chem. Solids*, 57:1393, 1996.

[111] P. Petrosa, G. Hollinger, and F.M. Michel-Calendini. Covalency effects in transition-metal perovskitelike compounds: Partial densities of p and d states and photoelectron valence-band spectra. *Phys. Rev. B*, 18:5177, 1978.

[112] P. Petrosa and F.M. Michel-Calendini. X-ray photoelectron spectra, theoretical band structures, and densities of states for $BaTiO_3$ and $KNbO_3$. *Phys. Rev. B*, 17:2011, 1978.

[113] R. Courths. Valence band UPS spectra and partial p and d density of states in $SrTiO_3$, $BaTiO_3$ and $LiNbO_3$. *Ferroelectrics*, 26:749, 1980.

[114] Y. Haruyama, S. Kodaira, Y. Aiura, H. Bando, Y. Nishihara, T. Maruyama, Y. Sakisaka, and H. Kato. Angle-resolved photoemission study of $SrTiO_3$ (100) and (110) surfaces. *Phys. Rev. B*, 53:8032, 1996.

[115] G.M. Choi, H.L. Tuller, and D. Goldschmidt. Electronic-transport behavior in single-crystalline $Ba_{0.03}Sr_{0.97}TiO_3$. *Phys. Rev. B*, 34:6972, 1986.

[116] W.S. Baer. Free-carrier absorption in reduced $SrTiO_3$. *Phys. Rev.*, 144:734, 1966.

[117] J.P. Boyeaux and F.M. Michel-Calendini. Small polaron interpretation of $BaTiO_3$ transport properties from drift mobility measurements. *J. Phys. C. Solid State Phys.*, 12:545, 1979.

[118] P.A. Cox. *Transition Metal Oxides.* Oxford University Press, New York, 1992.

[119] T. Wolfram, R. Hurst, and F.G. Morin. Cluster surface states for TiO_2, $SrTiO_3$, and $BaTiO_3$. *Phys. Rev. B*, 15:1151, 1977.

[120] S. Ellialtioglu and T. Wolfram. Surface electronic properties of d-band perovskites: Study of the π bands. *Phys. Rev. B*, 18:4509, 1978.

[121] S. Ellialtioglu, T. Wolfram, and V.E. Henrich. Surface states on n-type $SrTiO_3$. *Solid State Communications*, 27:321, 1978.

[122] S.M. Mukhopadhyay and T.C.S. Chen. Surface chemical states of barium titanate: Influence of sample processing. *J. Mater. Res.*, 10:1502, 1995.

[123] D.F. Thomas, T.V. Kolodiazhnyi, and A.G. Belous. Scanning tunnelling microscopy and spectroscopy of n-doped $BaTiO_3$ ceramics. *J. Europ. Ceram. Soc.*, 18:1637, 1998.

[124] T.V. Kolodiazhnyi and D.F. Thomas. Hysteresis in the I-V tunneling characteristics of n-type $BaTiO_3$ ceramics. *J. Am. Ceram. Soc.*, 83:129, 2000.

[125] I. Tamm. *Phys. Z. Soviet Union*, 1:733, 1932.

[126] W. Shockley. *Phys. Rev.*, 56:317, 1939.

[127] A. Zangwill. *Physics of Surfaces.* Cambridge University Press, Cambridge, 1988.

[128] V.E. Henrich and P.A. Cox. *The Surface Science of Metal Oxides.* Cambridge University Press, Cambridge, 1994.

[129] E.Iguchi, N. Kubota, T. Nakamori, N. Yamamoto, and K.J. Lee. Polaronic conduction in n-type $BaTiO_3$ doped with La_2O_3 orGd_2O_3. *Phys. Rev. B*, 43:8646, 1991.

[130] C. Gillot, J.P. Michenaud, M. Maglione, and B. Jannot. DC electrical resistivity of Nb-doped $BaTiO_3$ and EPR measurements. *Solid State Communications*, 84:1033, 1992.

[131] L.D. Landau. *Phys. Z. Sowjetunion*, 3:664, 1933.

[132] A.S. Alexandrov and N. Mott. *Polarons and Bipolarons.* World Scientific, Singapore, 1995.

[133] I.G.Austin and N.F. Mott. Polarons in crystalline and non-crystalline materials. *Adv. Phys.*, 18:41, 1969.

[134] L. Gnininvi and J. Bouillot. *J. Phys. (Paris)*, 33:1049, 1972.

[135] O.F. Schirmer and E. Salje. Conduction bipolarons in low-temperature crystalline WO_{3-x}. *J. Phys. C: Solid St. Phys.*, 13:L1067, 1980.

[136] J.T. Devreese. Polarons. *Encyclopedia of Applied Physics*, 14:383, 1996.

[137] A.L. Shluger and A.M. Stoneham. Small polarons in real crystals: Concepts and problems. *J. Phys.: Condens. Matter*, 5:3049, 1993.

[138] G.A. Cox and R.H. Tredgold. Hole drift mobility in $BaTiO_3$ single crystals. *Phys. Letters*, 11:22, 1964.

[139] D.L. Ridpath and D.A. Wright. Electrical conductivity of reduced barium titanate crystals. *J. Mater. Sci.*, 5:487, 1970.

[140] S. Ikegami and I. Ueda. Semiconductive single crystal of $BaTiO_3$ reduced in hydrogen atmosphere. *J. Phys. Soc. Japan*, 19:159, 1964.

[141] P. Gerthsen, R. Groth, K.H. Hardtl, D. Heese, and H.G. Reik. The small polaron problem and optical effects in barium titanate. *Solid State Communications*, 3:165, 1965.

[142] C.N. Berglund and H.J. Braun. Optical absorption in single-domain ferroelectric barium titanate. *Phys. Rev.*, 164:790, 1967.

[143] H. Ihrig. On the polaron nature of the charge transport in $BaTiO_3$. *J. Phys. C: Solid State Phys.*, 9:3469, 1976.

[144] E.V. Bursian, Ya.G. Girshberg, and E.N. Starov. Temperature dependence of carrier mobility in barium titanate. *Soviet Physics- Solid State*, 14:872, 1972.

[145] T. Takeda and A. Watanabe. Electron spin resonances in reduced $BaTiO_3$. *J. Phys. Soc. Japan*, 21:267, 1966.

[146] H. Ihrig and D. Hennings. Electrical transport properties of n-type $BaTiO_3$. *Phys. Rev. B*, 17:4593, 1978.

[147] D. Emin. Lattice relaxation and small-polaron hopping motion. *Phys. Rev. B*, 4:3639, 1971.

[148] G. Goodman. Electrical conductivity anomaly in samarium-doped barium titanate. *J. Am. Ceram. Soc.*, 46:48, 1963.

[149] P. Gerthsen and B. Hoffmann. Current-voltage characteristics and capacitance of single grain boundaries in semiconducting $BaTiO_3$ ceramics. *Solid-State Electron.*, 16:617, 1973.

[150] H. Sumino, O. Sakurai, K. Shinozaki, and N. Mizutani. Direct measurement of the PTC effect of single grain boundary. *J. Ceram. Soc. Jpn.*, 100:97, 1992.

[151] M. Kuwabara, K. Morimo, and T. Matsunaga. Single-grain boundaries in PTC resistors. *J. Am. Ceram. Soc.*, 79:997, 1996.

[152] B. Huybrechts, K. Ishizaki, and M. Takata. Review:The positive temperature coefficient of resistivity in barium titanate. *J. Mater. Sci.*, 30:2463, 1995.

[153] W.T. Peria, W.R. Bratshun, and R.D. Fenity. Possible explanation of positive temperature coefficient in resistivity of semiconducting ferroelectrics. *J. Am. Ceram. Soc.*, 44:249, 1961.

[154] W. Heywang. Barium titanate as a semiconductor with blocking layers. *Solid St. Electron*, 3:51, 1961.

[155] G.H. Jonker. Some aspects of semiconducting barium titanate. *Solid St. Electron*, 7:895, 1964.

[156] W. Heywang and H. Brauer. The structure of the potential barriers in semiconducting barium titanate. *Solid St. Electron*, 8:129, 1965.

[157] G.H. Jonker. Equilibrium barriers in PTC thermistors. *Adv. Ceram.*, 1:155, 1981.

[158] A.Belous, T.Kolodiazhnyi, and O.Janchevsky. Voltage dependence of resistivity in PTC ceramics based on semiconducting $BaTiO_3$. *Ukrainian Chemical Journal*, 61:86, 1995.

[159] V.J. Tennery and R.L. Cook. Investigation of rare-earth doped barium titanate. *J. Am. Ceram. Soc.*, 44:187, 1961.

[160] J.P. Michenaud, C. Gillot, H. Duvigneaud, and M. Gilbert. Anomalous thermopower in Nb-doped $BaTiO_3$ ceramics. *Solid State Communications*, 77:347, 1991.

[161] H.M. Al-Allak, J. Illingsworth, A.W. Brinkman, and J. Woods. Current-voltage characteristics of donor-doped $BaTiO_3$ semiconducting ceramics. *J. Phys. D*, 22:1393, 1989.

[162] D. Kajfez and P. Guillon. *Dielectric Resonators.* Artech Hause, Inc, Dedham, MA, 1986.

[163] J. Konopka and I. Wolff. Dielectric properties of substrates for deposition of high-T_C thin films up to 40 GHz. *IEEE Trans. Microwave Theory Tech.*, 40:2418, 1992.

[164] A. Vogt and W. Jutzi. An HTS narrow bandwidth coplanar shunt inductively coupled microwave bandpass filter on $LaAlO_3$. *IEEE Trans. Microwave Theory Tech.*, 45:492, 1997.

[165] S.J. Fiedziuszko, J.A. Curtis, S.C. Holme, and R.S. Kwok. Low loss multiplexers with planar dual mode HTS resonators. *IEEE Trans. Microwave Theory Tech.*, 44:1248, 1996.

[166] S.J. Fiedziuszko. Dielectric resonators shrink satellite filters and multiplexers. *Microwave Syst. News*, August 1985.

[167] J-F. Liang and W.D. Blair. High-Q TE01 mode DR filters for PCS wireless base stations. *IEEE Trans. Microwave Theory Tech.*, 46:2493, 1998.

[168] K. Hosoya. Systematic evaluation and analysis for 60-GHz dielectric resonators coupled to microstrip line on a GaAs substrate. *IEEE Trans. Microwave Theory Tech.*, 46:352, 1998.

[169] O. Ishihara, T. Mori, H. Sawano, and M. Nakatani. A highly stabilized GaAs fet oscillator using a dielectric resonator feedback circuit in 9-14 GHz. *IEEE Trans. Microwave Theory Tech.*, 28:817, 1980.

[170] N. Klein, A. Scholen, N. Tellmann, C. Zuccaro, and K.W. Urban. Properties and applications of HTS-shielded dielectric resonators: A state-of-the-art report. *IEEE Trans. Microwave Theory Tech.*, 44:1369, 1996.

[171] N. Klein, M. Schuster, S. Vitusevich, M. Winter, and H.R. Yi. Novel dielectric resonator structures for future microwave communication systems. *J. Europ. Ceram. Soc.*, 21:2687, 2001.

[172] R.D. Richtmyer. Dielectric resonators. *J. Appl. Phys.*, 10:391, 1939.

[173] D. Kajfez, A.W. Glisson, and J. James. Computed modal field distribution for isolated dielectric resonators. *IEEE Trans. Microwave Theory Tech.*, 32:1609, 1984.

[174] Z-Y. Shen, C. Wilker, P. Pang, W.L. Holstein, D. Face, and D.J. Kountz. High T_c superconductor-sapphire microwave resonator with exptremely high Q-values up to 90 K. *IEEE Trans. Microwave Theory Tech.*, 40:2424, 1992.

[175] N. Klein, C. Zuccaro, U. Dahne, H. Schultz, N. Tellmann, R. Kutzner, A.G. Zaitsev, and R. Wordenweber. Dielectric properties of rutile and its use in high temperature superconducting resonators. *J. Appl. Phys.*, 78:6683, 1995.

[176] J. Krupka, R.G. Geyer, M. Kuhn, and J.H. Hinken. Dielectric properties of single crystals of Al_2O_3, $LaAlO_3$, $NdGaO_3$, $SrTiO_3$, and MgO at cryogenic temperatures. *IEEE Trans. Microwave Theory Tech.*, 42:1886, 1994.

[177] C.C. Lee and P. Lin. Microwave dielectric properties and microstructures of $(Ba_{1-x}Pb_x)O \cdot La_2O_3 \cdot 4.7TiO_2$ ceramics. *Jpn. J. Appl. Phys.*, 37:878, 1998.

[178] J.J. Wu and X.M. Chen. Modified $Ba_{6-3x}Nd_{8+2x}Ti_{18}O_{54}$ microwave dielectric ceramics. *J. Europ. Ceram. Soc.*, 19:1123, 1999.

[179] A.G. Belous and O.V. Ovchar. Mw dielectrics with perovskite-like structure based on sm-containing systems. *J. Europ. Ceram. Soc.*, 19:1119, 1999.

[180] M. Onoda, J. Kuwata, K. Kaneta, K. Toyama, and S. Nomura. $Ba(Zn_{1/3}Nb_{2/3})O_3$-$Sr(Zn_{1/3}Nb_{2/3})O_3$ solid solution ceramics with temperature-stable high dielectric constant and low microwave loss. *Jpn. J. Appl. Phys.*, 21:1707, 1982.

[181] H. Banno, F. Mizuno, T. Takeuchi, T. Tsunooka, and K. Ohya. Dielectric properties of $Sr(Ni_{1/3}Nb_{2/3})O_3$-$Ba(Ni_{1/3}Nb_{2/3})O_3$ ceramics at microwave frequencies. *Proceedings of the 5th Meeting on Ferroelectric Materials and Their Applications, Kyoto 1985, Jpn. J. Appl. Phys.*, 21 Supplement 24-3:87, 1985.

[182] H. Tamura, T. Konoike, Y. Sakabe, and K. Wakino. Improved high-Q dielectric resonator with complex perovskite structure. *J. Am. Ceram. Soc.*, 67:C–59, 1984.

[183] M. Valant, D. Suvorov, C. Hoffmann, and H. Sommariva. $Ag(Nb,Ta)O_3$-based ceramics with suppressed temperature dependence of permittivity. *J. Europ. Ceram. Soc.*, 21:2647, 2001.

[184] A.G. Belous. Physicochemical aspects of the development of MW dielectrics and their use. *J. Europ. Ceram. Soc.*, 21:2717, 2001.

[185] S. Nishigaki, H. Kato, S. Yano, and R. Kamimura. Microwave dielectric properties of $(Ba,Sr)O \cdot Sm_2O_3 \cdot TiO_2$ ceramics. *Bulletin Amer. Ceram. Soc.*, 66:1405, 1987.

[186] J-H. Choy, Y-S. Han, S-H. Hwang, S-H. Byeon, and G. Demazeau. Citrate route to sn-doped $BaTi_4O_9$ with microwave dielectric properties. *J. Am. Ceram. Soc.*, 81:3197, 1998.

[187] J.K. Plourde, D.F. Linn, H.M. O'Bryan Jr., and J. Thomson Jr. $BaTi_4O_9$ as a microwave dielectric resonator. *J. Am. Ceram. Soc.*, 58:418, 1975.

[188] W-Y. Lin, R.F. Speyer, W.S. Hackenberger, and T.R. Shrout. Microwave properties of $BaTi_4O_9$ doped with zirconium and tin oxides. *J. Am. Ceram. Soc.*, 82:1207, 1999.

[189] S. Nomura. Ceramics for microwave dielectric resonator. *Ferroelectrics*, 49:61, 1983.

[190] Y.H. Park, J.M. Ryu, M.Y. Shin, K.H. Ko, D.W. Kim, and K-S. Hong. Effect of Nb_2O_5/ZnO addition on microwave properties of $Zr_{0.8}Sn_{0.2}TiO_4$ ceramics. *J. Am. Ceram. Soc.*, 84:2542, 2001.

[191] *Murata. Co. Technical Catalog*, 49, 1996.

[192] A. Templeton, X. Wang, S.J. Penn, S.J. Webb, L.F. Cohen, and N.McN. Alford. Microwave dielectric loss of titanium oxide. *J. Am. Ceram. Soc.*, 83:95, 2000.

[193] V.L. Gurevich and A.K. Tagantsev. Intrinsic dielectric loss in crystals. *Adv. Phys.*, 40:719, 1991.

[194] J. Petzelt and N. Setter. Far infrared spectroscopy and origin of microwave losses in low-loss ceramics. *Ferroelectrics*, 150:89, 1993.

[195] S. Nomura, K. Toyama, and K. Kaneta. $Ba(Mg_{1/3}Ta_{2/3})O_3$ ceramics with temperature-stable high dielectric constant and low microwave loss. *Jpn. J. Appl. Phys.*, 21:L624, 1982.

[196] W.C. Mackrodt. Classical quantum simulation of the surface properties of α-Al_2O_3. *Phil. Trans. Roy. Soc. Lond.*, A341:301, 1992.

[197] E.A. Kotomin, E. Heifets, W.A. Goddard, P.W.M. Jacobs, and G. Borstel. Theoretical simulations of surface relaxation for perovskite titanates. In *Defects and Surface-Induced Effects in Advanced Perovskites*, volume 77 of *NATO Science Series*, page 209. Kluwer Academic Publishers, 2000.

[198] S.J. Penn, N.McN. Alford, A. Templeton, X. Wang, M. Xu, M. Reece, and K. Schrapel. Effect of porosity and grain size on the microwave dielectric properties of sintered alumina. *J. Am. Ceram. Soc.*, 80:1885, 1997.

[199] M. Furuya and A. Ochi. Microwave dielectric properties for $Ba(Mg_{1/3}Ta_{2/3})O_3$ - $A(Mg_{1/2}W_{1/2})O_3$ (A = Ba, Sr, and Ca) ceramics. *Jpn. J. Appl. Phys.*, 33:5482, 1994.

[200] H. Matsumoto, H. Tamura, and K. Wakino. $Ba(Mg,Ta)O_3$-$BaSnO_3$ high-Q dielectric resonator. *Jpn. J. Appl. Phys.*, 30:2347, 1991.

[201] Y.I. Gornikov, Z.Y. Makarova, A.G. Belous, L.G. Gavrilova, V.M. Paskov, and V.P. Chalyi. The effect of zinc oxide additions on the phase composition and dielectric properties of barium tetratitanate. *Soviet Prog. Chem.*, 50:1243, 1984.

[202] P.K. Davies, J. Tong, and T. Negas. Effect of ordering-induced domain boundaries on the low-loss $Ba(Zn_{1/3}Ta_{2/3})O_3$-$BaZrO_3$ perovskie microwave dielectrics. *J. Am. Ceram. Soc.*, 80:1727, 1997.

[203] M.A. Akbas and P.K. Davies. Ordering-induced microstructures and microwave dielectric properties of the $Ba(Zn_{1/3}Ta_{2/3})O_3$-$BaZrO_3$ system. *J. Am. Ceram. Soc.*, 81:670, 1998.

[204] P.J.W. Debye. *Berichte Deutschen Physikalischen Gesellschaft*, 15:777, 1913.

[205] V.V. Daniel. *Dielectric Relaxation.* Academic Press, London, 1967.

[206] V.L. Gurevich. *Transport in Phonon Systems.* North-Holland, Amsterdam, 1986.

[207] V.B. Braginsky, V.S. Ilchenko, and Kh.S. Bagdassarov. Experimental observation of fundamental microwave absorption in high quality dielectric crystals. *Phys. Lett. A*, 120:300, 1987.

[208] M. Sparks et al. *Phys. Rev. B*, 26:6987, 1982.

[209] R. Stolen and K. Dransfeld. *Phys. Rev.*, 139:1295, 1965.

[210] B.Ya. Balagurov, V.G. Vaks, and B.I. Shklovskii. *Fiz. Tverd. Tela*, 12:89, 1970.

[211] N. Setter. 1.1.1998- 30.6.2000. Technical report, Ceramics Laboratory, Materials Department, EPFL, 2000.

[212] F.S. Galasso. *Structure, Properties and Preparation of Perovskite-Type Compounds.* Pergamon Press, Oxford, first edition, 1969.

[213] F. Galasso and J Pyle. Ordering in compounds of the $A(B'_{0.33}Ta_{0.67})O_3$ type. *Inorganic Chemistry*, 2:482, 1962.

[214] N. Setter and L.E. Cross. The contribution of structural disorder to diffuse phase transitions in ferroelectrics. *J. Mater. Sci.*, 15:2478, 1980.

[215] X-W. Zhang, Q. Wang, and B-L. Gu. Study of the order-disorder transition in $A(B'B'')O_3$ perovskite type ceramics. *J. Am. Ceram. Soc.*, 74:2846, 1991.

[216] M.A. Akbas and P.K. Davies. Structure and dielectric properties of the $Ba(Mg_{1/3}Nb_{2/3})O_3$-$La(Mg_{2/3}Nb_{1/3})O_3$ system. *J. Am. Ceram. Soc.*, 81:2205, 1998.

[217] L. Chai, M.A. Akbas, P.K. Davies, and J.P. Parise. Cation ordering transformations in $Ba(Mg_{1/3}Ta_{2/3})O_3$-$BaZrO_3$ solid solutions. *Mater. Res. Bull.*, 32:1261, 1997.

[218] C-C. Lee, C-C. Chou, and D-S. Tsai. Effect of La/K A-site substitutions on the ordering of $Ba(Zn_{1/3}Ta_{2/3})O_3$. *J. Am. Ceram. Soc.*, 80:2885, 1997.

[219] M.A. Akbas and P.K. Davies. Cation ordering transformations in the $Ba(Zn_{1/3}Nb_{2/3})O_3$-$La(Zn_{2/3}Nb_{1/3})O_3$ system. *J. Am. Ceram. Soc.*, 81:1061, 1998.

[220] L. Chai and P.K. Davies. Effect of M^{4+} (Ce, Sn, Ti) B-site substitutions on the cation ordering in $Ba(Mg_{1/3}Ta_{2/3})O_3$. *Mater. Res. Bull.*, 33:1283, 1998.

[221] L. Chai and P.K. Davies. Formation and structural characterization of 1:1 ordered perovskites in the $Ba(Zn_{1/3}Ta_{2/3})O_3$-$BaZrO_3$ system. *J. Am. Ceram. Soc.*, 80:3193, 1997.

[222] H-J. Youn, K. S. Hong, and H. Kim. Coexistence of 1:2 and 1:1 long-range ordering types in La-modified $Ba(Mg_{0.33}Ta_{0.67})O_3$ ceramics. *J. Mater. Res.*, 12:589, 1997.

[223] S.B. Desu and H.M. O'Bryan. Microwave loss quality of $Ba(Zn_{1/3}Ta_{2/3})O_3$ ceramics. *J. Am. Ceram. Soc.*, 68:546, 1985.

[224] A. Sawada and T. Kuwabara. Infrared study of $Ba(Mg_{1/3}Ta_{2/3})O_3$ ceramics for microwave resonators. *Ferroelectrics*, 95:205, 1989.

[225] K. Tochi and N. Takeuchi. Far-infrared reflection spectra of $Ba(Mn_{1/3}Ta_{2/3})O_3$ sintered in nitrogen and in air. *J. Mater. Sci. Let.*, 7:1080, 1988.

[226] H. Tamura, D.A. Sagala, and K. Wakino. Lattice vibrations of $Ba(Zn_{1/3}Ta_{2/3})O_3$ crystal with ordered perovskite structure. *Jpn. J. Appl. Phys.*, 25:787, 1986.

[227] K. Wakino, M. Murata, and H. Tamura. Far infrared reflection spectra of $Ba(Zn_{1/3}Ta_{2/3})O_3$ - $BaZrO_3$ dielectric resonator material. *J. Am. Ceram. Soc.*, 69:34, 1986.

[228] K. Fukuda, R. Kitoh, and I. Awai. Far infrared reflection spectra of dielectric ceramics for microwave applicatons. *J. Am. Ceram. Soc.*, 77:149, 1994.

[229] J. Venkatesh, V. Sivasubramanian, V. Subramanian, and V.R.K. Murthy. Far-IR reflectance study on B-site disordered $Ba(Zn_{1/3}Ta_{2/3})O_3$ dielectric resonator. *Mater. Res. Bull.*, 35:1325, 2000.

[230] M. Furuya. Microwave dielectric properties and characteristics of polar lattice vibrations for $Ba(Mg_{1/3}Ta_{2/3})O_3$ - $A(Mg_{1/2}W_{1/2})O_3$ (A = Ba, Sr, and Ca) ceramics. *J. Appl. Phys.*, 85:1084, 1999.

[231] I.G. Siny, R. Tao, R.S. Katiyar, R. Guo, and A.S. Bhalla. Raman spectroscopy of Mg-Ta order-disorder in $Ba(Mg_{1/3}Ta_{2/3})O_3$. *J. Phys. Chem. Solids*, 59:181, 1998.

[232] A. Dias, V.S.T. Ciminelli, F.M. Matinaga, and R.L. Moreira. Raman scattering and X-ray diffraction investigations of hydrothermal barium magnesium niobate ceramics. *J. Europ. Ceram. Soc.*, 21:2739, 2001.

[233] H.J. Lee, H.M. Park, Y.W. Song, and Y.K. Cho. Microstructure and dielectric properties of barium strontium magnesium niobate. *J. Am. Ceram. Soc.*, 84:2105, 2001.

[234] A.J. Jacobson, B.M. Collins, and B.E.F. Fender. A powder neutron and X-ray diffraction determination of the structure of $Ba_3Ta_2ZnO_9$: an investigation of perovskite phases in the sydtem Ba-Ta-Zn-O and the preparation of $Ba_2TaCdO_{5.5}$ and $Ba_2CeInO_{5.5}$. *Acta Cryst. B*, 32:1083, 1976.

[235] K. Matsumoto, T. Hiuga, K. Takada, and H. Ichimura. $Ba(Mg_{1/3}Ta_{2/3})O_3$ ceramics with ultra-low loss at microwave frequencies. In *6^{th} IEEE International Symposium on Applications of Ferroelectrics*, page 118, 1986.

[236] H-J. Youn, K-Y. Kim, and H. Kim. Microstructural characteristics of $Ba(Mg_{1/3}Ta_{2/3})O_3$ ceramics and its related microwave dielectric properties. *Jpn. J. Appl. Phys.*, 35:3947, 1996.

[237] S. Kawashima, N. Nishada, I. Ueda, and H. Ouchi. $Ba(Zn_{1/3}Ta_{2/3})O_3$ ceramics with low dielectric loss at microwave frequencies. *J. Am. Ceram. Soc.*, 66:421, 1983.

[238] D.A. Sagala and S. Nambu. Lattice energy calculations for ordered and disordered $Ba(Zn_{1/3}Ta_{2/3})O_3$. *J. Phys. Soc. Jpn.*, 61:1791, 1992.

[239] F. Galasso and J. Pyle. Preparation and study of ordering in $A(B'_{1/3}B''_{2/3})O_3$ perovskite-type compounds. *J. Phys. Chem.*, 67:1561, 1963.

[240] K.S. Hong, I-T. Kim, and C-D. Kim. Order-disorder phase formation in the complex perovskite compounds $Ba(Ni_{1/3}Nb_{2/3})O_3$ and $Ba(Zn_{1/3}Nb_{2/3})O_3$. *J. Am. Ceram. Soc.*, 79:3218, 1996.

[241] L. Bellaiche and D. Vanderbilt. Electrostatic model of atomic ordering in complex perovskite alloys. *Phys. Rev. Letters*, 81:1318, 1998.

[242] B.P. Burton. Empirical cluster expansion models of cation order-disorder in $A(B'_{1/3}B''_{2/3})O_3$ perovskites. *Phys. Rev. B*, 59:6087, 1999.

[243] B.P. Burton and E. Cockayne. Why $Pb(B,B')O_3$ perovskites disorder more easily than $Ba(B,B')O_3$ perovskites. *Phys. Rev. B*, 60:R12542, 1999.

[244] T. Takahashi, E.J. Wu, and G. Ceder. First-principles estimate of the order-disorder transition in $Ba(Zn_xNb_{1-x})O_3$ microwave dielectrics. *J. Mater. Res.*, 15:2061, 2000.

[245] T. Takahashi. First-principles investigation of the phase stability for $Ba(B'_{1/3}B''_{2/3})O_3$ microwave dielectrics with complex perovskite structure. *Jpn. J. Appl. Phys.*, 39:5637, 2000.

[246] B.P. Burton. Why $Pb(B_{1/3}B'_{2/3})O_3$ perovskites disorder more easily than $Ba(B_{1/3}B'_{2/3})O_3$ perovskites and the thermodynamics of 1:1-type short-range order in PMN. *J. Phys. Chem. Solid.*, 61:327, 2000.

[247] I. Qazi, I.M. Reaney, and W.E. Lee. Order-disorder phase transition in $Ba(Zn_{1/3}Ta_{2/3})O_3$. *J. Europ. Ceram. Soc.*, 21:2613, 2001.

[248] H. Yoshioka. Ordering of cations in $Ba(Mg_{1/3}Nb_{2/3})O_3$ and $Ba(Zn_{1/3}Nb_{2/3})O_3$. *Bull. Chem. Soc. Jpn.*, 60:3433, 1987.

[249] W. Kingery. *Introduction to Ceramics.* J. Wiley & Sons, New York, second edition, 1976.

[250] A.A. Bokov, I.P. Rayevskii, V.G. Smotrakov, and O.I. Prokopalo. Kinetics of compositional ordering in $Pb_2B'B''O_6$ crystals. *Phys. Stat. Sol. (a)*, 93:411, 1986.

[251] M.A. Akbas and P.K. Davies. Domain growth in $Pb(Mg_{1/3}Ta_{2/3})O_3$ perovskite relaxor ferroelectric oxides. *J. Am. Ceram. Soc.*, 80:2933, 1997.

[252] A.K. Tagantsev, J. Petzelt, and N. Setter. Relation between intrinsic microwave and submillimeter losses and permittivity in dielectrics. *Solid State Comm.*, 87:1117, 1993.

[253] K. Tochi, T. Ohgaku, and N. Takeuchi. Long-wavelength phonons and effective charges in complex perovskite compounds $Ba(Mn_{1/3}Ta_{2/3})O_3$ and $Ba(Ni_{1/3}Ta_{2/3})O_3$. *J. Mater. Sci. Lett.*, 8:1331, 1989.

[254] L-C. Tien, C-C. Chou, and D-S. Tsai. Microstructure of $Ba(Mg_{1/3}Ta_{2/3})O_3$-$BaSnO_3$ microwave dielectrics. *Ceram. Intern.*, 26:57, 2000.

[255] X.M. Chen, Y. Suzuki, and N. Sato. Sinterability improvement of $Ba(Mg_{1/3}Ta_{2/3})O_3$ dielectric ceramics. *J. Mater. Sci., Materials in Electronics*, 5:244, 1994.

[256] O.Z. Yanchevsky. Synthesis and properties of niobium and tantalum complex oxides with perovskite-type structure. *Ph.D. Thesis, Institute of General and Inorganic Chemistry, Kyiv, Ukraine*, 1996.

[257] F. Galasso. *Structure and Properties of Inorganic Solids.* Pergamon Press, Oxford, first edition, 1970.

[258] O. Renoult, J-P. Boilot, F. Chaput, R. Papiernik, L.G. Hubert-Pfalzgraf, and M. Lejeune. Sol-gel processing and microwave characteristics of $Ba(Mg_{1/3}Ta_{2/3})O_3$ dielectrics. *J. Am. Ceram. Soc.*, 75:3337, 1992.

[259] A.M. Cherepanov. *J. Tech. Phys. U.S.S.R.*, 27:2280, 1957.

[260] J.P. Remeika. A method for growing barium titanate single crystals. *J. Am. Chem. Soc.*, 76:940, 1954.

[261] H.S. Maiti and R.N. Basu. Complex-plane impedance analysis for semiconducting barium titanate. *Mat. Res. Bull.*, 21:1107, 1986.

[262] R. Zurmühlen, J Petzelt, S. Kamba, G. Kozlov, A. Volkov, B. Gorshunov, D. Dube, A. Tagantsev, and N. Setter. Dielectric spectroscopy of $Ba(B'_{1/2}B''_{1/2})O_3$ complex perovskite ceramics: Correlations between ionic parameters and microwave dielectric properties. II. Studies below the phonon eigenfrequencies (10^2 - 10^{12}). *J. Appl. Phys.*, 77:5351, 1995.

[263] A.A. Bokrinskaya and M.E. Ilchenko. Dielectric mw resonator in the transmission line. *Izvestiya Vuzov SSSR, Ser. Radioelectronika*, 14(2):151, 1971.

[264] Murata DRD065FD029A, Q = 30000, f_c = 9.98 GHz, $\varepsilon' = 24 \pm 1$, $\tau_f = 2 \pm 1$ ppm/K.

[265] OXIDE, $BaTi_4O_9$, Q = 6000, f_c = 9.6 GHz, $\varepsilon' = 36 \pm 0.5$, $\tau_f = 0 \pm 0.3$ ppm/K.

[266] L.K. Templeton and J.A. Pask. *J. Am. Ceram. Soc.*, 42:212, 1959.

[267] T. Ishii, R. Furuichi, T. Nagasawa, and K. Jokoyama. *J. Therm. Anal.*, 19:467, 1980.

[268] G.Ya. Rebrov, A.G. Gorohovskij, and I.I. Shelokov. *Electronnaya Technika, Seriya 6. Materialy (in Russian)*, 10:112, 1972.

[269] P. Blanchart, J.F. Baumard, and P. Abelard. Effects of yttrium doping on the grain and grain-boundary resistivities of $BaTiO_3$ for positive temperature coefficient thermistors. *J. Am. Ceram. Soc.*, 75:1068, 1992.

[270] C-J. Kim and K. No. Impedance analyses of cooling-rate effects on the depletion layer of PTCR materials. *J. Mater. Sci.*, 28:5765, 1993.

[271] *CRC Handbook of Chemistry and Physics.* CRC Press Inc., Boca Rator, 74 edition, 1996.

[272] Z. Jing. Dielectric properties of $BaTiO_3$ doped with cerium and yttrium. *Ph.D. Thesis, University of Aveiro, Portugal*, 1999.

[273] D.R. Turner and H.A. Sauer. Ohmic contacts to semiconducting ceramics. *J. Am. Ceram. Soc.*, 43:250, 1960.

[274] T. Murakami. Properties of barrier layers of metal-to-reduced $BaTiO_3$ single crystal contacts. *Rev. Electr. Commun. Lab.*, 16:551, 1968.

[275] W. Heywang. Semiconducting barium titanate. *J. Mater. Sci.*, 6:1214, 1971.

[276] O. Saburi. Properties of semiconducting barium titanates. *J. Phys. Soc. Jpn.*, 14:1159, 1959.

[277] H.A. Sauer and J.R. Fisher. Processing of positive temperature coefficient thermistors. *J. Am. Ceram. Soc.*, 43:297, 1960.

[278] O. Saburi and K. Wakino. Processing techniques and applications of positive temperature coefficient thermistors. *IEEE Transactions on component parts*, page 53, 1963.

[279] D.Y. Wang. Electric and dielectric properties of barium titanate schottky barrier diodes. *J. Am. Ceram. Soc.*, 77:897, 1994.

[280] K. Ito and T. Fukami. Positive temperature coefficient of resistance in metal-semiconductor contacts. *J. Appl. Phys.*, 65:1982, 1989.

[281] K. Okazaki. *Ceramic Engineering for Dielectrics.* Tokyo, 1969.

[282] E.H. Rhoderick. *Metal-Semiconductor Contacts.* Clarendon Press, Oxford, 1978.

[283] *CRC Handbook of Chemistry and Physics.* CRC Press Inc., Boca Rator, 77 edition, 2000.

[284] Y. Tsur, T.D. Dunbar, and C.A. Randall. Crystal and defect chemistry of rare earth cations in $BaTiO_3$. *J. Electroceram.*, 7:25, 2001.

[285] F.D. Morrison, A.M. Coats, D.C. Sinclair, and A.R. West. Charge compensation mechanisms in La-doped $BaTiO_3$. *J. Electroceram.*, 6:219, 2001.

[286] D. Melnick. Zinc oxide photoconduction, an oxygen adsorption process. *J. Chem. Phys.*, 26:1136, 1957.

[287] H.D. Wiemhöfer. Sensing effects at gas-solid interfaces. *Solid St. Ionics*, 75:167, 1995.

[288] W. Göpel. Oxygen interaction of stoichiometric and non-stoichiometric ZnO prismatic surfaces. *Surf. Sci.*, 62:165, 1977.

[289] W. Göpel and U. Lampe. Influence of defects on the electronic structure of zinc oxide surfaces. *Phys. Rev. B*, 22:6447, 1980.

[290] G. Er, N. Takeuchi, S. Ishida, K. Hosokawa, K. Yamazakiand N. Kitoh, Y. Namikawa, and H. Niimi. Degradation behaviour of PTCR $BaTiO_3$ in reducing gases. *J. Ceram. Soc. Jpn.*, 104:1091, 1996.

[291] A.B. Alles, V.R.W. Amarakoon, and V.L. Burdick. Positive temperature coefficient of resistivity effect in undoped, atmospherically reduced barium titanate. *J. Am. Ceram. Soc.*, 72:148, 1989.

[292] D.C. Sinclair and A.R. West. Impedance and modulus spectroscopy of semiconducting $BaTiO_3$ showing positive temperature coefficient of resistance. *J. Appl. Phys.*, 66:3850, 1989.

[293] R. Böhmer, M. Maglione, P. Lunkenheimer, and A. Loidl. Radio-frequency dielectric measurements at temperatures from 10 to 450 K. *J. Appl. Phys.*, 65:901, 1989.

[294] J. Helmbold, G. Borchardt, R. Meyer, R. Waser, S. weber, and S. Scherrer. Oxygen diffusion in donor doped $SrTiO_3$: Influence of thermal pretreatment. In *Defects and Surface-Induced Effects in Advanced Perovskites*, volume 77 of *NATO Science Series*, page 461. Kluwer Academic Publishers, 2000.

[295] J. Crank. *The Mathematics of Diffusion.* Oxford University Press, Oxford, 1970.

[296] F. Cora and C.R.A. Catlow. QM study on transition metal perovskites. In *Defects and Surface-Induced Effects in Advanced Perovskites*, volume 77 of *NATO Science Series*, page 175. Kluwer Academic Publishers, 2000.

[297] H. Ihrig. Physics and technology of PTC-type $BaTiO_3$ ceramics. *Advances in Ceramics*, 7:117, 1984.

[298] T. Kolodiazhnyi, A. Petric, and G.P. Johari. Models of the current-voltage dependence of $BaTiO_3$ with positive temperature coefficient of resistivity. *J. Appl. Phys.*, 89:3939, 2001.

[299] O.F. Schirmer. EPR investigations of small electron and hole polarons in oxide perovskites. In *Defects and Surface-Induced Effects in Advanced Perovskites*, volume 77 of *NATO Science Series*, page 75. Kluwer Academic Publishers, 2000.

[300] R.R. Heikes. *Thermoelectricity.* Interscience, New York, 1961.

[301] D. Emin. Enhanced Seebeck coefficient from carrier-induced vibrational softening. *Phys. Rev. B*, 59:6205, 1999.

[302] G.D. Mahan. Polarons in heavily doped semiconductors. In *Polarons in Ionic Crystals and Polar Semiconductors*, page 553. North-Holland Publishing Company, 1972.

[303] K. Seeger. *Semiconductor Physics.* Springer-Verlag, Berlin, 4th edition, 1989.

[304] T. Varnhorst, O.F. Schirmer, H. Kröse, R. Scharfschwerdt, and Th.W. Kool. O^- holes associated with alkali acceptors in $BaTiO_3$. *Phys. Rev. B*, 53:116, 1996.

[305] S. Köhne, O.F. Schirmer, H. Hesse, Th.W. Kool, and V. Vikhnin. Ti^{3+} Jan-Teller polarons and bipolarons in $BaTiO_3$. *Journal of Superconductivity*, 12:193, 1999.

[306] E. Possenriede, H. Kröse, T. Varnhorst, R. Scharfschwerdt, and O.F. Schirmer. Shallow acceptor and electron conduction states in $BaTiO_3$. *Ferroelectrics*, 151:199, 1994.

[307] R. Scharfschwerdt, O.F. Schirmer, H. Kröse, and Th.W. Kool. Oxygen vacancy related defects in $BaTiO_3$. *Ferroelectrics*, 185:9, 1996.

[308] S. Lakkis, C. Schlenker, B.K. Chakraverty, R. Buder, and M. Marezio. Metal-insulator transitions in Ti_4O_7 single crystals: Crystal characterization, specific heat, and electron paramagnetic resonance. *Phys. Rev. B*, 14:1429, 1976.

[309] E. Possenriede, P. Jacobs, and O.F. Schirmer. Paramagnetic defects in $BaTiO_3$ and their role in light-induced charge transport: I. ESR studies. *J. Phys. Condens. Matter*, 4:4719, 1992.

[310] M. Bersohn and J.C. Baird. *An Introduction to Electron Paramagnetic Resonance.* W.A. Benjamin, Inc, New York, 1966.

[311] P.A. Cox. *The Electronic Structure and Chemistry of Solids.* Oxford University Press, Oxford, 1987.

[312] B.M. Kulwicki. PTC materials technology, 1955-1980. *Adv. Ceram*, 1:138, 1981.

[313] B. Hoffmann. Comment on "A systematic experimental and theoretical investigation of the grain-boundary resistivities of n-doped $BaTiO_3$ ceramics". *J. Appl. Phys.*, 50:1156, 1979.

[314] J.B. MacChesney and J.F. Potter. Factors and mechanisms affecting the positive temperature coefficient of resistivity of barium titanate. *J. Am. Ceram. Soc.*, 48:81, 1965.

[315] J. Frenkel. On the pre-breakdown phenomena in insulators and electronic semi-conductors. *Phys. Rev.*, 54:647, 1938.

[316] T. Matsuoka, Y. Matsuo, H. Sasaki, and S. Hayakawa. PTCR behavior of $BaTiO_3$ with Nb_2O_5 and MnO_2 additives. *J. Am. Ceram. Soc.*, 55:108, 1972.

[317] M.A. Lampert and P. Mark. *Current Injection in Solids*. Academic, New York, 1970.

[318] D.I. Aladashvili. In *Hopping and Related Phenomena edited by H. Fritzsche and M. Pollak*, page 283. World Scientific, Singapore, 1990.

[319] J.L. Hartke. The three-dimensional Poole-Frenkel effect. *J. Appl. Phys.*, 39:4871, 1968.

[320] H. Böttger and V. Bryksin. *Hopping Conduction in Solids*. Academie, Berlin, 1985.

[321] A.L. Efros. Theory of kinetic phenomena in semiconductors having a small mobility. *Sov. Phys. Solid State*, 9:901, 1967.

[322] H. Ihrig and W. Puschert. A systematic experimental and theoretical investigation of the grain-boundary resistivities of n-doped $BaTiO_3$ ceramics. *J. Appl. Phys.*, 48:3081, 1977.

[323] A. Broniatowski. Electronic states at the grain boundaries in semiconductors. In *Polycrystalline Semiconductors edited by G. Harbeke*, volume 57 of *Spriner Series in Solid-State Sciences*, page 95. Springer, Berlin, 1985.

[324] R. Einzinger. Development of physical models of zno varistors. In *Polycrystalline Semiconductors edited by G. Harbeke*, volume 57 of *Spriner Series in Solid-State Sciences*, page 228. Springer, Berlin, 1985.

[325] K. Hayashi, T. Yamamoto, and T. Sakuma. Grain orientation dependence of the PTCR effect in niobium-doped barium titanate. *J. Am. Ceram. Soc.*, 79:1669, 1996.

[326] I. Qazi, I.M. Reaney, and W.E. Lee. Order-disorder phase transition in $Ba(Zn_{1/3}Ta_{2/3})O_3$. *J. Europ. Ceram. Soc.*, 21:2613, 2001.

[327] S.L. Swartz and T.R. Shrout. Fabrication of perovskite lead magnesium niobate. *Mater. Res. Bull.*, 17:1245, 1982.

[328] Powder Diffraction File # 83-0713.

[329] N.E. Hill, W.E. Vaughan, A.H. Price, and M. Davies. *Dielectric Properties and Molecular Behaviour*. Van Nostrand Reinhold Company, London, 1969.

[330] H.M. O'Bryan Jr., J. Thomson Jr., and J.K. Plourde. A new BaO·TiO_2 compound with temperature-stable high permittivity and low microwave loss. *J. Am. Ceram. Soc.*, 57:450, 1974.

[331] Y. Fang, A. Hu, S. Ouyang, and J. Oh. The effect of calcination on the microwave dielectric properties of $Ba(Mg_{1/3}Ta_{2/3})O_3$. *J. Europ. Ceram. Soc.*, 21:2745, 2001.

[332] H.J. Lee, H.M. Park, Y.K. Cho, H. Ryu, J.H. Paik, S. Nahm, and J.D. Byun. Dielectric and structural characteristics in barium lanthanum magnesium niobate. *J. Am. Ceram. Soc.*, 83:937, 2000.

[333] T. Hiuga and K. Matsumoto. Ordering of $Ba(B_{1/3}B_{2/3})O_3$ ceramics and their microwave dielectric properties. *Proceddings of the 7th Meeting on Ferroelectric Materials and Their Applications, Jpn. J. Appl. Phys.*, 28:56, 1989.

[334] D.J. Barber, K.M. Moulding, J. Zhou, and M.Q. Li. Structural order in $Ba(Zn_{1/3}Ta_{2/3})O_3$, $Ba(Zn_{1/3}Nb_{2/3})O_3$, and $Ba(Mg_{1/3}Ta_{2/3})O_3$ microwave dielectric ceramics. *J. Mater. Sci.*, 32:1531, 1997.

[335] B.D. Cullity. *Elements of X-ray Diffraction.* Addison-Wesley Publishing Co., Reading, MA, 1978.

[336] Dr. J. Bartoll. Private communication.